

Nonlinear physics in soliton microcombs

Thesis by
Qifan Yang

In Partial Fulfillment of the Requirements for the
Degree of
Doctor of Philosophy

The logo for the California Institute of Technology (Caltech), featuring the word "Caltech" in a bold, orange, sans-serif font.

CALIFORNIA INSTITUTE OF TECHNOLOGY
Pasadena, California

2019
Defended March 13th 2019

© 2019

Qifan Yang

ORCID: 0000-0002-7036-1712

All rights reserved

ACKNOWLEDGEMENTS

First and foremost, I am deeply grateful to my advisor, Prof. Kerry Vahala, for his support and guidance over the years. More than an distinguished scientist, Prof. Vahala is no doubt the best mentor that I can ever imagine. He has given me complete freedom to exploit my research interest with valuable instructions. His devotion in science has motivated me to always stay hungry and stay foolish. Prof. Vahala is the perfect example as a scientist and mentor that I wish to follow throughout my career. It is a pride and a privilege to have ever been his student.

I would like to express my gratitude to Prof. Oskar Painter, Prof. Paul Bellan, and Prof. Andrei Faraon for their service as my graduation committee and insightful input to my thesis. I would also like to thank Dr. Scott Diddams, Prof. Tobias Kippenberg, Prof. Lan Yang, Prof. John Bowers, Prof. Amnon Yariv, and Prof. Qiang Lin for their support of my research and academic career.

My heartfelt appreciation goes to my colleagues. I would like to offer my special thanks to Dr. Xu Yi, Dr. Ki Youl Yang and Dr. Myoung-Gyun Suh for their helpful advice as well as productive collaborations. I gratefully acknowledge Dr. Seunghoon Lee, Dr. Dongyoon Oh, Dr Hansuek Lee, Dr. Yu-Hung Lai, Dr. Xinbai Li and Dr. Chengying Bao for their support. I also want to thank Boqiang Shen, Heming Wang, Xueyue Zhang, Lue Wu, and Zhiquan Yuan for their fidelity in research. I likewise thank Zhewei Zhang, Yonghwi Kim, Wen Hui Cheng, and Wei-Siang Lin in Caltech, Junqiu Liu from EPFL, and Dr. Minh Tran and Dr. Nicolas Volet from UCSB, as well as Yang He from Rochester for the exciting collaborations.

Special thanks also to my former advisor, Prof. Yun-Feng Xiao, for his hand-by-hand training and continuous support. I was fortunate to start my research under his guidance.

Finally, I owe my deepest gratitude to my family for their continuous and unparalleled love, help, and support. They sparked my curiosity for the world in my childhood, without which I would have never been a scientist by now. I am also deeply thankful to my wife, Yi Xin, for the resonance between us which has infinite Q factor. The journey we have survived has been an invaluable and unforgettable experience. With her company, I feel fearless facing any challenges in the future.

ABSTRACT

Like rulers of light, optical frequency combs consist of hundreds to millions of coherent laser lines, which are capable of measuring time and frequency with the highest degree of accuracy. Used to rely on table-top mode-locked lasers, optical frequency combs have been recently realized in a miniaturized form, namely the microcomb, using monolithic microresonators. Besides a reduction of footprint, microcombs could also achieve parity with traditional frequency combs in performance by mode-locking through the formation of “light bullets” called dissipative Kerr solitons. These soliton microcombs not only serve as a unique platform to study nonlinear physics, but also offer scalable and cost-effective solutions to many groundbreaking applications, spanning spectroscopy to time standards. In this thesis I will trace the physical origin of soliton microcombs, followed by their experimental realization in high-Q silica microresonators. The impact of several nonlinear process on solitons will be discussed, which leads to novel soliton systems, e.g., Stokes solitons and counter-propagating solitons. Utilizing these nonlinear properties, we show that soliton microcombs can be adapted for high-precision spectroscopic applications. In the end, a real-time method for monitoring transient behavior of solitons will be presented.

PUBLISHED CONTENT AND CONTRIBUTIONS

- [1] Yang He*, Qi-Fan Yang*, Jingwei Ling, Rui Luo, Hanxiao Liang, Mingxiao Li, Boqiang Shen, Heming Wang, Kerry Vahala, and Qiang Lin. A self-starting bi-chromatic LiNbO₃ soliton microcomb. *arXiv preprint arXiv:1812.09610*, 2018. URL: <https://arxiv.org/abs/1812.09610>
Q.-F.Y conducted the experiment, prepared the data, and participated in the writing of the manuscript.
- [2] Seung Hoon Lee*, Dong Yoon Oh*, Qi-Fan Yang*, Boqiang Shen*, Heming Wang*, Ki Youl Yang, Yu-Hung Lai, Xu Yi, Xinbai Li, and Kerry Vahala. Towards visible soliton microcomb generation. *Nat. Commun.*, 8(1295), 2017. DOI: 10.1038/s41467-017-01473-9
Q.-F.Y participated in the conception of the project, conducted the experiment, prepared the data, and participated in the writing of the manuscript.
- [3] Xinbai Li*, Boqiang Shen*, Heming Wang*, Ki Youl Yang*, Xu Yi, Qi-Fan Yang, Zhiping Zhou, and Kerry Vahala. Universal isocontours for dissipative kerr solitons. *Opt. Lett.*, 43(11):2567–2570, 2018. DOI: 10.1364/OL.43.002567
Q.-F.Y participated in the experiment.
- [4] Myoung-Gyun Suh*, Qi-Fan Yang*, and Kerry J Vahala. Phonon-limited-linewidth of brillouin lasers at cryogenic temperatures. *Phys. Rev. Lett.*, 119(14):143901, 2017. DOI: 10.1103/PhysRevLett.119.143901
Q.-F.Y participated in the conception of the project, conducted the experiment, prepared the data, and participated in the writing of the manuscript.
- [5] Myoung-Gyun Suh*, Qi-Fan Yang*, Ki Youl Yang, Xu Yi, and Kerry J Vahala. Microresonator soliton dual-comb spectroscopy. *Science*, 354(6312):600–603, 2016. DOI: 10.1126/science.aah651
Q.-F.Y participated in the conception of the project, conducted the experiment, prepared the data, and participated in the writing of the manuscript.
- [6] Nicolas Volet, Xu Yi, Qi-Fan Yang, Eric J Stanton, Paul A Morton, Ki Youl Yang, Kerry J Vahala, and John E Bowers. Micro-resonator soliton generated directly with a diode laser. *Laser Photonics Rev.*, 12(5):1700307, 2018. DOI: 10.1002/lpor.201700307
Q.-F.Y participated in the experiment.
- [7] Ki Youl Yang*, Dong Yoon Oh*, Seung Hoon Lee*, Qi-Fan Yang, Xu Yi, Boqiang Shen, Heming Wang, and Kerry Vahala. Bridging ultrahigh-q devices and photonic circuits. *Nat. Photon.*, 12(5):297–302, 2018. DOI: 10.1038/s41566-018-0132-5

Q.-F.Y participated in the experiment, prepared the data, and participated in the writing of the manuscript.

- [8] Qi-Fan Yang*, Boqiang Shen*, Heming Wang*, Minh Tran, Zhewei Zhang, Ki Youl Yang, Lue Wu, Chengying Bao, John Bowers, Amnon Yariv, et al. Vernier spectrometer using counterpropagating soliton microcombs. *Science*, 363(6430):965–968, 2019. DOI: 10.1126/science.aaw2317
Q.-F.Y conceived the project, conducted the experiment, prepared the data, and participated in the writing of the manuscript.
- [9] Qi-Fan Yang*, Xu Yi*, Ki Youl Yang, and Kerry Vahala. Spatial-mode-interaction-induced dispersive waves and their active tuning in microresonators. *Optica*, 3(10):1132–1135, 2016. DOI: 10.1364/OPTICA.3.001132
Q.-F.Y participated in the conception of the project, conducted the experiment, prepared the data, and participated in the writing of the manuscript.
- [10] Qi-Fan Yang*, Xu Yi*, Ki Youl Yang, and Kerry Vahala. Stokes solitons in optical microcavities. *Nat. Phys.*, 13(1):53–57, 2017. DOI: 10.1038/nphys3875
Q.-F.Y participated in the conception of the project, conducted the experiment, prepared the data, and participated in the writing of the manuscript.
- [11] Qi-Fan Yang*, Xu Yi*, Kiyoul Yang, and Kerry Vahala. Counter-propagating solitons in microresonators. *Nat. Photon.*, 11(9):560–564, 2017. DOI: 10.1038/nphoton.2017.117
Q.-F.Y participated in the conception of the project, conducted the experiment, prepared the data, and participated in the writing of the manuscript.
- [12] Xu Yi*, Qi-Fan Yang*, Ki Youl Yang*, Myoung-Gyun Suh, and Kerry Vahala. Soliton frequency comb at microwave rates in a high-Q silica microresonator. *Optica*, 2(12):1078–1085, 2015. DOI: 10.1364/OPTICA.2.001078
Q.-F.Y participated in the conception of the project, conducted the experiment, prepared the data, and participated in the writing of the manuscript.
- [13] Xu Yi*, Qi-Fan Yang*, Ki Youl Yang, and Kerry Vahala. Active capture and stabilization of temporal solitons in microresonators. *Opt. Lett.*, 41(9):2037–2040, 2016. DOI: 10.1364/OL.41.002037
Q.-F.Y participated in the conception of the project, conducted the experiment, prepared the data, and participated in the writing of the manuscript.
- [14] Xu Yi*, Qi-Fan Yang*, Ki Youl Yang, and Kerry Vahala. Theory and measurement of the soliton self-frequency shift and efficiency in optical microcavities. *Opt. Lett.*, 41(15):3419–3422, 2016. DOI: 10.1364/OL.41.00341
Q.-F.Y participated in the conception of the project, conducted the experiment, prepared the data, and participated in the writing of the manuscript.
- [15] Xu Yi*, Qi-Fan Yang*, Ki Youl Yang, and Kerry Vahala. Imaging soliton dynamics in optical microcavities. *Nat. Commun.*, 9(3565), 2018. DOI: 10.1038/s41467-018-06031-5

Q.-F.Y participated in the conception of the project, conducted the experiment, prepared the data, and participated in the writing of the manuscript.

- [16] Xu Yi*, Qi-Fan Yang*, Xueyue Zhang*, Ki Youl Yang, Xinbai Li, and Kerry Vahala. Single-mode dispersive waves and soliton microcomb dynamics. *Nat. Commun.*, 8:14869, 2017. DOI: 10.1038/ncomms14869

Q.-F.Y participated in the conception of the project, conducted the experiment, prepared the data, and participated in the writing of the manuscript.

*These authors contributed equally to this work.

TABLE OF CONTENTS

Acknowledgements	iii
Abstract	iv
Published Content and Contributions	v
Bibliography	v
Table of Contents	viii
List of Illustrations	x
Chapter I: Introduction	1
1.1 A brief history of time standards	1
1.2 Microcombs and soliton mode-locking	4
1.3 Thesis outline	10
Chapter II: Theory of dissipative Kerr solitons	12
2.1 Pulse propagation and optical solitons	13
2.2 Lugiato-Lefever equation	16
2.3 Modulational instability	19
2.4 Lagrangian formalism and moment analysis	21
2.5 Numerical method: split-step Fourier transform	24
2.6 Conclusion	26
Chapter III: Soliton microcombs in high-Q silica microresonators	27
3.1 Silica wedge resonators	27
3.2 Dispersion engineering of silica resonators	28
3.3 Active capturing and stabilization of soliton microcombs	31
3.4 Soliton microcombs at 1550 nm	35
3.5 Soliton microcombs at 1064 nm	39
3.6 Measurement of soliton properties	40
3.7 Conclusion	44
Chapter IV: Raman self-frequency shift in soliton microcombs	45
4.1 Lugiato-Lefever equation augmented by Raman terms	46
4.2 Theory of Raman self frequency shift	48
4.3 Measurement of Raman self frequency shift	51
4.4 Conclusion	54
Chapter V: Stokes solitons	55
5.1 Principle of Stokes solitons	55
5.2 Theory of Stokes solitons	57
5.3 Observation of Stokes solitons	63
5.4 Characterization of Stokes solitons	66
5.5 Threshold behavior	68
5.6 Conclusion	69
Chapter VI: Spatial-mode-interaction-induced dispersive-waves and their ac- tive tuning in microresonators	70

6.1	Observation of spatial-mode-interaction induced dispersive waves . .	70
6.2	Active tuning of dispersive waves	73
6.3	Conclusion	76
Chapter VII: Single-mode dispersive waves and soliton microcomb dynamics		78
7.1	Observation of single mode dispersive waves	78
7.2	Hysteretic behavior	81
7.3	Theory of single mode dispersive waves	82
7.4	Numerical simulation	89
7.5	Soliton repetition rate quiet point	90
7.6	Conclusion	97
Chapter VIII: Microresonator soliton dual-comb spectroscopy		98
8.1	Concept of microresonator soliton dual comb spectroscopy	99
8.2	Experimental setup and soliton generation	100
8.3	Electrical interferogram and spectra	102
8.4	Trace gas spectroscopy	104
8.5	Conclusion	105
Chapter IX: Counter-propagating solitons		107
9.1	Generation of counter-propagating solitons	107
9.2	Tuning and locking of soliton repetition rates	109
9.3	Phase-locking of counter-propagating solitons	115
9.4	Conclusion	121
Chapter X: Vernier spectrometer using counterpropagating soliton microcombs		123
10.1	Concept of Vernier spectrometer and measurement of static lasers . .	124
10.2	Measurement of dynamic lasers and high-resolution spectroscopy . .	126
10.3	Measurement of multi-line spectra	128
10.4	Signal processing	129
10.5	Conclusion	133
Chapter XI: Imaging soliton dynamics in microresonators		135
11.1	Coherent sampling of soliton motion	136
11.2	Observation of transient soliton dynamics	139
11.3	Tracking relative soliton motion and soliton decay	141
11.4	Numerical simulation	143
11.5	Experimental details	144
11.6	Conclusion	145
Chapter XII: Summary		147
Bibliography		148

LIST OF ILLUSTRATIONS

<i>Number</i>	<i>Page</i>
1.1 Time and frequency domain representation of an optical frequency comb. (a) A periodic pulse train with period T (repetition rate f_r). The carrier wave (red) and envelope (grey) are propagating at phase velocity and group velocity, respectively, which causes an increasing carrier-envelope phase offset ($\Delta\phi_o$) between consecutive pulses. (b) The optical spectrum of an OFC. The comb teeth (red) are separated by f_r , while the offset frequency is related to the carrier-envelope phase offset by $f_o = f_r\Delta\phi_o/2\pi$. The frequency of the comb tooth of order n can be expressed as $f_n = f_o + n f_r$. A common method to determine the offset frequency is called frequency comb self referencing. Specifically, the low-frequency portion of the OFC is frequency-doubled and mixed with its high-frequency portion, which gives the offset frequency f_o . (c) The optical spectrum of a fiber mode-locked laser. The repetition rate is 250 MHz, and the comb teeth are not resolved by the optical spectral analyzer. The inset shows a fiber mode-locked laser.	3
1.2 Multiple types of microresonators. (a) A Fabry-Pérot-type microresonator. (b) A whispering-gallery-mode microresonator. (c) A ring-shaped microresonator. (d) A silica whispering-gallery-mode microresonator on a chip. The photo is provided in courtesy of Lue Wu.	6
1.3 Principle of microcomb generation. (a)-(b) Level diagrams showing degenerate and non-degenerate FWM process. (c) The optical spectrum of a microcomb, where the central arrow represents the pump. Process I (II) corresponds to the degenerate (non-degenerate) FWM process. (d) Schematic representation of comb teeth and resonant modes. When moving away from the pump, the increasing offset between the comb tooth and the modes is induced by group velocity dispersion of the resonator.	7

1.4	Soliton microcombs. (a)-(b) Schematic illustrations showing a mode-unlocked comb and a soliton comb. The oscillations in the resonator represent spectral components of the comb, while the exterior red lines indicate the intracavity power. (c) A typical spectrum of a soliton microcomb. The repetition rate is 22 GHz. Inset: silica microresonators.	8
2.1	Schematic illustration of a continuously-driven microresonator. (a) Coordinates of lab frame. (b) Coordinates of rotational frame.	17
2.2	Numerical simulation of LLE. (a) Total intracavity power versus detuning while the pump is tuned across a resonance with increasing detuning. Parameters used in simulation: $f = 50$; $D_2/\kappa = 0.01$. 512 modes are involved. (b) Intracavity intensity versus polar angle at different detunings as marked in (a). I: Turing pattern; II: modulational instability comb; III: solitons.	26
3.1	Silica wedge resonator. (a) Top view of a silica wedge resonator taken by scanning electron microscope (SEM). The scale bar is 1 mm. Image is from Lue Wu. (b) SEM image showing cross section of a wedge resonator. The scale bar is $5 \mu\text{m}$. Image is from Dr. Seung Hoon Lee. (c) Finite element method (FEM) simulation of TM_1 mode profile. (d) Typical transmission spectrum while tuning a laser across a high-Q mode in a wedge resonator with 3 mm in diameter and $8 \mu\text{m}$ in thickness. The Lorentzian fitting (red) reveals intrinsic Q factor over 300 million.	28
3.2	Dispersion engineering via resonator thickness control. (a) A rendering of a silica resonator with the calculated mode profile of the TM_1 mode superimposed. (b) Cross-sectional SEM images of the fabricated resonators with different thickness. White scale bar is $5 \mu\text{m}$. (c) Simulated regions of normal and anomalous dispersion are shown versus silica resonator thickness (t) and pump wavelength. The zero dispersion wavelength (λ_{ZDW}) for the TM_1 mode appears as a blue curve. Plot is made for a 3.2-mm-diameter silica resonator. Three different device types, I, II, and III, which correspond to top, mid, and bottom panels in (b), are indicated for soliton generation at 1550 nm, 1064 nm, and 778 nm. The simulation is performed by Dr. Seung Hoon Lee.	29

- 3.3 Measured frequency dispersion (blue points) belonging to the soliton-forming mode families are plotted versus relative mode number, μ . To construct this plot, mode frequency relative to a $\mu = 0$ mode (mode to be pumped) is measured using a calibrated Mach-Zehnder interferometer (fiber optic based). To second order in the mode number, the mode frequency is given by the Taylor expansion $\omega_\mu = \omega_0 + \mu D_1 + \frac{1}{2}\mu^2 D_2$ and the dashed red curves are parabolic fittings with fitted parameters on the top of each panel. In the plot, the mode frequencies are offset by the linear term in the Taylor expansion to make clear the second-order group dispersion. The measured modes span wavelengths from 1520 nm to 1580 nm and $\mu = 0$ corresponds to a wavelength close to 1550 nm. 30
- 3.4 Pump power transmission versus tuning across a resonance used to generate the solitons. The data show the formation of steps as the pump tunes red relative to the resonance. Both blue-detuned and red-detuned operation of the pump relative to the resonance are inferred from generation of an error signal using a Pound-Drever-Hall system operated open loop. 32
- 3.5 (a) Simulated intracavity power in which the pump laser scans over the resonance from the blue side to the red side. The steps on the red-detuned side indicate soliton formation. (b) Schematic of experimental setup. (c) Four phases of feedback-controlled soliton excitation: (I) pump laser scans into cavity resonance from blue-detuned side; (II) laser scan stops and pump power is reduced ($\sim 10 \mu s$) to trigger solitons, and then increased ($\sim 100 \mu s$) to extend soliton existence range; (III) servo-control is engaged to actively lock the soliton power by feedback control of laser frequency; (IV) lock sustains and solitons are fully stabilized. The cavity-pump detuning (vertical axis) is relative to the hot cavity resonant frequency. 32

- 3.6 Demonstration of capture and locking of a soliton state. (a) Soliton excitation with "power kicking" but no active locking is shown. The soliton state destabilizes around 22ms due to thermal transients. Soliton power is shown in red and a Mach Zehnder (MZI) reference is in blue. (b) Soliton excitation with active locking is shown with conditions similar to panel (a). (c) Zoom-in view of panel (b). The four phases are indicated using the same background color scheme as in Figure 3.5. 35
- 3.7 Continuous soliton measurement over 19 hours. Soliton power are plotted versus time in hours. The soliton power experiences a slow drift to lower values which is attributed to a slow variation in either the power set point of the electronic control or in the detected power (perhaps due to temperature drift). 36
- 3.8 Experiment setup, soliton mode-family dispersion, optical spectrum and autocorrelation. (a) Experimental setup. EDFA: erbium-doped-fiber-amplifier; AOM: acousto-optic modulator; PD: photodetector; ESA: electrical spectral analyzer; OSA: optical spectral analyzer; FROG: frequency resolved optical gatings. (b) Measured mode family dispersion (blue points) belonging to the soliton-forming mode family is plotted versus relative mode number, μ . The presence of non-soliton forming mode families can be seen through the appearance of avoided mode crossings (spur-like features) that perturb the parabolic shape. Simulations of the non soliton mode families believed to be responsible for these spurs are provided (see mode 1 and mode 2 dashed curves). In addition, the normalized transverse intensity profiles for the soliton and non-soliton spatial modes are provided at the top of the panel (red indicates higher mode intensity). The simulation used the Sellmeier equation for the refractive index of silica. Oxide thickness, wedge angle, and radius were fine-adjusted to produce the indicated fits. (c) Optical spectrum of single soliton state is shown with a sech^2 envelope (red dashed line) superimposed for comparison. The pump laser is suppressed by 20 dB with an optical Bragg filter. (d) FROG (upper) and autocorrelation trace (lower) of the soliton state in c. The optical pulse period is 46 ps and the fitted pulse width is 250 fs (red solid line). 37

- 3.9 Detected phase noise and electrical spectra for three devices with corresponding mode dispersion and soliton data. Phase noise spectral density function plotted versus offset frequency from the detected soliton repetition frequency of three different devices. A Rohde Schwarz phase noise analyzer was used in the measurement. Inset shows the electrical spectrum of the soliton repetition frequency (21.92 GHz) for one device. The other devices had similar spectra with repetition frequencies of 22.01 and 21.92 GHz. The phase noise of the fiber pump laser is shown in green and was generated by mixing 2 nominally identical pump lasers to create a 2.7 GHz electrical beatnote. Several features in the pump laser phase noise are reproduced in the soliton phase noise (see features near and above 20 kHz). The black line connecting square dots is the measurement floor of the phase noise analyzer. 38
- 3.10 Microresonator dispersion engineering and soliton generation at 1064 nm. (a) Simulated dispersion (GVD) of TM mode families versus resonator thickness. The angle of the wedge ranges from 30° to 40° in the colored regions. Measured data points are indicated and agree well with the simulation. (b) Measured relative mode frequencies (blue points) plotted versus relative mode number of a soliton-forming TM1 mode family in a 3.4 μm thick resonator. The red curve is a parabolic fit yielding $D_2/2\pi=3.3$ kHz. (c) Experimental setup for soliton generation. A continuous-wave (CW) fiber laser is modulated by an electro-optic phase modulator (PM) before coupling to a ytterbium-doped-fiber-amplifier (YDFA). The pump light is then coupled to the resonator using a tapered fiber. Part of the comb power is used to servo-lock the pump laser frequency. FBG: fiber Bragg grating. PD: photodetector. PC: polarization controller. (d) Optical spectra of solitons at 1064 nm generated from the mode family shown in **b**. The two soliton spectra correspond to different power levels with the blue spectrum being a higher power and wider bandwidth soliton. The dashed vertical line shows the location of the pump frequency. The solid curves are sech^2 fittings. Inset: typical detected electrical beatnote showing soliton repetition rate. RBW: resolution bandwidth. 40

- 3.11 Control of soliton properties. (a) Measured soliton comb output power is plotted versus measured soliton pulse width (red points) with comparison to Eq. (3.1) (dashed red line). The measured power per central comb tooth is plotted versus pulse width (blue points) with comparison to Eq. (3.4) (dashed blue line). (b) The observed soliton spectra at the limits of the measurement in Figure 3.8(a) is shown (see arrows A and B in Figure 3.8(a)). Solid orange and green curves are simulations using the Lugiato Lefever equation including Raman terms. The indicated wavelength shifts between the pump and the center of the soliton spectrum result from Raman interactions with the soliton. The location of the pump line for both spectra is indicated by the dashed black line and has been suppressed by filtering. The inset shows a magnified view near the central region of the blue spectrum. The green (purple) envelope provides the Lugiato Lefever simulation with (without) Raman terms. The green spike is the location of the pump. (c) Measured minimum pump power for soliton existence is plotted versus measured soliton pulse width (red points) with comparison to Eq. (3.5) (dashed red line). Measured efficiency is plotted versus measured soliton pulse width (blue points) with comparison to Eq. (3.6) (dashed blue line). Simulation using Lugiato-Lefever equation including Raman terms improves agreement with data (small dashed red and blue lines). . . . 42
- 4.1 (a) Optical spectra measured for a dissipative Kerr cavity soliton at two operating points. The pump power is suppressed using a fiber grating filter. A $sech^2$ fit is shown as the orange curves and pulse widths inferred from the fitting are shown in the legend. The location of the pump line is indicated as the black line. The centers of the spectra are indicated by the green lines. (b) The measured Raman self-frequency-shift plotted versus $1/\tau_s^4$ for two devices. The red line is a linear fit according to Eq. (4.17). 52

4.2	The measured efficiency versus soliton pulse width is plotted (blue points) for two devices and compared with theory. Theory comparison with Raman (solid blue lines) and without Raman (dash blue lines) is presented. There are no free parameters in the comparison. The small deviations between the measurement and the theory could result from the presence of weak avoided mode crossings in the dispersion spectrum.	53
5.1	Principle of Stokes soliton generation. The Stokes soliton (red) maximizes Raman gain by overlapping in time and space with the primary soliton (blue). It is also trapped by the Kerr-induced effective optical well created by the primary soliton.	56
5.2	Stokes soliton formation in a microresonator. (a) Simulated intracavity comb power during a laser scan over the primary soliton pumping resonance from the blue (left) to the red (right) of the resonance. The detuning is normalized to the resonance linewidth. The initial step corresponds to the primary soliton formation, and the subsequent decrease in power corresponds to the onset of the Stokes soliton. The Stokes soliton power is shown in red. (b) Zoomed-in view of the indicated region from panel a. (c) Experimentally measured primary and Stokes soliton power during a laser scan showing the features simulated in panels a and b. (d) Simulation of the intracavity field in the moving frame of the solitons plotted versus the pump laser detuning. The detuning axis is scaled identically to Figure panel a. The Figure shows the primary soliton step region (below threshold) as well as the onset of the Stokes soliton (above threshold). (e) Temporal overlap of the primary and Stokes solitons is numerically confirmed in the plot of normalized power versus location angle within the resonator. The overlap confirms trapping and co-propagation. (f) Intracavity optical spectra of the primary and Stokes solitons.	62

- 5.3 Experimental setup and observation of Stokes soliton. (a) Experimental setup. (b) Free spectral range (FSR) versus wavelength measured for four mode families in a 3mm disk resonator. The mode families for the primary and Stokes soliton are shown in green and red, respectively. The FSR at the spectral center of the primary soliton is shown as a dashed horizontal line. Extrapolation of the Stokes soliton data (red) to longer wavelengths gives the FSR matching wavelength where the Stokes soliton forms. The background coloration gives the approximate wavelength range of the Raman gain spectrum. (c) Measured primary and Stokes soliton spectra. The Stokes soliton spectral center closely matches the prediction in (c). Sech^2 envelopes are shown on each spectrum. The primary soliton spectrum features a small Raman self-frequency shift. 64
- 5.4 Observation of Stokes solitons in multiple devices. (a) Dispersion spectra (see Figure 5.3(c)) for the Stokes soliton forming mode family measured in three devices (the upper spectrum is the device from Figure 5.3). Other mode families have been omitted in the plots for clarity. The horizontal dashed lines give the repetition frequency of the primary soliton in each device. Extrapolation of the dispersion data attained by simulation is provided to graphically locate the predicted Stokes soliton wavelength. (b) The measured primary and Stokes soliton spectra corresponding to the devices in (a). The spectral locations of the Stokes solitons agree well with the graphical predictions. 65
- 5.5 Soliton pulse and frequency measurements. (a) Frequency-resolved-optical-gating (FROG) traces of the primary and Stokes solitons. The primary soliton is amplified to 500 mW by an EDFA before coupling into the FROG setup, while the Stokes soliton is amplified to 10 mW by two cascaded semiconductor optical amplifiers with gain centered around 1620 nm. The period of the primary and Stokes solitons are 46 ps, the cavity round trip time. (b) Electrical spectra of the detected primary soliton pulse stream (blue) and the Stokes pulse stream (red). (c) Beatnote between neighboring comb teeth of the primary and Stokes solitons for a device like that in Figure 5.3. The beatnote is much noisier than the repetition frequency in (b). 67

- 5.6 Stokes soliton spectra, power and threshold measurements. (a) Soliton spectra are plotted below and above threshold. The upper insets show the spatial mode families associated with the primary and Stokes solitons. (b) Measurement of Stokes soliton power and primary soliton peak power versus total soliton power. The primary soliton peak power (blue) versus total power experiences threshold clamping at the onset of Stokes soliton oscillation. The theoretical threshold peak power from Eq. (5.13) is also shown for comparison as the horizontal blue dashed line. 68
- 6.1 Dispersive wave generation by spatial mode interaction. (a) Measured relative-mode-frequencies (blue points) of the soliton-forming mode family and the interaction mode family. Mode number $\mu = 0$ corresponds to the pump laser frequency of 193.45 THz (1549.7 nm). Hybrid mode frequencies calculated from Eq. (6.1) are shown in green and the unperturbed mode families are shown in orange. The dashed, horizontal black line determines phase matching for $\omega_r = D_{1A}$. (b) Measured soliton optical spectrum with dispersive wave feature is shown. For comparison, a Sech^2 fitting is provided in red. The pump frequency (black) and soliton center frequency (green) indicate a Raman-induced soliton self-frequency shift (also see Figure 6.2(c)). A microwave beatnote of the photo-detected soliton and dispersive wave is shown in the inset (frequency scale is offset by 21.973 GHz; resolution bandwidth is 10 kHz). 71

- 6.2 Dispersive wave phase matching condition and Raman-induced frequency shift. (a) Soliton and interaction mode family dispersion curves are shown (see Figure 6.1(a)) with phase matching dashed lines (see Eq. (6.4)). The black line is the case where $\omega_r = D_{1A}$ and the green line includes a Raman-induced change in ω_r . The intersection of the soliton branch with these lines is the dispersive wave phase matching point (arrows). (b) Soliton optical spectra corresponding to small (red) and large (blue) cavity-laser detuning ($\delta\omega$). Sech² fitting of the spectral envelope is shown as the orange curves. (c) Left: soliton self-frequency-shift, Ω , versus $1/\tau_s^4$ (τ_s is pulse width). The theoretical line is calculated with $Q = 166$ million (measured) and Raman shock time 2.7 fs. Right: dispersive wave spectra with cavity-laser detuning (soliton power and bandwidth) increasing from lower to upper trace. (d) Measured dispersive-wave peak frequencies (red points) and soliton repetition rate (blue points) are plotted versus soliton self-frequency shift. The dashed blue line is a plot of Eq. (6.3). The dashed red line uses Eq. (6.4) to determine the dispersive wave frequency ($\approx \mu_{DW}D_{1A} + \omega_0$) as described in the text. The offset for the repetition rate vertical scale is $D_{1A} = 21.9733$ GHz. 75
- 7.1 observation of single mode dispersive wave. (a) Measured relative mode frequencies are shown as blue points. The green and yellow dashed lines represent the fitted relative mode frequencies ($\Delta\omega_{\mu A}$ and $\Delta\omega_{\mu B}$) of the unperturbed soliton-forming mode family A and crossing mode family B, respectively. Relative mode frequencies for upper and lower branch hybrid-modes are $\Delta\omega_{\mu+}$ and $\Delta\omega_{\mu-}$. The red line illustrates the frequencies of a hypothetical soliton frequency comb. A non-zero slope on this line arises from the repetition rate change relative to the FSR at mode $\mu = 0$. (b) Measured optical spectra at soliton operating points I and II, corresponding to closely matched cavity-pump detuning frequencies, $\delta\omega$. A strong single-mode dispersive wave at $\mu = 72$ is observed for operating point II and causes a soliton recoil frequency shift. This frequency shift adds to the shift resulting from the Raman-induced SSFS. 79

- 7.2 Soliton hysteretic behavior induced by mode interaction. (a-b) Dispersive-wave power and soliton spectral center frequency shift versus cavity-pump detuning. Inset in (a): Measured (blue dots) and theoretical (red line) recoil frequency versus the dispersive wave power. 81
- 7.3 Numerical simulation and analytical model of single-mode dispersive wave generation and recoil. (a) Numerical (blue dots) and analytical (red solid line) soliton total frequency shift versus cavity-pump detuning. Points i, ii, iii, and iv correspond to specific soliton operating points noted in other Figure panels. (b) Numerical (blue dots) and analytical (red solid line) dispersive wave power (normalized to total soliton power) versus cavity-pump detuning. Inset: recoil frequency versus the dispersive wave power. (c) Comb spectra contributions from the two mode families (blue: soliton forming mode family A; red: crossing mode family B). (d) Time domain intracavity power. T_R is the cavity round trip time. 90
- 7.4 Soliton repetition frequency and phase noise measurement. (a) Measured (blue dots) and theoretical (red) soliton repetition frequency versus pump-cavity detuning. The offset frequency is 22.0167 GHz. The distinct soliton operating points I, II and III refer to phase noise measurements in panel b. Point III is near the quiet operation point. (b) Phase noise spectra of detected soliton pulse stream at three operating points shown in panel a. The black line connecting the square dots is the measurement floor of the phase noise analyzer. (c) Phase noise of soliton repetition rates at 25 kHz offset frequency plotted versus the cavity-pump detuning. The blue and red dots (lines) denote the experimental (theoretical) phase noise of the upper (blue) and lower (red) branch operating points, respectively. 91

- 7.5 Experimental setup and details on detuning-noise measurement. (a) The experimental setup includes both the soliton generation and characterization setup and a Pound-Drever-Hall (PDH) system operated open loop. The PDH is added to make possible the pump-cavity detuning noise measurement. Components included in the set up are an EOM: electro-optic modulator; EDFA: Erbium-doped fiber amplifier; AOM: acousto-optic modulator; PC: polarization controller; FBG: fiber Bragg grating; PD: photodetector; OSA: optical spectral analyzer; PNA: phase noise analyzer; LO: local oscillator. The OSA and PNA are shown for completeness. They are used to measure the soliton spectrum and repetition rate phase noise. They are not involved in measuring the detuning frequency noise. (b) Measurements that illustrate the pump-cavity detuning measurement. The green trace is the measured power transmission when scanning the pump laser frequency across a cavity resonance. The pump laser is phase modulated, the transmitted signal is detected and the resulting photocurrent is then mixed with the PDH local oscillator signal to generate the PDH error signal. Upon laser scan the PDH error signal (as measured on the oscilloscope) is generated as shown in the red trace. The pump laser is filtered using the fiber Bragg grating. The monitoring point for the detuning frequency measurement is indicated by the black dot. In order to convert scanning time into laser frequency, a calibrated Mach-Zehnder interferometer (MZI) records power transmission (blue trace) on an oscilloscope. The free-spectral-range of the MZI is 40 MHz. 93
- 7.6 Existence study for the quiet point. The maximum ratios of $|\partial\Omega_{\text{Recoil}}/\partial\delta\omega|$ to $|\partial\Omega_{\text{Raman}}/\partial\delta\omega|$ at varying normalized modal coupling rate G and normalized crossing-mode damping rate κ_B (dashed curve is unity ratio). The quiet point exists when this ratio is greater than unity (red region). Parameters correspond to a silica resonator. 96
- 7.7 Contour plot of detuning range. Color plot of detuning range of bistability versus spatial-mode coupling strength, G , and dissipation rate of crossing mode, κ_B . All quantities are normalized to the dissipation rate, κ_A , of the soliton-forming mode. 96

- 8.1 Microresonator-based dual-comb spectroscopy. Two soliton pulse trains with slightly different repetition rates are generated by continuous optical pumping of two microresonators. The pulse trains are combined in a fiber bidirectional coupler to produce a signal output path that passes through a test sample as well as a reference output path. The output of each path is detected to generate an electrical interferogram of the two soliton pulse trains. The interferogram is Fourier transformed to produce comb-like electrical spectra having spectral lines spaced by the repetition rate difference of the soliton pulse trains. The absorption features of the test sample can be extracted from this spectrum by normalizing the signal spectrum by the reference spectrum. Also shown is the image of two, silica wedge disk resonators. The disks have a 3 mm diameter and are fabricated on a silicon chip. 99
- 8.2 Detailed experimental setup and soliton comb characterization. (A) Continuous-wave (CW) fiber lasers are amplified by erbium-doped fiber amplifiers (EDFA) and coupled into high-Q silica wedge microresonators via tapered fiber couplers. An acousto-optic modulator (AOM) is used to control pump power to trigger soliton generation in the microresonators. Polarization controllers (PC) are used to optimize resonator coupling. A fiber Bragg grating (FBG) removes the transmitted pump power in the soliton microcomb. The pump laser frequency is servo controlled to maintain a fixed detuning from the microresonator resonance by holding the soliton average power to a fixed setpoint. An optical spectrum analyzer (OSA) monitors the spectral output from the microresonators. The two soliton pulse streams are combined in a bidirectional coupler and sent to a gas cell (or a WaveShaper) and a reference path. The interferograms of the combined soliton pulse streams are generated by photodetection (PD) and recorded on an oscilloscope. The repetition rates of the soliton pulse streams are also monitored by an electrical spectrum analyzer (ESA). The temperature of one resonator is controlled by a thermoelectric cooler (TEC) to tune the optical frequency difference of the two solitons. (B)-(C) Optical spectra of the microresonator soliton pulse streams. (D)-(E) Electrical spectra showing the repetition rates of the soliton pulse streams. The rates are given in the legends. . . . 101

- 8.3 Measured electrical interferogram and spectra. (A) The detected interferogram of the reference soliton pulse train. (B) Typical electrical spectrum obtained by Fourier transform of the temporal interferogram in A. To obtain the displayed spectra, ten spectra each are recorded over a time of $20 \mu\text{s}$ and averaged. (C) Resolved (multiple and individual) comb teeth of the spectrum in panel b are equidistantly separated by 2.6 MHz, the difference in the soliton repetition rate of the two microresonators. The linewidth of each comb tooth is $< 50 \text{ kHz}$ and set by the mutual coherence of the pumping lasers. (D)-(E) Fourier-transform (black) of the signal interferogram produced by coupling the dual-soliton pulse trains through the WaveShaper (see Fig. 8.2(A)) with programmed absorption functions (spectrally flat and sine-wave). The obtained dual-comb absorption spectra (red) are compared with the programmed functions (blue curves) from 1545 nm to 1565 nm. 103
- 8.4 Measured molecular absorption spectra. (A) Absorption spectrum of $2\nu_1$ band of H^{13}CN measured by direct power transmission using a wavelength-calibrated scanning laser (see Methods section) and comparison to the microresonator-based dual-comb spectrum. The residual difference between the two spectra is shown in green. (B) Overlay of the directly measured optical spectrum and the dual-comb spectrum showing line-by-line matching. The vertical positions of the two spectra are adjusted to compensate insertion loss. 105
- 9.1 Observation of counter-propagating solitons. (a) Rendering showing counter-propagating solitons within a high-Q wedge resonator. (b) Experimental setup. A continuous-wave fiber laser is amplified by an erbium-doped-fiber-amplifier (EDFA) and sent into two acousto-optic modulators (AOMs). The outputs from the AOMs are counter-coupled into the microresonator and generate counter-propagating solitons. The optical power of solitons in one direction is used to servo lock the pump laser to a certain frequency detuning relative to the cavity mode. FBG: fiber-Bragg grating; PD: photodetector. (c) Optical spectra of counter-propagating solitons. The location of the pump line is indicated by a dashed line. Measured autocorrelation traces are provided as insets. 108

- 9.2 Counter-propagating solitons with independently tuned repetition rates. (a) Electrical spectrum of photo-detected CW and CCW soliton pulse streams with pump frequency difference $\Delta\nu = 3.9$ MHz. Strong central peaks give the repetition rate of each soliton. The weaker spectral lines occurring over a broader spectral range are inter-soliton beat frequencies. Beat frequencies produced by the pump line of one soliton beating with higher and lower frequency comb teeth that neighbor the pump line of the other soliton are indicated by arrows. These spectral lines are shifted by $\Delta\nu = \pm 3.9$ MHz relative to the two, strong repetition-rate lines. (b) Upper trace is gray-banded region from (a). The pair of strong central peaks give the CW and CCW soliton repetition rates. Lower trace is the same electrical spectrum when the soliton repetition rates have locked to the same frequency (pump frequencies differ by $\Delta\nu = 77$ kHz). (c) Temporal interferogram of the baseband inter-soliton beat signal under unlocked condition in (a). (d) Plot of the difference in CW and CCW repetition rates versus difference in pump frequencies. The red line is a fit using the model in the Methods section. The inset shows that the two soliton repetition rates are locked over approximately 150 kHz pump difference frequency range. 110
- 9.3 Mechanism of CP soliton synchronization. (a) Rate locking occurs when the repetition rates of A_p and B_p are injection-locked by the backscattering of B_b and A_b , respectively. The upper panel shows four-wave-mixing sidebands (dashed blue lines) on the comb teeth of the CCW soliton (solid blue lines). These are created by taper backscattering of the CW pump. These sidebands are subsequently backscattered within the resonator into the CW direction (middle panel), where they (and their CW counter-parts) induce injection locking of the CW and CCW solitons (lower panel). (b) Simulation of CP soliton repetition rate locking. ϕ_{Ac} and ϕ_{Bc} are the peak position of solitons in CW and CCW rotation frames, respectively. See text for discussion of four panels. 113

- 9.4 Counter-propagating soliton phase locking at different repetition rates. (a) Schematic view of the counter-propagating soliton comb teeth. $\Delta\nu$ and Δf denote the pump frequency and repetition rate differences, respectively, and μ is mode number relative to the pump mode ($\mu = 0$). (b) Illustration of inter-soliton radio-frequency (RF) beatnotes produced under locked and unlocked conditions. (c) Measured RF beatnotes of unlocked CP solitons ($\Delta\nu = 1.5$ MHz). (d) Measured RF beatnotes of locked CP solitons ($\Delta\nu = 1.5$ MHz, $\Delta f = 25$ kHz). (e) Measured beat-note frequency spacing for locked and unlocked conditions plotted versus beatnote number. (f) High-resolution, zoom-in spectrum of RF beatnotes in (c). The corresponding beat note frequency is provided in the legend (25kHz is the fundamental beat note frequency). (g) Phase noise of the beatnotes at 1 Hz and 10 Hz offset frequencies in the phase noise spectrum plotted versus beatnote frequency. The fitting lines have an f^2 dependence. 116
- 9.5 Zoom-in of RF spectra showing dual soliton beatnotes. The blue trace denotes the CP solitons with integration time 50 ms. The red trace represents the results from solitons generated in two distinct microresonators with integration time 200 μ s. 118

- 10.1 Spectrometer concept, experimental setup and static measurement. (A) Counter propagating soliton frequency combs (red and blue) feature repetition rates that differ by Δf_r , phase-locking at the comb tooth with index $\mu = 0$ and effective locking at $\mu = N$ thereby setting up the Vernier spectrometer. Tunable laser and chemical absorption lines (grey) can be measured with high precision. (B) Experimental setup. AOM: acousto-optic modulator; CIRC: circulator; PD: photodetector. Small red circles are polarization controllers. Inset: scanning electron microscope image of a silica resonator. (C) Optical spectra of counter-propagating solitons. Pumps are filtered and denoted by dashed lines. (D) Typical measured spectrum of $V_1 V_2$ used to determine order n . For this spectrum: $\Delta f_{n1} - \Delta f_{n2} = 2.8052$ MHz and $\Delta f_r = 52$ kHz giving $n = 54$. (E) The spectrograph of the dual soliton interferogram (pseudo color). Line spacing gives $\Delta f_r = 52$ kHz. White squares correspond to the index $n = 54$ in panel C. (F) Measured wavelength of an external cavity diode laser operated in steady state. (G) Residual deviations between ECDL laser frequency measurement as given by the MSS and a wavemeter. Error bars give the systematic uncertainty as limited by the reference laser in panel B. 125
- 10.2 Laser tuning and spectroscopy measurements. (A) Measurement of a rapidly tuning laser showing index n (upper), instantaneous frequency (middle), and higher resolution plot of wavelength relative to average linear rate (lower), all plotted versus time. (B) Measurement of a broadband step-tuned laser as for laser in panel A. Lower panel is a zoom-in to illustrate resolution of the measurement. (C) Spectroscopy of $\text{H}^{12}\text{C}^{14}\text{N}$ gas. A vibronic level of $\text{H}^{12}\text{C}^{14}\text{N}$ gas at 5 Torr is resolved using the laser in panel A. (D) Energy level diagram showing transitions between ground state and $2\nu_1$ levels. The measured (reference) transition wavenumbers are noted in red (blue). 127

- 10.3 Measurement of a fiber mode-locked laser. (A) Pulse trains generated from a fiber mode-locked laser (FMLL) are sent into an optical spectral analyzer (OSA) and the MSS. (B) Optical spectrum of the FMLL measured by the OSA. (C) Optical spectrum of the FMLL measured using the MSS over a 60-GHz frequency range (indicated by dashed line). (D) Measured (blue) and fitted (red) FMLL mode frequencies versus index. The slope of the fitted line is set to 249.7 MHz, the measured FMLL repetition rate. (E) Residual MSS deviation between measurement and fitted value. 129
- 10.4 Multi-frequency measurements. (A) A section of $\tilde{V}_{1,2}$. Pairs of beatnotes coming from the same laser are highlighted and the derived n value is marked next to each pair of beatnotes. (B) Zoom-in on the highlighted region near 858 MHz in (A). Two beatnotes are separated by 1.0272 MHz. (C) Cross-correlation of \tilde{V}_1 and \tilde{V}_2 is calculated for each n and the maximum can be found at $n = 63$ 132

- 11.1 Coherent sampling of dissipative Kerr soliton dynamics. (a) Conceptual schematic showing microresonator signal (red) combined with the probe sampling pulse train (blue) using a bidirectional coupler. The probe pulse train repetition rate is offset slightly from the microresonator signal. It temporally samples the signal upon photo detection to produce an interferogram signal shown in the lower panel. The measured interferogram shows several frame periods during which two solitons appear with one of the solitons experiencing decay. (b) Left panel is the optical spectrum and right panel is the FROG trace of the probe EO comb (pulse repetition period is shown as 46 ps). An intensity autocorrelation in the inset shows a full-width-half-maximum pulse width of 800 fs. (c) Microresonator pump power transmission when the pump laser frequency scans from higher to lower frequency. Multiple ‘steps’ indicate the formation of solitons. (d) Imaging of soliton formation corresponding to the scan in panel (c). The x-axis is time and the y-axis is time in a frame that rotates with the solitons (full scale is one round-trip time). The right vertical axis is scaled in radians around the microresonator. Four soliton trajectories are labeled and fold-back into the cavity coordinate system. The color bar gives their signal intensity. (e) Soliton intensity patterns measured at four moments in time are projected onto the microresonator coordinate frame. The patterns correspond to initial parametric oscillation in the modulation instability (MI) regime, non-periodic behavior (MI regime), four soliton and single soliton states. 137
- 11.2 Measurements of non-repetitive soliton events. (a) Two solitons collide and annihilate. A wave splash appears in the collision. (b) Two solitons survive a collision, but collide again and one soliton is annihilated. (c) Two solitons collide and merge into a single soliton. (d) A soliton hops in location when another soliton is annihilated. The measurement frame rate is 50 MHz in all panels. Inset panels show similar collision events from numerical simulation, including the appearance of the wave splash (inset in panel (a)). 140

- 11.3 Temporal and spectral measurements of breather solitons. (a) Motion of a single soliton state showing peak power breathing along its trajectory. Panel (c) presents the zoom-in view of the white rectangular region. (b) Spectral dynamics corresponding to panel (a). The y-axis is the relative longitudinal mode number corresponding to specific spectral lines of the soliton. Mode zero is the pumped microresonator mode. The soliton spectral width breaths as the soliton peak power modulates. The spectrum is widest when peak power is maximum. (c) Zoom-in view of the white rectangular region in panel (a). (d) Soliton amplitude and pulse width breathing corresponding to panel (c). The frame rate is 50 MHz for all panels. 141
- 11.4 Measurement of relative soliton positions and soliton decay. (a) Plot of the relative positions of four solitons while the pumping laser frequency is scanned (high to low). The reference soliton, used to establish zero angular position, is indicated and all solitons have stable relative positions after only several μs of motion. (b) The relative positions of five solitons is measured versus time as the pump laser frequency is scanned. The soliton relative positions stabilize and then destabilize at 22 μs . The frame rates for panels (a) and (b) are 10 and 50 MHz, respectively. (c) Interferogram envelope showing a single soliton experiencing decay. An exponential fitting is given as the dashed black line. (d) The measured pulse width (blue) is plotted versus time and its resolution limit (dashed blue line) is set by the EO comb pulse width. The product of soliton amplitude and pulse width is plotted in red. 142
- 11.5 Simulation of microresonator soliton formation. (a) Simulated intracavity power plotted versus time as the pumping laser is tuned across a cavity resonance from higher to lower frequencies. The step features correspond to the formation of solitons. (b) Simulation results corresponding to panel (a) and showing the formation of multiple solitons. In the simulation, the Raman effect and avoided mode crossing are included. 143

- 11.6 Experimental setup. Schematic showing the three functional sections in the experiment. CW laser: continuous-wave laser; EDFA: erbium-doped-fiber-amplifier; AOM: acousto-optic modulator; BPF: bandpass filter; PC: polarization controller; PM: phase modulator; IM: intensity modulator; PS: phase shifter; ATT: attenuator; Amp: RF amplifier; DC: DC voltage source; WS: optical waveshaper; FBG: fiber-Bragg-gating; PD: photodetector. 144

Chapter 1

INTRODUCTION

1.1 A brief history of time standards

Recorded human history started with time measurement. The seasonal floods, the migration of animals, and the moon phases, are all natural events that announce the passage of time. Ancient Egyptians used sundials, whose shadows tracks the movement of the sun, to measure the length of the day, later followed by water clocks which rely on steady water flows. However, these “clocks” did not represent a universal time standard, as the solar time varies by seasons and latitudes, and water flows depend on different instruments. Until the Renaissance, Christiaan Huygens first introduced general physical quantities - at that time the gravitational acceleration - into time measurement by connecting a pendulum to a mechanical clock. The error of a pendulum clock, which was 1 minute per day at its invention, was reduced to less than 1 seconds per day in later refinements.

The standardized measure of time, which no longer relied on celestial bodies, has revolutionized astronomy, navigation, and geography. To unify such time standards for scientific, political, and commercial purposes, the International Meridian Conference held in 1884 agreed that global time should be synchronized to the best pendulum clock in Greenwich Observatory via telegraphs. Other time standards were later adopted for higher precision, e.g., the Shortt–Synchronome clocks which deliver the pendulum cycles to the mechanical clocks using electrical pulses [1], and quartz oscillators which serve as tuning forks to produce radio frequency signals [2]. These clocks are capable of measuring a day with error below 1 ms, but their stability is still subject to size and temperature, which requires further calibration.

The atomic clocks and cesium standard

The search for more precise, stable, and universal time standards continued [3]. The idea of using atoms as natural standard of time was conceived by Lord Kelvin as early as 1879, and the first atomic clock was experimentally demonstrated by Harold Lyons with ammonia gas cells [4], whose performance is comparable to quartz oscillators. The foundation of modern atomic standards was established by Isidor Rabi, whose study unveiled the dynamics of molecular beams in oscillatory magnetic fields [5]. Specifically, an oscillatory driving field causes cyclic transition in a two-level system

known as the Rabi cycle. The number of atoms that are in excitation level reaches its maximum when the frequency of the driving field matches the energy difference between the two levels. Using such approach, microwave signals can be locked to atomic transitions and harness their stability. Rabi's student, Norman Ramsey, improved this method by introducing successive oscillatory fields [6], which was later found exceptionally useful. The first cesium clock was built in 1955, whose error was below 1 second in 300 years, surpassing all existing means of time measurement [7]. Therefore, in 1967, the SI unit of time was defined by hyperfine structure of a cesium atom, which marked that cesium standard came of age.

The stability of an atomic clock can be described by its fractional instability defined as $\delta\nu/\nu$, where $\delta\nu$ and ν denote the linewidth and frequency of the transition used, respectively. The random thermal motion of atoms would broaden its spectral linewidth via Doppler shift, which can be suppressed using laser cooling technique [8–10]. By shining laser beams whose frequencies are slightly lower than certain atomic transitions, the chance of an atom absorbing photons that are propagating oppositely is promoted, which in turn slows the atom. If this process is repeated multiple times, an atomic ensemble can be cooled to a limit very close to absolute zero, leading to significant narrowing of their spectral linewidths. Such Doppler-cooling method paves the way to new concepts like atomic fountain clocks [11] and optical lattices [12].

Optical frequency combs: counting light cycles

Another approach to reduce the instability is by increasing the frequency ν , i.e., counting more ticks within a second (a periodic signal ticks once every cycle). The state-of-the-art microwave oscillators can work up to 100 GHz, which is an order of magnitude higher than the frequency of a cesium clock, 9.2 GHz. For better precision, microwave oscillators could be superseded by light, which counts time by femtosecond. The development of ultrastable lasers locked to atoms and molecules enables the possibility of time standards at optical frequencies.

However, counting optical cycles is never easy, since no electronics are functional at optical frequencies. The optical signal has to be divided down to radio frequency/microwave region for detection. To solve this issue and measure the speed of light more accurately, Researchers in NIST constructed a frequency-synthesis chain, where a series of lasers/oscillators are locked by heterodyne method so that optical signals are linked via microwaves in a cascaded manner [13]. Regardless

of its complexity, the frequency chain indeed conveyed the fundamental principles of optical frequency combs (OFCs): rulers of optical frequencies which consist multiple coherent lasers.

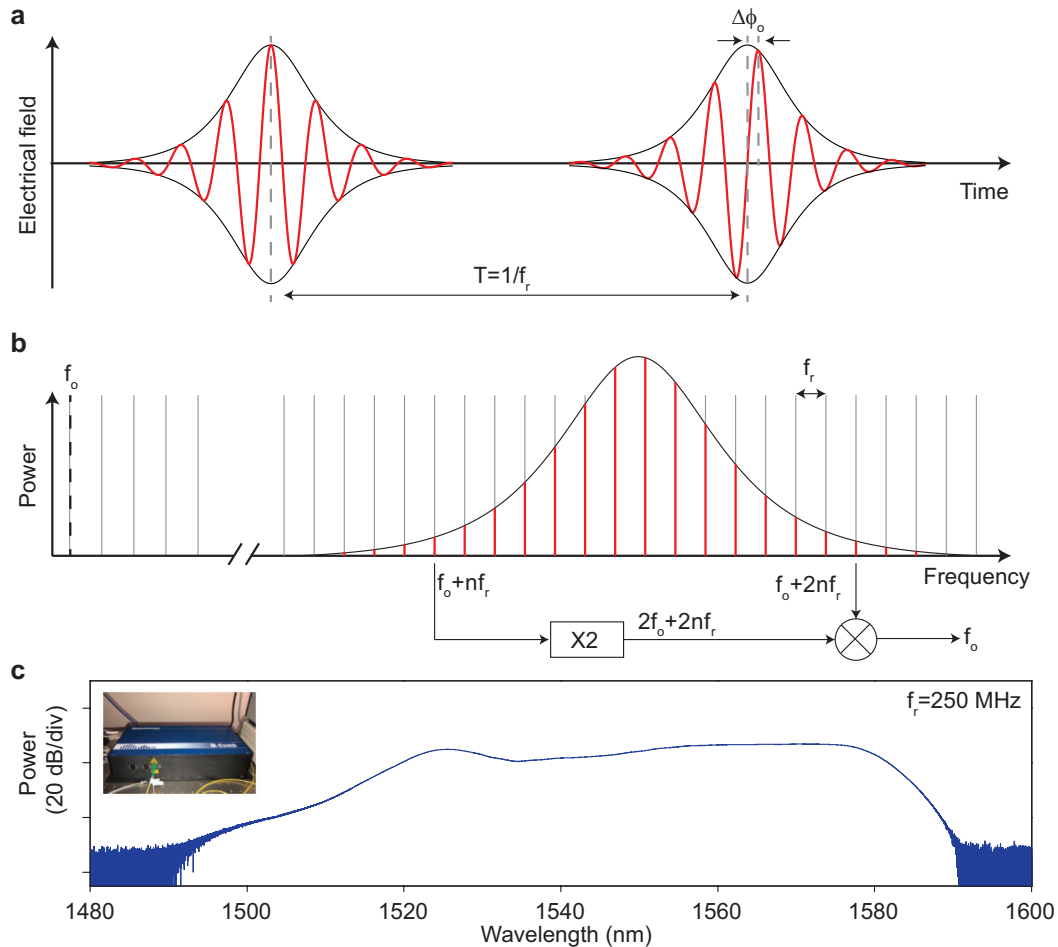


Figure 1.1: Time and frequency domain representation of an optical frequency comb. (a) A periodic pulse train with period T (repetition rate f_r). The carrier wave (red) and envelope (grey) are propagating at phase velocity and group velocity, respectively, which causes an increasing carrier-envelope phase offset ($\Delta\phi_o$) between consecutive pulses. (b) The optical spectrum of an OFC. The comb teeth (red) are separated by f_r , while the offset frequency is related to the carrier-envelope phase offset by $f_o = f_r\Delta\phi_o/2\pi$. The frequency of the comb tooth of order n can be expressed as $f_n = f_o + nf_r$. A common method to determine the offset frequency is called frequency comb self referencing. Specifically, the low-frequency portion of the OFC is frequency-doubled and mixed with its high-frequency portion, which gives the offset frequency f_o . (c) The optical spectrum of a fiber mode-locked laser. The repetition rate is 250 MHz, and the comb teeth are not resolved by the optical spectral analyzer. The inset shows a fiber mode-locked laser.

The development of OFCs has been thoroughly covered in the Nobel lectures by John Hall and Theodor Hansch [14, 15]. The first rudiments of OFCs date back to '60s, when mode-locked lasers were invented [16–19]. They produced periodic pulse trains, which give equally spaced, comb-like fringes in spectral domain, as shown in Figure 1.1. However, there still exists substantial discrepancy between those early mode-locked lasers and modern OFCs. In order to turn a mode-locked laser into an OFC, the parameters that define a comb, namely the offset frequency f_o and the repetition rate f_r , need to be measured and controlled. The repetition rate f_r can be easily derived from the beatnotes between adjacent comb teeth, while the determination of the offset frequency remained a challenge. Until late '90s, the development of photonic crystal fibers for supercontinuum generation [20] gave rise to octave-spanning OFCs [21, 22], which allowed the detection of the offset frequency via a method called self-referencing, as depicted in Figure 1.1(b).

Optical-rate signals derived from lasers and atomic transitions can now be accurately measured by referencing them to specific comb teeth. Soon OFC-based optical clocks were developed, showing unparalleled performance which, of course, surpassed cesium standard [23–28]. To date, the best optical clock, which uses Strontium atoms trapped in optical lattices, is able to reach 10^{-19} level in relative accuracy, which is akin to a second versus the entire age of the universe (13.8 billion years) [29].

Besides next generation time standard, OFCs also have a broad impact in science and technology, including but not limited to, optical frequency synthesis [30–33], spectroscopy [34–37], ranging [38], astronomical calibration [39–41], and attosecond physics [42]. It is noted that, for many applications, resolving the offset frequencies is not mandatory, while the stability of repetition rates and the equidistance of comb teeth is crucial. Therefore, in this thesis, we take the loose definition of optical frequency combs: a series of phase-locked, coherent lasers featuring equally spaced frequencies.

1.2 Microcombs and soliton mode-locking

The great success of optical frequency combs is primarily built on mode-locked lasers [43]. The first mode-locking was achieved by acousto-optic modulating a piece of fused quartz in a laser cavity [16]. If the modulation period matched cavity round trip time, pulsed output was observed from the cavity. Later saturable absorbers were introduced to Q-switch the laser cavity so as to generate mode-

locked pulses [17, 18], and their implementation in continuously-driven laser cavities was theoretically studied [44] and demonstrated [19]. More approaches such as additive pulse mode-locking and Kerr mode-locking were developed, which have been reviewed in detail by Haus [45].

Nowadays, Ti-sapphire mode-locked lasers [46] and fiber mode-locked lasers [47] have become the most conventional platforms for OFCs, since they are able to generate ultrashort pulses. Besides mode-locking, electro-optic modulating a continuous-wave laser has provided an alternative route to produce a frequency comb [48–50]. These instruments are generally power-consuming, and require delicate laboratory environment to operate. Integrating these systems on a photonic chip would revolutionize instrumentation, and enable applications in more cluttered environment, e.g., space, a miniaturized form of the OFC is desired. Recent advance in microphotonics has led to a miniaturized form of optical frequency combs, namely microcombs [51, 52]. They are generated in monolithic optical microresonators with a dramatic reduction in footprint and power consumption. Some of them are compatible with integrated photonic systems, and could be massively produced using conventional complementary metal–oxide–semiconductor (CMOS) technology [52].

Optical microresonators

Optical microresonators are able to trap light at discrete resonant frequencies in a tiny space [53]. Two figures of merit are often used to compare microresonators: quality (Q) factor and effective mode volume. The quality factor is a dimensionless parameter defined as the ratio between the resonant frequency, ω_o , and the photon damping rate, κ , which is given by

$$Q = \frac{\omega_o}{\kappa}. \quad (1.1)$$

Therefore, a higher Q means slower dissipation of intracavity photons, i.e., a longer photon lifetime. The effective mode volume determines the field confinement of the resonator, and a smaller effective mode volume would lead to a denser light field.

Microresonators can be classified according to their trapping mechanism. As shown in Figure 1.2, a Fabry-Pérot-type microresonator traps photons using a pair of high-reflectivity mirrors, while whispering-gallery-mode (WGM) microresonators and microrings confine light via total internal reflection [53]. To date, over 10 billion Q has been reported in a crystalline WGM microresonator [54], and Q factors close to a billion have been realized on chip-based platforms [55]. In these high-Q devices, the optical intensity can be dramatically enhanced by many orders of

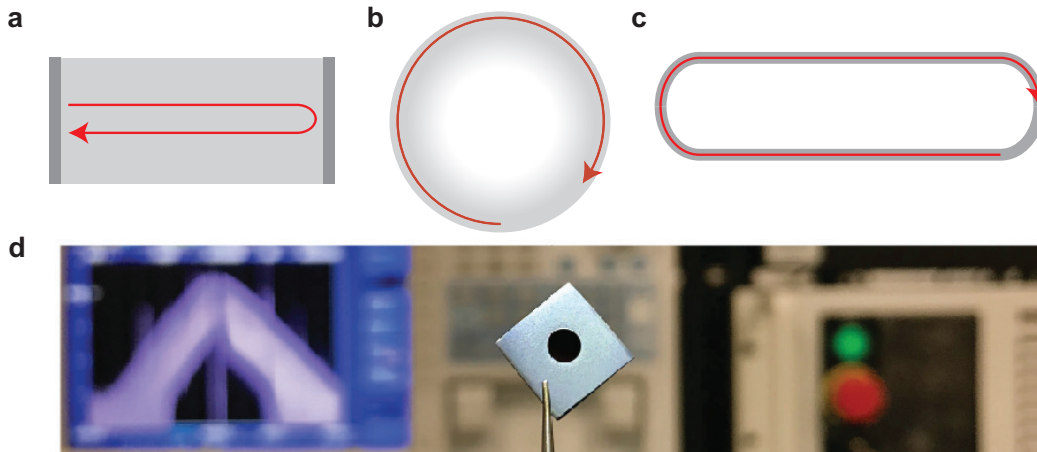


Figure 1.2: Multiple types of microresonators. (a) A Fabry-Pérot-type microresonator. (b) A whispering-gallery-mode microresonator. (c) A ring-shaped microresonator. (d) A silica whispering-gallery-mode microresonator on a chip. The photo is provided in courtesy of Lue Wu.

magnitude, which is sufficient to trigger many nonlinear process, e.g., thermo-optic effect [56, 57], Raman lasing [58], harmonic generation [59], cavity-optomechanics [60] and Brillouin scattering [55].

Microcombs

The process that gives rise to the formation of microcombs is four wave mixing (FWM), which is associated with optical Kerr effect [61]. There are two types of FWM, (i) the degenerate case where two photons of identical frequencies are converted to two frequency-shifted photons, and (ii) the non-degenerate case where all four photons feature different frequencies, as depicted in Figure 1.3(a)-(b).

FWM occurs in a series of longitudinal modes in the microresonator with proper group velocity dispersion (usually anomalous dispersion). Pumped by a monochromatic laser, the first few optical sidebands were generated spontaneously via degenerate FWM process, which can be further cascaded via FWM process to create an OFC, as shown in Figure 1.3(c) [51, 52, 62]. It is noted that the pump also serves as a comb tooth. In a fully-developed microcomb where each longitudinal mode is filled by a comb tooth, the repetition rate is defined by the free-spectral-range (FSR) of the microresonator.

The microcomb can be mode-locked if the initial pair of sidebands are generated natively-spaced to the pump, since the phase of each comb tooth can be defined via

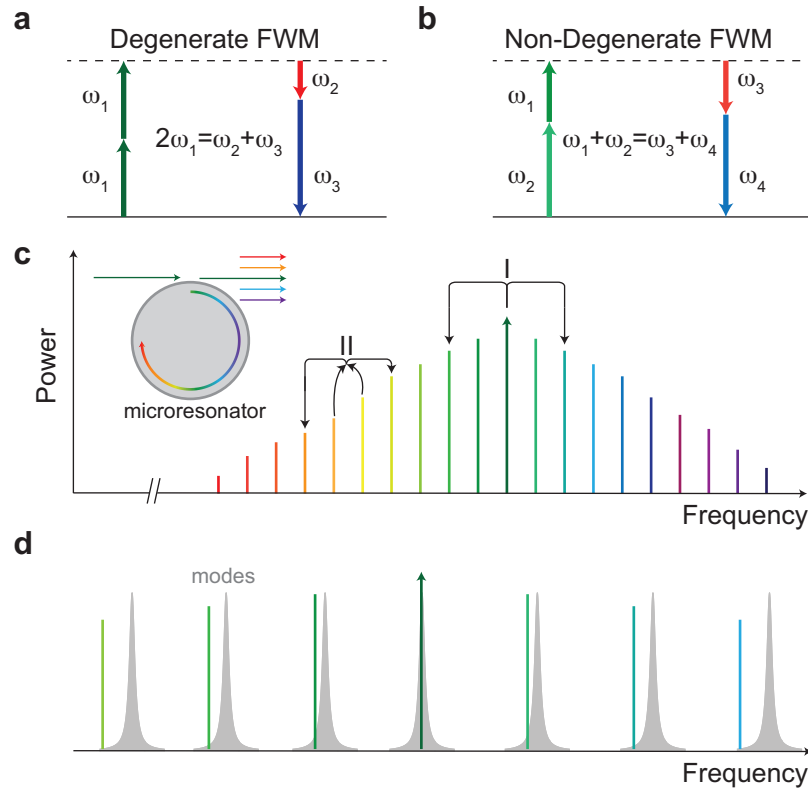


Figure 1.3: Principle of microcomb generation. (a)-(b) Level diagrams showing degenerate and non-degenerate FWM process. (c) The optical spectrum of a microcomb, where the central arrow represents the pump. Process I (II) corresponds to the degenerate (non-degenerate) FWM process. (d) Schematic representation of comb teeth and resonant modes. When moving away from the pump, the increasing offset between the comb tooth and the modes is induced by group velocity dispersion of the resonator.

the cascaded FWM process [51, 52]. However, it requires a strong anomalous group velocity dispersion, which limits the spectral bandwidth of the comb due to the frequency walking-off between the modes and the comb tooth, as shown in Figure 1.3(d). Moreover, it is found that, if such requirement is not satisfied, noise would build up during the formation of the comb, which results in non-equidistance of the comb spacing [62]. Indication of mode-locking was observed [63–65], but for a long time, reliably mode-locking a microcomb has remained a challenge.

Soliton microcombs

The recent development of soliton mode-locking technique has provided a route to stably mode lock microcombs [66–68]. Once soliton mode-locking occurs, non-dispersive wavepackets called dissipative Kerr solitons (DKSs) form and recirculate

along the microresonators indefinitely. The phases of the comb teeth are synchronized, distinct from the mode-unlocked case, as depicted in Figure 1.4(a)-(b). A typical spectrum of a soliton microcomb is shown in Figure 1.4(c), which features a smooth, reproducible spectral envelope in addition to equidistant comb teeth.

Soliton mode-locking was first demonstrated in a fiber-ring resonator upon pulsed seeding [69], while in microresonators soliton pulses can form spontaneously on continuous-wave background [70]. To date, soliton microcombs have been demonstrated on a wide range of material platforms, including magnesium fluoride [66, 71], silica [67, 72–75], silicon nitride [68, 76–78], silicon [79], lithium niobate [80] and aluminum nitride [81]. Their performance has reached parity with their table-top counterparts in both spectral bandwidth [82, 83] and coherence [71, 84]. The boost of Q factors in integrated devices has dramatically reduced the power consumption of soliton microcombs [73, 85], which paves the way towards fully-integrated soliton microcomb sources [86].

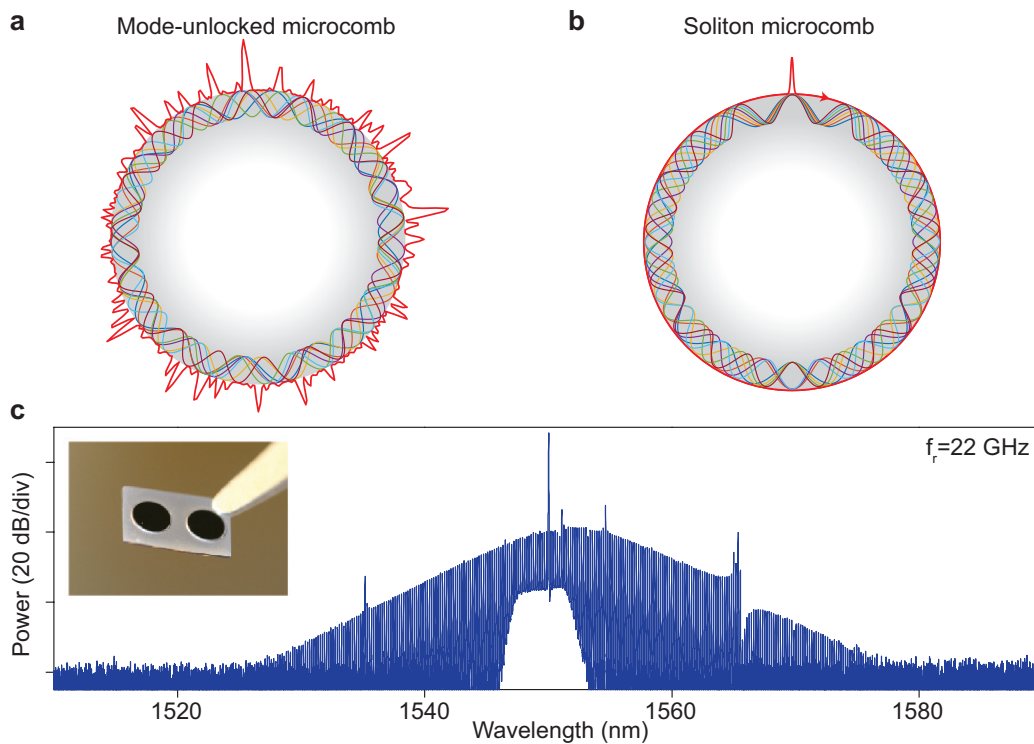


Figure 1.4: Soliton microcombs. (a)-(b) Schematic illustrations showing a mode-unlocked comb and a soliton comb. The oscillations in the resonator represent spectral components of the comb, while the exterior red lines indicate the intracavity power. (c) A typical spectrum of a soliton microcomb. The repetition rate is 22 GHz. Inset: silica microresonators.

Physics of soliton microcombs

The realization of particle-like optical solitons in microresonators has offered a rich landscape of nonlinear phenomena, including:

Raman-effect-related phenomena Raman nonlinearity can induce a spectral red-shifting of the soliton microcomb, known as the soliton-self-frequency-shift [87, 88]. Under certain circumstances, it can also serve as a gain medium for the regeneration of parasite solitons called Stokes solitons [89].

Higher-order dispersion Local spectral enhancement called dispersive waves are created on top of soliton microcombs by introducing higher-order dispersion, with behavior similar to Cherenkov radiation [68, 82, 83].

Mode-interaction-induced dispersive waves Dispersive waves can also emerge via the interaction between different transverse modes, which have shown to affect DKSs in their formation and dynamics [84, 90–93].

Breather solitons The pulse width and spectrum of a soliton microcomb can experience periodic modulation in a recurring manner, usually with the presence of a strong continuous background [93–96].

Multiple soliton dynamics More than one DKS can reside in a microresonator, forming assemblies analogous to molecules [97] and crystals [98], or in a spatial multiplexing manner [99, 100]. It is also possible to synchronize solitons that are generated in separate microresonators [101].

Dark solitons In contrast to bright solitons, dark solitons appear in microresonators featuring normal dispersion with local dispersion perturbation, which shows a high pump-to-comb conversion efficiency [102].

Harmonic generation Second and third-order nonlinearity could extend the spectral coverage of soliton microcombs via harmonic generation, which is potentially useful for microcomb self-referencing [80].

Application of soliton microcombs

Besides novel physics, the development of soliton microcombs has also given a rapid rise of a number of applications, with representative examples listed as follows:

Optical clocks Soliton microcombs could provide a coherent microwave-to-optical link so as to harness the stability of atomic transition. A dual-reduction scheme involving two soliton microcombs are currently used for power efficiency [103].

Optical frequency synthesis Operated in a reverse way of optical clocks, an optical frequency synthesizer generates optical signals from stable microwave sources, which can be implemented on photonic chips using dual soliton microcombs [104].

Spectroscopy Dual-comb spectroscopy is a powerful tool for chemical sensing, and soliton microcombs could offer a portable solution [105–108]. High-resolution spectroscopy has also been realized using soliton microcombs with the assist of a tunable laser [109].

LIDAR The interference between two DKSs can be used to discriminate submicron change in distance, creating a chip-based LIDAR source [110, 111].

Astronomical calibration The relatively large FSR of soliton microcombs make them ideal for calibrating astronomical signals, especially in the search for exoplanets [112, 113].

Coherent communications The coherent, equally spaced comb teeth of DKSs can be utilized for massive data transmission via wavelength multiplexing, with data rate up to 50 Tbit/s demonstrated [114, 115].

1.3 Thesis outline

In this thesis we focus on the nonlinear physics associated with soliton microcombs, including its impact on spectroscopic applications. The thesis is organized as follows:

Chapter 2 introduces the theoretical background of soliton formation in microresonators. The physical origin of soliton microcombs and their dynamics is derived analytically from Lugiato-Lefever equation, and methods of numerical simulation are also included, which will be used throughout the thesis.

Chapter 3 describes the experimental realization of soliton microcombs in high-Q silica microresonators near 1550 nm and 1064 nm [67, 88, 116]. Details of dispersion engineering will be discussed. The properties of soliton microcombs are characterized and compared with theoretical predictions.

Chapter 4 and **Chapter 5** discuss the effect of Raman nonlinearity on soliton microcombs, which gives rise to two novel phenomena, soliton self-frequency shift [88] and Stokes solitons [89].

Chapter 6 and **Chapter 7** study the impact of modal interaction on soliton microcombs, which can induce dispersive waves and thereby affect soliton dynamics [84, 90].

Chapter 8 presents a spectroscopic application based on dual soliton microcombs [105]. Their interference can be used to trace optical absorption of chemicals using electronics.

Chapter 9 and **Chapter 10** describe a dual soliton system propagating in clockwise and counterclockwise directions within a single microresonator [99]. They are shown to feature excellent relative coherence so as to be applied for acquisition of laser frequency across a broadband [109].

Chapter 11 utilizes a tunable electro-optic frequency comb to monitor soliton dynamics in real time, where various transient phenomena are observed [117].

Chapter 2

THEORY OF DISSIPATIVE KERR SOLITONS

Dispersion distorts most wavepackets while propagating in a medium. As an exception, solitons or solitary waves sustain their waveform by balancing dispersion with nonlinearity. First observed as water waves by Scottish physicist John Russell in 1834, solitons have been discovered in many forms such as assemblies of photons [118, 119] and cold atoms [120, 121]. Once considered as potential candidates in modern telecommunications [122], solitons in optical systems are the most well-known as they are relatively easy to generate and manipulate. For most optical solitons, the compensation of group velocity dispersion is provided by Kerr nonlinearity, which locally alters the refractive index to induce an effective potential well. Such confinement could occur either in parallel or orthogonal direction to wave propagation, depending on which optical solitons can be classified as being either temporal or spatial [119]. In this thesis we will focus on temporal solitons that are bullet-like light pulses, which the term “soliton” will mostly refer to.

Although first restricted to integrable systems, the concept of soliton was challenged when localized structures were also observed in open, non-conservative systems such as mode-locked lasers [123, 124]. Besides balancing dispersion and nonlinearity, these “solitons” also exchange energy with environment to reach a balance and are thereby able to survive indefinitely. The name “dissipative solitons” was gradually adopted to identify such class of wavepackets since dissipation occurs in almost all physical systems [125].

Recently dissipative solitons have been proposed and demonstrated in continuously and periodically driven Kerr resonators [66–69, 72, 126]. In particular, they provide a route to achieve mode locking in monolithic microresonators and hence give rise to highly coherent frequency combs in integrated platforms. The terminology “dissipative Kerr soliton (DKS)” was invented to specify such type of solitons whereas in these passive resonators Kerr nonlinearity provides parametric gain in addition to balancing dispersion [70]. In this chapter, theoretical background of dissipative Kerr solitons will be introduced, primarily based on Lugiato-Lefever equation (LLE) which is adopted to describe pulse propagation in resonators [127]. The dynamical formation of solitons and their steady-state property will be also

studied, which reveals the conversion efficiency and existing range of solitons.

2.1 Pulse propagation and optical solitons

In this section, we will introduce the pulse propagation equation and its key parameters. The mathematical description of optical solitons will also be reviewed. The derivation is adapted from Ref. [128].

Dispersion and effective mode area

Begin with the Helmholtz equation

$$[\nabla^2 + \frac{n(\omega)^2 \omega^2}{c^2}] \tilde{\mathbf{E}}(\mathbf{r}, \omega) = 0, \quad (2.1)$$

where c is the speed of light, ω is the frequency and $n(\omega)$ is the wavelength-dependent refractive index of the medium. Consider an optical mode propagating in z direction, the electrical field $\tilde{\mathbf{E}}$ can be written in the form

$$\tilde{\mathbf{E}}(\mathbf{r}, \omega) = \hat{x}[F(x, y)e^{i\beta z} + c.c.]. \quad (2.2)$$

The modal distribution $F(x, y)$ is defined by

$$[\nabla^2 + \frac{n(\omega)^2 \omega^2}{c^2} - \beta(\omega)^2]F(x, y) = 0, \quad (2.3)$$

With certain boundary condition, the eigenvalue of propagation constant β can be solved, which can be written in Taylor series around ω_o as

$$\beta(\omega) = \beta_o + (\omega - \omega_o)\beta_1 + \sum_{n=2}^{\infty} \frac{1}{n!}(\omega - \omega_o)^n \beta_n, \quad (2.4)$$

where $\beta_o = \beta(\omega_o)$, β_1 is the inverse of the group velocity, and β_2 denotes the group velocity dispersion (GVD). Positive β_2 corresponds to normal dispersion while negative β_2 indicates anomalous dispersion. Now consider a pulse formed in this mode with carrier frequency ω_o . The slowly varying envelope approximation applies in the case that the pulse width is much longer than an optical cycle. Therefore, the x -polarized electrical field of the pulse, \mathbf{E} , can be expressed as

$$\mathbf{E}(\mathbf{r}, t) = \frac{1}{2} \hat{x}[F(x, y)E'(z, t)e^{i(\beta_o z - i\omega_o t)} + c.c.]. \quad (2.5)$$

By normalizing the slowly varying envelope E' to

$$E = E' \sqrt{\frac{1}{2} \epsilon_o n_o c \iint_{-\infty}^{\infty} |F(x, y)|^2 dx dy}, \quad (2.6)$$

the optical power can now be simply calculated as $|E|^2$. Here ϵ_o is the vacuum permittivity, while $n_o = n(\omega_o)$ is the refractive index at ω_o .

The Kerr effect would induce a local change of the refractive index [128]:

$$\Delta n(\mathbf{r}, t) = \frac{3\chi_{xxxx}^{(3)}}{4n_o} |\mathbf{E}(\mathbf{r}, t)|^2, \quad (2.7)$$

where $\chi_{xxxx}^{(3)}$ is the nonlinear susceptibility. The average change of refractive index over the modal field distribution is given by

$$\begin{aligned} \Delta \bar{n} &= \frac{\iint_{-\infty}^{\infty} \Delta n |F(x, y)|^2 dx dy}{\iint_{-\infty}^{\infty} |F(x, y)|^2 dx dy} \\ &= \frac{3\chi_{xxxx}^{(3)}}{8n_o} |E'(z, t)|^2 \frac{\iint \Delta n |F(x, y)|^4 dx dy}{\iint_{-\infty}^{\infty} |F(x, y)|^2 dx dy} \\ &= \frac{3\chi_{xxxx}^{(3)}}{4\epsilon_o c n_o^2} |E(z, t)|^2 \frac{\iint |F(x, y)|^4 dx dy}{(\iint_{-\infty}^{\infty} |F(x, y)|^2 dx dy)^2}. \end{aligned} \quad (2.8)$$

By introducing the nonlinear Kerr parameter

$$n_2 = \frac{3\chi^{(3)}}{4\epsilon_o c n_o^2} \quad (2.9)$$

and the effective mode area

$$A_{\text{eff}} = \frac{(\iint_{-\infty}^{\infty} |F(x, y)|^2 dx dy)^2}{\iint_{-\infty}^{\infty} |F(x, y)|^4 dx dy}, \quad (2.10)$$

Equation (2.8) can be simplified so we have

$$\Delta \bar{n} = n_2 \frac{|E|^2}{A_{\text{eff}}}. \quad (2.11)$$

Pulse-propagation equation

Using Fourier transform

$$\tilde{\mathbf{E}}(\mathbf{r}, \omega) = \int_{-\infty}^{\infty} \mathbf{E}(\mathbf{r}, t) e^{i\omega t} dt, \quad (2.12)$$

the spectral component of the pulse $\tilde{\mathbf{E}}(\mathbf{r}, \omega)$ can be written in the form

$$\tilde{\mathbf{E}}(\mathbf{r}, \omega) = \hat{x}[F(x, y)\tilde{E}(z, \omega)e^{i\beta_o z} + c.c.]. \quad (2.13)$$

Taking Kerr nonlinearity into account, the wavelength-dependent refractive index \tilde{n} is defined as

$$\tilde{n}(\omega) = n(\omega) + \Delta \bar{n}. \quad (2.14)$$

By substituting Eq. (2.13) into Eq. (2.1) and separating the variables, we obtain

$$[\nabla^2 F + \frac{\tilde{n}(\omega)^2 \omega^2}{c^2} - \tilde{\beta}(\omega)^2]F(x, y) = 0, \quad (2.15)$$

$$[2i\beta_o \frac{\partial}{\partial z} + (\tilde{\beta}(\omega)^2 - \beta_o^2)]\tilde{E}(z, \omega) = 0. \quad (2.16)$$

The value of $\tilde{\beta}$ can be deduced from Eq. (2.15) and Eq. (2.3), yielding

$$\tilde{\beta}(\omega)^2 = \beta(\omega)^2 + 2n\Delta\bar{n}\frac{\omega^2}{c^2}. \quad (2.17)$$

Hence, Eq. (2.16) can be written in the form

$$\begin{aligned} \frac{\partial \tilde{E}(\omega)}{\partial z} &= i \frac{\beta(\omega)^2 - \beta_o^2 + 2n\Delta\bar{n}\frac{\omega^2}{c^2}}{2\beta_o} \tilde{E} \\ &= i[(\omega - \omega_o)\beta_1 + \sum_{n=2}^{\infty} \frac{1}{n!}(\omega - \omega_o)^n \beta_n + \frac{n_o \omega^2}{\beta_o c^2} \Delta\bar{n}] \tilde{E} \\ &= i[(\omega - \omega_o)\beta_1 + \sum_{n=2}^{\infty} \frac{1}{n!}(\omega - \omega_o)^n \beta_n + \frac{\omega}{c} \Delta\bar{n}] \tilde{E}, \end{aligned} \quad (2.18)$$

where approximations $n(\omega) \approx n_o$ and $\beta(\omega) \approx n(\omega)\omega/c$ are used.

Fourier transforming Eq. (2.18) gives the equation that describes the evolution of pulse envelope E :

$$\frac{\partial E}{\partial z} = -\beta_1 \frac{\partial E}{\partial t} - \sum_{n=2}^{\infty} \frac{i^{n-1}}{n!} \beta_n \frac{\partial^2 E}{\partial t^2} - \frac{\alpha}{2} E + i\gamma(\omega_o)|E|^2 E, \quad (2.19)$$

where α denotes the propagation loss. The nonlinear parameter γ takes the form

$$\gamma(\omega_o) = \frac{\omega_o n_2}{c A_{\text{eff}}}. \quad (2.20)$$

It is customary to study a pulse in the frame of reference moving at its group velocity. Applying the coordinate transformation,

$$T = t - \beta_1 z, \quad (2.21)$$

Equation (2.19) yields

$$\frac{\partial E}{\partial z} = - \sum_{n=2}^{\infty} \frac{i^{n-1}}{n!} \beta_n \frac{\partial^2 E}{\partial T^2} - \frac{\alpha}{2} E + i\gamma(\omega_o)|E|^2 E, \quad (2.22)$$

which is known as the pulse-propagation equation. It is noted that corrections from high-order nonlinear effects, such as Raman effect and self-steepening effect [128], are currently not included and will be discussed later in this thesis.

Optical solitons

Ignoring the loss and considering dispersion up to second order, Equation (2.22) becomes

$$\frac{\partial E}{\partial z} = -\frac{i}{2}\beta_2 \frac{\partial^2 E}{\partial T^2} + i\gamma|E|^2 E, \quad (2.23)$$

which is identical to the nonlinear Schrödinger equation. Bright solitons exist when β_2 and γ have opposite signs. Since most materials are self-focusing ($n_2 > 0$), the formation of bright solitons usually requires anomalous dispersion ($\beta_2 < 0$). If β_2 and γ have the same sign, another class of solutions called dark solitons would emerge [128]. Inverse scattering method can be employed to solve such solutions [129]. We will not go through the detailed derivation here, but instead show the result of bright solitons:

$$E = B \operatorname{sech} \frac{T}{T_s} e^{ikz}, \quad (2.24)$$

where

$$B = \frac{1}{T_s} \sqrt{-\frac{\beta_2}{\gamma}}, \quad (2.25)$$

$$k = -\frac{\beta_2}{2T_s^2}. \quad (2.26)$$

It is noted that the solution features a sech envelope, a characteristic feature of optical solitons. The amplitude of the optical (B) is dependent on its pulse width (T_s).

2.2 Lugiato-Lefever equation

If the phase of light changes by an integer multiple of 2π during a round trip in an optical resonator, the light is resonantly enhanced, forming a set of resonances at discrete frequencies. The propagation of pulses in resonators should be subject to such resonant condition, i.e., taking the phase change in each round trip into account. The equation we use is Lugiato-Lefever equation (LLE), which was designated to model dynamics of continuously driven resonator filled with Kerr medium [127]. Although first used for spatial pattern formation, it can be adapted to study temporal dynamics with proper transformation of coordinates. To date, LLE has been widely accepted as the master equation of microcombs, and will be extensively used throughout the thesis. In this section, we will present the derivation of LLE from the pulse propagation equation.

Continuously-driven microresonator

Without loss of generality, we consider a circular whispering-gallery-mode microresonator, which has a set of longitudinal modes sorted by their azimuthal number

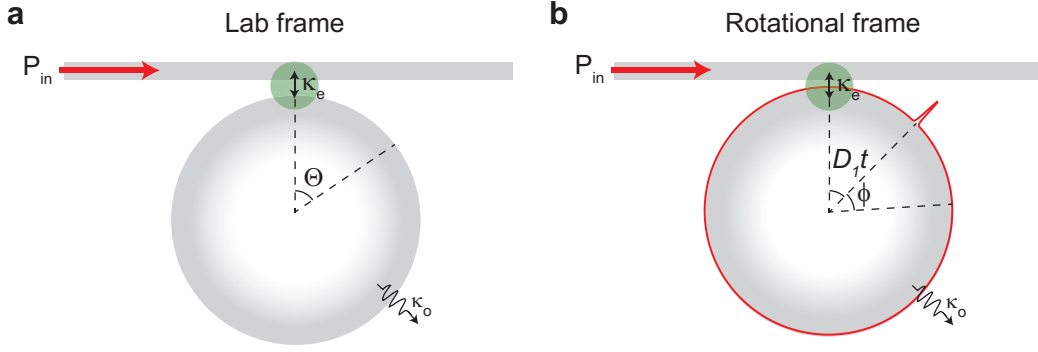


Figure 2.1: Schematic illustration of a continuously-driven microresonator. (a) Coordinates of lab frame. (b) Coordinates of rotational frame.

m . The electrical field of a mode of mode number m is expressed as

$$\tilde{\mathbf{E}}_m(\Theta, t) = \hat{x} \tilde{E}_m e^{im\Theta - i\omega_m t}, \quad (2.27)$$

where ω_m is the resonant frequency. Θ is the angular coordinate in lab frame as shown in Figure 2.1(a). The modal distribution is set unity for simplicity. \tilde{E}_m is normalized so that $|\tilde{E}_m|^2$ represents the energy stored in this mode ($|\tilde{E}_m|^2 / \hbar\omega_m$ is the photon number). If the resonator is continuously driven by an external pump laser with frequency ω_p , the equation of motion of \tilde{E}_m can be written in the form [130]

$$\frac{\partial \tilde{E}_m}{\partial t} = -\frac{\kappa}{2} \tilde{E}_m + \sqrt{\kappa_e P_{\text{in}}} e^{-i(\omega_p - \omega_m)t}, \quad (2.28)$$

where P_{in} is the input power in the waveguide. κ is the total loss rate of the resonator, which is a summation of the intrinsic loss κ_o and the coupling loss κ_e .

Resonator dispersion and rotation frame

Next we will add more frequency components into Equation (2.28). The intracavity field can be written as

$$\mathbf{E}(\Theta, t) = \hat{x} \sum_m \tilde{E}_m e^{im\Theta - i\omega_m t} = \hat{x} \tilde{E} e^{im_o\Theta - i\omega_o t}, \quad (2.29)$$

where

$$E(\Theta, t) = \sum_m \tilde{E}_m e^{i(m-m_o)\Theta - i(\omega_m - \omega_o)t}. \quad (2.30)$$

Here m_o is the azimuthal number of the mode that is closest to the pump laser in frequency, while ω_o denotes its resonant frequency. We further introduce the relative mode index μ which is defined by $\mu \equiv m - m_o$, so now we have $E_\mu \equiv \tilde{E}_m$.

The resonant frequencies noted by $\{\omega_\mu\}$ can be expanded in a Taylor series around $\mu = 0$ as

$$\omega_\mu = \omega_o + D_1\mu + \sum_{n=2}^{\infty} \frac{D_n}{n!} \mu^n. \quad (2.31)$$

D_1 is the free-spectral-range (FSR) of the microresonator at ω_o , while D_2 is related to the GVD of the resonator by $D_2 = -cD_1^2\beta_2/n_o$. Substituting Eq. (2.31) into Eq. (2.30), we have

$$E(\Theta, t) = \sum_m E_\mu e^{i\mu(\Theta - D_1 t) - i \sum_{n=2}^{\infty} \frac{D_n}{n!} \mu^n t}. \quad (2.32)$$

The equation of motion for E yields

$$\begin{aligned} \frac{\partial E(\Theta, t)}{\partial t} &= \sum_\mu -\left(\frac{\kappa}{2} + iD_1\mu + i \sum_{n=2}^{\infty} \frac{D_n}{n!} \mu^n\right) E_\mu e^{i\mu(\Theta - D_1 t) - i \sum_{n=2}^{\infty} \frac{D_n}{n!} \mu^n t} \\ &\quad + \sqrt{\kappa_e P_{\text{in}}} e^{-i(\omega_p - \omega_o)t} \\ &= -\left(\frac{\kappa}{2} + D_1 \frac{\partial}{\partial \Theta} - \sum_{n=2}^{\infty} i^{n-1} D_n \frac{\partial^n}{\partial \Theta^n}\right) E(\Theta, t) + \sqrt{\kappa_e P_{\text{in}}} e^{-i(\omega_p - \omega_o)t}. \end{aligned} \quad (2.33)$$

The system is better studied in rotation frame, whose coordinates (ϕ, t) are transformed from those in the lab frame (Θ, t) by $\phi \equiv \Theta - D_1 t$, as shown in Figure 2.1(b). In rotation frame, Equation (2.33) can be written as

$$\frac{\partial E(\phi, t)}{\partial t} = -\left(\frac{\kappa}{2} - \sum_{n=2}^{\infty} i^{n-1} D_n \frac{\partial^n}{\partial \phi^n}\right) E(\phi, t) + \sqrt{\kappa_e P_{\text{in}}} e^{-i(\omega_p - \omega_o)t}. \quad (2.34)$$

Kerr nonlinearity

The term that describes the Kerr effect can be obtained by comparing Eq. (2.34) with Eq. (2.22). Since the effective circulating power in the resonator is

$$P_c = |E(\phi, t)|^2 D_1 / 2\pi, \quad (2.35)$$

we have the scaling relation $E(T, z) \approx E(\phi, t) \sqrt{D_1 / 2\pi}$. Also as the coordinates are related by $z = ct/n_o$, the nonlinear parameter γ' associated with $E(\phi, t)$ becomes

$$\gamma' = cD_1\gamma = \frac{\omega_o n_2 D_1}{2\pi n_o A_{\text{eff}}}. \quad (2.36)$$

This Kerr term can be embedded into Equation (2.22) such that

$$\frac{\partial E(\phi, t)}{\partial t} = \sum_{n=2}^{\infty} i^{n-1} D_n \frac{\partial^n}{\partial \phi^n} E + i\gamma' |E|^2 E - \frac{\kappa}{2} E + \sqrt{\kappa_e P_{\text{in}}} e^{-i(\omega_p - \omega_o)t}. \quad (2.37)$$

Lugiato-Lefever equation

To eliminate temporal dependence of the pump term, we introduce the slowly-varying envelope of the photon density, $|A(\phi, t)|^2$, which is defined as

$$A(\phi, t) = \frac{E(\phi, t)}{\sqrt{\hbar\omega_o}} e^{i(\omega_p - \omega_o)t}. \quad (2.38)$$

Substituting A into Eq. (2.37), we obtain the Lugiato-Lefever equation:

$$\frac{\partial A(\phi, t)}{\partial t} = \sum_{n=2}^{\infty} i^{n-1} \frac{D_n}{n!} \frac{\partial^n A}{\partial \phi^n} + ig|A|^2 A - \left(\frac{\kappa}{2} + i\delta\omega\right)A + \sqrt{\frac{\kappa\eta P_{\text{in}}}{\hbar\omega_o}}, \quad (2.39)$$

where $\delta\omega = \omega_o - \omega_p$ represents the frequency difference between the resonance and pump laser (laser-cavity detuning). $\eta = \kappa_{\text{ext}}/\kappa$ represents the ratio between the coupling loss κ_{ext} and the total loss. The normalized Kerr nonlinear coefficient g is given by

$$g = \frac{\hbar\omega_o^2 n_2 D_1}{2\pi n_o A_{\text{eff}}}. \quad (2.40)$$

LLE is also equivalent to a set of coupled-mode equations [131]. A dimensionless form of Eq. (2.39) is often used for simplicity, which is written as [66]

$$\frac{\partial \psi(\theta, \tau)}{\partial \tau} = -(1 + i\zeta)\psi + i\frac{1}{2} \frac{\partial^2 \psi}{\partial \theta^2} + i|\psi|^2 \psi + f. \quad (2.41)$$

Here we only consider dispersion up to second order. The normalized intracavity field $\psi = \sqrt{2g/\kappa}A$. Other normalized parameters are defined as: $\tau = \kappa t/2$; $\theta = \phi\sqrt{\kappa/2D_2}$; $\zeta = 2\delta\omega/\kappa$; $f = \sqrt{8g\eta P_{\text{in}}/\kappa^2 \hbar\omega_o}$.

2.3 Modulational instability

The formation of Kerr combs starts with the generation of sidebands from a homogeneous background [51, 52, 61]. This process, namely modulational instability (MI), relies on the parametric amplification of quantum fluctuations or noisy seeds. In this section the condition of modulational instability is derived from the Lugiato-Lefever equation, which gives the threshold of parametric oscillation [61, 127] and the location of primary combs.

Parametric oscillation threshold

The homogeneous steady-state solution ψ_o to Eq. (2.41) is given by

$$(1 + i\zeta - i|\psi_o|^2)\psi_o = f. \quad (2.42)$$

Introduce a perturbation $\delta\psi$, whose equation of motion can be derived from Eq. (2.41) as

$$\frac{\partial \delta\psi}{\partial \tau} = -(1 + i\zeta)\delta\psi + i\frac{1}{2}\frac{\partial^2 \delta\psi}{\partial \theta^2} + i(2|\psi_o|^2\delta\psi + \psi_o^2\delta\psi^*). \quad (2.43)$$

Here $\delta\psi^*$ is the conjugate of $\delta\psi$. Take the Ansatz

$$\delta\psi(\theta, \tau) = e^{\lambda\tau} \cos(n\theta\sqrt{2D_2/\kappa})\delta\psi, \quad (2.44)$$

where n is a positive integer due to the periodic boundary condition. Therefore, equation (2.43) yields

$$(\lambda + 1 + in^2D_2/\kappa + i\zeta - 2i|\psi_o|^2)\delta\psi = i\psi_o^2\delta\psi^*. \quad (2.45)$$

Defining $n^2D_2/\kappa \equiv a_n$, the eigenvalue equation of λ is given by

$$(\lambda + 1)^2 = |\psi_o|^4 - (a_n + \zeta - 2|\psi_o|^2)^2. \quad (2.46)$$

Positive solution of λ at at least one choice of n should lead to exponential growth of $\delta\psi$ and the solution ψ_o becomes unstable. Under such circumstances the RHS of Eq. (2.46) should be greater than 1, and we have

$$a_n^2 - (4|\psi_o|^2 - 2\zeta)a_n + (3|\psi_o|^2 - \zeta)(|\psi_o|^2 - \zeta) + 1 < 0, \quad (2.47)$$

which gives the interval of a_n as

$$2|\psi_o|^2 - \zeta - \sqrt{|\psi_o|^4 - 1} < a_n < 2|\psi_o|^2 - \zeta + \sqrt{|\psi_o|^4 - 1}. \quad (2.48)$$

This equation sets the limits of ψ_o as

$$|\psi_o|^2 \geq 1 \quad (2.49)$$

and

$$2|\psi_o|^2 - \zeta + \sqrt{|\psi_o|^4 - 1} > 0. \quad (2.50)$$

Equation (2.50) is valid upon negative value of ζ . Since the maximum $|\psi_o|^2$ is set by Eq. (2.42) as

$$|\psi_o|^2 = \frac{f^2}{1 + (\zeta - |\psi_o|^2)^2} \leq f^2, \quad (2.51)$$

the condition for f to satisfy Eq. (2.49) is given by

$$f^2 \geq 1, \quad (2.52)$$

which corresponds to the threshold power of modulational instability (parametric oscillation) to occur as

$$P_{\text{th}} = \frac{\kappa^2 \hbar \omega_o}{8g\eta} = \frac{\pi n_o \kappa^2 A_{\text{eff}}}{4\omega_o n_2 D_1 \eta}. \quad (2.53)$$

It is noted that the calculated threshold is identical to the result derived from coupled-mode equations [62].

Primary combs

When the input power exceeds such parametric oscillation threshold, intracavity noise will be amplified, which gives rise to sidebands. The location of the first sidebands that are called primary combs, can be inferred from Eq. (2.44), where the integer n corresponds to the mode number of the primary combs. To solve n near thresholding condition, we set $f = 1$ such that

$$|\psi_o|^2 = 1, \zeta = 1, \quad (2.54)$$

which can be substituted into Eq. (2.48) to obtain

$$a_n = 1. \quad (2.55)$$

Hence, the mode indexes of the primary combs relative to the pump mode are given by

$$n = \pm \sqrt{\frac{\kappa}{D_2}}, \quad (2.56)$$

which is exactly the result derived from coupled mode equations [62].

2.4 Lagrangian formalism and moment analysis

The modulational instability strongly breaks the homogeneity of intracavity field, providing seed to the formation of various inhomogenous waveforms. Among them, dissipative Kerr solitons are steady, self-localized wavepackets insensitive to perturbations [66, 132, 133]. In this section, the mathematical description of DKSSs and their stability will be discussed using two methods: Lagrangian formalism and moment analysis. Similar approaches have been described in Ref. [133, 134].

Lagrangian formalism

The LLE can be considered as a nonlinear Schrodinger equation (NLS) perturbed by external driving and damping. To solve the LLE analytically, we construct the Lagrangian density \mathcal{L} of the system whose variation to $\delta\psi^*$ is given by

$$\frac{\delta\mathcal{L}}{\delta\psi^*} = \underbrace{\frac{1}{2} \frac{\partial^2 \psi}{\partial \theta^2} + |\psi|^2 \psi - \zeta \psi}_{\mathcal{L}_s} + \underbrace{i\psi - if}_{\mathcal{L}_p} = 0. \quad (2.57)$$

The Lagrangian density of the NLS is

$$\mathcal{L}_s = \frac{i}{2} \left(\psi^* \frac{\partial \psi}{\partial \tau} - \psi \frac{\partial \psi^*}{\partial \tau} \right) - \frac{1}{2} \left| \frac{\partial \psi}{\partial \theta} \right|^2 + \frac{1}{2} |\psi|^4 - \zeta |\psi|^2, \quad (2.58)$$

which satisfies

$$\begin{aligned}\frac{\delta \mathcal{L}_s}{\delta \psi^*} &= \frac{\partial \mathcal{L}_s}{\partial \psi^*} - \frac{\partial}{\partial \tau} \frac{\partial \mathcal{L}_s}{\partial \psi_\tau^*} - \frac{\partial}{\partial \theta} \frac{\partial \mathcal{L}_s}{\partial \psi_\theta^*} \\ &= \frac{1}{2} \frac{\partial^2 \psi}{\partial \theta^2} + |\psi|^2 \psi - \zeta \psi.\end{aligned}\quad (2.59)$$

Similarly, the Lagrangian density of the perturbation is determined by

$$\frac{\delta \mathcal{L}_p}{\delta \psi^*} = i\psi - if = -\mathcal{R}. \quad (2.60)$$

According to the principle of least action, at stationary condition the Lagrangian of the entire system $L = \int \mathcal{L} d\theta$ should satisfy

$$\delta L = L_s - \int (\mathcal{R} \delta \psi^* + \mathcal{R}^* \delta \psi) d\theta = 0, \quad (2.61)$$

where $L_s = \int \mathcal{L}_s d\theta$. Concerning a set of time dependent coordinates $\{r_i\}$ of ψ , the variations in the above equation can be expanded so we get

$$\sum_i \left(\frac{\partial L_s}{\partial r_i} - \frac{d}{d\tau} \frac{\partial L_s}{\partial \dot{r}_i} \right) \delta r_i = \sum_i \int (\mathcal{R}^* \frac{\partial \psi}{\partial r_i} + \text{c.c.}) \delta r_i d\theta. \quad (2.62)$$

According to the first lemma of calculus of variations, the corresponding Euler-Lagrangian equation yields

$$\frac{\partial L_s}{\partial r_i} - \frac{d}{d\tau} \frac{\partial L_s}{\partial \dot{r}_i} = \int (\mathcal{R}^* \frac{\partial \psi}{\partial r_i} + \text{c.c.}) d\theta. \quad (2.63)$$

Since the analytic solution to the NLS is $\sqrt{2\zeta} \text{sech}(\sqrt{2\zeta}\theta)$, we use the ansatz that $\psi = \psi_s(\theta_o) = B e^{i\varphi} \text{sech}[C(\theta - \theta_o)]$. Assuming that the soliton pulse width is much shorter compared with cavity round trip time, the bounds of the integral can be extended to infinity. The Lagrangian yields

$$L_s = -2 \frac{\partial \varphi}{\partial \tau} \frac{B^2}{C} - \frac{1}{3} B^2 C + \frac{2}{3} \frac{B^4}{C} - 2\zeta \frac{B^2}{C}. \quad (2.64)$$

The equations of motion for the coordinates $\{B, \varphi, C\}$ can be derived from Eq. (2.63)

as

$$-4 \frac{\partial \varphi}{\partial \tau} \frac{B}{C} - \frac{2}{3} B C + \frac{8}{3} \frac{B^3}{C} - 4\zeta \frac{B}{C} = -\frac{2i\pi f \sin \varphi}{C}, \quad (2.65)$$

$$2 \frac{\partial \varphi}{\partial \tau} \frac{B^2}{C^2} - \frac{1}{3} B^2 - \frac{2}{3} \frac{B^4}{C^2} + 2\zeta \frac{B^2}{C^2} = \frac{2i\pi f B \sin \varphi}{C^2}, \quad (2.66)$$

$$2 \frac{d}{d\tau} \left(\frac{B^2}{C} \right) = \frac{2\pi f B \cos \varphi - 4B^2}{C}. \quad (2.67)$$

At steady state, from Eq. (2.67) we have

$$\cos \varphi = \frac{2B}{\pi f} \leq 1, \quad (2.68)$$

which sets the requirement of the pump for the survival of soliton as

$$f_{\min} = \frac{\sqrt{8\zeta}}{\pi}. \quad (2.69)$$

If the system is operating around minimal pump condition, we have $\varphi \approx \pi/2$ so that $\sin \varphi \approx 0$. Therefore, solutions to Eq. (2.65) and Eq. (2.66) are

$$B = C = \sqrt{2\zeta}. \quad (2.70)$$

For better approximation, in addition to the soliton, a weak continuous wave (c.w.) background should be also included. Thereby we have

$$\psi = \underbrace{\psi_o}_{\text{c.w.background}} + \underbrace{\psi_s}_{\text{soliton}}, \quad (2.71)$$

where

$$\psi_o = \frac{f}{\zeta^2} - i\frac{f}{\zeta} \quad (2.72)$$

is a homogeneous solution to Eq. (2.41) [66, 134]. When there are more than 1 soliton pulse circulating along the resonator, a more generic solution yields

$$\psi = \psi_o + \sum_i \psi_s(\theta_i), \quad (2.73)$$

where θ_i denotes the pulse center of the i_{th} soliton.

It should be noted that when pump greatly exceeds the minimal power requirement, the contribution of $\sin \varphi$ cannot be neglected. Higher order correction to the analytical solution should be taken into consideration [135]. Further increasing the pump power will give rise to instability which appears as periodically oscillating wavepackets known as breather solitons [94–96].

Moment analysis

A convenient way to determine the coefficients in the ansatz is the moment analysis. To begin with, we choose the ansatz

$$\psi = B e^{i\varphi} \text{sech}[B(\theta - \theta_o)], \quad (2.74)$$

where $B = \sqrt{2\zeta}$ so as to satisfy the NLS part of Eq. (2.41). Two quantities are important to define a soliton: its energy and momentum. The energy of the soliton is given by

$$E_{\text{sol}} = \int |\psi|^2 d\theta = 2B, \quad (2.75)$$

whose equation of motion can be written as

$$\frac{\partial E_{\text{sol}}}{\partial \tau} = \int \frac{\partial |\psi|^2}{\partial \tau} d\theta = -2E_{\text{sol}} + \int f(\psi^* + \psi) d\theta. \quad (2.76)$$

At steady state, the soliton energy should be invariant ($\partial E_{\text{sol}}/\partial \tau = 0$), which sets the phase of soliton as Eq. (2.68).

The momentum of the soliton is related to the spectral envelope center of the soliton, which will be studied in Chapter 4. The moment analysis will be extensively used throughout the thesis, especially for studying soliton dynamics.

Measurable quantities of soliton microcombs

By converting the results back to dimensional forms, we obtain a set of physical quantities of the soliton microcomb, which can be measured experimentally. The output comb power of a single soliton regardless of the background is given by

$$P_{\text{sol}} = \frac{2\eta A_{\text{eff}}}{n_2 Q} \sqrt{-2n_o c \beta_2 \delta \omega}, \quad (2.77)$$

while the pulse width is

$$\tau = \sqrt{-\frac{c \beta_2}{2n_o \delta \omega}}. \quad (2.78)$$

The spectral envelope of the soliton frequency comb in the case of single soliton yields

$$P(\Delta\omega) = -\frac{\pi c \eta A_{\text{eff}} \beta_2 D_1}{2 n_2 Q} \text{sech}^2\left(\frac{\pi \tau}{2} \Delta\omega\right), \quad (2.79)$$

which gives the power of comb teeth at center of the envelope. The minimum power is

$$P_{\text{in}}^{\text{min}} = -\frac{2c A_{\text{eff}} \beta_2}{\pi \eta n_2 \tau^2 Q D_1}. \quad (2.80)$$

These theoretical predictions will be verified experimentally in Chapter 3.

2.5 Numerical method: split-step Fourier transform

In this section the method used for numerical simulation of LLE will be presented. Similar to the modeling of pulse propagation in waveguides, the split-step Fourier transform method [128] is employed to compute the temporal evolution of intracavity field.

Split-step Fourier transform method

The split-step Fourier transform divides Eq. (2.39) into three parts and computes their contribution in sequence. Considering a small time step δt , the contribution of Kerr nonlinearity will be first calculated from

$$\frac{\partial A}{\partial t} = ig|A|^2 A, \quad (2.81)$$

which gives

$$A_1 = e^{ig|A|^2 \delta t} A. \quad (2.82)$$

Secondly, we consider the contribution of damping, detuning, and dispersion, given by

$$\frac{\partial A}{\partial t} = -(1 + i\delta\omega)A + \sum_{n=2}^{\infty} i^{n-1} \frac{D_n}{n!} \frac{\partial^n A}{\partial \phi^2}. \quad (2.83)$$

By Fourier transforming the above equation with respect to ϕ , we obtain

$$\frac{\partial \tilde{A}(\mu)}{\partial t} = -(1 + i\delta\omega + i \sum_{n=2}^{\infty} \frac{\mu^n D_n}{n!}) \tilde{A}(\mu), \quad (2.84)$$

where $\tilde{A}(\mu) = \int_{-\pi}^{\pi} e^{-i\mu\phi} A d\phi$ with integer mode number μ , given the periodic boundary condition. Fast Fourier transform (FFT) can be used to compute such Fourier transform numerically, which gives

$$A_2 = \mathcal{F}^{-1}[e^{-(1+i\delta\omega+i \sum_{n=2}^{\infty} \frac{\mu^n D_n}{n!})\delta t} \mathcal{F}[A_1]]. \quad (2.85)$$

Including the pump term, the final expression yields

$$A(\phi, t + \delta t) = \mathcal{F}^{-1}[e^{-(1+i\delta\omega+i \sum_{n=2}^{\infty} \frac{\mu^n D_n}{n!})\delta t} \mathcal{F}[e^{ig|A|^2 \delta t} A]] + \sqrt{\frac{\kappa\eta P_{\text{in}}}{\hbar\omega_o}} \delta t. \quad (2.86)$$

Proper seeding is required to initiate modulational instability. Usually an average occupation of half a photon in each mode is chosen to mimic quantum noise. The simulation can be performed on a personal computer, which usually takes minutes to hours depending on the number of optical modes and time steps involved. Proper choice of mode number (2^N with integer N) could greatly reduce the consumption of computational power. To give an example, we simulate a case that a laser is scanning across a cavity resonance from the blue side to the red side, as shown in Figure 2.2. The build up of intracavity power is interrupted by the formation of periodic Turing pattern when the intracavity power exceeds parametric oscillation threshold. Increasing detuning will give rise to irregular fluctuations in intracavity

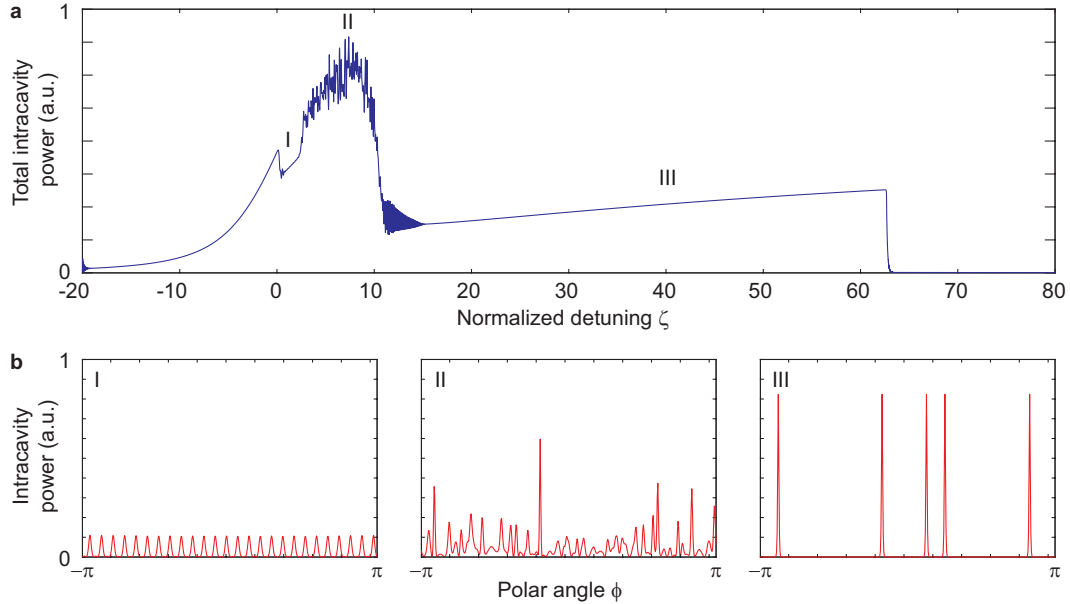


Figure 2.2: Numerical simulation of LLE. (a) Total intracavity power versus detuning while the pump is tuned across a resonance with increasing detuning. Parameters used in simulation: $f = 50$; $D_2/\kappa = 0.01$. 512 modes are involved. (b) Intracavity intensity versus polar angle at different detunings as marked in (a). I: Turing pattern; II: modulational instability comb; III: solitons.

power, which corresponds to modulational instability combs as shown in Figure 2.2(b). Upon further tuning of the laser frequency, such noise diminishes and a clean “step” appears instead, showing 5 pulses in the resonator. This is the regime where solitons form, with detuning range predicted by Eq. (2.69).

2.6 Conclusion

In this Chapter we have reviewed the theoretical background of dissipative Kerr solitons. The master equation of microcomb, Lugiato-Lefever equation, has been derived from the pulse-propagation equation. The closed-form solution of DKS has been obtained using Lagrangian formalism and moment analysis. Numerical simulation based on split-step Fourier transform has shown good agreement with theoretical predictions.

Chapter 3

SOLITON MICROCOMBS IN HIGH-Q SILICA MICRORESONATORS

¹The keys to soliton microcombs are high-Q microresonators, which are dielectric structures that trap light in a tiny space for a long time [53]. Owing to their ultralow material absorbance, silica microresonators possess the record high Q factors among all chip-based devices [55, 73, 136], leading to a low threshold for comb generation, as indicated in Eq. (2.53). Besides, silica also features a spectrally-broad transparency window so that optical Q factors can be high at short wavelengths. In this chapter, generation of soliton frequency combs in silica microresonators will be presented. The geometries of resonators are designed to fulfill requirements of dispersion for soliton generation. An active capturing technique is employed to stabilize solitons at 1550 nm and 1064 nm. These soliton pulses feature femtosecond temporal width, and are repeating at microwave rates. As a validation of the Lugiato-Lefever equation, the soliton properties are also measured and compared with theoretical predictions.

3.1 Silica wedge resonators

The primary platform we use for soliton generation is a silica wedge microresonator [55]. An integrated version of these microresonators are reported in Ref. [73]. The silica layer is thermally grown on a float-zone silicon wafer with thickness up to 8 μm . The patterns are first defined through photolithography, and then are transferred to the silica layer using Buffered Hydrofluoric Acid (BHF) etching. To suspend and air clad the silica layer where the mode is confined, the silicon substrate is dry-etched using XeF_2 as etchant. Finally, the resonator is annealed to expel residual hydrogen from the silica layer for further Q improvement.

The diameter of the resonators can vary from tens of microns to a few centimeters depending on the choice of projection or contact photolithography [55, 137]. Shown in Figure 3.1(b) is the cross section of a resonator which has a wedge angle at its exterior [55, 138]. The mode is primarily confined near the wedge, as shown in

¹Work presented in this chapter has been published in “Soliton frequency comb at microwave rates in a high-Q silica microresonator”, *Optica* 2,1078 (2015), “Active capture and stabilization of temporal solitons in microresonators”, *Opt. Lett.* 41,2037 (2016) and “Towards visible soliton microcomb generation”, *Nat. Commun.* 8(1):1295 (2017).

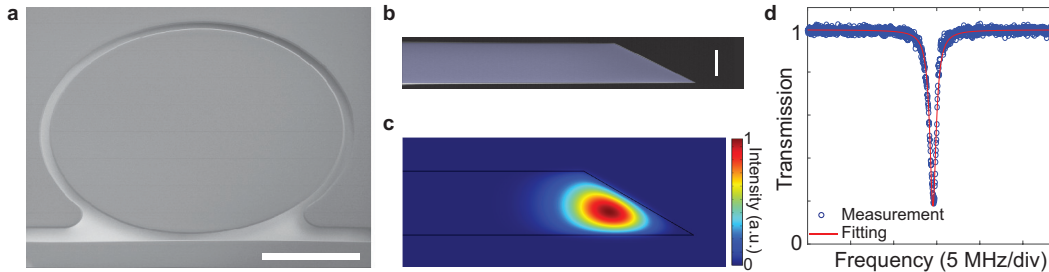


Figure 3.1: Silica wedge resonator. (a) Top view of a silica wedge resonator taken by scanning electron microscope (SEM). The scale bar is 1 mm. Image is from Lue Wu. (b) SEM image showing cross section of a wedge resonator. The scale bar is 5 μm . Image is from Dr. Seung Hoon Lee. (c) Finite element method (FEM) simulation of TM_1 mode profile. (d) Typical transmission spectrum while tuning a laser across a high-Q mode in a wedge resonator with 3 mm in diameter and 8 μm in thickness. The Lorentzian fitting (red) reveals intrinsic Q factor over 300 million.

Figure 3.1(c), which can be efficiently coupled using a tapered fiber [55, 130, 139]. To measure its Q factor, we record the transmission while the frequency of a laser is tuned across a mode. The relative frequency of the laser is calibrated using a fiber-based Mach-Zehnder interferometer (MZI). The total linewidth of the mode, κ , can be extracted by fitting the Lorentzian-shape transmission spectrum. The intrinsic loss κ_{int} is related to the total loss by $\kappa_{\text{int}} = (1 - \eta)\kappa$, where the loading coefficient $\eta = (1 - \sqrt{T})/2$ ($\eta = (1 + \sqrt{T})/2$) according to transmission T at under (over) coupling condition [130, 139]. Typical Q factors for a 3-mm-diameter wedge resonator can exceed 300 million, as shown in Figure 3.1(d). Q factors can approach 1 billion in resonators with larger diameters [55].

3.2 Dispersion engineering of silica resonators

Dispersion control

The mode family that is phase locked to form the soliton pulse train must feature anomalous dispersion [61, 70], which is straightforward in silica wedge resonators when operated in the 1.5 micron band [140], but can be challenging at shorter wavelengths since most materials feature large normal dispersion that dramatically increases into the visible and ultraviolet bands. Dispersion engineering by proper design of the resonator geometry [138, 141–148] offers a possible way to offset the normal dispersion. Typically, by compressing a resonator's waveguide dimension, geometric dispersion will ultimately compensate a large normal material dispersion component to produce overall anomalous dispersion. For example, in silica, strong confinement in bubble resonators [148] and straight waveguides [149] has been

used to push the anomalous dispersion transition wavelength from the near-IR into the visible band. Phase matching to ultraviolet dispersive waves has also been demonstrated using this technique [149]. However, to compensate the rising material dispersion this compression must increase as operational wavelength is decreased, and as a side effect highly-confined waveguides tend to suffer increased optical losses. This happens because mode overlap with the dielectric waveguide interface is greater with reduced waveguide cross section. Consequently, the residual fabrication-induced roughness of that interface degrades the resonator Q factor and increases pumping power (i.e., comb threshold power varies inverse quadratically with Q factor [61]).

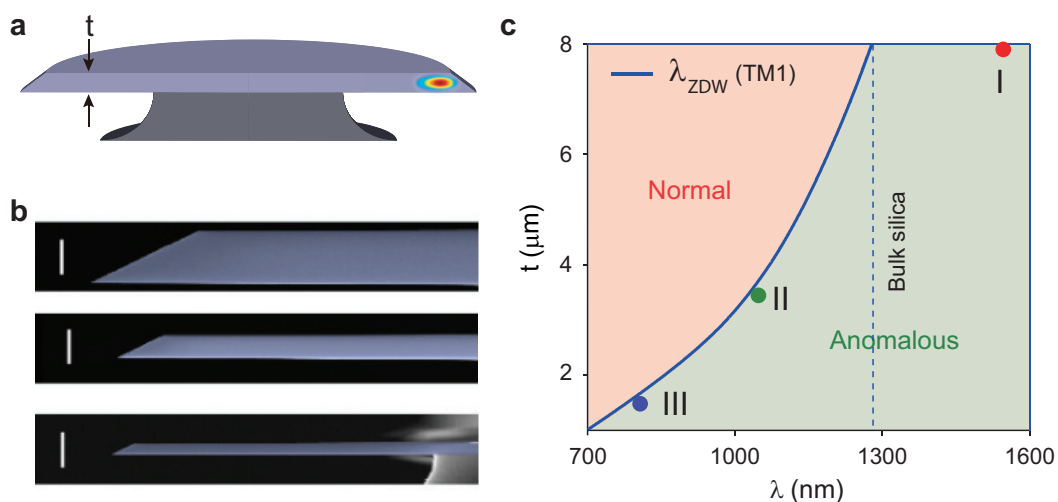


Figure 3.2: Dispersion engineering via resonator thickness control. (a) A rendering of a silica resonator with the calculated mode profile of the TM1 mode superimposed. (b) Cross-sectional SEM images of the fabricated resonators with different thickness. White scale bar is 5 μm . (c) Simulated regions of normal and anomalous dispersion are shown versus silica resonator thickness (t) and pump wavelength. The zero dispersion wavelength (λ_{ZDW}) for the TM1 mode appears as a blue curve. Plot is made for a 3.2-mm-diameter silica resonator. Three different device types, I, II, and III, which correspond to top, mid, and bottom panels in (b), are indicated for soliton generation at 1550 nm, 1064 nm, and 778 nm. The simulation is performed by Dr. Seung Hoon Lee.

Minimizing material dispersion provides one way to ease the impact of these constraints. In this sense, silica offers an excellent material for short wavelength operation, because it has the lowest dispersion among all on-chip integrable materials. For example, at 778 nm, silica has a group velocity dispersion (GVD) equal to 38 ps^2/km , which is over 5X smaller than the GVD of silicon nitride at this wavelength

(> 200 ps²/km) [150]. Other integrable materials that are also transparent in the visible, such as diamond [151] and aluminum nitride [152], have dispersion that is similar to or higher than silicon nitride.

The silica wedge resonator used in this thesis is shown schematically in Figure 3.2(a). A fundamental mode profile is overlaid in the cross-sectional rendering. The thickness of the resonator can be precisely controlled via oxidation time, as shown in Figure 3.2(b), which can lead to net anomalous dispersion at the design wavelengths. Figure 3.2(c) illustrates the dispersion design space by showing regions of anomalous and normal dispersion for the TM₁ mode family versus resonator thickness t and pumping wavelength. The plot shows that as the pump wavelength decreases the resonator needs to be thinner to access the anomalous dispersion regime. With this in mind, we have selected three different device types for soliton frequency comb operation at three different pump wavelengths. These are indicated in Figure 3.2(c) as I, II and III with colored dots. At a pump wavelength of 1550 nm, the anomalous dispersion window is wide because bulk silica possesses anomalous dispersion at wavelengths above 1270 nm. For this device (Type I), an 8- μm thickness was used. Devices of type II and III have thicknesses near 3.5 μm and 1.5 μm for operation with pump wavelengths of 1064 nm and 778 nm, respectively.

Reducing avoided-mode-crossings

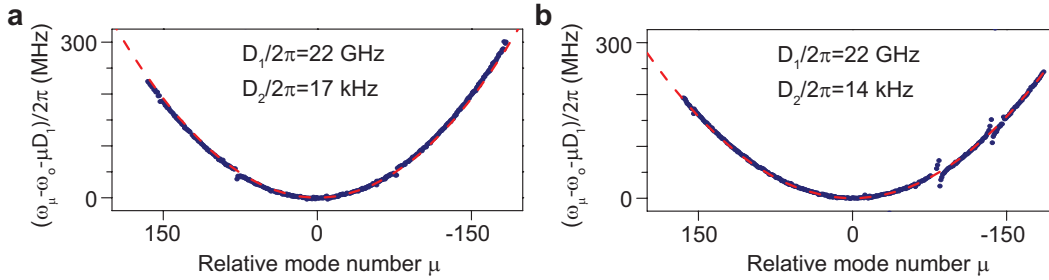


Figure 3.3: Measured frequency dispersion (blue points) belonging to the soliton-forming mode families are plotted versus relative mode number, μ . To construct this plot, mode frequency relative to a $\mu = 0$ mode (mode to be pumped) is measured using a calibrated Mach-Zehnder interferometer (fiber optic based). To second order in the mode number, the mode frequency is given by the Taylor expansion $\omega_\mu = \omega_0 + \mu D_1 + \frac{1}{2} \mu^2 D_2$ and the dashed red curves are parabolic fittings with fitted parameters on the top of each panel. In the plot, the mode frequencies are offset by the linear term in the Taylor expansion to make clear the second-order group dispersion. The measured modes span wavelengths from 1520 nm to 1580 nm and $\mu = 0$ corresponds to a wavelength close to 1550 nm.

Another requirement for soliton generation is minimizing the interference with other transverse modes, which can severely alter dispersion locally and thereby prohibit the soliton formation [153]. It is achieved by screening wedge disks to find combinations of diameter, thickness, and wedge angle that produce avoided-crossing-free spectral regions. In addition, it is observed that high-Q-factor mode families are generally more immune to avoided-crossing distortion. To characterize both mode family dispersion and avoided mode crossing behavior, mode frequencies are measured using a tunable laser that was calibrated with a fiber Mach-Zehnder interferometer [67] or a frequency comb [154, 155]. Measurements on typical mode families used to produce solitons are presented in Figure 3.3. Parabolic fitting to the data featuring an anomalous dispersion of $17 \text{ kHz}/FSR$ and $14 \text{ kHz}/FSR$ is provided for comparison to the data. Several avoided mode crossings are apparent in the spectra.

3.3 Active capturing and stabilization of soliton microcombs

Observation of soliton “steps”

The formation of soliton microcombs relies on continued pump tuning to the red side of the cavity resonance, where abrupt, “step-like” features in the intracavity power and an accompanying cavity tuning transient emerge (see Figure 3.4) [66]. Curiously, while the red-detuned regime is normally unstable, once formed, solitons actually reverse the thermal stability condition of the two thermal regimes. This happens because the average circulating soliton power increases with further red-detuning of the pump laser (i.e., opposite to the normal continuous-wave circulating power detuning dependence), inferred from Eq. (2.77). This unusual detuning dependence of soliton power thereby enables red-detuned operation provided that the soliton state persists long enough so as to permit decay of the initial non-soliton (destabilizing) transient.

Protocol of active capturing technique

Two passive methods have been demonstrated to overcome thermal destabilization during soliton formation. In MgF_2 resonators, where the thermal effect is relatively weak, the red-detuned soliton regime can be achieved by pump laser sweep rate control [66]. In cases where there is a stronger thermal effect, the two-step “power kicking” protocol was developed in silicon nitride resonators [68] and has also been applied in silica resonators [67]. However, these passive approaches are challenging to implement, requiring a customized pump power time dependence. Also, excitation of a specific soliton state is not guaranteed and, significantly, the

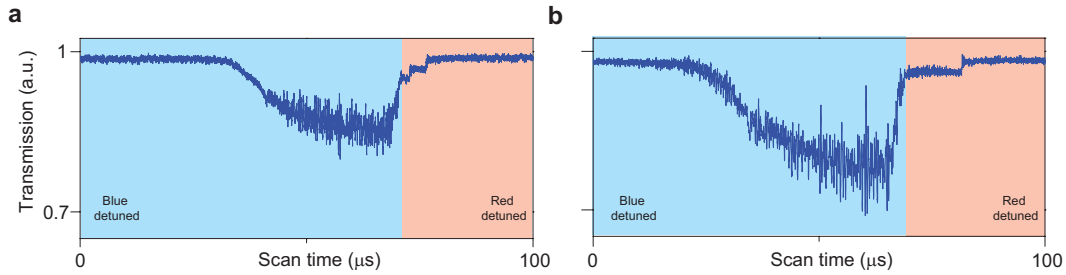


Figure 3.4: Pump power transmission versus tuning across a resonance used to generate the solitons. The data show the formation of steps as the pump tunes red relative to the resonance. Both blue-detuned and red-detuned operation of the pump relative to the resonance are inferred from generation of an error signal using a Pound-Drever-Hall system operated open loop.

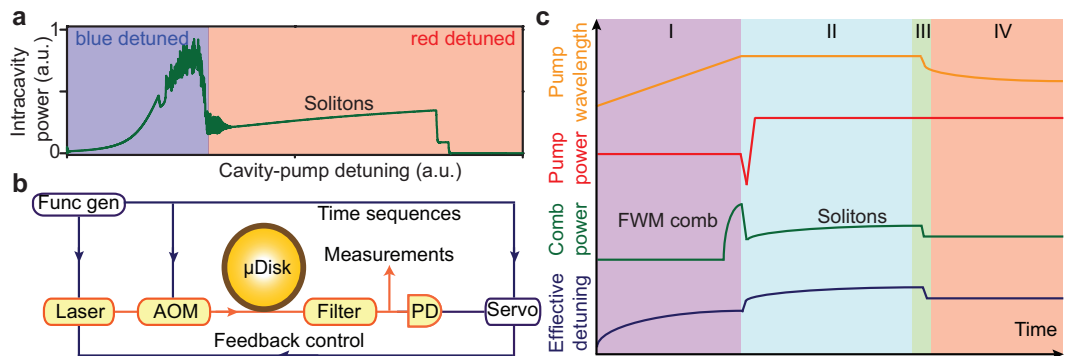


Figure 3.5: (a) Simulated intracavity power in which the pump laser scans over the resonance from the blue side to the red side. The steps on the red-detuned side indicate soliton formation. (b) Schematic of experimental setup. (c) Four phases of feedback-controlled soliton excitation: (I) pump laser scans into cavity resonance from blue-detuned side; (II) laser scan stops and pump power is reduced ($\sim 10 \mu\text{s}$) to trigger solitons, and then increased ($\sim 100 \mu\text{s}$) to extend soliton existence range; (III) servo-control is engaged to actively lock the soliton power by feedback control of laser frequency; (IV) lock sustains and solitons are fully stabilized. The cavity-pump detuning (vertical axis) is relative to the hot cavity resonant frequency.

soliton power and pulse width still vary as a result of long term drift of the cavity and pump laser frequencies. Ultimately, these drifts result in loss of the soliton state when the cavity-pump detuning drifts outside of the so-called soliton existence detuning range [66, 67, 132, 133]. Concerning generation of specific numbers of solitons, injection of “addressing” pulses has been used in fiber soliton lasers to trigger specific numbers of solitons [69], and laser backward tuning has been recently reported in microresonators [135]. However, neither technique achieves stabilization. Also, a separate mode locked laser is required to generate the “addressing” pulses.

The capture and stabilization method described here is simple to implement, relying on servo-control of the pump laser frequency by measuring the soliton average power. The key parameter in understanding this servo control method is the relative cavity-pump detuning, which for fixed cavity loading determines soliton power and pulse width. The one-to-one relationship between detuning and several soliton properties was recently noted to provide a way to provide long-term locking of the laser-cavity detuning [67]. Recall the expression of soliton power [66, 67, 132, 133]

$$P_{\text{sol}} = \frac{2\eta A_{\text{eff}}}{n_2 Q} \sqrt{-2n_o c \beta_2 \delta\omega}, \quad (3.1)$$

where c is light speed, A_{eff} is the effective mode area, $n_2(n_o)$ is the nonlinear index (refractive index), Q is the total quality factor, $\eta = Q/Q_{\text{external}}$ is the coupling coefficient, β_2 is the group velocity dispersion and $\delta\omega = \omega_o - \omega_p$ is the cavity-pump frequency detuning (ω_o is temperature dependent). It is important to note that the typical frequency detuning values for soliton generation are in the range of 10s of cavity linewidths. As a result, it is not clear how conventional locking methods can be applied in these circumstances. On the other hand, leveraging the one-to-one dependence of soliton power on detuning given by Eq. (3.1) avoids the complexities associated with actual measurement of the detuning frequency itself.

The experimental setup in Figure 3.5(b) shows the resonator (a high-Q silica resonator described in references [55, 67]) pumped with a continuous-wave fiber laser amplified by an erbium-doped fiber amplifier. The high-Q resonators are 3 mm in diameter and produce solitons at a repetition frequency of approximately 22 GHz. The laser's frequency is piezo controlled by a function generator and also the servo box. An acoustic-optic modulator (AOM) is used to control the pump power coupled into the resonator. At the resonator output port, the comb power is separated from the pump power with a fiber Bragg grating filter and sent to a photodiode (PD). An error signal is generated from the detected photocurrent after subtracting a set point in the servo control box.

The function generator produces signals to create a time sequence for all instruments. The time sequence is composed of four phases illustrated in Figure 3.5(c). The first two are similar to the "power kicking" technique [68] with the exception that the precise shape of the pump power waveform is less important than when power kicking is applied alone. In phase I, the laser is first scanned into resonance from the blue side, causing FWM comb formation [52]. In phase II, the laser stops scanning and the pump power is decreased over a few microseconds by controlling the acousto-optic modulator. This reduces the intracavity power so that the cavity resonance blue

shifts due to the Kerr and thermal effects. At some point, the laser wavelength will reside on the red side of the cavity resonance where soliton formation is possible. The laser power is then ramped to a higher level. Ramp times ranging from $\sim 20 \mu\text{s}$ to $\sim 500 \mu\text{s}$ were used. Ramping the power extends the existence detuning range of the solitons given by $\delta\omega_{\text{max}} = \pi^2 P_{\text{in}}/16P_{\text{th}}$ [66, 67, 133] where P_{in} and P_{th} are the pump power and parametric oscillation threshold [67]. If the waveform used to control the pump ramp is carefully designed, then the soliton can be stabilized during this phase for extended periods. More typically, however, the soliton will be lost on account of the residual thermal transients and the associated cavity frequency drift, (i.e., cavity-pump detuning frequency drifts beyond the soliton existence range).

To overcome these transients, the servo control is activated in phase III using the function generator. The servo controls the laser frequency to maintain a setpoint for average soliton power. Significantly, the cavity-pump detuning is also locked because it determines the soliton power (see Eq. 3.1). This frequency locking compensates the short term thermal transients that normally complicate soliton formation, as well as the long term thermal drift of the cavity and the pump laser. The net effect is that the soliton can be reliably captured and sustained indefinitely as illustrated in phase IV. For successful capture of soliton state the soliton free running time in phase II should be longer than the turn-on time of feedback loop. In the present case it is limited by the speed of laser controller and is around $100 \mu\text{s}$.

Demonstration of active capturing and stabilization technique

The demonstration of active capture and locking of a single soliton is presented in Figure 3.6. The comb power is shown in red and a Mach–Zehnder interferometer (MZI) signal in blue is used to track the pump laser frequency (the free spectral range of the interferometer is 40 MHz). The MZI is a similar design to that used in ref. [55] and incorporates two, fiber bidirectional couplers with about a 5 meter path length imbalance. The MZI signal gives an indication of tuning of the pump relative to the interferometer (which is stable over the time period of the scan). Soliton excitation without active capture is shown in Figure 3.6 (a). Here, the power kicking is employed and the soliton persists for about 20 ms before destabilizing. The MZI signal shows that the pump laser is thermally drifting during this period. In Figure 3.6(b), the feedback loop is switched on around 2 ms after the power kicking. A zoomed-in view is provided in Figure 3.6(c). During phase II, it is interesting to observe the transition from the FWM comb to the soliton step which is accompanied by an abrupt decrease in comb power at $\sim 3.2 \text{ ms}$ (red trace). Also,

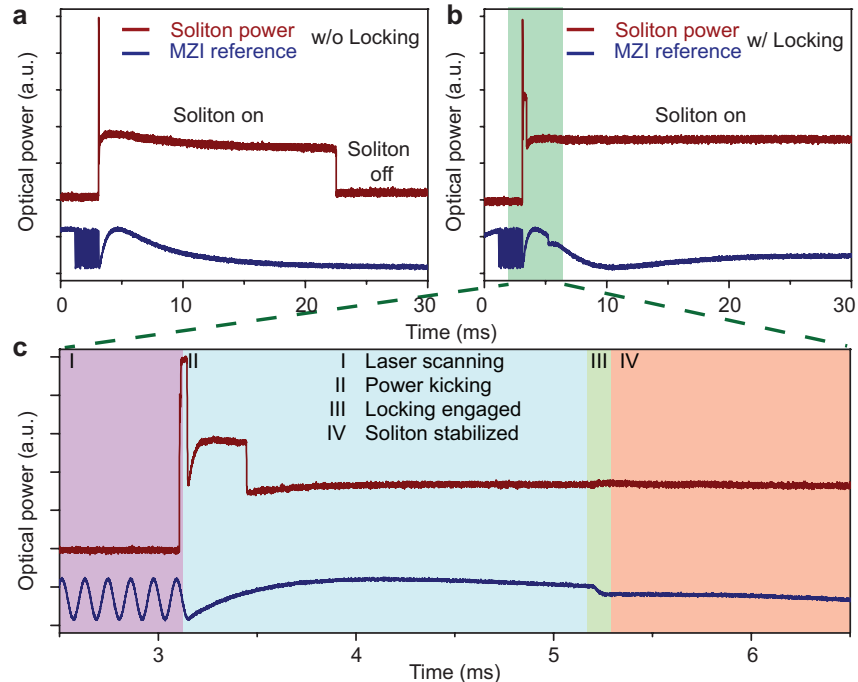


Figure 3.6: Demonstration of capture and locking of a soliton state. (a) Soliton excitation with "power kicking" but no active locking is shown. The soliton state destabilizes around 22ms due to thermal transients. Soliton power is shown in red and a Mach Zehnder (MZI) reference is in blue. (b) Soliton excitation with active locking is shown with conditions similar to panel (a). (c) Zoom-in view of panel (b). The four phases are indicated using the same background color scheme as in Figure 3.5.

in the early part of phase II at ~ 3.5 ms, a further decrease in comb power indicates thermal drift from a two-soliton to a single soliton state. During phase III there is a jump in the MZI signal upon engaging the servo control (~ 5.2 ms) and stable comb power indicates the feedback loop is activated. Long-term stability upon locking is confirmed by measuring soliton power. In Figure 3.7 the soliton is shown to be stabilized for nearly 20 hours until the pump laser is turned off.

3.4 Soliton microcombs at 1550 nm

Using the active capturing technique, both single and multiple soliton states were stably excited in different resonators. In this section, soliton microcombs at 1550 nm band will be characterized.

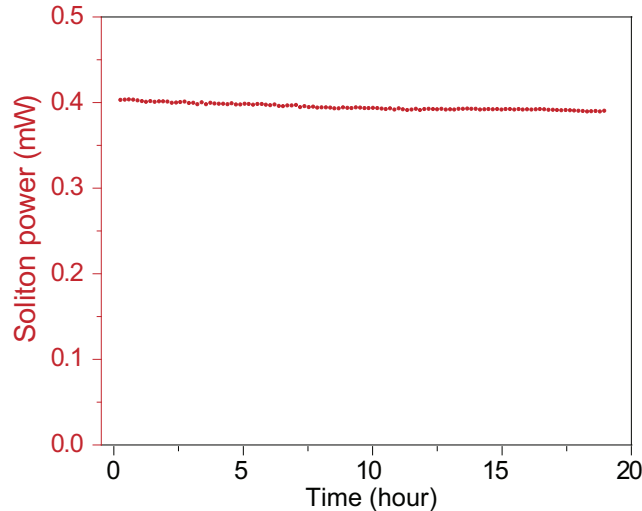


Figure 3.7: Continuous soliton measurement over 19 hours. Soliton power are plotted versus time in hours. The soliton power experiences a slow drift to lower values which is attributed to a slow variation in either the power set point of the electronic control or in the detected power (perhaps due to temperature drift).

Spectral and temporal characterization of soliton microcombs

Figure 3.8(c) shows the spectrum measured for a single-soliton state. The sech^2 function is also overlaid onto the spectrum to verify the characteristic single-soliton spectral shape. From this fitting the soliton pulse width τ_s is inferred to be 130 fs where the pulse shape is $\text{sech}^2(t/\tau_s)$. (Note: this definition of pulse width is $0.57 \times$ the FWHM width of the soliton pulse). The presence of small spurs in the spectrum of Figure 3.8(c) correlate with the appearance of avoided crossings in the mode dispersion spectrum in Figure 3.8(b).

Direct confirmation of single-soliton generation is provided by Frequency-Resolved Optical Gating (FROG) and autocorrelation traces (see Figure 3.8(d)). In these measurements, the pump laser was suppressed by fiber Bragg filters and dispersion compensation of -1.5 ps/nm was applied using a programmable optical filter before the comb was amplified by an Erbium-doped fiber amplifier (EDFA). A pulse width of 250 fs with a pulse period of 46 ps is inferred from this data. The measured pulse width is larger than that fitted from the optical spectrum (130 fs) due to the limited wavelength bandwidth of the optical pre-amplifier used in this measurement. The FROG data was also used to reconstruct the phase of the spectrum and showed a constant phase across the comb teeth.

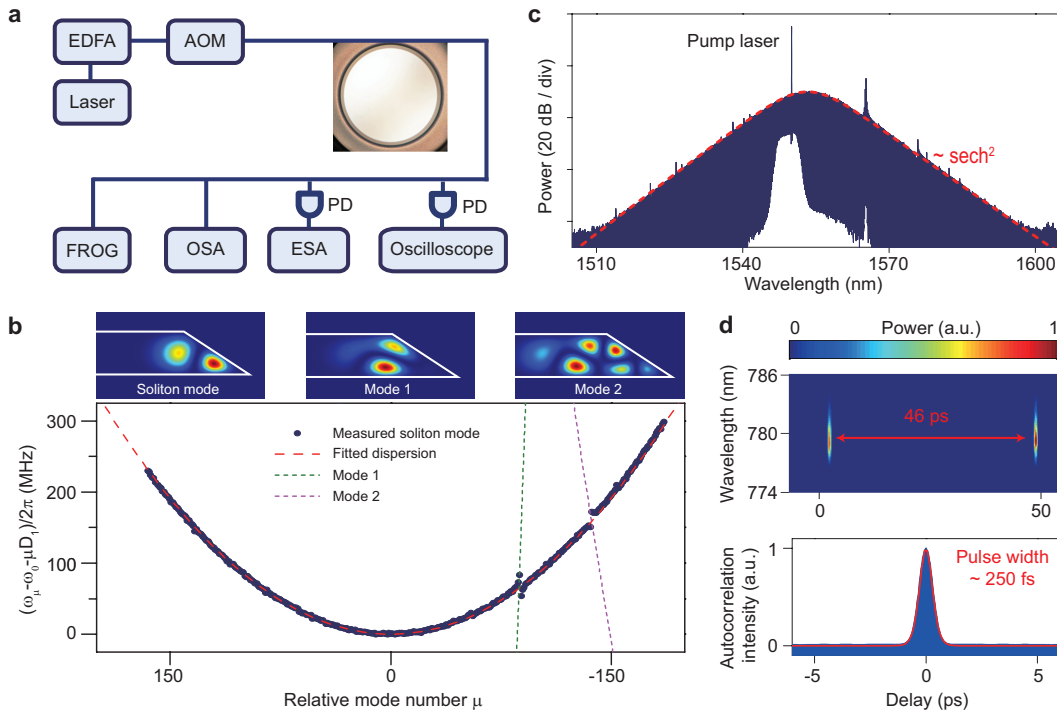


Figure 3.8: Experiment setup, soliton mode-family dispersion, optical spectrum and autocorrelation. (a) Experimental setup. EDFA: erbium-doped-fiber-amplifier; AOM: acousto-optic modulator; PD: photodetector; ESA: electrical spectral analyzer; OSA: optical spectral analyzer; FROG: frequency resolved optical gatings. (b) Measured mode family dispersion (blue points) belonging to the soliton-forming mode family is plotted versus relative mode number, μ . The presence of non-soliton forming mode families can be seen through the appearance of avoided mode crossings (spur-like features) that perturb the parabolic shape. Simulations of the non soliton mode families believed to be responsible for these spurs are provided (see mode 1 and mode 2 dashed curves). In addition, the normalized transverse intensity profiles for the soliton and non-soliton spatial modes are provided at the top of the panel (red indicates higher mode intensity). The simulation used the Sellmeier equation for the refractive index of silica. Oxide thickness, wedge angle, and radius were fine-adjusted to produce the indicated fits. (c) Optical spectrum of single soliton state is shown with a sech^2 envelope (red dashed line) superimposed for comparison. The pump laser is suppressed by 20 dB with an optical Bragg filter. (d) FROG (upper) and autocorrelation trace (lower) of the soliton state in **c**. The optical pulse period is 46 ps and the fitted pulse width is 250 fs (red solid line).

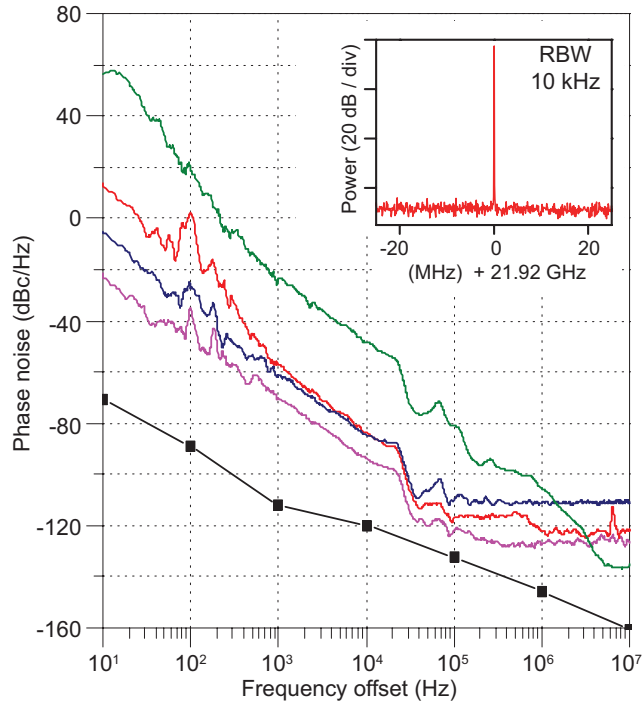


Figure 3.9: Detected phase noise and electrical spectra for three devices with corresponding mode dispersion and soliton data. Phase noise spectral density function plotted versus offset frequency from the detected soliton repetition frequency of three different devices. A Rohde Schwarz phase noise analyzer was used in the measurement. Inset shows the electrical spectrum of the soliton repetition frequency (21.92 GHz) for one device. The other devices had similar spectra with repetition frequencies of 22.01 and 21.92 GHz. The phase noise of the fiber pump laser is shown in green and was generated by mixing 2 nominally identical pump lasers to create a 2.7 GHz electrical beatnote. Several features in the pump laser phase noise are reproduced in the soliton phase noise (see features near and above 20 kHz). The black line connecting square dots is the measurement floor of the phase noise analyzer.

Microwave-rate repetition rate

An important feature of the soliton states generated in this work is their detectable and stable repetition rate. Figure 3.9 contains phase noise spectra of the detected soliton fundamental repetition frequency measured using single solitons generated with three different resonators. The upper right inset to Figure 3.9 is a typical, radio frequency spectrum of the fundamental repetition frequency. The repetition frequency can be seen to be 21.92 GHz (resolution bandwidth is 10 kHz) and has an excellent stability that is comparable to a good K-band microwave oscillator. For example, one of the devices measured has a phase noise level of -100 dBc/Hz at 10 kHz offset (referenced to a 10 GHz carrier frequency). We believe that some of the

variations observable in these spectra are not fundamental, but instead are related to pump laser noise. For example, the step feature in the spectrum near 20kHz offset frequency also appears in the frequency noise of the pump laser (see green curve in Figure 3.9).

3.5 Soliton microcombs at 1064 nm

Dispersion simulations for TM modes near 1064 nm are presented in Figure 3.10(a) and show that TM modes with anomalous dispersion occur in silica resonators having oxide thicknesses less than 3.7 μm . Aside from the thickness control, a secondary method of manipulating dispersion is by changing the wedge angle (see Figure 3.10(a). Here, wedge angles between 30 and 40 degrees were chosen in order to maximize the Q factors[55]. The measured frequency spectrum of the TM₁ mode family in a 3.4 μm thick resonator is plotted in Figure 3.10(b). The plot gives the frequency as relative frequency (i.e., $\omega_\mu - \omega_o - \mu D_1$) to make clear the second-order dispersion contribution. Also shown is a fitted parabola (red curve) revealing $D_2/2\pi = 3.3$ kHz (positive parabolic curvature indicates anomalous dispersion). Some avoided mode crossings are observed in the spectrum. The dispersion measured in resonators of different thicknesses, marked as solid dots in Figure 3.10(a), is in good agreement with numerical simulations.

The experimental setup for generation of 1064 nm pumped solitons is shown in Figure 3.10(c), which is slight different from the approach using acousto-optic modulators. The microresonator is pumped by a CW laser amplified by a YDFA. The pump light and comb power are coupled to and from the resonator by a tapered fiber [130, 139]. Solitons are generated while scanning the laser from higher frequencies to lower frequencies across the pump mode [66–68]. The pump light is modulated by an electro-optic phase modulator to overcome the thermal transient during soliton generation [67, 68, 156]. A servo control referenced to the soliton power is employed to capture and stabilize the solitons [156]. Shown in Figure 3.10(d) are the optical spectra of solitons pumped at 1064 nm. These solitons are generated using the mode family whose dispersion is characterized in Figure 3.10(b). Due to the relatively low dispersion (small D_2), these solitons have a short temporal pulse width. Using the hyperbolic-secant-squared fitting method (see orange and green curves in Figure 3.10(d) a soliton pulse width of 52 fs is estimated for the red spectrum. By increasing the soliton power (blue spectrum) the soliton can be further compressed to 44 fs, which corresponds to a duty cycle of 0.09% at the 20 GHz repetition rate. Finally, the inset in Figure 3.10(d) shows the electrical spectrum of

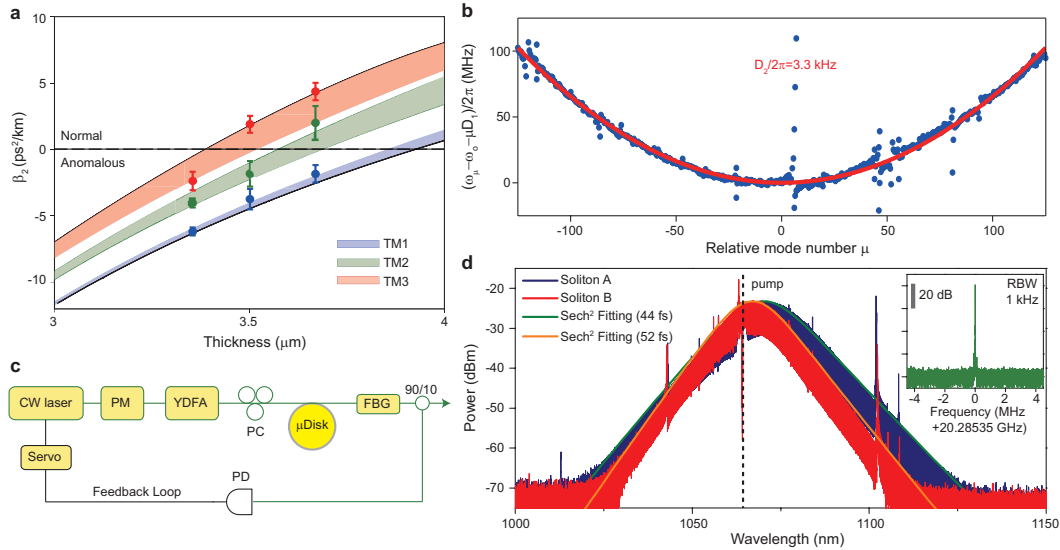


Figure 3.10: Microresonator dispersion engineering and soliton generation at 1064 nm. (a) Simulated dispersion (GVD) of TM mode families versus resonator thickness. The angle of the wedge ranges from 30° to 40° in the colored regions. Measured data points are indicated and agree well with the simulation. (b) Measured relative mode frequencies (blue points) plotted versus relative mode number of a soliton-forming TM1 mode family in a $3.4 \mu\text{m}$ thick resonator. The red curve is a parabolic fit yielding $D_2/2\pi = 3.3$ kHz. (c) Experimental setup for soliton generation. A continuous-wave (CW) fiber laser is modulated by an electro-optic phase modulator (PM) before coupling to a ytterbium-doped-fiber-amplifier (YDFA). The pump light is then coupled to the resonator using a tapered fiber. Part of the comb power is used to servo-lock the pump laser frequency. FBG: fiber Bragg grating. PD: photodetector. PC: polarization controller. (d) Optical spectra of solitons at 1064 nm generated from the mode family shown in **b**. The two soliton spectra correspond to different power levels with the blue spectrum being a higher power and wider bandwidth soliton. The dashed vertical line shows the location of the pump frequency. The solid curves are sech^2 fittings. Inset: typical detected electrical beatnote showing soliton repetition rate. RBW: resolution bandwidth.

the photodetected soliton pulse stream. Besides confirming the repetition frequency, the spectrum is very stable with excellent signal-to-noise ratio (SNR) greater than 70 dB at 1 kHz RBW.

3.6 Measurement of soliton properties

Measurement of soliton properties is enabled by stabilization of the detuning of the pump relative to the cavity. For example, soliton pulse width is given by the following expression [66, 67, 133, 156, 157]:

$$\tau = \sqrt{-\frac{c\beta_2}{2n\delta\omega}}, \quad (3.2)$$

where $\beta_2 = -n_o D_2 / c D_1^2$ is the group velocity dispersion and is negative for anomalous dispersion. To test theoretical predictions, several soliton properties were measured. Comb power and the maximum power per comb tooth were measured at a series of detuning values, $\delta\omega/2\pi$, estimated to range from 12.8 MHz ($\tau=187$ fs) to 29.6 MHz ($\tau=123$ fs) or approximately 13 to 30 cavity linewidths. At each point the soliton spectrum was also recorded, which enables calculation of the soliton pulse width τ . The results of these measurements are compiled in Figure 3.11(a). Also, Figure 3.11(b) shows the soliton spectrum measured at the detuning limits presented in Figure 3.11(a). The dashed lines in Figure 3.11(a) give the predicted comb power and maximum comb tooth power based on the following expressions for comb power and the comb power spectral envelope[66, 133, 157]:

$$P_{\text{sol}} = -\frac{2c\eta A_{\text{eff}}\beta_2}{n_2 Q} \frac{1}{\tau}, \quad (3.3)$$

$$P(\Delta\omega) = -\frac{\pi c \eta A_{\text{eff}}\beta_2}{2} \frac{D_1}{n_2 Q} \text{sech}^2\left(\frac{\pi\tau}{2} \Delta\omega\right), \quad (3.4)$$

where Eq. (3.4) results by eliminating $\delta\omega$ in Eqs. (3.2) and (3.3), and $\Delta\omega$ denotes the comb tooth frequency relative to the pump frequency. Note that the peak power of the spectral envelope (i.e., maximum comb tooth power) is determined entirely by the cavity properties. This feature is apparent in both the data in Figure 3.11(a) and the spectra in Figure 3.11(b). As an aside, Eqs. (3.2) and (3.3) are derived under an assumption of large frequency detuning in units of cavity linewidth, which is satisfied for the current measurements.

In units of cavity linewidth, the predicted maximum detuning for soliton existence is given by $\delta\omega_{\text{max}} \equiv \pi^2 P_{\text{in}} / 16 P_{\text{th}}$ [66, 133, 157]. This power dependence explains why increased pump power is effective in providing stable, non-locked soliton operation. At higher pumping powers, the solitons can survive over a wider range of tuning values as the pump laser frequency drifts relative to the cavity resonant frequency. However, as noted above, it is preferable to prevent this relative drift. In addition to the reasons mentioned in the previous section, locking of the detuning frequency, $\delta\omega$, enables operation at a lower (and hence more efficient) pump power setting that is close to the existence power limit for solitons of a desired pulse width.

To measure the minimum existence power, $\delta\omega$ was held constant while pump power is reduced to the point of drop-out of the soliton pulse train. Both this power level

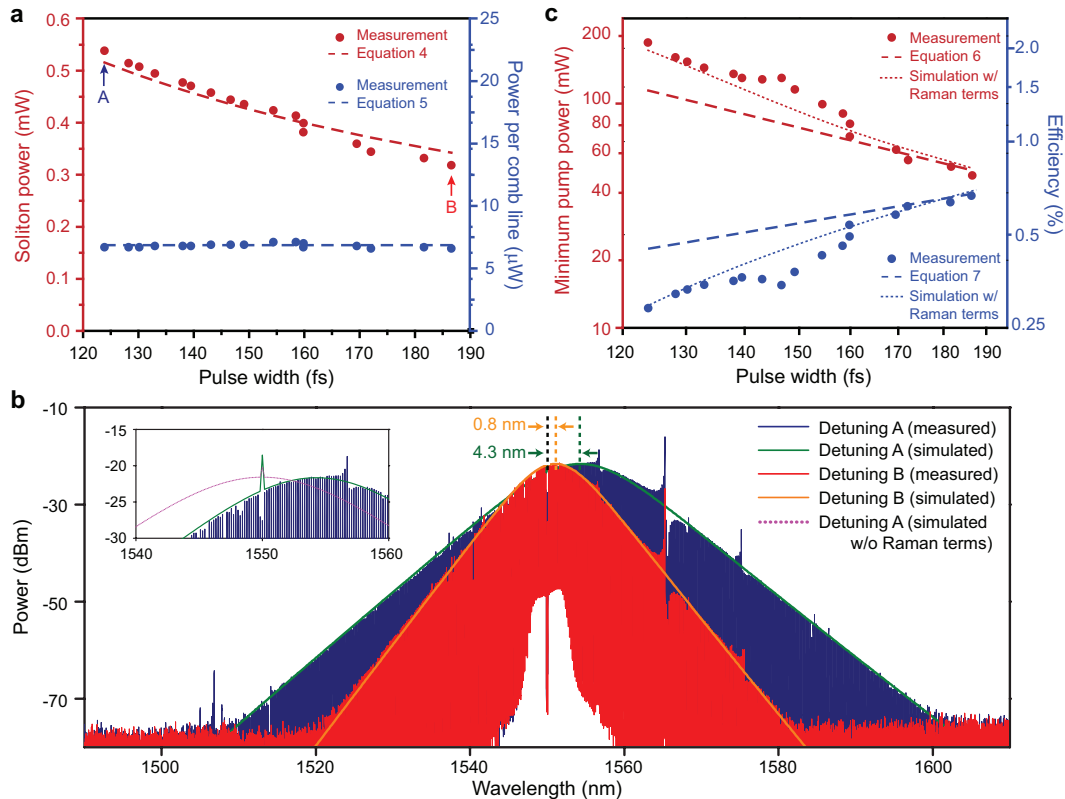


Figure 3.11: Control of soliton properties. (a) Measured soliton comb output power is plotted versus measured soliton pulse width (red points) with comparison to Eq. (3.1) (dashed red line). The measured power per central comb tooth is plotted versus pulse width (blue points) with comparison to Eq. (3.4) (dashed blue line). (b) The observed soliton spectra at the limits of the measurement in Figure 3.8(a) is shown (see arrows A and B in Figure 3.8(a)). Solid orange and green curves are simulations using the Lugiato Lefever equation including Raman terms. The indicated wavelength shifts between the pump and the center of the soliton spectrum result from Raman interactions with the soliton. The location of the pump line for both spectra is indicated by the dashed black line and has been suppressed by filtering. The inset shows a magnified view near the central region of the blue spectrum. The green (purple) envelope provides the Lugiato Lefever simulation with (without) Raman terms. The green spike is the location of the pump. (c) Measured minimum pump power for soliton existence is plotted versus measured soliton pulse width (red points) with comparison to Eq. (3.5) (dashed red line). Measured efficiency is plotted versus measured soliton pulse width (blue points) with comparison to Eq. (3.6) (dashed blue line). Simulation using Lugiato-Lefever equation including Raman terms improves agreement with data (small dashed red and blue lines).

and the soliton spectrum were recorded near the point of drop-out. $\delta\omega$ was then reset to a new value and the measurement repeated. Figure 3.11(c) gives the minimum

power measured this way plotted versus the pulse width (as before calculated from the soliton spectrum). Recall the following expression for minimum pump power for soliton existence as a function of pulse width [66, 133, 157],

$$P_{\text{in}}^{\text{min}} = -\frac{2c}{\pi} \frac{A_{\text{eff}}\beta_2}{\eta n_2 \tau^2} \frac{1}{QD_1}. \quad (3.5)$$

This expression is plotted in Figure 3.11c (dashed red line). A deviation from the predicted dependence is observed. Improved agreement with the data is provided by a simulation (small dashed red line) using the Lugiato-Lefever equation (LLE) augmented by Raman terms [88, 128, 158]. In this analysis, a Raman time constant of 2.4 fs was extracted by fitting the data. This time constant closely agrees with a value of 3 fs measured for silica optical fiber [159]. The contribution of the Raman terms is both predicted and measured to be stronger for shorter pulses (or equivalently larger $\delta\omega$). These observations are also consistent with modeling which shows modifications to soliton efficiency as a result of the Raman process [158]. In Chapter 4 the effects of Raman nonlinearity on soliton microcombs will be discussed in detail.

It is interesting that the predicted soliton power and power per line do not require a Raman correction (see Figure 3.11(a)). The Raman correction primarily influences the temporal phase of the soliton pulse and not the amplitude [87]. It would therefore be expected to alter the existence condition, which is associated with the phase of the soliton field and not the power per line or overall comb power.

All of the soliton spectra observed in this work were shifted to the red relative to the pump wavelength. Raman interaction with dissipative Kerr solitons has recently been shown to cause such self-shifting of the spectrum [87, 88, 160, 161]. The effect has also been observed in silicon nitride resonators [87]. Like the correction to the minimum power described above, this shift is stronger for shorter pulses and larger detuning frequencies. Shifted soliton spectra can be produced by several mechanisms besides Raman including soliton recoil caused by dispersive wave generation [68]. There was no evidence of dispersive wave generation at shorter wavelengths in this work. Consistent with other reports [87, 88] the Raman-augmented LLE simulation explains the soliton spectral shift observed here (see orange and green curves in Figure 3.11(b)).

Control of the pump-resonator detuning frequency enables stable operation near an optimal pumping efficiency limit. Defining efficiency [158] as the soliton power divided by the minimum pump power for soliton existence gives the following simple

expression:

$$\Gamma \equiv \pi\eta^2 D_1 \tau. \quad (3.6)$$

Comparison of this prediction with measurement is provided in Figure 3.11(c) ($\eta = 0.29$ in this measurement). A deviation between Eq. (3.6) and the data at small pulse widths occurs on account of Raman effects and has been corrected in the Figure (small dashed blue line) using the Raman augmented LLE result. A more detailed study in the impact of Raman nonlinearity on soliton microcombs will be presented in Chapter 4.

3.7 Conclusion

In this chapter, we have demonstrated the generation of soliton microcombs in high-Q silica microresonators. By designing the geometry of the microresonator, anomalous dispersion with minimal avoided-mode-crossings has been achieved in both 1550 nm and 1064 nm band. Soliton microcombs are triggered by scanning a continuous-wave laser across the resonance, and are stabilized using the active capturing technique. The soliton microcombs span about 100 nm and feature fs-level pulse width. A number of quantities of solitons have been measured, which are in good agreement with theoretical predictions.

Cavity dispersion can be further controlled using a modification to the standard wedge resonator process [138]. These same methods might be applied to control dispersive wave generation within the resonator to achieve direct generation of a broader comb. The ability to generate solitons on a chip at rates commensurate with detectors and low-noise electronics is an essential step in the ultimate goal of a fully-integrated comb system. Besides soliton generation, the silica wedge resonator platform has been used to generate ultra-narrow linewidth laser sources [162, 163], high-Q reference cavities [164] and for continuum generation [149]. These elements are required in both self-referenced combs as well their application to clocks [103], high-stability microwave sources [71, 84], and optical synthesizers [104]. The results presented here therefore add to this suite of technologically compatible devices.

*Chapter 4*RAMAN SELF-FREQUENCY SHIFT IN SOLITON
MICROCOMBS

¹While the Kerr effect is essential to soliton formation, other nonlinearities can alter soliton properties. For example, Raman effect refers to inelastic photon scattering by the vibrational modes of molecules, whose interaction with solitons causes the so-called self-frequency-shift (SFS). In optical fiber transmission, this effect causes the soliton's central frequency to experience increasing redshifting with propagation distance [160]. Intuitively, this is understood as a continuous energy transfer from the blue to red side of the soliton spectrum that is mediated by the Raman interaction [161]. The effect is of practical importance in supercontinuum generation using optical fibers [20]. It has also been used in difference frequency generation of mid-IR frequency combs [165]. Recently, the Raman self-frequency-shift has been numerically modeled [166] and observed to influence soliton microcombs [67, 87]. Here, rather than producing a continuously increasing red shift, the Raman effect produces a constant frequency offset between the optical pump and the soliton spectral maximum (i.e., a frequency locked Raman soliton [166]). Without the Raman self-frequency-shift, the optical pump would be centered on the soliton comb spectrum (at the spectral maximum). Instead, the soliton spectral maximum is red-shifted away from the pump. The amount of shift increases with soliton peak power and so far has been numerically calculated [67, 87, 166] by solving the Lugiato Lefever equation [127].

In this chapter, we present an analysis of the self-frequency-shift for soliton microcombs using the perturbed Lagrangian formalism and develop an analytical expression for the frequency shift in terms of soliton and cavity properties. In addition, an analytical expression for the soliton efficiency including the Raman effect is found and compared with new measurements as well as those reported earlier [67]. The Raman self frequency shift (SFS) and soliton efficiency expressions are first compared with measurements to confirm the predicted behavior, and then the derivation of these expressions is outlined.

¹Work presented in this chapter has been published in "Theory and measurement of the soliton self-frequency shift and efficiency in optical microresonators", *Opt. Lett.* 41(15):3419-3422 (2016)

4.1 Lugiato-Lefever equation augmented by Raman terms

Raman response function

Raman scattering is a third order nonlinear process, which excites the vibration of nuclei. Since the nuclei are much heavier than the electrons, the Raman process usually features a delayed response compared with the almost instantaneous Kerr effect. To make a correction to Eq. (2.7), the change of refractive index induced by Kerr and Raman effect is now given by

$$\delta n = \frac{3\chi_{xxxx}^3}{4n_o} \int_0^\infty R(t') |E(\mathbf{r}, t - t')|^2 dt'. \quad (4.1)$$

Here $R(t)$ is the nonlinear response function, which can be written as

$$R(t) = (1 - f_R)\delta(t) + f_R h_R(t). \quad (4.2)$$

The first term on the R.H.S. represents the instantaneous electronic contribution, while the second term is the delayed Raman response. f_R is the fractional contribution. $R(t)$ is normalized such that $\int_0^\infty R(t) = 1$. A widely-used approximate form of $h_R(t)$ in silica fibers is given by the following expression [167]:

$$h_R(t) = (\tau_1^{-2} + \tau_2^{-2})\tau_1 e^{-\frac{t}{\tau_2}} \sin \frac{t}{\tau_1}, \quad (4.3)$$

where $\tau_1 = 12.2$ fs and $\tau_2 = 32$ fs are generally used. $f_R = 0.18$ is derived from the measured value of peak Raman-gain. A more accurate fit to the actual Raman-gain spectrum in silica fibers is given in Ref. [168].

Raman-augmented pulse propagation equation

Replacing Eq. (2.7) with Eq. (4.1), the pulse propagation equation yields

$$\frac{\partial E(z, T)}{\partial z} = - \sum_{n=2}^{\infty} \frac{i^{n-1}}{n!} \beta_n \frac{\partial^2 E}{\partial T^2} - \frac{\alpha}{2} E + i\gamma(\omega_o) E \int_0^\infty R(T') |E(z, T - T')|^2 dT'. \quad (4.4)$$

If the pulse width greatly exceeds the Raman response time τ_1 and τ_2 , i.e., the Raman response function $h_R(t)$ decays very fast compared with the pulse duration, the integration in Eq. (4.4) can be simplified as

$$\begin{aligned} \int_0^\infty R(T') |E(z, T - T')|^2 dT' &\approx \int_0^\infty R(T') (|E(z, T)|^2 - T' \frac{\partial}{\partial T} |E(z, T)|^2) dT' \\ &= |E(z, T)|^2 - \frac{\partial |E(z, T)|^2}{\partial T} \int_0^\infty T' R(T') dT'. \end{aligned} \quad (4.5)$$

Defining the Raman shock time

$$\tau_R = f_R \int_0^\infty t h_R(t) dt, \quad (4.6)$$

Equation (4.4) takes the approximate form

$$\frac{\partial E(z, T)}{\partial z} = - \sum_{n=2}^{\infty} \frac{i^{n-1}}{n!} \beta_n \frac{\partial^2 E}{\partial T^2} - \frac{\alpha}{2} E + i\gamma |E|^2 |E| - i\gamma \tau_R E \frac{\partial |E|^2}{\partial T}. \quad (4.7)$$

The Raman shock time can also be written in the following form:

$$\tau_R = f_R \frac{d(\text{Im} \tilde{h}_R(\Delta\omega))}{d(\Delta\omega)} \Big|_{\Delta\omega=0}, \quad (4.8)$$

which shows its proportionality to the slope of the gain spectrum at 0. \tilde{h}_R is the Fourier transform of h_R with respect to t .

Raman-augmented Lugiato-Lefever equation

Consider the propagation of a wide pulse in a microresonator, the Raman contribution to the change of refractive index in the lab frame (Θ, t) is given by

$$\Delta n \sim \int_0^{\infty} R(t') |A(\Theta, t - t')|^2 dt' \approx |A(\Theta, t)|^2 - \tau_R \frac{\partial |A(\Theta, t)|^2}{\partial t}. \quad (4.9)$$

Applying the coordinate transform $\phi = \Theta - D_1 t$, we obtain

$$\frac{\partial |A(\Theta, t)|^2}{\partial t} = \frac{\partial |A(\phi, t)|^2}{\partial t} - D_1 \frac{\partial |A(\phi, t)|^2}{\partial \phi}. \quad (4.10)$$

Since $A(\phi, t)$ is the slowly varying envelope of a pulse propagating in the rotational frame, it has a general form

$$|A(\phi, t)|^2 = f(\phi - \phi_c(t)), \quad (4.11)$$

where $\phi_c(t)$ is the location of the pulse peak. Using Eq. (4.11), the terms on the R.H.S. of Eq. (4.10) can be written as

$$\frac{\partial |A(\phi, t)|^2}{\partial t} = -f' \frac{\partial \phi_c}{\partial t}, \quad (4.12)$$

$$D_1 \frac{\partial |A(\phi, t)|^2}{\partial \phi} = D_1 f'. \quad (4.13)$$

The pulse is slowly moving in the rotational frame, resulting in $|\frac{\partial \phi_c}{\partial t}| \ll D_1$. Therefore, the first term on the R.H.S. of Eq. (4.10) is negligible compared to the second term, which gives

$$\frac{\partial |A(\Theta, t)|^2}{\partial t} \approx -D_1 \frac{\partial |A(\phi, t)|^2}{\partial \phi}. \quad (4.14)$$

Now the Raman term can be embedded into the Lugiato-Lefever equation by scaling with Eq. (4.7), yielding

$$\frac{\partial A(\phi, t)}{\partial t} = \sum_{n=2}^{\infty} i^{n-1} \frac{D_n}{n!} \frac{\partial^n A}{\partial \phi^n} + ig|A|^2 A - \left(\frac{\kappa}{2} + i\delta\omega\right)A + \sqrt{\frac{\kappa\eta P_{\text{in}}}{\hbar\omega_o}} + igD_1\tau_{RA} \frac{\partial |A|^2}{\partial \phi}. \quad (4.15)$$

The equation above is the Lugiato-Lefever equation augmented by Raman terms. It should be noted that the Raman shock time approximation only applies when the pulse duration is much longer than the Raman response. If the pulse width is comparable to the Raman response time, the full Raman term should be taken into consideration. Using the approximation in Eq. (4.14), the generalised form of Eq. (4.15) is given by

$$\begin{aligned} \frac{\partial A(\phi, t)}{\partial t} = & \sum_{n=2}^{\infty} i^{n-1} \frac{D_n}{n!} \frac{\partial^n A}{\partial \phi^n} + i \frac{g}{D_1} A \int_0^{\infty} R\left(\frac{\phi'}{D_1}\right) |A(\phi + \phi', t)|^2 d\phi' \\ & - \left(\frac{\kappa}{2} + i\delta\omega\right)A + \sqrt{\frac{\kappa\eta P_{\text{in}}}{\hbar\omega_o}}. \end{aligned} \quad (4.16)$$

4.2 Theory of Raman self frequency shift

The key theoretical results of this work are the following expressions for the Raman self-frequency-shift, Ω , the minimum input pump power required to generate a soliton, P_{min} , and the soliton pumping efficiency, $\Gamma = P_{\text{sol}}/P_{\text{min}}$ [158] (P_{sol} is the average soliton power),

$$\Omega = -\frac{8D_2 Q \tau_R}{15\omega_0 D_1^2} \frac{1}{\tau_s^4} = \frac{8c\tau_R Q \beta_2}{15n_0\omega_0} \frac{1}{\tau_s^4}, \quad (4.17)$$

$$P_{\text{min}} = P_0 \cosh^2 \frac{\pi\Omega\tau_s}{2}, \quad (4.18)$$

$$\Gamma = \Gamma_0 \text{sech}^2(\pi\Omega\tau_s/2), \quad (4.19)$$

where τ_s is the soliton pulse width. Also, P_0 and Γ_0 are the soliton minimum pumping power and soliton efficiency in the absence of the Raman SFS (i.e., $\Omega = 0$) and are given by [67]

$$P_0 = -\frac{2c}{\pi} \frac{A_{\text{eff}}\beta_2}{\eta n_2 Q D_1} \frac{1}{\tau_s^2}, \quad (4.20)$$

$$\Gamma_0 = \pi\eta^2 D_1 \tau_s. \quad (4.21)$$

In the following, we present the derivation of Eqs. (4.17) - (4.19) using the Lagrangian formalism.

Lagrangian formalism

An approximate solution of the LLE in the absence of Raman effect has been given in Chapter 2. Here, we extend this method by including the Raman term as a perturbation.

Recall the Lagrangian density for the soliton:

$$\mathcal{L}_s = \frac{i}{2}(A^* \frac{\partial A}{\partial t} - A \frac{\partial A^*}{\partial t}) - \frac{D_2}{2} \left| \frac{\partial A}{\partial \phi} \right|^2 + \frac{1}{2}g|A|^4 - \delta\omega|A|^2. \quad (4.22)$$

The dissipation, pumping, and the Raman terms are combined in a perturbation \mathcal{R} , where

$$\mathcal{R} = -\frac{i\kappa}{2}A + i\sqrt{\frac{\kappa\eta P_{in}}{\hbar\omega_o}} - gD_1\tau_R A \frac{\partial|A|^2}{\partial\phi}. \quad (4.23)$$

Eq. (4.15) is recovered by taking $\delta\mathcal{L}_f/\delta A^* = \mathcal{R}$ [169]. The form for the slowly varying field envelope of the solitons wherein the central frequency is shifted by Ω is given by

$$A = B \operatorname{sech} \frac{\phi - \phi_o}{D_1\tau_s} e^{i\Omega(\phi - \phi_o)/D_1} e^{i\psi}, \quad (4.24)$$

which is an exact solution for the case with no perturbation ($\mathcal{R} = 0$). This form is also consistent with measurement and numerical modeling of the soliton microcombs in the presence of Raman interactions [67, 87, 166]. For the proceeding analysis, the soliton phase (ψ), position (ϕ_o), amplitude (B), pulse width (τ_s), and shift frequency (Ω) are considered functions of t , the slow time variable. Finally, Eq. (4.24) assumes $\delta\omega \gg \kappa$ (i.e., large pump detuning). In this case the background field associated with soliton microcombs is much weaker than the soliton peak power and is not included in Eq. (4.24). However, it can be retrieved from Eq. (4.15) for $|(\phi - \phi_o)/D_1\tau_s| \gg 1$ where the soliton pulse is no longer dominant [66, 134, 170].

The equations of motion for the perturbed Lagrangian have the form [134, 169, 170]

$$\frac{\partial L_s}{\partial r_i} - \frac{d}{dt} \frac{\partial L_s}{\partial \dot{r}_i} = \int (\mathcal{R} \frac{\partial A^*}{\partial r_i} + \mathcal{R}^* \frac{\partial A}{\partial r_i}) dt, \quad (4.25)$$

where the coordinates r_i in the Lagrangian are taken as the parameters B , Ω , ϕ_o and ψ . Using Eq. (4.24) in the Lagrangian density, Eq. (4.22), gives the following result:

$$L_s = \int \mathcal{L}_s dt = 2B \sqrt{\frac{D_2}{gD_1^2}} \left(\frac{gB^2}{6} - \frac{D_2\Omega^2}{2D_1^2} - \delta\omega + \frac{\Omega}{D_1} \frac{\partial\phi_o}{\partial t} - \frac{\partial\psi}{\partial t} \right). \quad (4.26)$$

Inserting Eq. (4.24) and Eq. (4.22) into Eq. (4.25) yields the equations of motion for parameters B , ϕ_o , Ω , and ψ .

$$\frac{dB}{dt} = -\kappa B + \pi \sqrt{\frac{\kappa \eta P_{\text{in}}}{\hbar \omega_o}} \cos \psi \operatorname{sech}\left(\sqrt{\frac{D_2}{g D_1^2}} \frac{\pi \Omega}{2B}\right), \quad (4.27)$$

$$\frac{d\psi}{dt} = \frac{g}{2} B^2 - \delta\omega - \frac{D_2}{2D_1^2} \Omega^2 + \frac{\partial \phi_o}{\partial t} \frac{\Omega}{D_1}, \quad (4.28)$$

$$\frac{dB\Omega}{dt} = -\kappa B\Omega - \frac{8D_1^2 \tau_R g^2}{15D_2} B^5, \quad (4.29)$$

$$\frac{d\phi_o}{dt} = \frac{D_2}{D_1} \Omega, \quad (4.30)$$

where $\delta\omega \gg \kappa$ has been assumed. Equation (4.30) corresponds to the change of soliton repetition rate due to the self-frequency shift [133] and has recently been observed [90]. It is also observed experimentally that the central soliton comb tooth power is a constant (independent of the operating point) and in good agreement with the Raman-free Lugiato-Lefever prediction [67]. By Fourier transform of a train of periodic pulses (period = $2\pi/D_1$) of the form in Eq. (4.24), the power per comb tooth at the central maximum of the soliton spectrum is given by $\hbar\omega_o D_1^2 \eta \kappa / 4 \times B^2 \tau_s^2$. Accordingly, to be consistent with experimental observations, the product $B\tau_s$ is assumed to be given by the Raman-free result, $B\tau_s = \sqrt{D_2/gD_1^2}$. More rigorously, it is possible to show that this follows directly from variation of the Raman-perturbed system (Eqs. (4.22) and (4.23)) with B and τ_s treated as independent variables. This result is used to eliminate τ_s in the calculation below. Steady-state solution of Eq. (4.29) gives Eq. (4.17) for the self frequency shift Ω (also using $B\tau_s = \sqrt{D_2/gD_1^2}$), while Eq. (4.27) and (4.28) give the following steady-state results:

$$B = \sqrt{\frac{D_2}{g D_1^2}} \frac{1}{\tau_s} = \sqrt{\frac{2}{g} \left(\delta\omega - \frac{D_2}{2D_1^2} \Omega^2 \right)}, \quad (4.31)$$

$$\cos \psi = \frac{1}{\pi \tau_s} \sqrt{\frac{D_2 \kappa \hbar \omega_o}{\eta g D_1^2 P_{\text{in}}}} \cosh \frac{\pi \Omega \tau_s}{2}. \quad (4.32)$$

Combining Eq. (4.17) and (4.31), the self-frequency shift and soliton pulse width can be expressed in terms of laser-cavity detuning,

$$\delta\omega = \sqrt{\frac{-15D_2\omega_o}{32D_1^2Q}} \frac{\Omega}{\tau_R} + \frac{D_2}{2D_1^2} \Omega^2 \quad (4.33)$$

$$\delta\omega = \frac{D_2}{2D_1^2} \frac{1}{\tau_s^2} \left(1 + \frac{64D_2^2\tau_R^2}{225D_1^2\kappa^2} \frac{1}{\tau_s^6}\right). \quad (4.34)$$

It is important to remember that despite the form of these equations, detuning ($\delta\omega$) is the parameter that is controlled in a measurement. Also, in Eq. (4.33), note that in the limit of $\tau_R \rightarrow 0$, $\Omega \rightarrow 0$ for finite $\delta\omega$.

The minimum input power for soliton existence given by Eq. (4.18) can be obtained by requiring $|\cos \psi| \leq 1$ in Eq. (4.32). The average soliton power is given by [66, 67],

$$P_{\text{sol}} = -\frac{2c\eta A_{\text{eff}}\beta_2}{n_2Q} \frac{1}{\tau_s}, \quad (4.35)$$

This expression follows from Eq. (4.24) and the relation between B and τ_s noted above. Using Eq. (4.18) and Eq. (4.35), the soliton efficiency in Eq. (4.19) can be obtained from $\Gamma = P_{\text{sol}}/P_{\text{min}}$.

4.3 Measurement of Raman self frequency shift

Soliton microcombs were generated in a 3 mm silica resonator (free spectral range ≈ 22 GHz). General information on the resonators and the techniques used to measure the solitons are described in references [67, 156]. Soliton spectra measured in a silica microresonator at two different operating points are shown in Figure 4.1(a). Soliton generation is confirmed by time domain intensity autocorrelation and frequency resolved optical gating (FROG) [67]. Additional confirmation is provided by fitting to the theoretically predicted hyperbolic-secant-squared spectrum (see spectral envelopes in Figure 4.1(a)). The Raman SFS offset of the pump line relative to the soliton spectral center is also indicated in the figure. It can be seen that the broader soliton spectrum (narrower pulse width) features a larger Raman SFS. Finally, soliton pulse width, power, and Raman SFS depend on a single operating point parameter, the frequency detuning of the resonator mode being pumped relative to the pump frequency, $\delta\omega = \omega_0 - \omega_p$ (ω_p is the pump frequency and ω_0 is the frequency of the resonator mode that is pumped). To set and hold this parameter (and, in turn, other soliton properties), soliton power was used to servo control the pump-laser frequency as described in Chapter 3 [67, 156].

To test the theory a series of soliton spectra of increasing spectral width were obtained using the operating point locking method [156]. The Raman SFS, Ω , and the pulse width, τ_s , were measured by least-squares-fitting of the soliton optical spectrum (see Figure 4.1(a)) to the theoretical soliton spectral envelope $P(\omega) =$

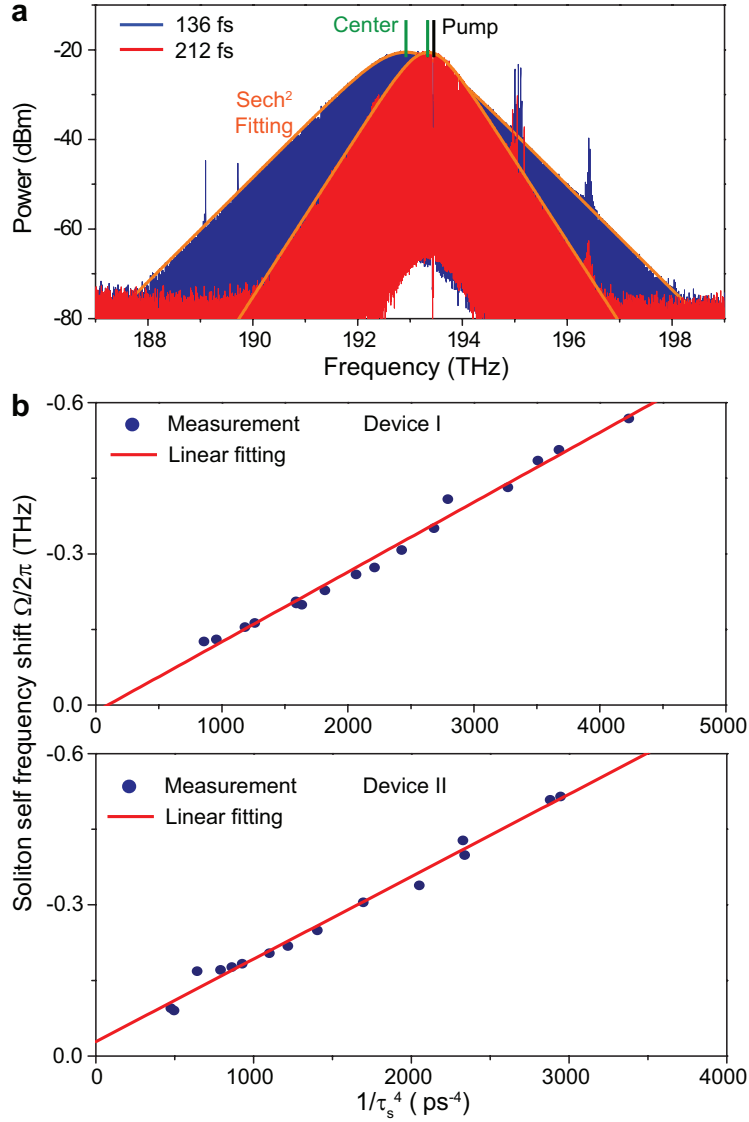


Figure 4.1: (a) Optical spectra measured for a dissipative Kerr cavity soliton at two operating points. The pump power is suppressed using a fiber grating filter. A $sech^2$ fit is shown as the orange curves and pulse widths inferred from the fitting are shown in the legend. The location of the pump line is indicated as the black line. The centers of the spectra are indicated by the green lines. (b) The measured Raman self-frequency-shift plotted versus $1/\tau_s^4$ for two devices. The red line is a linear fit according to Eq. (4.17).

$P_c sech^2[\pi\tau_s(\omega - \omega_p - \Omega)/2]$ (P_c is the maximum comb tooth power). Fig. 4.1(b) plots the measured Ω versus $1/\tau_s^4$ in two devices. For reference, device I is a device characterized previously [67]. A linear fitting to the two sets of data is also provided confirming the predicted theoretical dependence in Eq. (4.17). Furthermore, with measured parameters (device I: $Q = 142$ million, $D_1/2\pi = 22$ GHz, $D_2/2\pi = 17$

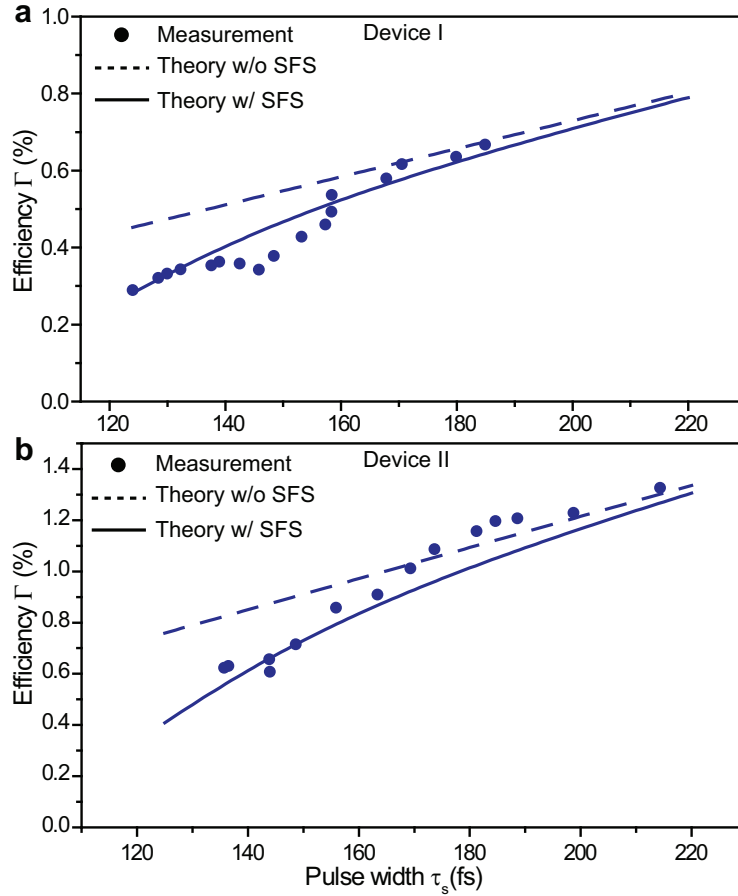


Figure 4.2: The measured efficiency versus soliton pulse width is plotted (blue points) for two devices and compared with theory. Theory comparison with Raman (solid blue lines) and without Raman (dash blue lines) is presented. There are no free parameters in the comparison. The small deviations between the measurement and the theory could result from the presence of weak avoided mode crossings in the dispersion spectrum.

kHz; and device II: $Q = 148$ million, $D_1/2\pi = 22$ GHz, $D_2/2\pi = 17$ kHz), a value of $\tau_R = 2.5 - 2.8$ fs is inferred from the linear fitting, which is in a reasonable agreement with the value of 2-4 fs reported in silica optical fibers [159]. The small non-zero intercept of the linear fitting is in the range of 1 free-spectral-range (22 GHz) of the two resonators.

To measure the soliton efficiency, Γ , the operating point is fixed (i.e., laser-cavity detuning $\delta\omega$ is fixed) while the pump power is decreased until the soliton disappears. Near the disappearance point, the soliton average power, P_{sol} , and the minimum pump power, P_{min} , are recorded and used to obtain efficiency as $\Gamma = P_{\text{sol}}/P_{\text{min}}$. The pulse width is obtained from the optical spectrum as before. Measured efficiency is

plotted versus the pulse width in Fig. 4.2 for devices I and II. The prediction given by Eq. (4.19) is shown as the solid line. The value of τ_R used in the plots is that inferred from the fitting in Figure 4.1(b). Also, $\eta=0.29, 0.37$ is measured for devices I and II. Device II has a higher efficiency as a result of a larger coupling coefficient. The agreement between the theory and measurement in Figure 4.2(b) is very good, especially considering that there are no free parameters. The dashed lines in the plots give the uncorrected efficiency prediction of Eq. (4.21) (i.e., Γ_0 vs. τ_s).

4.4 Conclusion

In summary, closed-form expressions for the self frequency shift and efficiency of dissipative Kerr cavity solitons have been derived using the Lagrangian perturbation approach. Even though the behavior of the Raman self-frequency-shift in microresonators differs in comparison to conventional soliton propagation in optical fiber (i.e., frequency locking behavior in microresonators [166]), it is interesting to note that both systems exhibit an inverse quadratic dependence on soliton pulse width [161]. These results have been experimentally verified, which further reveals the Raman shock time of silica. Finally, albeit the Raman self frequency shift will increase the demand of pump power, such loss of efficiency can be compensated by higher-order-dispersion-induced spectral recoil [171].

Chapter 5

STOKES SOLITONS

¹Solitons result from a balance of wave dispersion with a non-linearity. In optics, temporal solitons are readily formed in optical fiber waveguides [20, 118, 172, 173] and laser resonators [45, 174] and have recently been observed in dielectric microresonators [66]. In each of these cases nonlinear compensation of group velocity dispersion is provided by the Kerr effect (nonlinear refractive index). Besides the Kerr nonlinearity, a secondary effect associated with soliton propagation is the so-called soliton self-frequency shift caused by Raman interaction, which induces a continuously increasing red-shift with propagation in a waveguide [20] or a fixed shift of the soliton spectrum in cavities [87, 88]. More generally, the Raman interaction can produce optical amplification and laser action of waves red-shifted relative to a strong pumping wave or pulse [58, 175, 176]. In this chapter we show a new Raman-related effect, soliton generation through time and space varying Raman amplification created by the presence of a first temporal soliton. Because the new soliton is spectrally red-shifted relative to the initial soliton we call it a Stokes soliton. It is observed in a silica microresonator and obeys a threshold condition resulting from an optimal balancing of Raman gain with cavity loss when the soliton pulses overlap in space and time. Also, the repetition frequency of both the initial and the Stokes soliton are locked by the Kerr nonlinearity.

5.1 Principle of Stokes solitons

Consider a system comprising two solitons propagating in a circular-shaped whispering gallery microresonator. The first temporal soliton, a dissipative Kerr soliton (DKS) [66–69, 125], is referred to as the primary soliton. Consistent with its formation, the primary soliton creates a spatially varying refractive index via the Kerr nonlinearity that serves as an effective potential well. It travels with the soliton and counteracts optical dispersion. Moreover, on account of the Raman interaction, the primary soliton creates local Raman amplification that also propagates with the primary soliton. These propagating index and gain profiles are depicted in Figure 5.1. The primary soliton is composed of many longitudinal modes belonging to one of the

¹Work presented in this chapter has been published in “Stokes solitons in optical microcavities”, *Nat. Phys.* 13(1):53-57 (2017).

transverse mode families of the cavity. These phase-locked modes form a frequency comb. $\Delta\nu_P$ will denote the longitudinal mode separation or free spectral range for longitudinal modes near the spectral center of the primary soliton. $\Delta\nu_P$ also gives the approximate round trip rate of the primary soliton around the cavity ($T_{RT} = \Delta\nu_P^{-1}$ is the round trip time). Consider another transverse mode family besides the one that forms the primary soliton. Suppose that some group of longitudinal modes in this family satisfies two conditions: (1) they lie within the Raman gain spectrum created by the primary soliton; (2) they feature a free spectral range (FSR) that is close in value to that of the primary soliton ($\Delta\nu_P$). Any noise in these longitudinal modes will be amplified by Raman gain provided by the primary soliton. If the round trip amplification of a resulting waveform created by a superposition of these modes is sufficient to overcome round trip optical loss, then oscillation threshold is possible. The threshold will be lowest (Raman gain maximal) if the modes of the second family phase lock to form a pulse overlapping in both space and time with the primary soliton. This overlap is possible since the round trip time of the primary soliton and the new pulse are closely matched, i.e., condition (2) above is satisfied. Also, the potential well created by the primary soliton can be shared with the new optical pulse. This latter nonlinear coupling of the primary soliton with the new Stokes soliton pulse results from Kerr-mediated cross-phase modulation and locks the round trip rates of the two solitons (i.e., their soliton pulse repetition frequencies are locked).

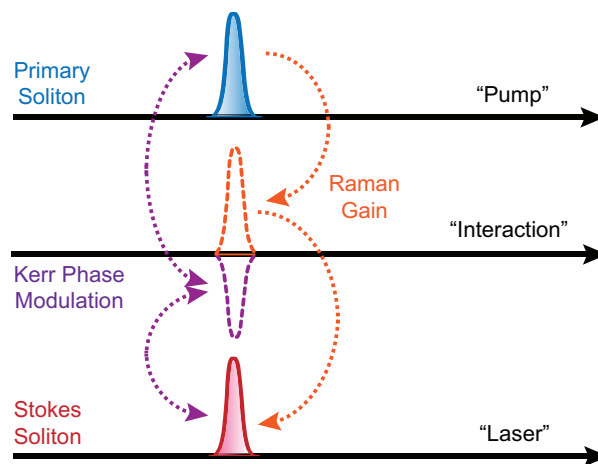


Figure 5.1: Principle of Stokes soliton generation. The Stokes soliton (red) maximizes Raman gain by overlapping in time and space with the primary soliton (blue). It is also trapped by the Kerr-induced effective optical well created by the primary soliton.

The generation of a fundamental soliton by another fundamental soliton in this way is new and also represents a form of mode locking of a soliton laser. It differs from mechanisms like soliton fission which also result in the creation of one or more fundamental solitons [20]. Specifically, soliton fission involves a higher order soliton breaking into multiple fundamental solitons; it is not a regenerative process. Also, co-existing and switching dissipative solitons have been observed [177] and modeled [177, 178] in an erbium-doped mode-locked fiber laser. However, in the present case, the Stokes soliton relies upon the primary soliton for its existence by leveraging spatial-temporal overlap for trapping and optical amplification. Raman gain produced for the Stokes soliton by the primary soliton is also distinctly different from the Raman self-frequency shift [160, 161], which is an effect of the Raman interaction on the primary soliton [67, 87, 88] (not the Stokes soliton). Also, this new Raman mechanism is responsible for oscillation of the Stokes soliton at a well defined threshold. Raman self shift is, on the other hand, not a thresholding process. Finally, concerning the trapping phenomena that accompanies the Stokes soliton formation, the trapping of temporal solitons belonging to distinct polarization states was proposed in the late 1980s [179] and was observed in optical fiber [180, 181] and later in fiber lasers [182]. However, trapping of temporal solitons belonging to distinct transverse mode families, as observed here, was proposed even earlier [183, 184], but has only recently been observed in graded-index fiber waveguides [185]. Trapping of solitons in microresonators has never been reported. Also, the spatial-temporal formation of a soliton through the Raman process has never before been described. The observation, measurement, and modeling of Stokes solitons is now presented.

5.2 Theory of Stokes solitons

Coupled Lugiato-Lefever equations

To study the Stokes soliton generation process, we consider the interaction between two solitons via cross phase modulation and the Raman process, which has been studied in optical fibers using coupled pulse propagation equations [128, 176]. A pair of coupled equations describing the intracavity slowly-varying field amplitudes for the primary and Stokes soliton system can be adapted from the Lugiato-Lefever

equation [66, 127, 131, 132] augmented by Raman interactions [128], which reads:

$$\begin{aligned}
\frac{\partial E_p(\phi)}{\partial t} = & i \frac{D_{2p}}{2} \frac{\partial^2 E_p}{\partial \phi^2} + i(1 - f_R)(g_p |E_p|^2 + 2G_p |E_s|^2)E_p \\
& + i \frac{f_R E_p}{D_{1p}} \int h_R\left(\frac{\phi'}{D_{1p}}\right) (g_p |E_p(\phi + \phi')|^2 + G_p |E_s(\phi + \phi')|^2) d\phi' \\
& + i \frac{f_R E_s}{D_{1p}} \int h_R\left(\frac{\phi'}{D_{1p}}\right) G_p E_p(\phi + \phi') E_s^*(\phi + \phi') \exp(i\Omega \frac{\phi'}{D_{1p}}) d\phi' \\
& - \left(\frac{\kappa_p}{2} + i\Delta\omega_p\right) E_p + \sqrt{\kappa_p^{ext} P_{in}},
\end{aligned} \tag{5.1}$$

$$\begin{aligned}
\frac{\partial E_s(\phi)}{\partial t} = & -\delta \frac{\partial E_s}{\partial \phi} + i \frac{D_{2s}}{2} \frac{\partial^2 E_s}{\partial \phi^2} + i(1 - f_R)(g_s |E_s|^2 + 2G_s |E_p|^2)E_s \\
& + i \frac{f_R E_s}{D_{1p}} \int h_R\left(\frac{\phi'}{D_{1p}}\right) (g_s |E_s(\phi + \phi')|^2 + G_s |E_p(\phi + \phi')|^2) d\phi' \\
& + i \frac{f_R E_p}{D_{1p}} \int h_R\left(\frac{\phi'}{D_{1p}}\right) G_s E_s(\phi + \phi') E_p^*(\phi + \phi') \exp(-i\Omega \frac{\phi'}{D_{1p}}) d\phi' \\
& - \left(\frac{\kappa_s}{2} + i\Delta\omega_s\right) E_s.
\end{aligned} \tag{5.2}$$

The slowly varying fields E_j (subscript $j = (p, s)$ for primary or Stokes soliton) are normalized to optical energy. To second order, the frequency of mode number μ in mode family $j = (p, s)$ is given by the Taylor expansion $\omega_{\mu j} = \omega_{0j} + D_{1j}\mu + \frac{1}{2}D_{2j}\mu^2$ where ω_{0j} is the frequency of mode $\mu = 0$, while D_{1j} and D_{2j} are the FSR and the second-order dispersion at $\mu = 0$. Ω is the carrier frequency difference $\omega_{0p} - \omega_{0s}$. Also, $\delta = D_{1s} - D_{1p}$ is the FSR difference between primary and Stokes solitons at mode $\mu = 0$. κ_j is the cavity loss rate and $\Delta\omega_j$ is the detuning of mode zero of the soliton spectrum relative to the cold cavity resonance. $h_R(t)$ is the Raman response function [128]. For the primary soliton, which is a dissipative Kerr soliton (DKS), the pump field is locked to one of the soliton spectral lines and this ‘‘pump’’ line is taken as mode $\mu = 0$. κ_p^{ext} is the external coupling coefficient and P_{in} is the pump power. g_j and G_j are self and cross phase modulation coefficients, defined as

$$g_j = \frac{n_2\omega_j D_{1j}}{2n\pi A_{jj}}, \quad G_j = \frac{n_2\omega_j D_{1j}}{2n\pi A_{ps}}, \tag{5.3}$$

where the nonlinear mode area A_{jk} is defined as [128]

$$A_{jk} = \frac{\iint_{-\infty}^{\infty} |u_j(x, y)|^2 dx dy \iint_{-\infty}^{\infty} |u_k(x, y)|^2 dx dy}{\iint_{-\infty}^{\infty} |u_j(x, y)|^2 |u_k(x, y)|^2 dx dy}, \tag{5.4}$$

where u_j is the transverse distribution of the mode. $f_R = 0.18$ is the Raman contribution parameter in silica.

As the pulse width of the solitons in our system is several hundred femtosecond, which is much longer than the Raman response time (~ 10 fs), the pulse fields E_p and E_s can be considered slowly varying variables when compared with $h_R(t)$. Therefore, the integrals of E_p and E_s in Eqs. (5.1) and (5.2) associated with Raman response function can be expanded into a Taylor series:

$$\int h_R\left(\frac{\phi'}{D_{1p}}\right)|E_j(\phi + \phi')|^2 d\phi' \approx |E_j(\phi)|^2 + D_{1p} \frac{\partial |E_j(\phi)|^2}{\partial \phi} \int \tau h_R(\tau) d\tau, \quad (5.5)$$

$$\begin{aligned} & \int h_R\left(\frac{\phi'}{D_{1p}}\right)E_j(\phi + \phi')E_k^*(\phi + \phi')e^{-i\Omega\frac{\phi'}{D_{1p}}} d\phi' \\ & \approx E_j(\phi)E_k^*(\phi) \int h_R(\tau)e^{-i\Omega\tau} d\tau, \end{aligned} \quad (5.6)$$

where $\tau = \phi'/D_{1p}$. The next highest order term in Eq. (5.6) is found to have a negligible effect on simulation and is neglected here. Using these approximate forms, the coupled equations simplify as follows:

$$\begin{aligned} \frac{\partial E_p}{\partial t} = & i\frac{D_{2p}}{2} \frac{\partial^2 E_p}{\partial \phi^2} + i[g_p |E_p|^2 + (2 - f_R)G_p |E_s|^2]E_p \\ & - iD_{1p}\tau_R E_p \frac{\partial(g_p |E_p|^2 + G_p |E_s|^2)}{\partial \phi} \\ & - \left(\frac{\kappa_p}{2} + i\Delta\omega_p\right)E_p - \frac{\omega_p}{\omega_s} R |E_s|^2 E_p + \sqrt{\kappa_p^{ext} P_{in}}, \end{aligned} \quad (5.7)$$

$$\begin{aligned} \frac{\partial E_s}{\partial t} = & -\delta \frac{\partial E_s}{\partial \phi} + i\frac{D_{2s}}{2} \frac{\partial^2 E_s}{\partial \phi^2} + i[g_s |E_s|^2 + (2 - f_R)G_s |E_p|^2]E_s \\ & - iD_{1p}\tau_R E_s \frac{\partial(g_s |E_s|^2 + G_s |E_p|^2)}{\partial \phi} \\ & - \left(\frac{\kappa_s}{2} + i\Delta\omega_s\right)E_s + R |E_p|^2 E_s, \end{aligned} \quad (5.8)$$

where $R = f_R G_s \text{Im}[\int h_R(\tau) \exp(i\Omega\tau) d\tau] = cD_{1p}g_R(\omega_s, \omega_p)/4n\pi A_{ps}$ and $g_R(\omega_s, \omega_p)$ is the Raman gain in silica. The Raman shock time is defined by $\tau_R = f_R \int \tau h_R(\tau) d\tau$ and is ~ 2 -3 fs in silica. For solitons with a few THz bandwidth, other effects are negligible (e.g., higher order dispersion, the self-steepening effect and Raman induced refractive index change [128]). If the soliton pulse width is well below 100 fs, i.e., it has a broadband spectrum, then the coupled equations with higher-order Raman correction might be required.

Phase-sensitive, four-wave-mixing terms have also been omitted in Eq. (5.7) and (5.8). In principle, these terms could introduce locking of the Stokes and primary

soliton fields (in addition to their repetition rates). However, for this to occur the underlying spatial mode families would need to feature mode frequencies that align reasonably well (both in FSR and offset frequency) within the same band. In this work, the mode frequencies were observed to not overlap using devices that featured spectrally overlapping solitons.

Calculation of threshold

Although an exact solution of the coupled solitons cannot be obtained, the near threshold behavior of the Stokes soliton can still be studied analytically. In this limit, the primary soliton is unperturbed by the Stokes soliton since the Stokes soliton is weak (i.e., near threshold). Its solution is therefore given by the Sech² DKS solution [66]. The Stokes soliton equation then uses this solution for the primary soliton. By selecting the carrier frequency of the Stokes soliton such that $\delta = 0$, the equation for the Stokes soliton can be simplified to the following,

$$\frac{\partial E_s}{\partial t} = i \frac{D_{2s}}{2} \frac{\partial^2 E_s}{\partial \phi^2} + i(2 - f_R)G_s |E_s|^2 E_s - \left(\frac{\kappa_s}{2} + i\Delta\omega_s\right)E_s + R|E_p|^2 E_s, \quad (5.9)$$

where $E_p = A \text{sech} B\phi$ is the uncoupled primary soliton solution [66] with $|A|^2 = 2\Delta\omega_p/g_p$ and $B = \sqrt{2\Delta\omega_p/D_{2p}}$. The Raman terms containing derivatives cause soliton self frequency shift and subsequently a phase change [87]. However, they minimally affect pulse width and peak power [67, 88]. As the primary soliton and Stokes soliton have no absolute phase coherence, these terms have been omitted. Accordingly, the Stokes soliton is treated as a wave trapped in a sech²-shape potential well created by the primary soliton, and also deriving optical gain from the primary soliton. The bounded solution of the wave function in such a potential has the following form:

$$E_s = V \text{sech}^\gamma B\phi, \quad (5.10)$$

where, consistent with the near threshold assumption, V is a small amplitude satisfying $|V|^2 \ll |A|^2$. Under these assumptions, the exponent γ is a root of the following equation:

$$\gamma(\gamma + 1) = 2(2 - f_R)G_s D_{2p}/g_p D_{2s}. \quad (5.11)$$

As a physical check of this equation, we note that under circumstances of $G_s = g_p/2$ the potential well created by the primary soliton for the Stokes soliton is identical to the primary soliton potential well (note: the factor of 1/2 comes about from cross phase modulation). In this case, assuming identical second-order dispersion ($D_{2s} = D_{2p}$) and also $f_R = 0$, the solution to Eq. (5.11) is $\gamma = 1$ which shows that the Stokes soliton acquires the same envelope as the primary soliton.

Once the peak power of the primary soliton reaches a point that provides sufficient Raman gain to overcome Stokes soliton roundtrip loss, the Stokes soliton will begin to oscillate. The threshold condition emerges as the condition for steady-state Stokes soliton power balance. This is readily derived from the Stokes soliton equation and takes the form,

$$\int_0^{2\pi} \partial_t |E_s|^2 d\phi = \int_0^{2\pi} d\phi (\kappa_s - 2R|E_p|^2) |E_s|^2 = 0. \quad (5.12)$$

By substituting the solutions for the primary and Stokes solitons into Eq. (5.12), the resulting threshold in primary soliton peak output power is found to be given by

$$P_{\text{th}} = \frac{\kappa_p^{ext} \kappa_s}{2R} \left(1 + \frac{1}{2\gamma}\right), \quad (5.13)$$

where P_{th} is the threshold peak output power of the primary soliton, above which the Stokes soliton starts to grow.

A continuous background field exists as part of the primary soliton (DKS) solution. In principle, this constant background could induce laser oscillation through the Raman process. However, the threshold power for this to occur can be shown to be close to the peak power required for Stokes soliton oscillation. Moreover, the background field has a power level that is many orders weaker than the peak power of the primary soliton [66]. This results because the pump laser is far red detuned from the microresonator resonance. As a result of these considerations, the observed Stokes oscillation results from pumping by the primary soliton and, specifically, spatio-temporal overlap of the Stokes soliton with the primary (pump) soliton. The good agreement between measurement with the theoretical threshold shown later provides additional confirmation.

Simulation of Stokes soliton formation

To reveal further details on the Stokes soliton formation, a pumping laser scan is performed numerically as shown in Fig. 5.2(a) (and zoom-in of scan in Fig. 5.2(b)). 128 modes are involved in the simulation. The formation of a step in the primary comb power (blue) indicates primary soliton formation [66, 67]. However, a decrease in power of the primary soliton is next observed that occurs with an increase in power of the Stokes soliton (red). The same features are also observed experimentally (see Fig. 5.2(c)). By studying the intracavity field evolution, the simulation shows the correspondence between these features and the soliton formation (see Fig. 5.2(d)). Also, the simulation shows that the primary and Stokes pulses overlap in space

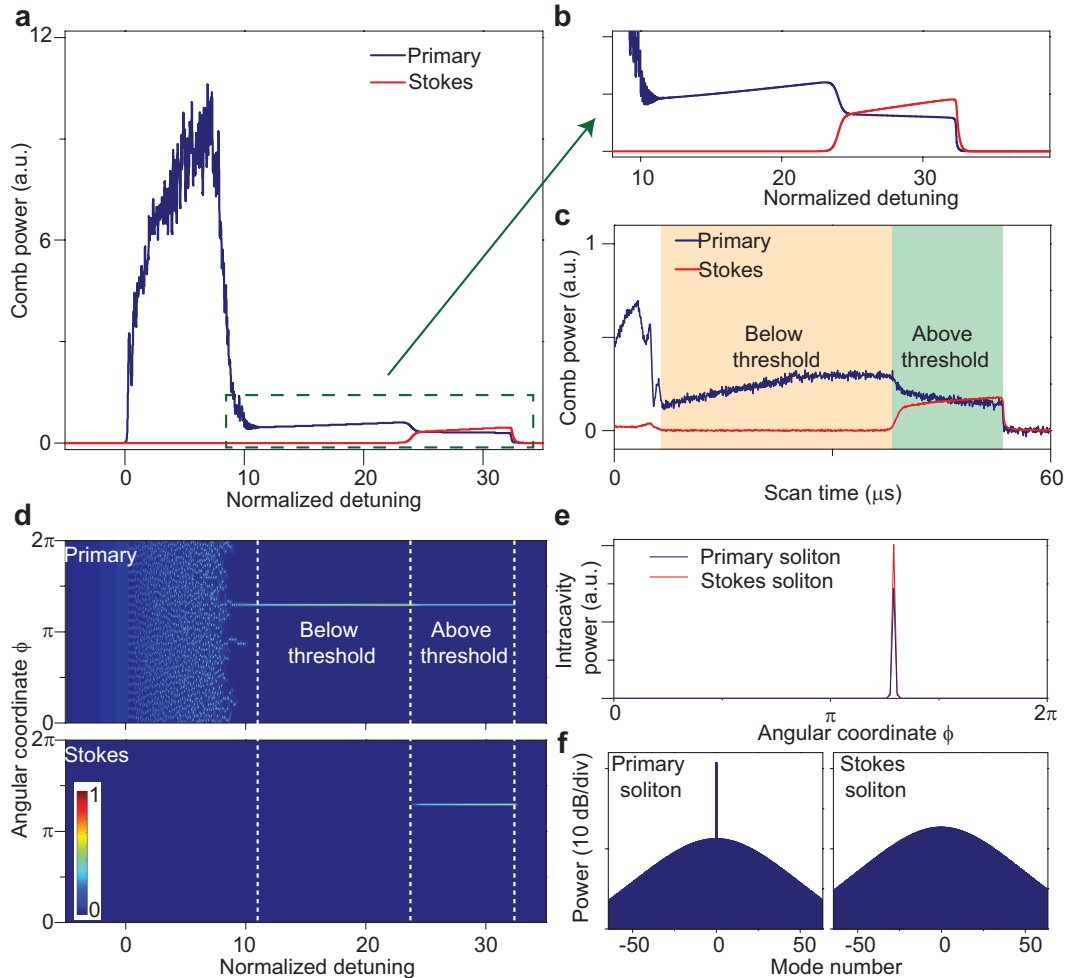


Figure 5.2: Stokes soliton formation in a microresonator. (a) Simulated intracavity comb power during a laser scan over the primary soliton pumping resonance from the blue (left) to the red (right) of the resonance. The detuning is normalized to the resonance linewidth. The initial step corresponds to the primary soliton formation, and the subsequent decrease in power corresponds to the onset of the Stokes soliton. The Stokes soliton power is shown in red. (b) Zoomed-in view of the indicated region from panel a. (c) Experimentally measured primary and Stokes soliton power during a laser scan showing the features simulated in panels a and b. (d) Simulation of the intracavity field in the moving frame of the solitons plotted versus the pump laser detuning. The detuning axis is scaled identically to Figure panel a. The Figure shows the primary soliton step region (below threshold) as well as the onset of the Stokes soliton (above threshold). (e) Temporal overlap of the primary and Stokes solitons is numerically confirmed in the plot of normalized power versus location angle within the resonator. The overlap confirms trapping and co-propagation. (f) Intracavity optical spectra of the primary and Stokes solitons.

and time, i.e., confirmation of optical trapping (see Figure 5.2(e)). The calculated spectra for the primary and Stokes solitons are provided in Figure 5.2(f).

5.3 Observation of Stokes solitons

The experimental setup is shown in Figure 5.3(a). The microresonators are about 3 mm in diameter, fabricated from silica on silicon, and have an unloaded optical Q factor of 300 million [55]. The requirements for DKS generation include a mode family that features anomalous dispersion. Other requirements as well as control and generation of DKS properties are described elsewhere [66, 67, 156]. The microresonator (shown as a ring) is pumped with a tunable, continuous-wave (CW) fiber laser amplified by an erbium-doped fiber amplifier (EDFA). An acousto-optic modulator (AOM) is used to control the pump power. The output soliton power is detected with a photo diode (PD) and monitored on an oscilloscope (OSCI). Wavelength division multiplexers (not shown) split the 1550 nm band primary soliton and 1600 nm band Stokes soliton so that their powers can be monitored separately on the oscilloscope. An optical spectrum analyzer (OSA), auto-correlator (A-CORR) and electrical spectrum analyzer (ESA) also monitor the output. In certain measurements (A-CORR and ESA), a fiber Bragg filter was used to remove the pump field from the soliton spectrum.

Measurement of the FSR versus wavelength of four spatial mode families in a single resonator is presented in Figure 5.3(b). The measurement is performed by scanning a tunable external cavity diode laser (ECDL) through the spectral locations of optical resonances from 1520 nm to 1580 nm. The resonances appear as minimal in the optical power transmitted past the microresonator, and the location of these resonances is calibrated using a fiber-based Mach-Zehnder interferometer. The resulting data provide the dispersion in the FSR of cavity modes versus the wavelength and readily enable the identification transverse mode families. Other details on this method are described elsewhere[67]. The green data plotted in Figure 5.3(b) correspond to the primary soliton forming mode family and the FSR of the pumping mode for that soliton is indicated by the horizontal dashed line. The measured spectrum for the primary soliton is shown in Figure 5.3(b). In the spectrum the pump spectral line (near 1550 nm) is indicated as well as the Sech^2 envelope for the soliton (green curve) [66–68]. Returning to Figure 5.3(b), the dispersion for another spatial mode family (red data) is extrapolated to longer wavelengths and crosses the dashed line near 1593 nm. At this wavelength the FSR of the red mode family closely matches that of the primary soliton. Moreover, this wavelength

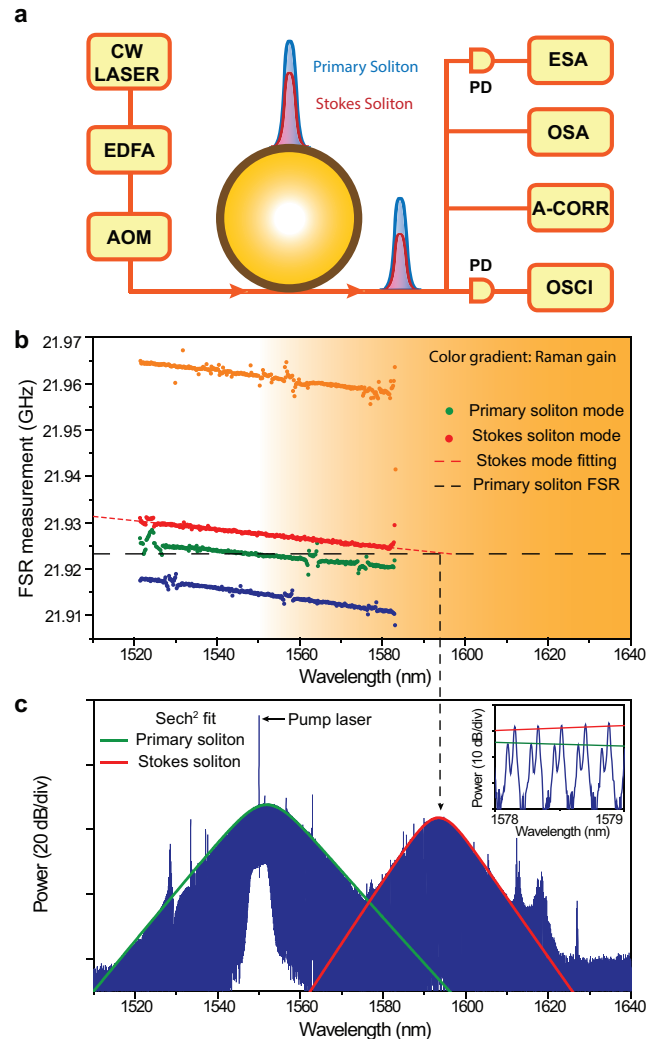


Figure 5.3: Experimental setup and observation of Stokes soliton. (a) Experimental setup. (b) Free spectral range (FSR) versus wavelength measured for four mode families in a 3mm disk resonator. The mode families for the primary and Stokes soliton are shown in green and red, respectively. The FSR at the spectral center of the primary soliton is shown as a dashed horizontal line. Extrapolation of the Stokes soliton data (red) to longer wavelengths gives the FSR matching wavelength where the Stokes soliton forms. The background coloration gives the approximate wavelength range of the Raman gain spectrum. (c) Measured primary and Stokes soliton spectra. The Stokes soliton spectral center closely matches the prediction in (c). Sech^2 envelopes are shown on each spectrum. The primary soliton spectrum features a small Raman self-frequency shift.

also lies within the Raman gain spectrum produced by the primary soliton (the amber region in Figure 5.3(b) gives the Raman gain band). As a result, conditions 1 and 2 above are satisfied at this wavelength for generation of a Stokes soliton.

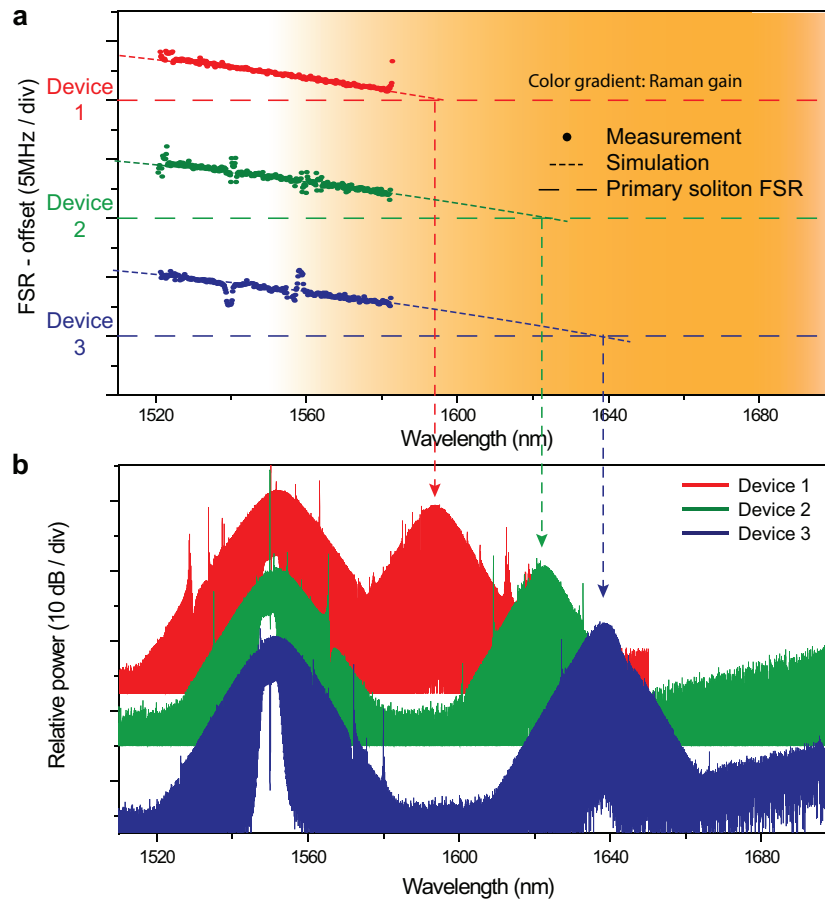


Figure 5.4: Observation of Stokes solitons in multiple devices. (a) Dispersion spectra (see Figure 5.3(c)) for the Stokes soliton forming mode family measured in three devices (the upper spectrum is the device from Figure 5.3). Other mode families have been omitted in the plots for clarity. The horizontal dashed lines give the repetition frequency of the primary soliton in each device. Extrapolation of the dispersion data attained by simulation is provided to graphically locate the predicted Stokes soliton wavelength. (b) The measured primary and Stokes soliton spectra corresponding to the devices in (a). The spectral locations of the Stokes solitons agree well with the graphical predictions.

The corresponding measured Stokes soliton is shown in Figure 5.3(c). Its spectral maximum occurs at a wavelength that agrees well with the prediction based on the FSR measurement in Figure 5.3(b). As an aside, the individual spectral lines of the primary and the Stokes solitons are spaced by approximately 22 GHz and resolved comb teeth in the overlapping spectral region between the solitons are provided in the inset to Figure 5.3(c).

These results were readily reproduced in other devices. Indeed, the FSR matching wavelength (i.e., condition 2) could be controlled by adjusting the geometry of

the resonator. Figure 5.4(a) shows the FSR dispersion measurements and Figure 5.4(b) shows the corresponding primary and Stokes soliton spectra that are measured using two other devices (green and blue spectra). For clarity, only the Stokes-soliton-forming mode family is presented in Figure 5.4(a) (including the data from Figure 5.4(c), red spectra, for comparison). The FSR of the primary soliton is indicated by the horizontal dashed lines in Figure 5.4(a). The FSR matching wavelengths are indicated by extrapolation of the dispersion data using simulation[138] and agree well with the location of the measured Stokes soliton spectral maximum in Figure 5.4(b).

5.4 Characterization of Stokes solitons

To confirm the temporal pulse nature of the Stokes soliton the frequency resolved optical gate (FROG) method was used to record the correlation traces in Figure 5.5(a). Optical filtering was applied to isolate the primary and Stokes soliton pulse streams. Also, before FROG measurement, the primary soliton stream was amplified by an erbium doped fiber amplifier (EDFA) and the Stokes soliton was amplified using a semiconductor optical amplifier (SOA). The data confirm that both streams consist of pulses. As an aside, the signal-to-noise level for the Stokes soliton measurement was limited by the saturation power of the SOA.

Photodetection of the isolated primary and Stokes soliton pulse streams was also possible. The measured electrical spectrum for each pulse stream is overlaid in Figure 5.5(b). The spectra are observed to align in frequency. As further confirmation of this frequency alignment, the optical pulse streams were simultaneously detected (no filtering to isolate the streams) and the measured electrical spectrum featured a single spectral peak at a resolution of 500 Hz. These results are expected on account of optical trapping of the Stokes soliton by the primary soliton which causes the line spacing (repetition rate) of the Stokes soliton and the primary soliton to match.

At the same time, the absolute optical frequency of the two solitons is not expected to be locked since the optical potential well depends upon the intensity of the primary soliton. To test this, the relative optical frequency stability of the two soliton streams was measured by using a resonator that featured spectrally overlapping primary and Stokes solitons such as in Figure 5.3(c). A high resolution optical scan from 1578-1579 nm of this overlap region is presented as the inset in Figure 5.3(c) and confirms that the underlying soliton lines are distinct. The beatnote between neighboring spectral lines of the primary and Stokes solitons shows large frequency

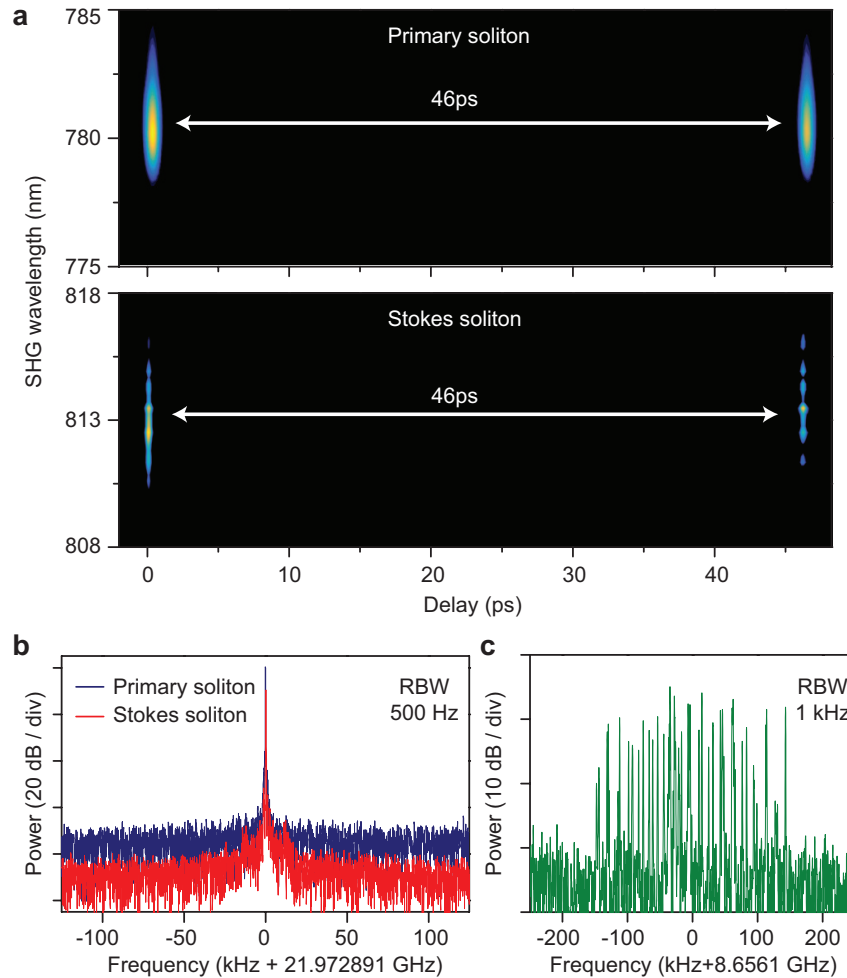


Figure 5.5: Soliton pulse and frequency measurements. (a) Frequency-resolved-optical-gating (FROG) traces of the primary and Stokes solitons. The primary soliton is amplified to 500 mW by an EDFA before coupling into the FROG setup, while the Stokes soliton is amplified to 10 mW by two cascaded semiconductor optical amplifiers with gain centered around 1620 nm. The period of the primary and Stokes solitons are 46 ps, the cavity round trip time. (b) Electrical spectra of the detected primary soliton pulse stream (blue) and the Stokes pulse stream (red). (c) Beatnote between neighboring comb teeth of the primary and Stokes solitons for a device like that in Figure 5.3. The beatnote is much noisier than the repetition frequency in (b).

variations (see Figure 5.5(c)) in comparison to the repetition frequency of each soliton (Figure 5.5(b)). Synchronization of the soliton repetition rates but not of the absolute optical frequencies is thus inferred from these measurements.

5.5 Threshold behavior

The thresholding nature of Stokes soliton formation is experimentally studied in Figure 5.6. The spectra in Figure 5.6(a) show the primary soliton and the corresponding Stokes soliton spectra for pumping levels below and above threshold. The transverse spatial mode profiles on which these solitons are formed are also provided and have been inferred by numerical fitting to the dispersion data. In Figure 5.6(b) power data are provided showing the primary soliton peak power and the Stokes soliton power plotted versus the total soliton power. To measure this data,

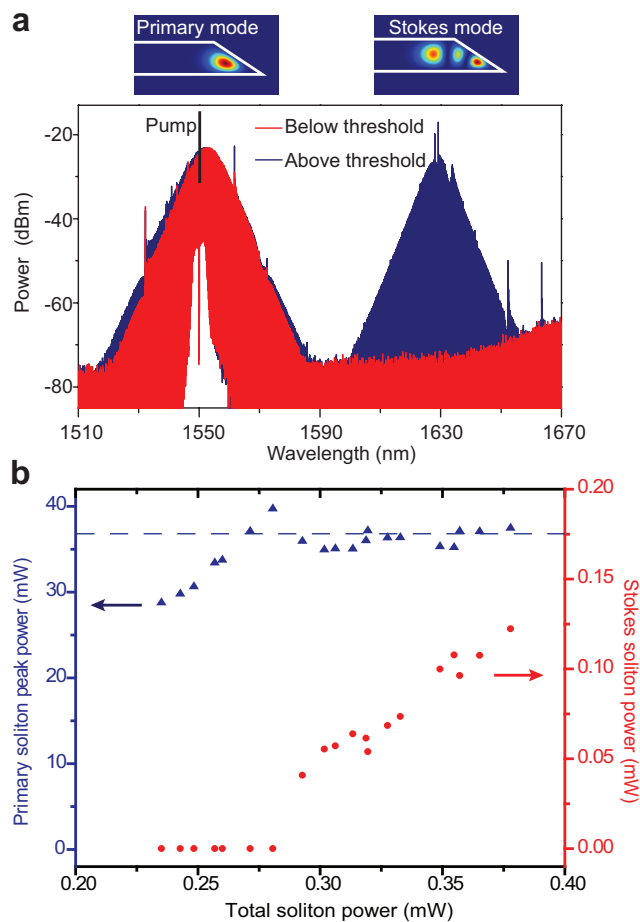


Figure 5.6: Stokes soliton spectra, power and threshold measurements. (a) Soliton spectra are plotted below and above threshold. The upper insets show the spatial mode families associated with the primary and Stokes solitons. (b) Measurement of Stokes soliton power and primary soliton peak power versus total soliton power. The primary soliton peak power (blue) versus total power experiences threshold clamping at the onset of Stokes soliton oscillation. The theoretical threshold peak power from Eq. (5.13) is also shown for comparison as the horizontal blue dashed line.

the power in the primary soliton was varied using the locking method described elsewhere[156]. Also, the transmitted pump spectral line was filtered out using a fiber Bragg filter. Power was measured by summing the power of the respective comb teeth for the primary and Stokes soliton as measured on the optical spectrum analyzer. Consistent with the thresholding nature of the process, the Stokes soliton power could be increased beyond the primary soliton power (see Figure 5.2). The threshold peak power predicted by Eq. (5.13) is plotted as the horizontal dashed line in Figure 5.6(b) for comparison to measurements. The measured values used in this calculation are, $\kappa_p/2\pi = 838$ kHz, $\kappa_p^{ext}/2\pi = 222$ kHz, $\lambda_p = 1550$ nm, $D_{1p}/2\pi = 22$ GHz, and $D_{2p}/2\pi = 16.1$ kHz. For the Stokes soliton mode family $\kappa_s/2\pi = 3.3$ MHz is measured near 1550 nm and is used for the Stokes soliton loss rate in the 1600 nm band. Calculated parameters (based on mode simulations) are, $D_{2s}/2\pi = 21.7$ kHz, $A_{ss} = 69.8 \mu\text{m}^2$, $A_{pp} = 39.7 \mu\text{m}^2$, $A_{ps} = 120 \mu\text{m}^2$, and $\delta = 0$ when $\lambda_s = 1627$ nm. Other constants are: $n = 1.45$, $n_2 = 2.2 \times 10^{-20} \text{ m}^2/\text{W}$, $g_R = 3.94 \times 10^{-14} \text{ m/W}$, $\tau_R = 3.2$ fs. $\gamma = 0.55$ is calculated and used in Figure 5.6.

5.6 Conclusion

The Stokes soliton is only the second type of soliton to be observed in microresonators (beyond dissipative Kerr solitons [66]) and also represents the first time soliton trapping has been observed in any microresonator. It also represents the first observation of trapping by solitons in different transverse modes in a laser. From a practical viewpoint, the Stokes and primary solitons overlap in space and time, and have a frequency separation that can be engineered to fall within the mid IR range. As a result, this soliton system is potentially interesting for mid IR generation by way of difference frequency generation. Not all devices are observed to produce Stokes solitons. However, dispersion engineering techniques are being advanced [138] and should enable control of both observation of the Stokes soliton as well as its placement in the optical spectrum. Indeed, the spectral placement of Stokes solitons in Figure 5.4(b) is largely the result of microresonator diameter control to shift the FSR crossing point. Also, engineering of dispersion could permit a Stokes soliton to form within the same mode family as the primary soliton. The specific implementation described here uses a compact microresonator on a silicon wafer which also suggests that monolithic integration will be possible. In an appropriately phase-matched multimode waveguide (optical fiber or monolithic) it should also be possible to observe non-cavity-based Stokes solitons.

*Chapter 6***SPATIAL-MODE-INTERACTION-INDUCED
DISPERSIVE-WAVES AND THEIR ACTIVE TUNING IN
MICRORESONATORS**

¹The nonlinear propagation of optical pulses in dielectric waveguides and resonators induces a wide range of remarkable interactions. One example is dispersive wave generation, the optical analog of Cherenkov radiation. These waves play an essential role in fiber-optic spectral broadeners used in spectroscopy and metrology. Dispersive waves form when a soliton pulse begins to radiate power as a result of higher-order dispersion. Recently, dispersive wave generation in microresonators has been reported by phase matching the waves to dissipative Kerr solitons. In this chapter we show that spatial mode interactions within a microresonator can be used to induce dispersive waves. The soliton self frequency shift is also shown to enable fine tuning control of the dispersive wave frequency. Both this mechanism and spatial mode interactions allow spectral control of these important waves in microresonators.

6.1 Observation of spatial-mode-interaction induced dispersive waves

If the spectrum of a soliton pulse extends into regions where second-order dispersion changes sign, then radiation into a new pulse, the dispersive wave, may occur at a phase matching wavelength [186, 187]. The generation of these waves is analogous to Cherenkov radiation [188] and extends the spectral reach of optical pulses [20]. The recent ability to control dispersion in microresonators has allowed accurate spectral placement of dispersive waves relative to a radiating cavity soliton [68]. Such dispersion-engineered control has made possible 2f-3f self referencing of frequency microcombs [189] and octave-spanning double-dispersive waves [82]. Dispersive wave generation in optical fibers has traditionally relied upon control of geometrical dispersion in conjunction with the intrinsic material dispersion of the dielectric [20] and this same method has been successfully demonstrated in microresonators [68]. Recently, spatial-mode-interactions in multimode-fiber have also been used for this purpose [190–192].

Here, spatial mode interactions within a microresonator are used to phase match

¹Work presented in this chapter has been published in “Spatial-mode-interaction-induced dispersive waves and their active tuning in microresonators”, *Optica* 3(10):1132-1135 (2016).

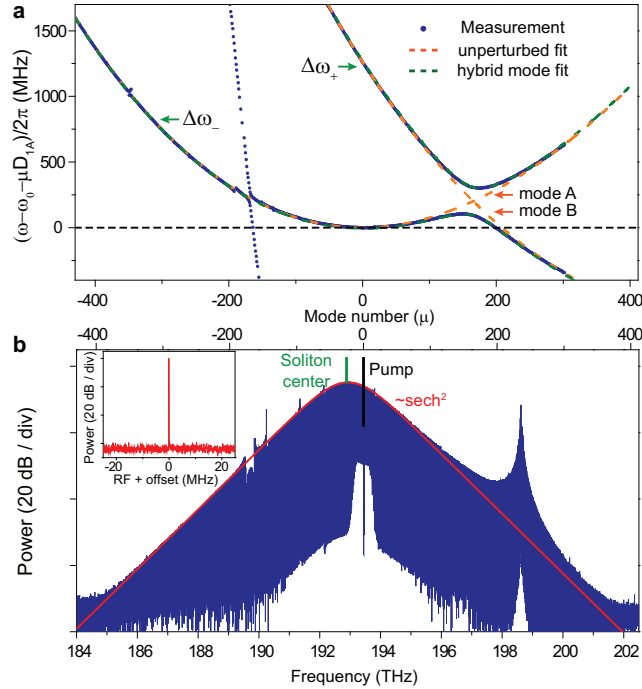


Figure 6.1: Dispersive wave generation by spatial mode interaction. (a) Measured relative-mode-frequencies (blue points) of the soliton-forming mode family and the interaction mode family. Mode number $\mu = 0$ corresponds to the pump laser frequency of 193.45 THz (1549.7 nm). Hybrid mode frequencies calculated from Eq. (6.1) are shown in green and the unperturbed mode families are shown in orange. The dashed, horizontal black line determines phase matching for $\omega_r = D_{1A}$. (b) Measured soliton optical spectrum with dispersive wave feature is shown. For comparison, a Sech^2 fitting is provided in red. The pump frequency (black) and soliton center frequency (green) indicate a Raman-induced soliton self-frequency shift (also see Figure 6.2(c)). A microwave beatnote of the photo-detected soliton and dispersive wave is shown in the inset (frequency scale is offset by 21.973 GHz; resolution bandwidth is 10 kHz).

a soliton pulse to a dispersive wave. These mode interactions often frustrate the formation of solitons [153] and, as a result, microresonators are typically designed to minimize or exclude entirely the resulting modal avoided crossings [66–68, 76, 77]. Also, while dispersive-wave phase matching is normally induced by more gradual variations in dispersion, spatial mode interactions produce spectrally abrupt variations that can activate a dispersive wave in the vicinity of a narrow-band soliton. Below, the observation of dispersive wave generation by this process is presented after characterizing two strongly interacting spatial mode families.

Device characterization

In the experiment, an ultra-high-Q silica micro-resonator (3 mm diameter) with a 22 GHz free-spectral-range (FSR) was prepared [55]. Typical intrinsic quality factors were in excess of 200 million (cavity linewidths were less than 1 MHz). Mode dispersion was characterized from 183.92 THz (1630 nm) to 199.86 THz (1500 nm) by fiber-taper coupling to a tunable external-cavity diode laser and calibrating the laser frequency scan using a Mach-Zehnder interferometer [67]. Multiple mode families were observed and their measured frequency dispersion spectra are presented as the blue points in Figure 6.1(a). In the plot, a linear dispersion term corresponding to the FSR of the soliton-forming mode family ($\Delta\omega_-$) at mode number zero is subtracted so that a *relative-mode-frequency* is plotted. Mode zero is by convention the mode that is optically pumped to form the soliton. Three weak perturbations of the soliton mode family dispersion are observed for $\mu < 0$. The mode family associated with one of the perturbations is plotted as the nearly vertical line of blue points. A much stronger interaction occurs near $\mu = 165$, causing a strong avoided mode crossing that redirects the soliton-forming branch to lower relative mode frequencies.

Modal hybridization

The dispersion can be accurately modeled using a coupled mode approach. Accordingly, consider two mode families (A and B) that initially do not interact and that feature frequency dispersion spectra $\omega_{A,B}(\mu)$. An interaction between the mode families is introduced that is characterized by a coupling rate G . The coupling produces two hybrid mode families with upper/lower-branch mode frequencies $\omega_{\pm}(\mu)$ given by the following expression [144, 193, 194],

$$\omega_{\pm}(\mu) = \frac{\omega_A(\mu) + \omega_B(\mu)}{2} \pm \sqrt{G^2 + [\omega_A(\mu) - \omega_B(\mu)]^2/4}. \quad (6.1)$$

Note that in the limit of $|\omega_A(\mu) - \omega_B(\mu)| \gg G$, the frequencies ω_{\pm} approach the frequencies, $\omega_{A,B}(\mu)$, of the non-interacting mode families. The form of $\omega_{A,B}(\mu)$ are determined using this fact by fitting them within the regions $\mu < 50$ and $\mu > 280$ of the measured dispersion spectra to the following equation: $\omega_{A,B}(\mu) = \omega_{A,B}(0) + D_{1A,B}\mu + D_{2A,B}\mu^2/2 + D_{3A,B}\mu^3/6$, which is a third-order Taylor expansion of each mode family about mode number $\mu = 0$. The corresponding fits are shown as the dashed orange curves in Figure 6.1(a). For mode family A : $D_{1A}/2\pi = 21.9733$ GHz, $D_{2A}/2\pi = 15.2$ kHz, $D_{3A}/2\pi = -14.7$ Hz; and for mode family B : $D_{1B}/2\pi = 21.9654$ GHz, $D_{2B}/2\pi = 18.6$ kHz, $D_{3B}/2\pi = -17.2$ Hz and $\omega_B(0) - \omega_A(0) =$

1.261 GHz. The coupling coefficient, G , is determined by the minimum frequency difference of two branches and gives $G/2\pi=106.5$ MHz. Using these parameters in Eq. (6.1), relative-mode-frequencies for the hybrid mode families ($\Delta\omega_{\pm}(\mu) \equiv \omega_{\pm}(\mu) - \omega_0 - \mu D_{1A}$, where $\omega_0 \equiv \omega_A(0)$) are plotted in Figure 6.1(a) (green) and show good agreement with the measurements (blue points). An improved fitting is possible using a least squares approach in Eq. (6.1). As an aside, the mode two families ($\Delta\omega_{\pm}$) were observed to couple nearly equally to the tapered fiber with approximately 20% transmission.

Observation of dispersive waves

The optical spectrum of a dissipative Kerr soliton (DKS) pumped at $\mu = 0$ (193.45 THz or 1549.7 nm) using a fiber laser is presented in Figure 6.1(b). The soliton is triggered and stabilized using the method described in [67, 156]. For comparison, the ideal Sech^2 spectral profile that would occur under conditions of pure second-order dispersion [66–68] (mode A dashed orange curve in Figure 6.1(a)) is provided as the red envelope in Figure 6.1(b). A small soliton self-frequency shift (SSFS) [67, 68, 87, 88, 166] is apparent in the measured soliton spectrum as indicated by the spectral displacement of the soliton spectral center relative to the pumping frequency. The perturbations to the ideal spectral envelope that are caused by both the weak modal crossings ($\mu < 0$) as well as the strong avoided modal crossing are apparent. For $\mu > 0$ a dispersive wave feature is apparent (maximum near 198.62 THz or $\mu = 235$). In contrast to the weak avoided crossing induced distortion for $\mu < 0$, the dispersive wave results from a resonance condition (see discussion below) and the comb teeth are accordingly enhanced in strength. The coherence of the soliton and dispersive wave is verified by measuring the electrical spectrum of the detected soliton and dispersive-wave pulse train using a photodetector (inset of Figure 6.1(b)).

6.2 Active tuning of dispersive waves

In this section the phase matching of the dispersive wave to the soliton is studied including for the first time the effect of soliton frequency offset relative to the pump as is caused by soliton recoil or by the Raman-induced soliton self-frequency shift [67, 68, 87, 88, 166]. It is shown that this mechanism enables active tuning control of the dispersive wave by pump tuning.

Phase matching condition

Phase matching between the soliton and the dispersive wave occurs when the μ^{th} soliton line at $\omega_p + \omega_r \mu$ (ω_p is the pump frequency and ω_r is the soliton repetition frequency) is resonant with the μ^{th} frequency of the soliton-forming mode family, i.e., $\omega_p + \omega_r \mu = \omega_-(\mu)$. As an aside, the Kerr shift for mode μ is much smaller than other terms in this analysis and is neglected in the phase matching condition. So that it is possible to use a graphical interpretation of the phase matching condition based on the relative-mode-frequency of Figure 6.1(a), $\omega_0 + D_{1A}\mu$ is subtracted from both sides of the phase matching condition to give the following condition,

$$\Delta\omega_-(\mu) = (\omega_r - D_{1A})\mu - \delta\omega, \quad (6.2)$$

where $\delta\omega \equiv \omega_0 - \omega_p$ is the detuning of the resonator relative to the pump frequency.

If the soliton repetition frequency equals the FSR at $\mu = 0$ (i.e., $\omega_r = D_{1A}$), then the r.h.s. of Eq. (6.2) is the horizontal dashed black line in Figure 6.1(a) (repeated in Figure 6.2(a)). Under these circumstances the dispersive wave phase matches to the soliton pulse at the crossing of that line with the soliton-forming mode branch. However, while the mode dispersion profile ($\Delta\omega_-(\mu)$) is determined entirely by the resonator geometry and the dielectric material properties, the soliton repetition rate ω_r depends upon frequency offsets between the pump and the soliton spectral maximum. Defining this offset as Ω , the repetition frequency is given by the following equation [133, 195]:

$$\omega_r = D_{1A} + \frac{D_{2A}}{D_{1A}}\Omega. \quad (6.3)$$

The offset frequency Ω can be caused by soliton recoil due to a dispersive wave and also by the Raman-induced soliton self-frequency shift (SSFS) [67, 68, 87, 88, 166]. Combining Eqs. (6.2) and (6.3) gives the following phase matching condition:

$$\Delta\omega_-(\mu) = \mu \frac{D_{2A}}{D_{1A}}\Omega - \delta\omega. \quad (6.4)$$

Tuning of dispersive waves

In this work, Ω is dominated by the Raman interaction, because the typical dispersive wave power is $< 0.2\%$ of the soliton power, causing a negligible dispersive wave recoil (recoil of less than one mode). Photo-thermal-induced change in D_{1A} is another possible contribution that will vary ω_r as pumping is varied [196]. However, the thermal tuning of D_{1A} is estimated to be ~ -4.5 kHz/mW (by measurement

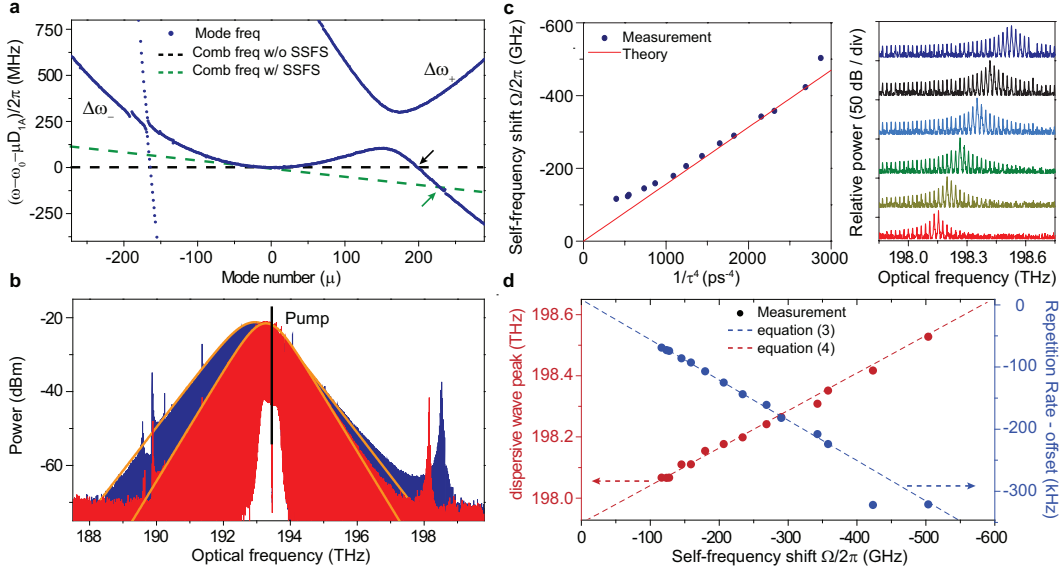


Figure 6.2: Dispersive wave phase matching condition and Raman-induced frequency shift. (a) Soliton and interaction mode family dispersion curves are shown (see Figure 6.1(a)) with phase matching dashed lines (see Eq. (6.4)). The black line is the case where $\omega_r = D_{1A}$ and the green line includes a Raman-induced change in ω_r . The intersection of the soliton branch with these lines is the dispersive wave phase matching point (arrows). (b) Soliton optical spectra corresponding to small (red) and large (blue) cavity-laser detuning ($\delta\omega$). Sech^2 fitting of the spectral envelope is shown as the orange curves. (c) Left: soliton self-frequency-shift, Ω , versus $1/\tau_s^4$ (τ_s is pulse width). The theoretical line is calculated with $Q = 166$ million (measured) and Raman shock time 2.7 fs. Right: dispersive wave spectra with cavity-laser detuning (soliton power and bandwidth) increasing from lower to upper trace. (d) Measured dispersive-wave peak frequencies (red points) and soliton repetition rate (blue points) are plotted versus soliton self-frequency shift. The dashed blue line is a plot of Eq. (6.3). The dashed red line uses Eq. (6.4) to determine the dispersive wave frequency ($\approx \mu_{DW}D_{1A} + \omega_0$) as described in the text. The offset for the repetition rate vertical scale is $D_{1A} = 21.9733$ GHz.

of resonant frequency photo-thermal shift of ~ -40 MHz/mW). With total soliton power less than 1 mW [67], this photo-thermal-induced change in repetition frequency is negligible compared with that caused by the Raman self-frequency-shift (see below).

The Raman-induced SSFS is a negative frequency shift ($\Omega < 0$) with a magnitude that increases with soliton bandwidth and average power. Accordingly, with increasing soliton power (and bandwidth), the plot of the R.H.S. of Eq. (6.4) versus μ acquires an increasingly negative slope (green dashed line in Figure 6.2(a)). The phase matching mode number, $\mu = \mu_{DW}$, therefore also increases (i.e., the disper-

sive wave shifts to a higher optical frequency) with increasing soliton power. The two soliton spectra presented in Figure 6.2(b) illustrate this effect (red spectrum is lower power and has the lower dispersive wave frequency). Figure 6.2(c) (right) also shows a series of higher-resolution scans of the dispersive wave with soliton power increasing from the lower to upper scans and is, again, consistent with the prediction.

The frequency shift, Ω , repetition frequency, ω_r , and the dispersive wave frequency were measured for a series of soliton powers that were set by controlling the cavity-pump detuning frequency ($\delta\omega$) using the method in ref. [67, 156]. ω_r was measured using an electrical spectrum analyzer after photodetection of the resonator optical output. The offset frequency Ω was measured on an optical spectrum analyzer by fitting the center of optical spectrum (see Figure 6.1(b)) to determine the spectral maximum and then measuring the wavelength offset relative to the pump. This same spectral fitting also allows determination of the soliton pulse width, τ_s [67]. Once the soliton pulsewidth is known, the pump-resonator frequency detuning operating point can be inferred using $\delta\omega \approx D_2/2D_1^2\tau_s^2$ [67]. $\delta\omega/2\pi$ ranged between 7.8 to 21.1 MHz during the measurement. As an aside, a plot of Ω vs. $1/\tau_s^4$ in Figure 6.2(c) (left) verifies that Ω is dominated by the Raman self frequency shift [88].

The soliton repetition rate is plotted versus Ω in Figure 6.2(d) and is fitted using Eq. (6.4). The intercept closely agrees with D_{1A} and the slope allows determination of $D_{2A}/2\pi = 14.7$ kHz (in good agreement with 15.2 kHz from fitting to the measured dispersion curve in Figure 6.1(a)). The dispersive wave frequency is also plotted in Figure 6.2(d) versus Ω and compared with a calculation using Eq. (6.4). In this calculation, $\Delta\omega_-(\mu)$ is approximated using a linear expansion in μ near $\mu = 200$. Also, a -60 kHz offset is added to $D_{1A}/2\pi$ in $\Delta\omega_-(\mu)$ due to the calibration uncertainty ($\sim \pm 100$ kHz) of FSR [140]. No other free parameters are used in the plot.

6.3 Conclusion

Spatial mode interactions provide a way to phase match a DKS to a dispersive wave. Interacting mode families must be closely matched in free-spectral-range (i.e., $D_{1A} \approx D_{1B}$) so that the soliton comb teeth which initially form on mode family A can transition to mode family B (see Figure 6.1(a)). As a second condition, the coupling strength G (see Eq. (6.1)) must be large enough to create hybrid modes near the modal avoided crossing that are strong admixtures of the A and B modes.

For example, this mixing allows the comb of lines to grow along the lower branch (beyond $\mu = 165$ in Figure 6.1(a)) after initiating near $\mu = 0$. The degree to which these interactions can be engineered and controlled is an active area of investigation. Geometrical control of dispersion over broad spectral spans using microfabrication methods [138] could be applicable for dispersive wave control.

It has been shown theoretically and through measurement that the dispersive wave frequency can be actively tuned because of coupling to the soliton offset frequency Ω . In the silica microresonators tested here, this offset is dominated by the Raman-induced SSFS and the dispersive wave is predicted and observed to tune to higher frequencies with increasing soliton power and bandwidth. As a further test of the theory, the dependence of repetition frequency on SSFS was combined with measurement to extract resonator dispersion parameters, which compared well with direct measurements based on resonator dispersion characterization. The dispersion induced by modal interactions in the tested device has been measured and accurately modeled using a coupled-mode formalism. While the soliton existence limitations imposed upon placement of dispersive wave are under investigation, it seems possible that more complex resonator designs could not only engineer the placement of these crossings, but also locate multiple avoided crossings near a soliton so as to induce multiplets of dispersive waves.

Chapter 7

SINGLE-MODE DISPERSIVE WAVES AND SOLITON MICROCOMB DYNAMICS

¹Dissipative Kerr solitons can radiate power as a dispersive wave through a process that is the optical analogue of Cherenkov radiation. Dispersive waves typically consist of an ensemble of optical modes. In this chapter, a limiting case is studied in which the dispersive wave is concentrated into a single cavity mode assisted by avoided mode crossings. The coupling of this single-mode dispersive wave to the soliton is strongly influenced by the total soliton frequency shift produced by the combined Raman-induced soliton-self-frequency-shift (SSFS) [87, 88] and the dispersive-wave recoil. The combination is shown to induce hysteresis behavior in soliton properties. Included in this behavior is an operating point of improved pulse-rate stability (a quiet point) where the coupling of repetition rate and cavity-pump detuning is greatly reduced. Pulse-rate stability is centrally important in many frequency comb applications [71, 105, 197]. Coupling of pulse rate and cavity-pump detuning through avoided-mode-crossing recoil effects has been observed in crystalline resonators [92]. Also, the fundamental contributions to phase noise in the pulse train have been considered theoretically [133]. However, technical noise mechanisms are also present. For example, DKS generation using on-chip silica resonators exhibits phase noise that tracks in spectral profile the phase noise of the optical pump [67]. The quiet operation point is shown to reduce technical noise contributions to the soliton pulse repetition rate, which could be found useful in many applications. Both this regime of operation and the hysteresis behavior are measured and modeled theoretically.

7.1 Observation of single mode dispersive waves

Avoided mode crossings and dispersive waves

A silica whispering-gallery resonator [55] is used for soliton generation. The devices feature a free-spectral-range (FSR) of approximately 22 GHz (3 mm diameter resonator) and have intrinsic Q-factors around 250 million. Specific details on soliton formation in these resonators are given elsewhere [67, 156]. The resonators

¹Work presented in this chapter has been published in “Single-mode dispersive waves and soliton microcomb dynamics”, *Nat. Commun.* 8:14869 (2017).

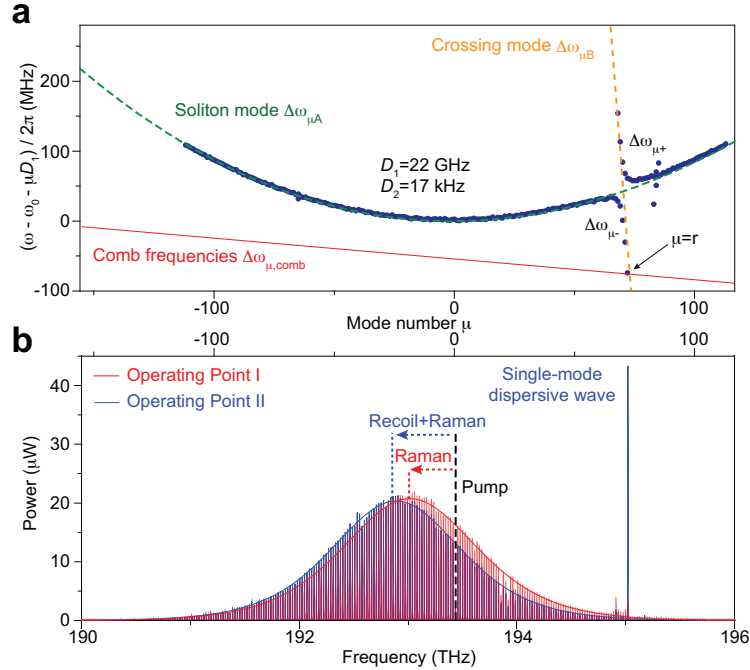


Figure 7.1: observation of single mode dispersive wave. (a) Measured relative mode frequencies are shown as blue points. The green and yellow dashed lines represent the fitted relative mode frequencies ($\Delta\omega_{\mu A}$ and $\Delta\omega_{\mu B}$) of the unperturbed soliton-forming mode family A and crossing mode family B, respectively. Relative mode frequencies for upper and lower branch hybrid-modes are $\Delta\omega_{\mu+}$ and $\Delta\omega_{\mu-}$. The red line illustrates the frequencies of a hypothetical soliton frequency comb. A non-zero slope on this line arises from the repetition rate change relative to the FSR at mode $\mu = 0$. (b) Measured optical spectra at soliton operating points I and II, corresponding to closely matched cavity-pump detuning frequencies, $\delta\omega$. A strong single-mode dispersive wave at $\mu = 72$ is observed for operating point II and causes a soliton recoil frequency shift. This frequency shift adds to the shift resulting from the Raman-induced SSFS.

support multiple, transverse mode families. It is essential that the soliton-forming mode family feature dispersion that is primarily second-order and anomalous [153]. To characterize the frequency spectrum of the resonator, mode frequencies were measured from 190.95 THz (1570 nm) to 195.94 THz (1530 nm) using an external-cavity diode laser (ECDL) calibrated by a fiber Mach-Zehnder interferometer (MZI) [67]. This provides a set of mode frequencies $\{\omega_{\mu,s}\}$ for each spatial mode family s with μ as the mode index.

The mode family frequency data are presented in Figure 7.1(a) by plotting the relative-mode-frequency, $\Delta\omega_{\mu,s} \equiv \omega_{\mu,s} - \omega_0 - \mu D_1$ versus mode index μ where ω_0 and D_1 are specific to the soliton-forming mode family. ω_0 is the frequency of the

mode (set to have index $\mu = 0$) that is optically pumped to produce the soliton, and D_1 is the FSR of the soliton-forming mode family at $\mu = 0$ (note: μ is a relative and not an absolute mode index). By plotting the data in this way the second- and higher-order dispersion of the soliton-forming mode family become manifest. To illustrate, the relative-mode-frequency of the soliton mode family is fit with a green, dashed parabolic curve of positive curvature in Figure 7.1(a) showing that it features anomalous second-order dispersion over a wide range of mode numbers.

A second mode family also appears in Figure 7.1(a) and causes an avoided-mode-crossing near $\mu = 72$. Hybridization of this “crossing-mode” mode family with the soliton mode family occurs near the avoided crossing[90, 144]. The relative-mode-frequencies of the unperturbed soliton-forming mode family and crossing-mode family are denoted as $\Delta\omega_{\mu A}$ and $\Delta\omega_{\mu B}$. Over the range of mode indices measured $\Delta\omega_{\mu A} = \frac{1}{2}D_2\mu^2$, where D_2 is the second-order dispersion at $\mu = 0$. The lower (upper) branch of the hybrid mode family is denoted by $\Delta\omega_{\mu-}$ ($\Delta\omega_{\mu+}$). Avoided mode crossing behavior has been intensively studied in the context of DKS formation and can interfere with soliton generation by creation of distortions in the dispersion spectrum [145, 153, 198]. In the present system the avoided-mode-crossing induces only minimal distortion in the otherwise parabolic shape of the soliton-forming mode family. Soliton spectra produced on this mode family by pumping at $\mu = 0$ are shown in Figure 7.1(b) along with theoretical sech^2 spectral envelopes predicted for DKSs. As an aside, the horizontal scales in Figure 7.1(a) and Figure 7.1(b) are identical and the location of the $\mu = 0$ pumping mode is indicated by a vertical dashed line in Figure 7.1(b).

Because the mode has a high optical Q-factor, slight shifts in the slope of the comb frequency line will cause large changes in the power coupled to the hybrid mode. These changes are observable in Figure 7.1(b) where a strong spectral line appears in the case of the blue soliton spectrum. Note that scattering from the soliton into the spectral line is strong enough so that the power in the line is greater than the comb tooth power near the spectral center of the soliton, itself. The strong spectral line can be understood as a single-mode dispersive wave and it induces a recoil in the spectral center of the soliton. This recoil contribution is indicated for the blue soliton spectrum in the figure. In the case of the red soliton spectrum, the operating point was changed and the resonance between the soliton and the mode is diminished. Accordingly, most of the spectral shift in this case results from the Raman SSFS.

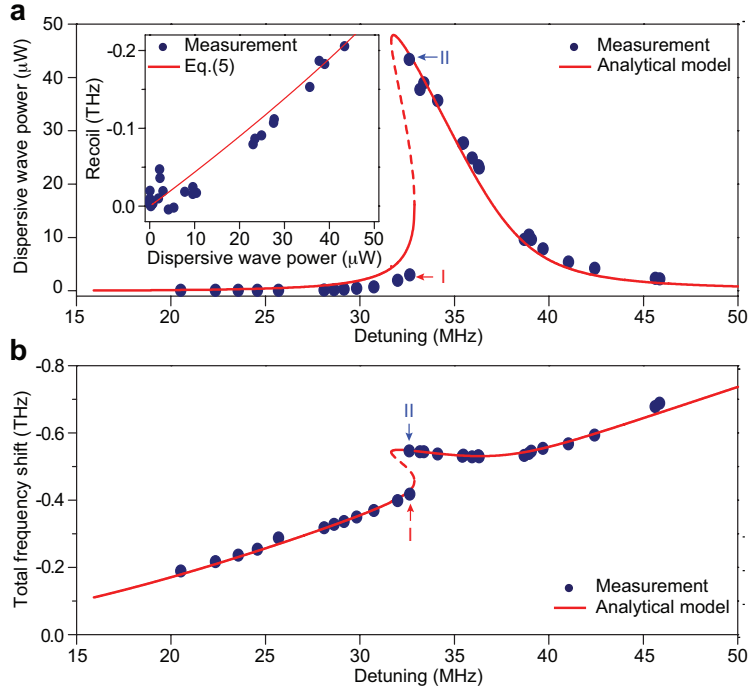


Figure 7.2: Soliton hysteretic behavior induced by mode interaction. (a-b) Dispersive-wave power and soliton spectral center frequency shift versus cavity-pump detuning. Inset in (a): Measured (blue dots) and theoretical (red line) recoil frequency versus the dispersive wave power.

7.2 Hysteretic behavior

It is noted that the two soliton spectra in Figure 7.1(b) (blue and red), which show very different dispersive wave powers, were produced at nearly identical detuning frequencies, $\delta\omega$. A more detailed survey of the dispersive wave power behavior is provided in Figure 7.2(a) and is again consistent with a hysteresis behavior versus detuning. Moreover, a corresponding behavior is observed in the overall soliton spectral shift (Figure 7.2(b)). Theoretical fits are provided in Figure 7.2(a) and Figure 7.2(b). The fitting procedure and parameter values are provided in the next section.

In plotting the data, the detuning frequency, $\delta\omega/2\pi$, was determined from the measured total soliton spectral shift (Ω) and pulse width (τ_s) using the relation $\delta\omega = (D_2/2D_1^2)(1/\tau_s^2 + \Omega^2)$. This expression is a generalization of a relationship derived elsewhere [88]. The generalization extends the shift Ω to include both the SSFS and the recoil and is derived as Eq. (7.31) in next section. As an aside, the pulse width is determined by fitting the soliton optical spectrum [67].

Likewise, the recoil frequency, Ω_{Recoil} , can also be extracted from the data as $\Omega - \Omega_{\text{Raman}}$ by first using the soliton pulse width to determine the Raman shift using $\Omega_{\text{Raman}} = -8\tau_{\text{R}}D_2/15\kappa_{\text{A}}D_1^2\tau_{\text{s}}^4$. A plot of the recoil shift determined this way versus the dispersive-wave power is given as the inset in Figure 7.2(a) and verifies the linear dependence (Eq. (7.22)). Equation (7.22) is also plotted for comparison using parameters given in next section. As an aside, the Raman shift formula noted above is also a generalization of a result proven elsewhere [88]. Curiously, as shown later, this formula maintains its previous form in the presence of the dispersive wave.

Within narrow detuning frequency bands in the vicinity of the hysteresis both measurements and calculations show that the total cavity power (soliton and dispersive-wave contributions) can decrease with increasing cavity-pump detuning as opposed to increasing with detuning as is typical for a soliton. Under these special conditions, the pump-cavity detuning will no longer be dynamically stable on account of the thermal nonlinearity [57]. Evidence of this was observable in the current work as it was not possible to completely map out the theoretically predicted hysteresis curves.

While the present results are produced using a dispersive wave that is blue-detuned relative to the soliton spectral maximum, the hysteresis behavior is also predicted to occur for a red-detuned dispersive wave. However, in the red-detuned case, the orientation of the curve in Figure 7.2(a) is reversed with respect to the detuning frequency. The essential feature for appearance of the hysteresis is that the recoil advances and retreats versus detuning. As a result, the existence of hysteresis behavior predicted in Eq. (7.24) is not limited to microresonator materials having a strong Raman SSFS. It is also predicted to occur, for example, in crystalline resonators given an appropriate avoided-mode crossing [92]. The requirements imposed on the device and mode crossing for this to occur are discussed further below.

7.3 Theory of single mode dispersive waves

Comb frequency and resonant frequency

The comb frequencies associated with a hypothetical soliton spectrum are plotted in the relative frequency frame, as shown in Figure 7.1(a). This comb tooth is given by

$$\Delta\omega_{\mu,\text{comb}} = \omega_{\mu,\text{comb}} - \omega_0 - D_1\mu = (\omega_{\text{rep}} - D_1)\mu - \delta\omega, \quad (7.1)$$

where $\omega_{\mu,\text{comb}} = \mu\omega_{\text{rep}} + \omega_{\text{p}}$ is the frequency of μ -th comb line, ω_{rep} is the soliton repetition frequency, ω_{p} is the pump frequency, ω_0 is the frequency of the cavity

mode that is being pumped, and $\delta\omega \equiv \omega_0 - \omega_p$ is the cavity-pump detuning frequency. It is necessary to distinguish between relative frequencies for the soliton comb and the resonator modes because the frequency components of the soliton comb are strongly red-detuned relative to the cold-cavity mode frequencies by the Kerr nonlinearity. Indeed, dispersive waves typically form when a set of modes break this rule and becomes resonant with a set of comb teeth. A limiting case of this condition is shown in Figure 7.2(a), where the occurrence of an isolated resonance between a hybrid mode with relative frequency $\Delta\omega_{r-}$ and a comb tooth at $\Delta\omega_{r,\text{comb}}$ is illustrated.

A change in the slope of the soliton comb tooth will occur when the soliton repetition frequency, ω_{rep} , is changed (see Eq. (7.1)). On account of second order dispersion ω_{rep} depends linearly on the frequency offset, Ω , of the soliton spectral maximum relative to the pump frequency [90, 133]. This frequency offset has contributions from both the Raman SSFS, Ω_{Raman} , and the dispersive-wave recoil, Ω_{Recoil} (i.e., $\Omega = \Omega_{\text{Raman}} + \Omega_{\text{Recoil}}$). Accordingly, the soliton repetition rate is given by

$$\omega_{\text{rep}} = D_1 + \frac{D_2}{D_1}(\Omega_{\text{Raman}} + \Omega_{\text{Recoil}}), \quad (7.2)$$

where D_2 (the second order dispersion of soliton-forming mode family at $\mu = 0$) is measured to be 17 kHz from Figure 7.2(a). Substituting for the repetition rate in the comb tooth expression (Eq. (7.1)) gives

$$\Delta\omega_{\mu,\text{comb}} = \frac{\mu D_2}{D_1}(\Omega_{\text{Raman}} + \Omega_{\text{Recoil}}) - \delta\omega. \quad (7.3)$$

Coupled-mode equations

We start from the coupled mode equations that include dispersion, mode interaction and Kerr nonlinearity. The intracavity field of mode μ in the soliton-forming mode family A can be represented by $A_\mu(t)e^{-i\omega_\mu t + i\mu\phi}$, where $A_\mu(t)$ is the slowly varying amplitude, t is the time and ϕ is the azimuthal angle along the resonator. In the rotation frame of comb frequencies $\omega_{\mu,\text{comb}} = \omega_0 - \delta\omega + \mu\omega_{\text{rep}}$, the intracavity field can be expressed as $a_\mu(t) = A_\mu(t)e^{-i(\omega_\mu - \omega_0 + \delta\omega - \mu\omega_{\text{rep}})t}$. We denote the intracavity field in the crossing-mode family B as b_μ and express it in the same reference frame as the soliton-forming mode a_μ . It should be noted that the relative mode number μ is referenced to the mode that is being optically pumped, and does not represent the actual azimuthal index. The intracavity fields can be calculated using the equations

of motion with Kerr nonlinearity terms [62, 131] and modal-coupling terms[144],

$$\begin{aligned} \frac{da_\mu}{dt} = & - \left[\frac{\kappa_A}{2} + i(\omega_{\mu A} - \omega_0 + \delta\omega - \mu\omega_{\text{rep}}) \right] a_\mu + iGb_\mu \\ & + ig \sum_{j,k} a_j a_k a_{j+k-\mu}^* + F\delta(\mu) \end{aligned} \quad (7.4)$$

$$\begin{aligned} \frac{db_\mu}{dt} = & - \left[\frac{\kappa_B}{2} + i(\omega_{\mu B} - \omega_0 + \delta\omega - \mu\omega_{\text{rep}}) \right] b_\mu + iGa_\mu \\ & + ig_B \sum_{j,k} b_j b_k b_{j+k-\mu}^* \end{aligned} \quad (7.5)$$

where $\kappa_{A,B} = \omega_0/Q_{A,B}$ is the dissipation rate. $g = \hbar\omega_0^2 n_2 D_1 / 2\pi n_0 A_{\text{eff}}$ represents the normalized Kerr nonlinear coefficient with A_{eff} the effective nonlinear mode area. g_B is defined similarly. G is the linear coupling coefficient between the two mode families [90] and F is the normalized coupled laser pump field. Also, to calculate Eq. (7.10) it is not necessary to include Raman coupling terms in Eq. (7.4) and Eq. (7.5) since the leading-order contribution to the forcing term, f_r , is from the Kerr nonlinearity.

Modal hybridization

Modal coupling causes two branches of hybrid modes to form as shown in Figure 7.1(a). The frequencies of the hybrid modes in the upper (+) and lower (-) branches are given by [144, 193, 194]

$$\omega_{\mu\pm} = \frac{\omega_{\mu A} + \omega_{\mu B}}{2} \pm \sqrt{G^2 + \frac{1}{4}(\omega_{\mu A} - \omega_{\mu B})^2}, \quad (7.6)$$

where the corresponding field amplitude of the hybrid modes is a linear combination of a_μ and b_μ . In the far-detuned regime where $\omega_{\mu A} - \omega_{\mu B} \gg G$, the field amplitude of the lower branch hybrid mode is approximately given by

$$\tilde{h}_{\mu-} = \frac{Ga_\mu + (\omega_{\mu A} - \omega_{\mu B})b_\mu}{\sqrt{G^2 + (\omega_{\mu A} - \omega_{\mu B})^2}}. \quad (7.7)$$

In this experiment, only one mode was observed to be near resonance with the soliton comb and that mode is assigned mode index $\mu = r$. Consistent with Figure 7.2(a), the hybridization of mode r is assumed weak (i.e., $|\omega_{rA} - \omega_{rB}| \gg |G|$ and $|\Delta\omega_{rA}| \gg |\Delta\omega_{rB}|$) so that b_r is the dominant contribution to \tilde{h}_{r-} . Also, since the amplitude of b_μ with $\mu \neq r$ is small, the Kerr interaction summation term can be neglected in Eq. (7.5) in this calculation.

Equation of motion

By taking the time derivative of Eq. (7.7) and then substituting using Eqs. (7.4) and (7.5) the following dynamical equation results for \tilde{h}_{r-} ,

$$\frac{d\tilde{h}_{r-}}{dt} = - \left[\frac{\kappa_{r-}}{2} + i(\omega_{r-} - \omega_0 + \delta\omega - r\omega_{\text{rep}}) \right] \tilde{h}_{r-} + f_r, \quad (7.8)$$

where f_r is the pumping term given by

$$f_r = i\Gamma g \sum_{j,k} a_j a_k a_{j+k-r}^* \quad (7.9)$$

and where $\Gamma = G/\sqrt{|G|^2 + |\omega_{\mu A} - \omega_{\mu B}|^2}$ is the fraction of the family A mode in $\tilde{h}_{\mu-}$ and $\kappa_{r-} \approx \kappa_B$ is assumed for r when $\Gamma \ll 1$. When converting Eq. (7.8) into the rotation frame of $(\omega_0 + \mu D_1)$ with $\tilde{h}_{r-} = h_{r-} e^{i\Delta\omega_{r,\text{comb}} t}$, the following expression results:

$$\frac{dh_{r-}}{dt} = [-i\Delta\omega_{r-} - \frac{\kappa_{r-}}{2}] h_{r-} + f_r e^{-i\Delta\omega_{r,\text{comb}} t}, \quad (7.10)$$

where $\Delta\omega_{r-} = \omega_{r-} - \omega_0 - \mu D_1$ is the relative-mode-frequency of hybrid mode h_{r-} . This resembles the equation of motion for the single mode dispersive wave.

Modified Lugiato-Lefever equation

The pumping term in Eq. (7.8) can be expressed in parameters of the resonator and soliton. The soliton field envelope takes the form [66, 88]

$$A(\phi, t) = B_s \text{sech}[(\phi - \phi_c)/D_1 \tau_s] e^{i\Omega(\phi - \phi_c)/D_1 + i\varphi}, \quad (7.11)$$

where soliton properties are: amplitude B_s , angular position ϕ_c , temporal pulse width τ_s , spectral-center frequency shift (relative to pump) Ω and phase relative to the pump laser φ . Also, this solution assumes $\delta\omega \gg \kappa_A$. By applying the Fourier transform to $A(\phi, t)$, a_μ can be expressed in terms of the soliton properties,

$$A(\phi, t) = \sum_{\mu} a_\mu(t) e^{i\mu(\phi - \phi_c)} \quad (7.12)$$

$$a_\mu = \frac{B_s \tau_s D_1}{2} \text{sech}\left(\frac{\pi \tau_s}{2} (D_1 \mu - \Omega)\right) e^{i\varphi}. \quad (7.13)$$

The pump f_r can therefore be derived by inserting Eq. (7.13) into Eq. (7.9). The following expression results from simplification of the summation:

$$f_r = i\Gamma \frac{D_2}{4D_1^2} [(D_1 r - \Omega)^2 + \frac{1}{\tau_s^2}] B_s \tau_s D_1 \text{sech}\left(\frac{\pi \tau_s}{2} (D_1 r - \Omega)\right) e^{i\varphi}, \quad (7.14)$$

where g has been replaced using equation $B_s^2 \tau_s^2 = D_2/gD_1^2$, which holds for DKSs [88, 133] and is also verified in a section below. Finally, by using [88] $\delta\omega = \frac{D_2}{2D_1^2}(\frac{1}{\tau_s^2} + \Omega^2)$ (see derivation below), f_r can be further reduced to

$$f_r = i\Gamma(\Delta\omega_{rA} - \Delta\omega_{r,\text{comb}})a_r. \quad (7.15)$$

In addition to the Raman SSFS [87, 88], the spectral center of the DKS is also shifted by the single-mode dispersive wave recoil. The effect of the recoil and Raman shift can be calculated using the moment analysis method [87, 199]. Using the Fourier transform, Eq. (7.4) is transformed into the perturbed Lugiato-Lefever equation (LLE) [131]

$$\begin{aligned} \frac{\partial A(\phi, t)}{\partial t} = & -\left(\frac{\kappa_A}{2} + i\delta\omega\right)A + i\frac{D_2}{2}\frac{\partial^2 A}{\partial \phi^2} + F + ig|A|^2A \\ & + ig\tau_R D_1 A \frac{\partial |A|^2}{\partial \phi} + iGB, \end{aligned} \quad (7.16)$$

where the Raman shock term has been added [87, 88] and τ_R is the Raman time constant. The moment analysis method treats the soliton as a particle. The energy E and the spectral center mode number μ_c are given by

$$E = \sum_{\mu} |a_{\mu}|^2 = \frac{1}{2\pi} \int_{-\pi}^{+\pi} |A|^2 d\phi = B_s^2 \tau_s D_1 / \pi \quad (7.17)$$

$$\mu_c = \frac{\sum_{\mu} \mu |a_{\mu}|^2}{E} = \frac{-i}{4\pi E} \int_{-\pi}^{+\pi} \left(A^* \frac{\partial A}{\partial \phi} - A \frac{\partial A^*}{\partial \phi} \right) d\phi. \quad (7.18)$$

Taking the time derivative of Eq. (7.18) and substituting $\partial A/\partial t$ using Eq. (7.16), the following equation of motion for μ_c is obtained:

$$\begin{aligned} \frac{\partial \mu_c}{\partial t} = & -\kappa_A \mu_c - \frac{g\tau_R D_1}{2\pi E} \int_{-\pi}^{+\pi} \left(\frac{\partial |A|^2}{\partial \phi} \right)^2 d\phi \\ & - \frac{1}{2\pi E} \int_{-\pi}^{+\pi} \left(G^* B^* \frac{\partial A}{\partial \phi} - G A^* \frac{\partial B}{\partial \phi} \right) d\phi. \end{aligned} \quad (7.19)$$

The second term on the right-hand-side corresponds to the Raman-induced frequency shift and the third term is the frequency shift caused by recoil.

The Raman term can be calculated by substituting Eq. (7.11) into the integral. When calculating the recoil term, B is simplified to $B \approx b_r e^{i\pi(\phi - \phi_c)}$ as the power in mode B is dominated by the near resonance mode r . In addition, because the integral of

ϕ is over 2π , only $a_r e^{ir(\phi-\phi_c)}$ has nonzero contribution. Furthermore, equation (7.5) is used to relate $G a_r$ to b_r and finally leads to

$$\frac{\partial \mu_c}{\partial t} = -\frac{8\tau_R D_2}{15D_1^3 \tau_s^4} - \frac{r\kappa_B}{E} |b_r|^2 - \kappa_A \mu_c. \quad (7.20)$$

The steady-state spectral center mode number is therefore given by

$$\begin{aligned} \mu_c &= -\frac{8\tau_R D_2}{15\kappa_A D_1^3 \tau_s^4} - \frac{r\kappa_B}{\kappa_A E (1 - \Gamma^2)} |h_{r-}|^2 \\ &= \frac{1}{D_1} (\Omega_{\text{Raman}} + \Omega_{\text{Recoil}}), \end{aligned} \quad (7.21)$$

where $|\omega_{\mu_A} - \omega_{\mu_B}| \gg \kappa_B$, $\Delta\omega_{r-}$ (equivalent to $|b_r| \gg |a_r|$) is assumed and the recoil and Raman shifts are

$$\Omega_{\text{Recoil}} = \gamma |h_{r-}|^2 = -\frac{r\kappa_B D_1}{\kappa_A E (1 - \Gamma^2)} |h_{r-}|^2, \quad (7.22)$$

$$\Omega_{\text{Raman}} = -\frac{8\tau_R D_2}{15\kappa_A D_1^2 \tau_s^4}. \quad (7.23)$$

Here, $\Gamma^2 \ll 1$ is assumed. The form for the Raman SSFS, Ω_{Raman} , is identical to the form previously derived in the absence of the dispersive-wave coupling [88].

Solving Eq. (7.10) for the steady-state power in the hybrid mode at the soliton comb tooth frequency and using Eq. (7.3) and Eq. (7.22) gives the following result:

$$|h_{r-}|^2 = \frac{|f_r|^2}{(\Delta\omega_{r-} + \delta\omega - \frac{rD_2}{D_1} [\Omega_{\text{Raman}} + \gamma |h_{r-}|^2])^2 + \frac{\kappa_r^2}{4}}. \quad (7.24)$$

Equation (7.24) suggests that a bistable state and hysteresis behavior in the dispersive-wave power is possible when varying the soliton operating point.

Lagrangian approach

In the presence of recoil and Raman, the relations between soliton parameters in Eq. (7.11) can be derived from the Lagrangian approach [66, 88, 133]. In addition, the Lagrangian approach verifies the expression for Ω_{Recoil} obtained above as well as providing a path for calculation of the repetition-rate phase noise [133]. As detailed in previous literature[88, 133], the perturbation Lagrangian method is applied to the LLE equation of A (Eq. (7.16)). However, now an additional perturbation term is added to account for the mode coupling to the crossing-mode family. Taking $B \approx b_r e^{ir(\phi-\phi_c)}$ produces the following equations of motion:

$$\frac{\Omega}{D_1} \frac{\partial \phi_c}{\partial t} - \frac{\partial \varphi}{\partial t} - \delta\omega - \frac{D_2 \Omega^2}{2D_1^2} - \frac{D_2}{6\tau_s^2 D_1^2} + \frac{2}{3} g B_s^2 = 0 \quad (7.25)$$

$$\frac{\Omega}{D_1} \frac{\partial \phi_c}{\partial t} - \frac{\partial \phi}{\partial t} - \delta\omega - \frac{D_2 \Omega^2}{2D_1^2} + \frac{D_2}{6\tau_s^2 D_1^2} + \frac{1}{3} g B_s^2 = 0 \quad (7.26)$$

$$\frac{\partial(B_s^2 \tau_s \Omega)}{\partial t} = -\kappa_A B_s^2 \tau_s \Omega - \frac{8g\tau_R B_s^4}{15\tau_s} - \kappa_B \pi r |b_r|^2 \quad (7.27)$$

$$\frac{\partial \phi_c}{\partial t} = \frac{D_2}{D_1} \Omega \quad (7.28)$$

$$\frac{\partial(B_s^2 \tau_s)}{\partial t} = -\kappa_A B_s^2 \tau_s + f \cos \varphi B_s \tau_s \pi \operatorname{sech}(\Omega \tau_s \frac{\pi}{2}), \quad (7.29)$$

where we have assumed the mode r is far from the mode center $\mu_c = \Omega/D_1$ and the coupling coefficient G is smaller than or around the same order of magnitude with $\delta\omega$. Also, higher order terms are neglected. Subtracting Eq. (7.26) from Eq. (7.25) yields

$$B_s \tau_s = \sqrt{\frac{D_2}{g D_1^2}} \quad (7.30)$$

This equation was previously verified in the presence of Raman-only interactions [88].

An additional relation between $\delta\omega$, τ_s and Ω is derived for steady state by substituting Eq. (7.28) and (7.30) into Eq. (7.25):

$$\delta\omega = \frac{D_2}{2D_1^2} \left(\frac{1}{\tau_s^2} + \Omega^2 \right), \quad (7.31)$$

where Ω can be obtained from Eqs. (7.27) and (7.30),

$$\Omega = \Omega_{\text{Raman}} + \Omega_{\text{Recoil}} = -\frac{8D_2\tau_R}{15\kappa_A D_1^2 \tau_s^4} - \frac{\Gamma \kappa_B D_1}{\kappa_A E (1 - \Gamma^2)} |h_{r-}|^2. \quad (7.32)$$

This result provides an independent confirmation of Eq. (7.21). Also, Eq. (7.31) is identical in form to an expression which included only the Raman SSFS [88]. Significantly, however, Eq. (7.31) is more general since Ω is the total spectral center shift provided by the combined effects of Raman SSFS and dispersive-wave recoil.

Comparison with measurements

Measurements are compared with the analytical model in figures 7.2(a), 7.2(b), and 7.4(a). Measured parameters used for the analytical model are $\kappa_A/2\pi = 2.12$ MHz, $D_1/2\pi = 22$ GHz, $D_2/2\pi = 17$ kHz, and $G/2\pi = 42.4$ MHz. $\tau_R = 2.49$ fs can be extracted from the measured Ω in the regime without the mode recoil effect ($\delta\omega/2\pi < 30$ MHz and $\delta\omega/2\pi > 40$ MHz). Two free parameters are used

to optimize the fitting in Figure 7.2 and 7.4 and they are in reasonable agreement with the measurement: $\Delta\omega_{r-} = -62.2$ MHz (-75 ± 7 MHz in measurement) and $\kappa_{r-}/2\pi = 3.6$ MHz (6 MHz in measurement). The procedure for fitting is as follows: a detuning frequency, $\delta\omega$, (horizontal axis in Figure 7.2(a), 7.2(b), and 7.4(a) plots) is selected. By eliminating Ω in Eq. (7.31) and Eq. (7.32) a single condition relating τ_s and $|h_{r-}|^2$ results. Likewise, with $\delta\omega$ selected a second condition relating τ_s and $|h_{r-}|^2$ results from Eq. (7.24) by replacing Ω_{Raman} using Eq. (7.23). This pair of equations is solved for τ_s and $|h_{r-}|^2$ from which Ω is determined by Eq. (7.32) and ω_{rep} is determined by Eq. (7.2).

7.4 Numerical simulation

Numerical simulations based on the coupled Lugiato-Lefever equation of mode family A and B (Eq. (7.16) and Fourier transform of Eq. (7.5)) are implemented to further validate the analytical model. The two mode families are coupled using a model studied elsewhere [90]. The coupling is characterized by a rate constant G and is designed to induce an avoided-mode-crossing around mode index $\mu = 72$, similar to the experimental mode family dispersion. The Raman term in mode family B is ignored since the power in mode family B is too small to induce Raman related effects. Dispersion of 3rd order and higher as well as the self-steepening effect [128] are neglected. The simulations are implemented with the split-step Fourier method [128] where 2048 modes in the frequency domain are taken into account. The parameters for two mode families used in Figure 2 and 4 are $\kappa_A/2\pi = 2.12$ MHz, $\kappa_B/2\pi = 3.4$ MHz, $D_1/2\pi = 22$ GHz for mode A, $D_{1B}/2\pi = D_1/2\pi + 50.9$ MHz for mode B, $D_2/2\pi = 17$ kHz for both mode A and B, $\tau_R = 2.489$ fs, $g = g_B = 9.8 \times 10^{-4}$ rad s $^{-1}$, and $G/2\pi = 42.4$ MHz.

Figure 7.3 shows the results of the numerical simulation. The hysteresis behavior in the soliton total frequency shift and the dispersive-wave power resembles the experimental observation and is also in agreement with the analytical model (see Figure 7.3(a),(b)). As predicted by Eq. (7.22) (and observed in the Figure 7.2(c) inset), the recoil is numerically predicted to vary linearly with the dispersive wave power (Figure 7.3(b) inset).

Frequency and time domain features of the soliton (blue) and dispersive wave (red) are also studied in Figure 7.3(c),(d) in units of intracavity power. They show that the dispersive wave emerges on mode family B and consists primarily of a single mode. The single-mode dispersive wave leads to a modulated background field in

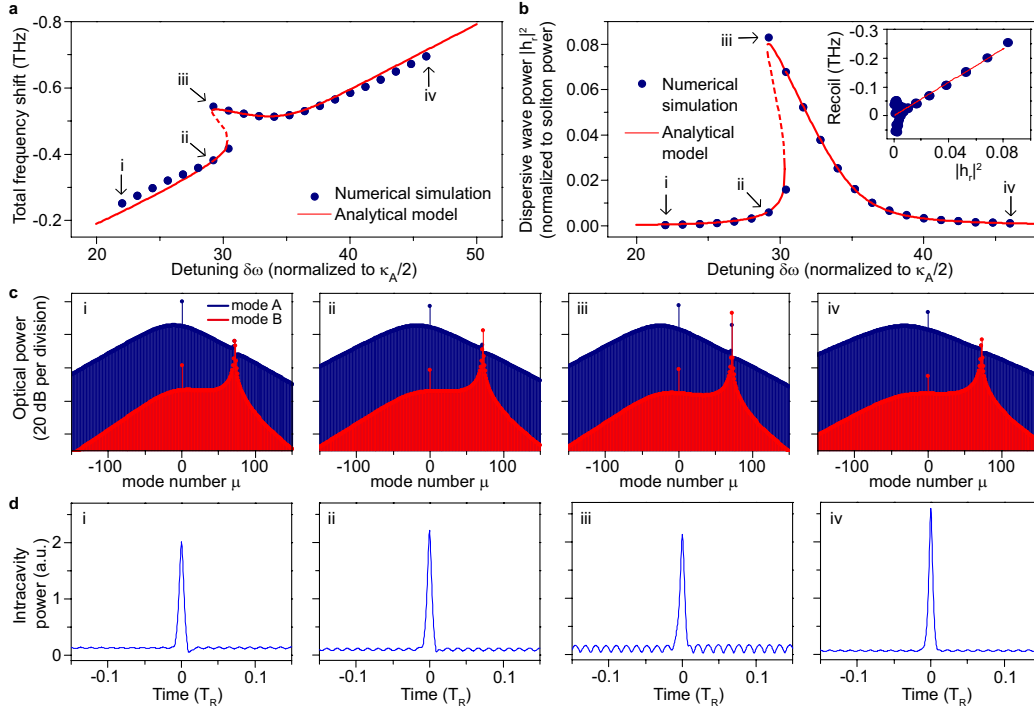


Figure 7.3: Numerical simulation and analytical model of single-mode dispersive wave generation and recoil. (a) Numerical (blue dots) and analytical (red solid line) soliton total frequency shift versus cavity-pump detuning. Points i, ii, iii, and iv correspond to specific soliton operating points noted in other Figure panels. (b) Numerical (blue dots) and analytical (red solid line) dispersive wave power (normalized to total soliton power) versus cavity-pump detuning. Inset: recoil frequency versus the dispersive wave power. (c) Comb spectra contributions from the two mode families (blue: soliton forming mode family A; red: crossing mode family B). (d) Time domain intracavity power. T_R is the cavity round trip time.

the resonator with a period determined by the beating between the pump and the dispersive wave. This modulation is observable in Figure 7.3(d). Spectral recoil of the soliton is also observable in the numerical spectra. The combined power of mode A and B spectra in Figure 7.3(c) is the total intracavity power.

7.5 Soliton repetition rate quiet point

Phase noise of soliton repetition rate at different operation points

The nonlinear behavior associated with soliton coupling to the single-mode dispersive wave can be used to suppress soliton repetition rate noise produced by coupling of pump-laser frequency noise. This noise source is suspected to be a significant contributor to repetition-rate noise in certain frequency-offset regimes [67]. From Eq. (7.2) the repetition frequency depends linearly on the total soliton spectral-

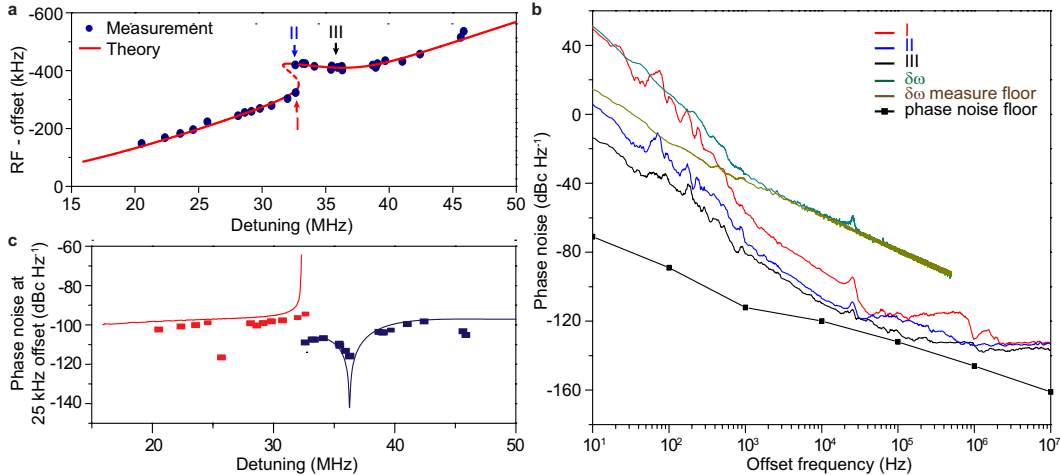


Figure 7.4: Soliton repetition frequency and phase noise measurement. (a) Measured (blue dots) and theoretical (red) soliton repetition frequency versus pump-cavity detuning. The offset frequency is 22.0167 GHz. The distinct soliton operating points I, II and III refer to phase noise measurements in panel b. Point III is near the quiet operation point. (b) Phase noise spectra of detected soliton pulse stream at three operating points shown in panel a. The black line connecting the square dots is the measurement floor of the phase noise analyzer. (c) Phase noise of soliton repetition rates at 25 kHz offset frequency plotted versus the cavity-pump detuning. The blue and red dots (lines) denote the experimental (theoretical) phase noise of the upper (blue) and lower (red) branch operating points, respectively.

center frequency shift, Ω . However, this total shift frequency versus cavity-pump detuning has a stationary point on the upper hysteresis branch (see Figure 7.2(d)). As expected from the simple dependence in Eq. (7.2), this same stationary point is observed in measurements of the repetition frequency versus detuning (Figure 7.4(a)). To measure the repetition frequency the soliton pulse train is directly detected and an electrical spectrum analyzer is used to observe the pulse train spectrum. The theoretical prediction using analysis from the Methods is also provided for comparison.

The coupling of pump-laser frequency noise into the soliton repetition rate is expected to be minimal at the stationary point. To verify this prediction, the phase noise of the detected soliton pulse train is measured at different soliton operating points on the upper and lower branches in Figure 7.4(a) using a phase noise analyzer. Phase noise spectra corresponding to operating points I, II, and III in Figure 7.4(a) are plotted in Figure 7.4(b). Operating points I and II correspond to nearly identical cavity-pump detuning, but lie on different branches. As expected, operating point II

in the upper branch has a lower phase noise level compared to operating point I on account of its reduced slope. Operating point III is close to the zero-slope detuning point in the upper branch. This quiet point has the lowest phase noise among the recorded phase noise spectra. At higher offset frequencies, the phase noise is shot noise limited, while at lower offset frequencies the phase noise indicates > 0 dBc Hz⁻¹ and is mainly contributed by frequency drift of the repetition rate.

Measurement of detuning noise

For comparison, the phase noise associated with the detuning frequency $\delta\omega$ was also measured. For this measurement, an additional Pound-Drever-Hall (PDH) loop is embedded into the setup and operated open loop (see Figure 7.5(a)). The pump frequency is red detuned relative to the cavity resonance in order to form the soliton pulse train. Moreover, the amount of cavity-laser detuning required to generate solitons is many cavity linedwidths so that the conventional PDH error signal near the resonance frequency cannot be used to monitor the detuning frequency. However, the higher-frequency PDH sideband can be tuned to reside close to the cavity resonance. Path phases in the PDH loop can be adjusted so that a PDH error signal is produced by the interaction of this sideband with the cavity resonance. When the soliton is formed, we tune the PDH local-oscillator (LO) frequency to approximately match the cavity-laser detuning. This is accomplished by monitoring the PDH error signal (see red trace in Figure 7.5(b)). For this measurement the transmitted pump light is filtered from the soliton spectrum using a fiber Bragg filter. By setting this LO frequency to the indicated monitoring point, the corresponding error-signal output will convert detuning frequency to a voltage output. This output can be recorded and then analyzed to produce a noise spectrum. The calibration of voltage into frequency is performed by using the Mach-Zehnder interferometer trace (see blue trace in Figure 7.5(b)). This calibration is performed on the resonator at reduced power levels where solitons do not form and where the Lorentzian lineshape of the resonator is unaffected by the Kerr nonlinearity.

The power spectral density of the error signal is converted into phase noise in Figure 7.4(b). The relatively high noise floor in this measurement is caused by the oscilloscope sensitivity. Nonetheless, a noise bump at 25 kHz offset frequency originates from the laser and provides a laser-noise reference point against which comparison to the soliton phase noise is possible. The soliton phase noise at 25 kHz offset frequency noise is plotted versus detuning in Figure 7.4(c). The soliton phase noise is calculated later in this section and the results are presented for comparison

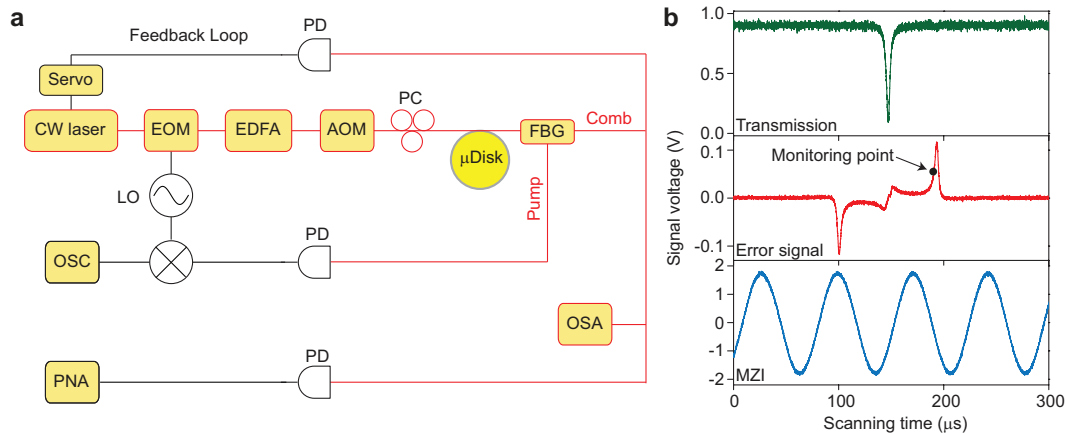


Figure 7.5: Experimental setup and details on detuning-noise measurement. (a) The experimental setup includes both the soliton generation and characterization setup and a Pound-Drever-Hall (PDH) system operated open loop. The PDH is added to make possible the pump-cavity detuning noise measurement. Components included in the set up are an EOM: electro-optic modulator; EDFA: Erbium-doped fiber amplifier; AOM: acousto-optic modulator; PC: polarization controller; FBG: fiber Bragg grating; PD: photodetector; OSA: optical spectral analyzer; PNA: phase noise analyzer; LO: local oscillator. The OSA and PNA are shown for completeness. They are used to measure the soliton spectrum and repetition rate phase noise. They are not involved in measuring the detuning frequency noise. (b) Measurements that illustrate the pump-cavity detuning measurement. The green trace is the measured power transmission when scanning the pump laser frequency across a cavity resonance. The pump laser is phase modulated, the transmitted signal is detected and the resulting photocurrent is then mixed with the PDH local oscillator signal to generate the PDH error signal. Upon laser scan the PDH error signal (as measured on the oscilloscope) is generated as shown in the red trace. The pump laser is filtered using the fiber Bragg grating. The monitoring point for the detuning frequency measurement is indicated by the black dot. In order to convert scanning time into laser frequency, a calibrated Mach-Zehnder interferometer (MZI) records power transmission (blue trace) on an oscilloscope. The free-spectral-range of the MZI is 40 MHz.

using the cavity-pump detuning noise level at 25 kHz offset. The dip of the phase noise occurs at the quiet point. One outlier point (red branch) is believed to have resulted from loss of lock of the phase noise analyzer. For lower offset frequencies, the contributions to noise are believed to originate from thermal contributions within the resonator and are under investigation. Nonetheless, the measured noise contributions at these frequencies show a trend of reduction for operation at the quiet point.

Coupling between detuning noise and repetition rate noise

To calculate the dependence of soliton repetition rate phase noise on the pump frequency noise, we start with the expression of repetition rate of the soliton which can be expressed as follows [90],

$$\omega_{\text{rep}} = D_1 + \frac{\partial \phi_c}{\partial t} = D_1 + \frac{D_2}{D_1} \Omega. \quad (7.33)$$

The variation in both D_1 and Ω contribute to fluctuations in the repetition rate. While D_1 is subject to thermo-refractive noise and fluctuations from the environment, a significant contributor to fluctuations in Ω results from fluctuations in the pump-laser frequency detuning frequency, $\delta\omega$. The noise conversion from cavity-pump detuning to repetition rate can be calculated by linearizing Eqs. (7.25)-(7.29) using the small signal approximation[133]. Accordingly, all soliton parameters (X) can be expressed as $X = X_0 + \Delta X$, where X_0 is the steady-state value and ΔX is a small-signal fluctuation. For simplicity, we further denote the Raman and recoil terms in Eq. (7.27) as $-8g\tau_R B_s^4/15\tau_s - \kappa_B \pi r |b_r|^2 \equiv \kappa_A B_s^2 \tau_s F(\delta\omega)$ so that $\Omega = F(\delta\omega)$ is the function of detuning measured in Figure 7.2(d) (i.e., steady-state Ω versus $\delta\omega$).

In the following derivation, τ_s in Eqs. (7.25)-(7.29) is eliminated using Eq.(7.30). Equation (7.27) can therefore be expressed as

$$\frac{\partial B_s \Omega}{\partial t} = -\kappa_A B_s [\Omega - F(\delta\omega)]. \quad (7.34)$$

Applying the small-signal approximation and Fourier transform to Eq. (7.34) gives the result,

$$(1 + i\omega/\kappa_A) \Delta \tilde{\Omega}(\omega) = \frac{\partial F}{\partial \delta\omega} \Delta \tilde{\delta\omega}(\omega) - \frac{i\omega \Omega_0}{\kappa_A B_{s0}} \Delta \tilde{B}_s(\omega), \quad (7.35)$$

where $\Delta \tilde{X}(\omega)$ is the Fourier transform of ΔX , ω is the Fourier frequency (i.e., offset frequency in the phase or frequency-noise spectrum) and where the Fourier transform of $\partial \Delta X / \partial t$ equals $i\omega \Delta \tilde{X}(\omega)$. $\Delta \tilde{\delta\omega}(\omega)$ represents the cavity-pump detuning noise. Similarly, Eq. (7.25) can be transformed to

$$g B_{s0} \Delta \tilde{B}_s(\omega) = \Delta \tilde{\delta\omega}(\omega) - \frac{D_2 \Omega_0}{D_1^2} \Delta \tilde{\Omega}(\omega), \quad (7.36)$$

where the contribution from $i\omega \Delta \tilde{\varphi}(\omega)$ is neglected as it is of order $(\omega/\delta\omega)$ smaller compared to the leading-order terms.

In the limit of $\omega^2/\kappa_A^2 \ll 1$ and $\Omega^2 \tau_s^2 \omega/\kappa_A \ll 1$, Eq. (7.35) and Eq. (7.36) are solved for $\Delta \tilde{\Omega}(\omega)$ in terms of $\Delta \tilde{\delta\omega}(\omega)$. The result is substituted into the Fourier transform

of Eq. (7.33) to give the following result:

$$\Delta\widetilde{\omega}_{\text{rep}}(\omega) = \frac{D_1}{D_2}\Delta\widetilde{\Omega}(\omega) = \frac{\Delta\widetilde{\delta\omega}(\omega)}{1 + i\omega/\kappa_A} \left(\frac{\partial\omega_{\text{rep}}}{\partial\delta\omega} - \frac{i\omega}{\kappa_A}\Omega D_1\tau_s^2 \right), \quad (7.37)$$

where sources of noise associated with D_1 in Eq. (7.33) are ignored.

The soliton repetition rate noise can be expressed as $\Delta\widetilde{\omega}_{\text{rep}}(\omega) = \alpha(\omega)\Delta\widetilde{\delta\omega}(\omega)$ where $\alpha(\omega)$, the noise transfer function, is the coefficient of $\Delta\widetilde{\delta\omega}(\omega)$ in Eq. (7.37). Accordingly, the phase noise of repetition rate is $S_\phi(\omega) = |\alpha(\omega)|^2 S_{\phi,\delta\omega}(\omega)$.

Typically, for the resonators in this study $\omega < \kappa_A$ so that the first term in Eq. (7.37) expresses the trivial result that the slope of the plot in Figure 7.4(a) acts as a transfer function of fluctuations in $\delta\omega$ into repetition-rate fluctuations. However, when $\partial\omega_{\text{rep}}/\partial\delta\omega$ approaches zero (the quiet point), the first term in Eq. (7.37) vanishes and the noise transfer function reaches a minimum determined by the second term. The phase noise plots in Figure 7.4(c) were fitted using the same parameters as in analytical fitting in Figure 7.2(c), 7.2(d) and 7.4(a), and $\partial\omega_{\text{rep}}/\partial\delta\omega$ extracted numerically from the fitting curves in Figure 7.4(a).

Existence of quiet points and hysteresis

An analytical study comparing the detuning response of the Raman and recoil effects was performed to determine conditions required to observe the quiet point. The quiet point occurs when the retreating soliton recoil balances the always advancing SSFS. Accordingly, Figure 7.6 is a contour plot of the maximum ratio of $|\partial\Omega_{\text{Recoil}}/\partial\delta\omega|$ to $|\partial\Omega_{\text{Raman}}/\partial\delta\omega|$ while varying the coupling strength between the soliton-mode and crossing-mode families and the damping rate of the crossing mode (see Methods). The existence regime for observation of the quiet point corresponds to the ratio > 1 shown in red. Stronger mode interaction and weaker dissipation are required to operate in this regime.

The detuning range of bistability is critical for observation of hysteresis behavior. Analysis shows that this range can be increased by increasing the spatial-mode coupling strength, optical quality factor or moving the mode crossing frequency closer to the pump laser frequency (smaller r). In Figure (7.7), the calculated detuning range of bistability is presented as a contour plot versus coupling strength, G , and the dissipation rate of crossing mode, κ_B . It can be seen that the range increases with G and decreases with κ_B . This is mainly because larger G and smaller κ_B enhance the dispersive wave power and therefore increase the strength of recoil and nonlinearity. In our experiment, we have measured $G/\kappa_A = 20$ and

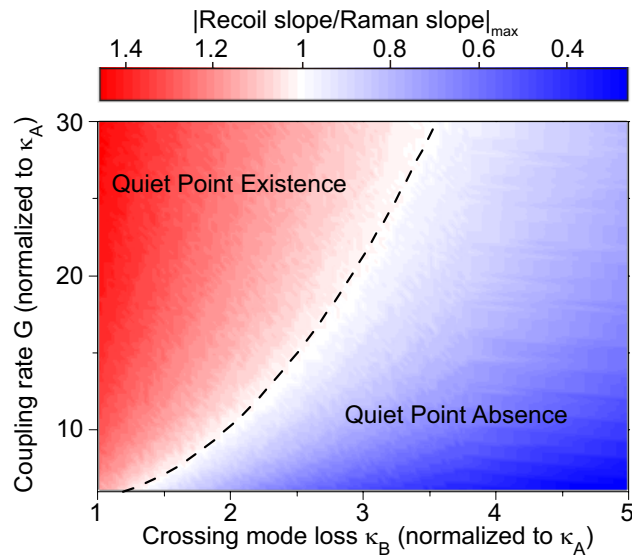


Figure 7.6: Existence study for the quiet point. The maximum ratios of $|\partial\Omega_{\text{Recoil}}/\partial\delta\omega|$ to $|\partial\Omega_{\text{Raman}}/\partial\delta\omega|$ at varying normalized modal coupling rate G and normalized crossing-mode damping rate κ_B (dashed curve is unity ratio). The quiet point exists when this ratio is greater than unity (red region). Parameters correspond to a silica resonator.

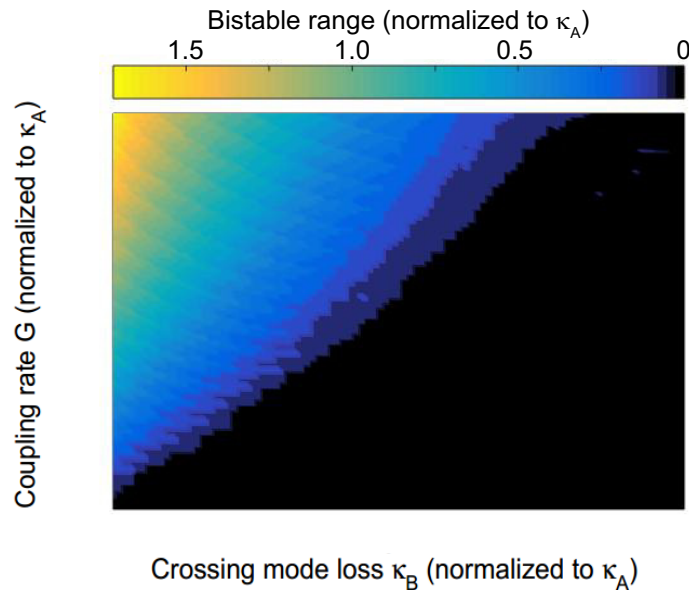


Figure 7.7: Contour plot of detuning range. Color plot of detuning range of bistability versus spatial-mode coupling strength, G , and dissipation rate of crossing mode, κ_B . All quantities are normalized to the dissipation rate, κ_A , of the soliton-forming mode.

fitted $\kappa_B/\kappa_A = 1.7$ and the corresponding normalized bistable range is estimated to be 0.67.

7.6 Conclusion

In summary, coupling of a dissipative Kerr soliton to a single-mode dispersive wave has been shown to produce hysteresis behavior in both the dispersive-wave power and in the soliton properties. These properties include the frequency shift of the soliton spectral center relative to the pumping frequency and the soliton repetition frequency. The hysteresis results from the dependence of the dispersive-wave phase matching condition upon the dispersive-wave power. The hysteresis behavior of the dispersive wave also leads to an operating point wherein coupling of laser pump frequency noise into the soliton repetition rate is greatly reduced. This reduction was modeled and measured, and the requirements for quiet point existence were also studied. The operating point for quiet soliton operation is of potential use for ultra-low-noise microwave generation.

MICRORESONATOR SOLITON DUAL-COMB SPECTROSCOPY

¹Since their demonstration in the late 1990s [23, 30, 31], optical frequency combs have revolutionized precision measurements of time and frequency and enabled new technologies such as optical clocks [23], low-noise microwave generation [200] and dual-comb spectroscopy [35, 201–207], while also adding performance capability to methods like coherent LIDAR [208–210]. In spectroscopic applications, frequency comb systems exist across a broad spectral range spanning ultraviolet to infrared, making them well suited for measurement of diverse molecular species. At the same time, the method of dual-comb spectroscopy leverages the coherence properties of combs for rapid, broad-band spectral analysis with high accuracy [211].

In parallel with advancements in frequency comb applications, the past decade has witnessed the appearance of a miniature optical frequency comb or microcomb [51, 52]. These microcombs have been demonstrated across a range of emission bands using several dielectric materials [51, 63, 151, 212–215]. Under continuous-wave laser pumping, the combs are initiated by way of parametric oscillation [61, 216] and are broadened by cascaded four-wave mixing [51, 52] to spectral widths that can encompass an octave of spectrum [215]. Four-wave mixing in the ultra-fast intraband gain medium of quantum cascade lasers (QCL) has also been shown to create frequency modulation (FM) combs [217]. These FM systems have been applied to demonstrate dual-comb spectroscopy in the mid infrared [218]. Also, heterodyne of two conventional microcombs in the mid infrared has been demonstrated, a key step towards dual-comb spectroscopy [108]. Direct heterodyne detection of two QCL FM combs in the laser current has also been shown [219].

A major advancement in microcombs has been the realization of soliton mode-locking [66–68, 76, 77]. Soliton microcombs feature dissipative Kerr solitons that leverage the Kerr nonlinearity to both compensate dispersion and to overcome cavity loss by way of parametric gain [170]. Unlike earlier microcombs, this new device provides phase-locked femtosecond pulses with well-defined, repeatable spectral en-

¹Work presented in this chapter has been published in “Microresonator soliton dual-comb spectroscopy”, *Science* 354, 600-603 (2016).

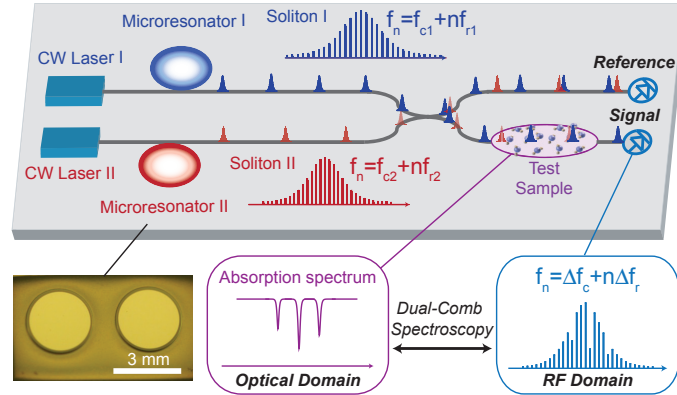


Figure 8.1: Microresonator-based dual-comb spectroscopy. Two soliton pulse trains with slightly different repetition rates are generated by continuous optical pumping of two microresonators. The pulse trains are combined in a fiber bidirectional coupler to produce a signal output path that passes through a test sample as well as a reference output path. The output of each path is detected to generate an electrical interferogram of the two soliton pulse trains. The interferogram is Fourier transformed to produce comb-like electrical spectra having spectral lines spaced by the repetition rate difference of the soliton pulse trains. The absorption features of the test sample can be extracted from this spectrum by normalizing the signal spectrum by the reference spectrum. Also shown is the image of two, silica wedge disk resonators. The disks have a 3 mm diameter and are fabricated on a silicon chip.

velopes, which is important for dual-comb spectroscopy. Their pulse repetition rate is detectable and has excellent phase noise characteristics [67]. Here, we demonstrate dual-comb spectroscopy using this new platform. The dual-comb source spans over 30 nm with 22 GHz optical spectral resolution and the interferogram spectra feature high signal-to-noise. Also, precise microfabrication control enables close matching of the repetition rates so that over 4 THz of optical bandwidth is measured within 500 MHz of electrical bandwidth.

8.1 Concept of microresonator soliton dual comb spectroscopy

A schematic view of the dual comb experimental setup is provided in Fig. 8.1. Two soliton trains having different repetition rates ($\Delta f_r = f_{r1} - f_{r2}$) are generated from distinct microresonators and then combined using a directional coupler. One of the combined streams is coupled through a gas cell of molecules whose absorption spectrum is to be measured. The other combined stream functions to provide a reference. The slight difference in repetition rates of the soliton streams creates a periodically time-varying interferogram in the detected current with a period $1/\Delta f_r$.

Fourier transform of this time-varying signal reveals the interfering soliton comb spectra, now shifted to radio-frequency rates. The signal spectrum containing the molecular absorption information is then normalized using the reference spectrum to reveal the spectral absorption of the gas cell.

8.2 Experimental setup and soliton generation

Figure 8.2(A) gives further details on the experimental setup. Solitons are generated and stabilized in two microresonators using the active-capture/locking technique [156]. The microresonators are pumped at 1549.736 nm and 1549.916 nm using two amplified fiber lasers (Orbits Lightwave), but in principle, pumping from a single laser is possible. The difference frequency of the pumps was determined to be 22.5 GHz by detecting their electrical beat note and measurement on a spectrum analyzer. After amplification, each pump laser is coupled to an acousto-optic frequency modulator (AOM). The frequency-shifted output of the AOM is used to provide a controllable optical pumping power that is required for soliton triggering [156]. The pump light is then evanescently coupled into the silica microresonator via a fiber taper [130, 139]. Residual pumping light that is transmitted past each resonator is filtered using a fiber Bragg grating (FBG). After the FBG, a 90/10 tap is used to monitor the soliton power for feedback control of the pump laser frequency so as to implement soliton locking [156]. The optical spectra of the individual soliton streams was monitored using a Yokogawa optical spectrum analyzer. Additional precision calibration of the spectra was possible using a Wavelength References Clarity laser locked to a molecular absorption line. Typical soliton optical spectra are presented in Fig. 8.2, (B) to (C), and feature the characteristic sech^2 envelope observed in this case over a 60 nm wavelength span. The detected electrical spectrum for each soliton source is also shown in Fig. 8.2, (D) to (E). The narrow spectral lines measured with a resolution bandwidth of 500 Hz have a signal-to-noise greater than 75 dB showing that corresponding repetition rates are extremely stable.

The high-Q resonators used in this work are described elsewhere [55]. Briefly, they are silica wedge devices fabricated on a silicon wafer using a combination of lithography and wet/dry etching. The unloaded quality factor of the microresonators exceeds 300 million, and the generated solitons have repetition rates determined primarily by the diameter of the devices (3 mm). The repetition rate difference of the two microcomb devices is controlled by varying the silica resonator etching time [55].

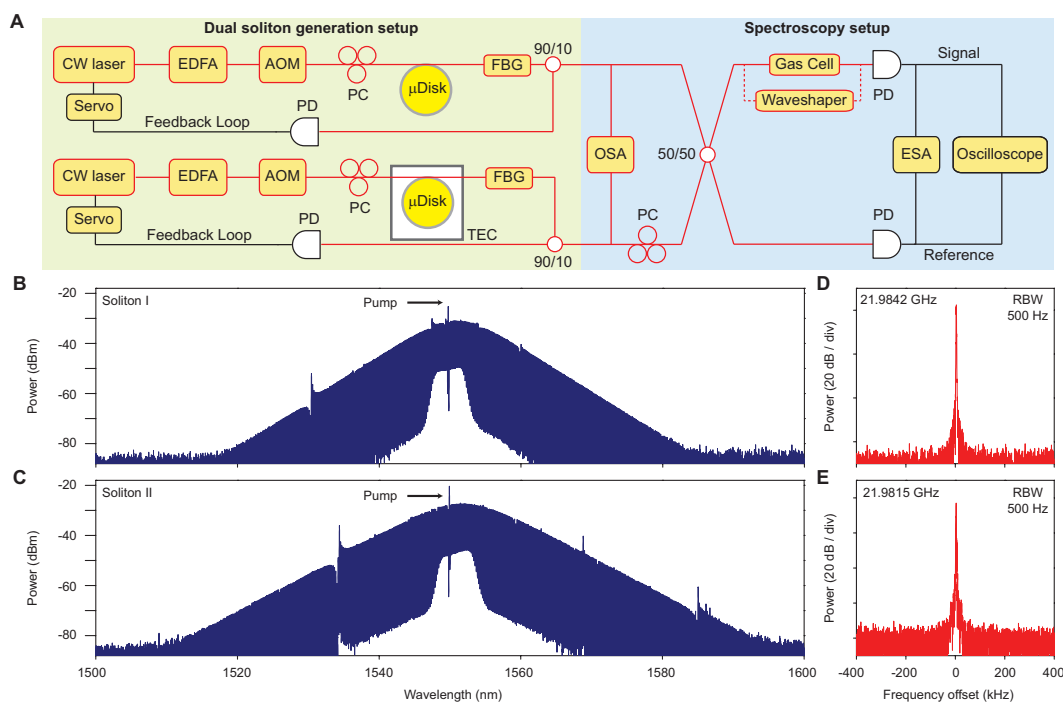


Figure 8.2: Detailed experimental setup and soliton comb characterization. (A) Continuous-wave (CW) fiber lasers are amplified by erbium-doped fiber amplifiers (EDFA) and coupled into high-Q silica wedge microresonators via tapered fiber couplers. An acousto-optic modulator (AOM) is used to control pump power to trigger soliton generation in the microresonators. Polarization controllers (PC) are used to optimize resonator coupling. A fiber Bragg grating (FBG) removes the transmitted pump power in the soliton microcomb. The pump laser frequency is servo controlled to maintain a fixed detuning from the microresonator resonance by holding the soliton average power to a fixed setpoint. An optical spectrum analyzer (OSA) monitors the spectral output from the microresonators. The two soliton pulse streams are combined in a bidirectional coupler and sent to a gas cell (or a WaveShaper) and a reference path. The interferograms of the combined soliton pulse streams are generated by photodetection (PD) and recorded on an oscilloscope. The repetition rates of the soliton pulse streams are also monitored by an electrical spectrum analyzer (ESA). The temperature of one resonator is controlled by a thermoelectric cooler (TEC) to tune the optical frequency difference of the two solitons. (B)-(C) Optical spectra of the microresonator soliton pulse streams. (D)-(E) Electrical spectra showing the repetition rates of the soliton pulse streams. The rates are given in the legends.

The optical outputs from the stabilized soliton sources are combined and coupled into two paths as shown in Fig. 8.2(A). One path contains a 16.5 cm-long 300 Torr H^{13}CN gas cell manufactured by Wavelength References, Inc. which functions as the test sample in the measurement. The other path is coupled directly to a

photodetector and functions as the reference. The test sample path also contained an alternate path in which a Finisar WaveShaper was inserted. The WaveShaper required an erbium fiber amplifier to compensate its insertion loss. As demonstrated below, the WaveShaper allowed synthesis of arbitrary spectral transmission profiles to further verify the dual comb operation. Detection to generate the interferograms used two photodetectors with bandwidths of 50 GHz. Temperature control of one of the microresonators was used to tune the relative optical frequency difference of the two soliton streams. In the measurements this difference was held below 1 GHz, allowing the observation of the temporal interferogram on an oscilloscope (bandwidth 1 GHz). The spectrum of the photocurrent signals was also measured to determine the soliton repetition rates (see Fig. 8.2, (D) to (E)) using an electrical spectrum analyzer (Rhode Schwartz) with a bandwidth of 26 GHz.

8.3 Electrical interferogram and spectra

The reference interferogram produced by detection of the lower path in Fig. 8.2A and as recorded on the oscilloscope is shown in Fig. 8.3(A). It has a period of 386 ns, corresponding to a soliton repetition rate difference of 2.6 MHz. This relatively small repetition rate difference was made possible by precise lithographic control of the 22 GHz soliton repetition rate. It was possible to fabricate disks with even more closely matched repetition rates (< 100 kHz). Figure 8.3(B) shows the calculated Fourier transform of the interferogram. The small repetition rate difference on the much larger 22 GHz soliton repetition rate makes it possible compress an optical span of 4 THz (1535 nm to 1567 nm) into 500 MHz of electrical spectrum. The measured wavelength span is actually narrower than the observable wavelength span of the original soliton pulse streams and is limited by the photodetector noise. The interferogram spectrum has a signal-to-noise ratio (SNR) in excess of 30 dB near the central lines. A zoom-in of the spectrum (multi- and single-line) is provided in Fig. 8.3(C). The electrical comb teeth are equidistantly separated by 2.6 MHz and have a full-width-half-maximum linewidth less than 50 kHz, limited by the mutual coherence of the independent fiber pump lasers. The pump laser line in a dissipative Kerr soliton is also a comb tooth in the soliton optical spectrum. As a result, the frequency jitter in each pump is transferred as an overall shift on the resulting soliton comb. Externally locking the two combs should reduce the observed linewidth in the interferogram spectrum.

It is interesting to note the placement of the pump lines toward the high frequency side (near 550 MHz) of the spectral maximum in the interferogram spectrum (see

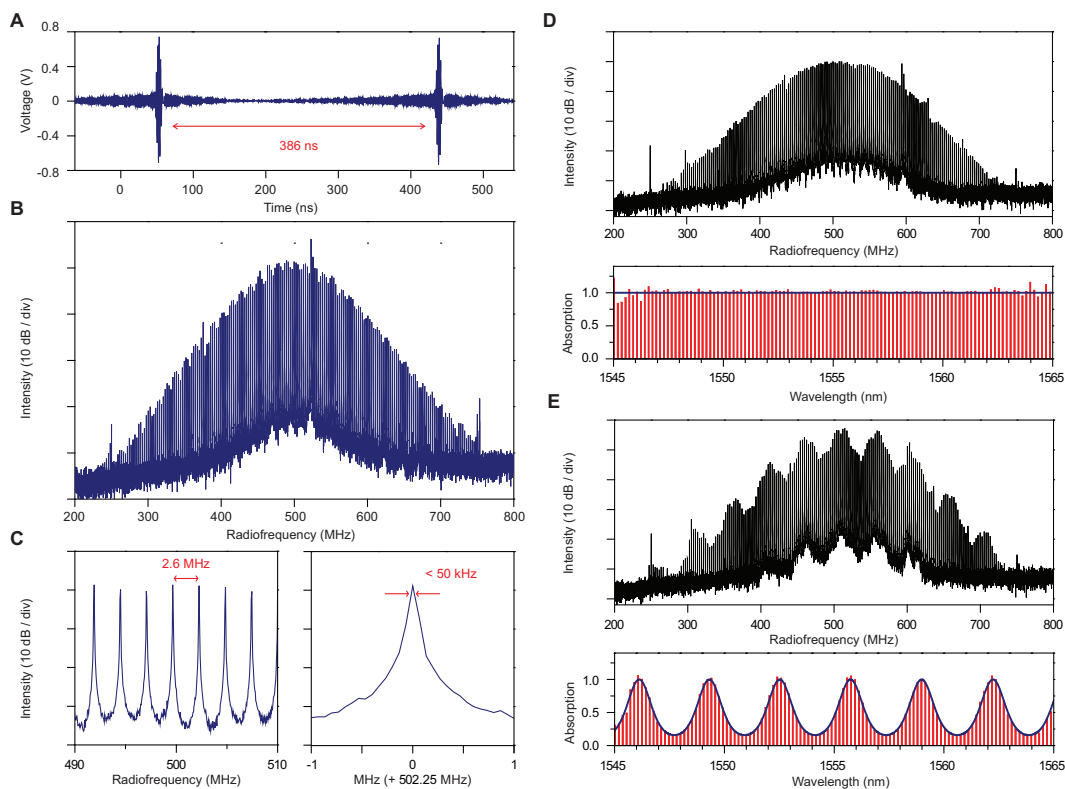


Figure 8.3: Measured electrical interferogram and spectra. (A) The detected interferogram of the reference soliton pulse train. (B) Typical electrical spectrum obtained by Fourier transform of the temporal interferogram in A. To obtain the displayed spectra, ten spectra each are recorded over a time of $20\ \mu\text{s}$ and averaged. (C) Resolved (multiple and individual) comb teeth of the spectrum in panel b are equidistantly separated by 2.6 MHz, the difference in the soliton repetition rate of the two microresonators. The linewidth of each comb tooth is $< 50\ \text{kHz}$ and set by the mutual coherence of the pumping lasers. (D)- (E) Fourier-transform (black) of the signal interferogram produced by coupling the dual-soliton pulse trains through the WaveShaper (see Fig. 8.2(A)) with programmed absorption functions (spectrally flat and sine-wave). The obtained dual-comb absorption spectra (red) are compared with the programmed functions (blue curves) from 1545 nm to 1565 nm.

Fig. 8.3B). In the optical spectra (Fig. 8.2, (B) to (C)) the pump is blue detuned relative to the soliton spectral maximum (this occurs on account of the Raman self-frequency-shift of the soliton[87, 88, 166]). This spectral landmark shows that the relative spectral placement of the soliton combs is such that high optical frequencies are mapped to high interferogram frequencies. It is also interesting to note how certain non-idealities in the soliton spectra map into the interferogram spectrum. Specifically, there are avoided-mode-crossing induced Fano-like spurs[67] in the soliton optical spectra (Fig. 8.2, (B) to (C)) occurring near 1535 nm and this

generates a corresponding feature at 750 MHz in Fig. 8.3(B).

As an initial test of the dual-comb source, artificial absorption spectra were programmed in a Finisar WaveShaper 1000S and then measured as dual-comb spectra. In Fig. 8.3, (D) to (E), electrical spectra Fourier-transformed from the signal interferograms after coupling through the WaveShaper are shown. The two programmed functions are a spectrally flat 3 dB absorption and a sine-wave absorption having a 4 dB amplitude. The absorption spectra, obtained by normalizing the signal and reference electrical spectra, are compared with the programmed functions in 8.3, (D) to (E). The ability to reconstruct these synthetic spectral profiles clearly demonstrates the reproducibility of solitonic spectral profile.

8.4 Trace gas spectroscopy

In this section the absorption spectrum of the $\text{H}^{13}\text{CN } 2\nu_1$ band is studied. In Fig. 8.4(A), the measured dual-comb absorption spectrum from 1538 nm to 1562 nm is shown in red and compared with a directly measured absorption spectrum shown in blue. Both absorption spectra are normalized. Sampling-induced choppiness of the dual-comb spectrum is caused by the relatively coarse spectral resolution of the solitons in comparison to the spectral scale of the H^{13}CN absorption lines. Nonetheless, the characteristic envelope of $\text{H}^{13}\text{CN } 2\nu_1$ band is clearly resolved. The residual difference between the two absorption spectra is shown in green and the calculated standard deviation is 0.0254. Furthermore, a line-by-line overlay of the measured optical and dual-comb spectra is shown in Fig. 8.4(B) to visually confirm the wavelength precision and absorption intensity accuracy of the dual-comb source. The directly measured H^{13}CN absorption spectrum in Fig. 8.4(A) is obtained by coupling an external cavity diode laser (ECDL) into the H^{13}CN gas cell and scanning the laser while monitoring the transmitted optical power. A separate signal is also tapped from the ECDL to function as a reference. The relative wavelength change of the ECDL during the scan is calibrated using a fiber Mach-Zehnder interferometer and absolute calibration is obtained using the Wavelength References Clarity laser mentioned above.

In principle, a finer comb spacing (lower repetition frequency) soliton source is possible. Non-soliton microcombs having mode spacing as narrow as 2.4 GHz have been demonstrated using the silica wedge resonator platform [63]. Modulating the microcombs by an integer factor of the repetition frequency using electro-optical modulators is another possible way to create a finer spectral comb grid. On the

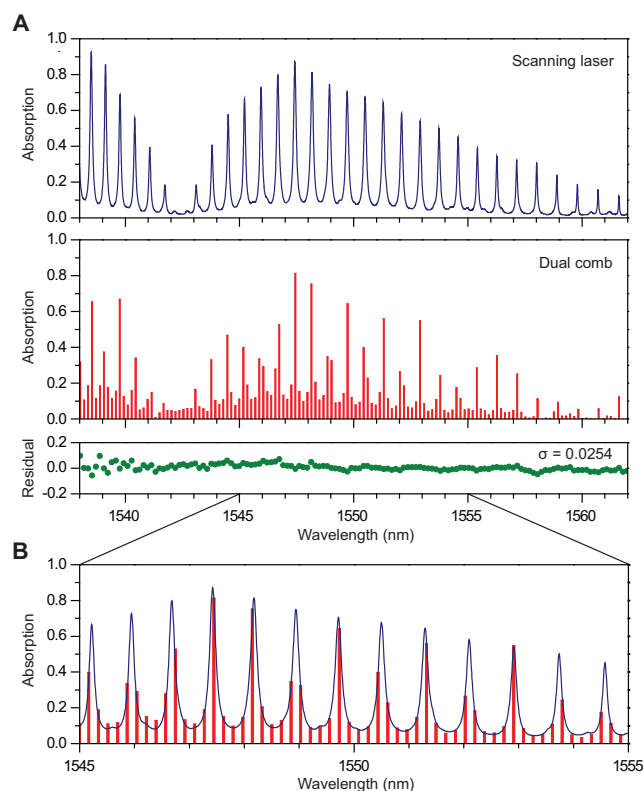


Figure 8.4: Measured molecular absorption spectra. (A) Absorption spectrum of $2\nu_1$ band of H^{13}CN measured by direct power transmission using a wavelength-calibrated scanning laser (see Methods section) and comparison to the microresonator-based dual-comb spectrum. The residual difference between the two spectra is shown in green. (B) Overlay of the directly measured optical spectrum and the dual-comb spectrum showing line-by-line matching. The vertical positions of the two spectra are adjusted to compensate insertion loss.

other hand, larger mode spacing could allow studies of fast dynamic processes such as chemical reactions and rapid measurements of the broad absorption features in liquids or solids [220, 221].

8.5 Conclusion

In conclusion, two soliton microcombs featuring highly balanced microwave repetition rates were used as a dual-comb spectroscopy system to measure the absorption spectrum of the $2\nu_1$ band of H^{13}CN . This is the first demonstration of a microresonator soliton-based dual-comb spectroscopy system. The dual-comb source has a high SNR and spans over 30 nm in optical C-band. Using fiber nonlinear broadening or internal (resonator) dispersive wave generation, it should be possible to greatly extend this spectral span [207, 222]. With careful engineering of the resonator

dispersion [138] it should also be possible to cover other spectral ranges within the transmission window of silica. More generally, a wide range of materials are available for microcombs enabling access to mid infrared spectra. With further improvements, it should also be possible to realize chip-based dual-comb coherent anti-Stokes Raman spectroscopy (CARS). The integration with other on-chip devices [73] makes soliton-based microcombs well suited for possible realization of a dual-comb spectroscopic system-on-a-chip.

COUNTER-PROPAGATING SOLITONS

¹Solitons occur in many physical systems when a nonlinearity compensates wave dispersion. Their recent formation in microresonators opens a new research direction for nonlinear optical physics [66–68, 76, 77]. Soliton mode locking also endows frequency microcombs with enhanced stability necessary for miniaturization of spectroscopy and frequency metrology systems [52]. These microresonator solitons orbit around a closed waveguide path and produce a repetitive output pulse stream at a rate set by the round-trip time. In this chapter counter-propagating solitons that simultaneously orbit in an opposing sense (clockwise/counter-clockwise) are studied. Despite sharing the same spatial mode family, their round-trip times can be precisely and independently controlled. Furthermore, a state is possible in which both the relative optical phase and relative repetition rates of the distinct soliton streams are locked. This state allows a single resonator to produce dual-soliton frequency-comb streams having different repetition rates, but with high relative coherence useful in both spectroscopy [105–107] and laser ranging systems [38].

9.1 Generation of counter-propagating solitons

Dissipative Kerr solitons orbit in closed optical paths within optical whispering-gallery microresonators. These paths support both clockwise (CW) and counter-clockwise (CCW) whispering gallery modes, which, in principle, could allow two soliton frequency combs to co-exist in the same spatial mode family. In this work counter-propagating (CP) solitons are generated by counter-pumping on a single microresonator resonance (Figure 9.1(a)). These CP solitons have several properties. First, because the pump wave of each DKS comb is also a tooth of the corresponding frequency comb (i.e., pump is phase coherent with the soliton), the tuning of two counter-propagating pumps also causes an offset in the optical frequency of the two soliton pulse streams. Moreover, because the two pumps can be derived from a single seed laser by radio-frequency-rate tuning of optical modulators (see AOMs in Figure 9.1(b)), the two solitons share the optical phase of the seed laser. Second, the precise frequency control of the two pumps afforded by the modulators enables

¹Work presented in this chapter has been published in “Counter-propagating solitons in microresonators”, *Nat. Photon.* 11(9):560-564 (2017).

independent tuning of the CW and CCW soliton repetition rates. This rate tuning is possible because of soliton self interactions mediated by the Raman process [88, 90]. Collectively, precise pump frequency control derived from a single seed laser creates two controllable microcombs in a single device with high relative optical coherence.

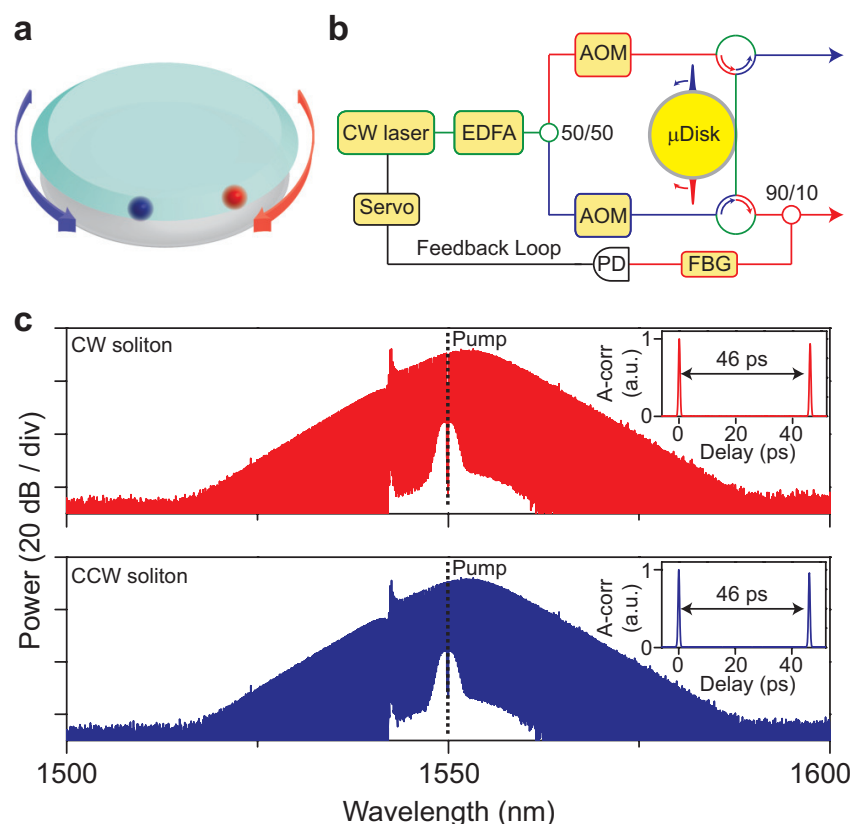


Figure 9.1: Observation of counter-propagating solitons. (a) Rendering showing counter-propagating solitons within a high-Q wedge resonator. (b) Experimental setup. A continuous-wave fiber laser is amplified by an erbium-doped-fiber-amplifier (EDFA) and sent into two acousto-optic modulators (AOMs). The outputs from the AOMs are counter-coupled into the microresonator and generate counter-propagating solitons. The optical power of solitons in one direction is used to servo lock the pump laser to a certain frequency detuning relative to the cavity mode. FBG: fiber-Bragg grating; PD: photodetector. (c) Optical spectra of counter-propagating solitons. The location of the pump line is indicated by a dashed line. Measured autocorrelation traces are provided as insets.

After reviewing the experimental setup and demonstrating CP soliton generation, the independent control of repetition rates is demonstrated. Tuning control of the repetition rates reveals two rate locking phenomena that are further studied. In one case, the CP solitons are observed to lock with identical repetition rates. In the second case, the CP solitons experience relative rate locking at different repetition

rates. This latter form of locking is potentially useful in dual comb spectroscopy and in laser ranging systems [38] (LIDAR) where it would eliminate the need for independent and mutually-locked frequency combs.

To produce the solitons, a continuous-wave fiber laser is amplified and split using a directional coupler so as to pump CW and CCW modes of a microresonator resonance using a fiber taper coupler (see experimental setup in Figure 9.1(b)). Two AOMs are used to control the pump power and frequencies in each pumping direction. The AOM frequency control allows precise tuning of the soliton repetition rates as detailed below while the amplitude of the AOM transmission is used during triggering of the solitons [68, 156]. The residual transmitted pump power is filtered by a fiber Bragg grating filter (FBG). The CP solitons are stabilized indefinitely using the active capture technique, which servo controls the pump frequency using the soliton power [156]. It is found that application of this locking technique to only one of the soliton pulse streams automatically locks the other pulse stream. The system can be controllably triggered and locked with a single or a specified number of solitons in each propagation direction.

In Figure 9.1(c) the measured optical spectra and the autocorrelation traces (insets) for typical CW and CCW soliton streams are shown. The counter-propagating solitons are typically several-hundred femtoseconds in duration. The microresonator, a high-Q silica wedge design [55] with 3 mm diameter, gives a soliton round-trip time of 46 ps as seen in the Figure 9.1(c) inset. The microresonator features anomalous dispersion at the pumping wavelength near 1.55 microns and is engineered to produce minimal avoided mode crossings over the optical band of the solitons [67].

9.2 Tuning and locking of soliton repetition rates

Tuning of soliton repetition rates

Soliton repetition rate control is achieved by varying the detuning frequency of each pump with respect to the cavity resonant frequency, ω_0 , that is pumped. For example, the repetition rate, f_{cw} , of the clockwise soliton is controlled by $\delta\omega_{cw} \equiv \omega_0 - \omega_{cw}$ where ω_{cw} is the CW pump frequency [88, 90]. Similarly, f_{ccw} is controlled by $\delta\omega_{ccw}$. This tuning is linked to the soliton self-Raman-shift [87, 88, 166], Ω_R , which is dependent on the pump-cavity detuning, $\delta\omega$, by [88]

$$\Omega_R = -\frac{32D_1^2\tau_R}{15\kappa D_2}\delta\omega^2, \quad (9.1)$$

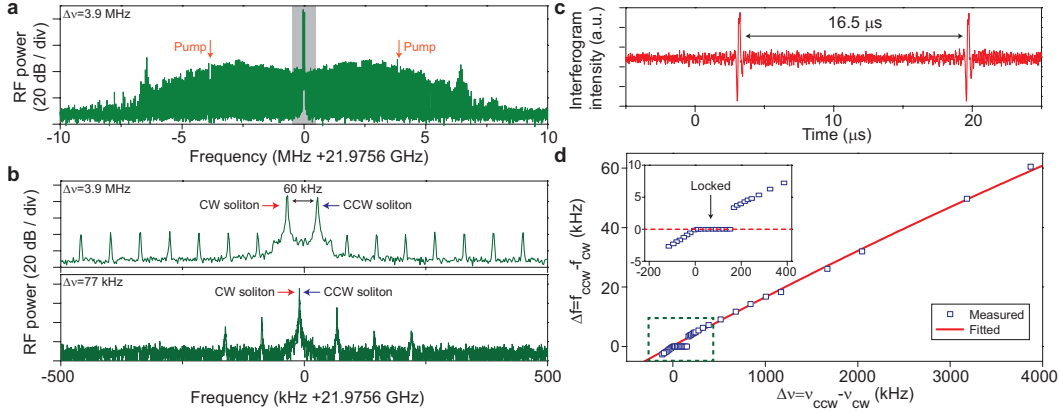


Figure 9.2: Counter-propagating solitons with independently tuned repetition rates. (a) Electrical spectrum of photo-detected CW and CCW soliton pulse streams with pump frequency difference $\Delta\nu = 3.9$ MHz. Strong central peaks give the repetition rate of each soliton. The weaker spectral lines occurring over a broader spectral range are inter-soliton beat frequencies. Beat frequencies produced by the pump line of one soliton beating with higher and lower frequency comb teeth that neighbor the pump line of the other soliton are indicated by arrows. These spectral lines are shifted by $\Delta\nu = \pm 3.9$ MHz relative to the two, strong repetition-rate lines. (b) Upper trace is gray-banded region from (a). The pair of strong central peaks give the CW and CCW soliton repetition rates. Lower trace is the same electrical spectrum when the soliton repetition rates have locked to the same frequency (pump frequencies differ by $\Delta\nu = 77$ kHz). (c) Temporal interferogram of the baseband inter-soliton beat signal under unlocked condition in (a). (d) Plot of the difference in CW and CCW repetition rates versus difference in pump frequencies. The red line is a fit using the model in the Methods section. The inset shows that the two soliton repetition rates are locked over approximately 150 kHz pump difference frequency range.

where τ_R is the Raman shock time, κ is the cavity decay rate, D_1 (D_2) is the free-spectral-range (second-order dispersion) at mode $\mu = 0$ (the pumping mode). The soliton repetition rate, f , is coupled to the SSFS as

$$2\pi f = D_1 + \frac{\Omega_R D_2}{D_1}. \quad (9.2)$$

Therefore the difference in the repetition rates (interferogram rate) between counter-propagating solitons with cavity-pump detuning $\delta\omega_{\text{CW}}$ and $\delta\omega_{\text{CCW}}$ is given by

$$\begin{aligned} f_{\text{CCW}} - f_{\text{CW}} &= -\frac{16D_1\tau_R}{15\pi\kappa}(\delta\omega_{\text{CCW}}^2 - \delta\omega_{\text{CW}}^2) \\ &= -\frac{16D_1\tau_R}{15\pi\kappa}(\Delta\omega^2 - 2\delta\omega_{\text{CW}}\Delta\omega). \end{aligned} \quad (9.3)$$

The second form of this equation uses $\Delta\omega = \omega_{\text{CCW}} - \omega_{\text{CW}} = 2\pi\Delta\nu$ and is applied for the theoretical plot in Figure 9.2(d).

To measure tuning control of the CW and CCW soliton repetition rates, their pulse streams are combined and simultaneously photodetected. The electrical spectrum of the photocurrent is shown in Figure 9.2(a) when the difference in pumping frequencies is set to $\Delta\nu \equiv (\omega_{\text{ccw}} - \omega_{\text{cw}})/2\pi = 3.9$ MHz and $\delta\omega_{\text{cw}}/2\pi \sim 20$ MHz. A zoom-in of the spectrum in Figure 9.2(a) is provided in the upper panel of Figure 9.2(b). The zoom-in shows two strong central spectral peaks that differ by 60 kHz. These peaks give the fundamental repetition rates associated with the CW and CCW soliton streams. The weaker, non-central beats appearing in Figure 9.2(a) and in the upper panel of Figure 9.2(b) are inter-soliton beat frequencies between comb teeth belonging to different soliton combs. These beat frequencies are equally separated by the difference in the repetition rates (60 kHz). As an aside, the maxima at the extreme wings of the spectrum in Figure 9.2(a) are caused by the mode crossing distortion in the comb spectra seen in Figure 9.1(c) near 1542 nm. An interferogram showing the electrical time trace of the co-detected dual-soliton pulse streams is shown in Figure 9.2(c). This time trace can be understood as a stroboscopic interference of the respective soliton pulses on the detector. The strobing occurs at the rate difference ($\Delta f \equiv (f_{\text{ccw}} - f_{\text{cw}})$) of the two soliton streams giving the repetitive signal a period of $16.5 \mu\text{s}$. By varying the pump detuning, $\Delta\nu$, it is possible to observe tuning of the repetition rate difference, Δf , as shown in Figure 9.2(d). A theoretical fit is provided in the figure.

Locking of soliton repetition rates

Near $\Delta\nu = 0$ in Figure 9.2(d), locking of the repetition rates is observed over a range of $\Delta\nu$ around 150 kHz. The associated electrical zoom-in spectrum under this locked condition is shown in the lower panel of Figure 9.2(b). Importantly, nearly all of the weaker peaks that appear in the unlocked spectrum shown in Figure 9.2(a) disappear as a result of locking. This can be understood to result from the high relative temporal stability of the two pulse streams. In particular, under the locking condition, inter-soliton pulse mixing on the photo-detector, which is guaranteed under conditions of unequal repetition rates, now requires strict spatial-temporal alignment of the two pulse streams at the detector. Consistent with this physical picture, the interferogram trace is observed to show no periodic strobing behavior. This locking behavior is believed to occur through backscattering of pump light, which can induce four-wave mixing on the soliton comb teeth and subsequently induce locking. As an aside, the weak sidebands in the lower panel of Figure 9.2(b) are believed to result from pump light from one direction interfering on the detector

with comb teeth of the soliton from the opposing direction.

Below the theoretical description of soliton repetition rate locking to an identical rate is discussed. For example, consider taper backscattering of the clockwise (CW) pump. The backscattered pump light propagates with the counter-clockwise (CCW) soliton in the resonator. The CCW soliton and the backscattered CW pump experience four-wave-mixing that creates sidebands on the CCW soliton. These sidebands lie at frequencies which are very close to the CW soliton. Backscatter coupling of these sidebands (and similar sidebands produced by taper backscattering of the CCW pump) causes the soliton repetition rates to lock through injection locking. This process is described schematically in Figure 9.3(a).

Such a dual-pumped microresonator with backscattering can be described by

$$\begin{aligned} \frac{\partial A(\phi, t)}{\partial t} = & -\left(\frac{\kappa}{2} + i\delta\omega_A\right)A + i\frac{D_2}{2}\frac{\partial^2 A}{\partial \phi^2} + F_A + \sqrt{\alpha}F_B e^{i\Delta\omega t} \\ & + igA(\phi, t) \int_0^\infty R(\phi'/D_1)|A(t, \phi + \phi')|^2 d\phi'/D_1, \end{aligned} \quad (9.4)$$

where F_A (F_B) is the pump field for the soliton described by amplitude A (B), α denotes the taper back-reflection portion of the pump power, κ is the decay rate of the soliton field, $\delta\omega_A$ is the frequency detuning of the pump field relative to the cavity mode being pumped, and D_2 is the second order dispersion. The last term includes both the Kerr and Raman nonlinearity [89, 128]. The nonlinear response term $R(t)$ has the form [128]

$$R(t) = (1 - f_R)\delta(t) + f_R h_R(t), \quad (9.5)$$

where the delay in electrical response is ignored and $h_R(t)$ accounts for the Raman response. The Raman fraction for silica ($f_R = 0.18$) is assumed.

By expanding the intracavity field at two pump frequencies as $A = A_p + A_b e^{i\Delta\omega t}$ where A_p is the amplitude for the existing soliton and A_b is the field that forms in response to the backscattered pump field, we can derive the following coupled amplitude equations [89, 128]

$$\begin{aligned} \frac{\partial A_p(\phi, t)}{\partial t} = & -\left(\frac{\kappa}{2} + i\delta\omega_A\right)A_p + i\frac{D_2}{2}\frac{\partial^2 A_p}{\partial \phi^2} + F_A + ig[|A_p|^2 + (2 - f_R)|A_b|^2]A_p \\ & + ig\tau_R D_1 A_p \frac{\partial(|A_p|^2 + |A_b|^2)}{\partial \phi}, \end{aligned} \quad (9.6)$$

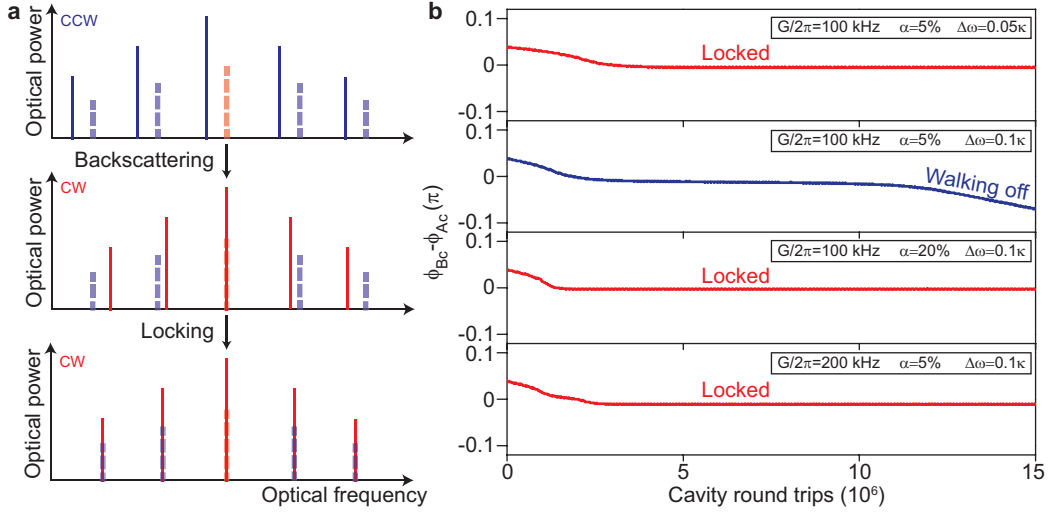


Figure 9.3: Mechanism of CP soliton synchronization. (a) Rate locking occurs when the repetition rates of A_p and B_p are injection-locked by the backscattering of B_b and A_b , respectively. The upper panel shows four-wave-mixing sidebands (dashed blue lines) on the comb teeth of the CCW soliton (solid blue lines). These are created by taper backscattering of the CW pump. These sidebands are subsequently backscattered within the resonator into the CW direction (middle panel), where they (and their CW counter-parts) induce injection locking of the CW and CCW solitons (lower panel). (b) Simulation of CP soliton repetition rate locking. ϕ_{Ac} and ϕ_{Bc} are the peak position of solitons in CW and CCW rotation frames, respectively. See text for discussion of four panels.

$$\begin{aligned} \frac{\partial A_b(\phi, t)}{\partial t} = & -\left(\frac{\kappa}{2} + i\delta\omega_B\right)A_b + i\frac{D_2}{2}\frac{\partial^2 A_b}{\partial \phi^2} + \sqrt{\alpha}F_B + ig[|A_b|^2 + (2 - f_R)|A_p|^2]A_b \\ & + ig\tau_R D_1 A_b \frac{\partial(|A_p|^2 + |A_b|^2)}{\partial \phi}, \end{aligned} \quad (9.7)$$

where the Raman gain between the two fields has been ignored as $\Delta\omega$ is much smaller than the material's Raman shift. $\tau_R \sim 2.4$ fs is the Raman shock time in silica [88, 89, 128].

As $\alpha \ll 1$, we assume that the backscattered field is a perturbation to the existing soliton field ($|A_b| \ll |A_p|$). The existing soliton therefore maintains propagation as a soliton. Next, the intracavity backscattering is added by including coupling from the existing soliton propagating in the opposing direction. The amplitude of this soliton is denoted by B_p and its weak pump backscattering component is denoted

by B_b such that $B = B_p + B_b e^{-i\Delta\omega t}$. The complete coupled equations are given by,

$$\begin{aligned} \frac{\partial A_p(\phi, t)}{\partial t} = & -\left(\frac{\kappa}{2} + i\delta\omega_A\right)A_p + i\frac{D_2}{2}\frac{\partial^2 A_p}{\partial\phi^2} + F_A + ig[|A_p|^2 + (2 - f_R)|A_b|^2]A_p \\ & + ig\tau_R D_1 A_p \frac{\partial(|A_p|^2 + |A_b|^2)}{\partial\phi} + iGB_b, \end{aligned} \quad (9.8)$$

$$\begin{aligned} \frac{\partial A_b(\phi, t)}{\partial t} = & -\left(\frac{\kappa}{2} + i\delta\omega_B\right)A_b + i\frac{D_2}{2}\frac{\partial^2 A_b}{\partial\phi^2} + \sqrt{\alpha}F_B + ig[|A_b|^2 + (2 - f_R)|A_p|^2]A_b \\ & + ig\tau_R D_1 A_b \frac{\partial(|A_p|^2 + |A_b|^2)}{\partial\phi} + iGB_p. \end{aligned} \quad (9.9)$$

$$\begin{aligned} \frac{\partial B_p(\phi, t)}{\partial t} = & -\left(\frac{\kappa}{2} + i\delta\omega_B\right)B_p + i\frac{D_2}{2}\frac{\partial^2 B_p}{\partial\phi^2} + F_B + ig[|B_p|^2 + (2 - f_R)|B_b|^2]B_p \\ & + ig\tau_R D_1 B_p \frac{\partial(|B_p|^2 + |B_b|^2)}{\partial\phi} + iG^* A_b, \end{aligned} \quad (9.10)$$

$$\begin{aligned} \frac{\partial B_b(\phi, t)}{\partial t} = & -\left(\frac{\kappa}{2} + i\delta\omega_A\right)B_b + i\frac{D_2}{2}\frac{\partial^2 B_b}{\partial\phi^2} + \sqrt{\alpha}F_A + ig[|B_b|^2 + (2 - f_R)|B_p|^2]B_b \\ & + ig\tau_R D_1 B_b \frac{\partial(|B_p|^2 + |B_b|^2)}{\partial\phi} + iG^* A_p, \end{aligned} \quad (9.11)$$

where, for simplicity, only a single scatterer is assumed in the cavity so that $\Gamma(\theta) = G\delta(\theta)$.

Figure 9.3(b) numerically studies locking of the CP soliton repetition rates by solution of the above coupled soliton equations. By plotting the time evolution of the difference in the CP solitons' peak position ($\phi_{Ac} - \phi_{Bc}$) within their own moving frames, we can extract their repetition rate difference from the slope of the curves. The upper panel in Figure 9.3(b) shows how the solitons rate lock after a few cavity round trips. Backscatter coupling values (internal and taper) are indicated, as is the pump detuning, in normalized units. In the second panel, the pump detuning is increased and this leads to unlocking. However, in the third and fourth panels locking is again restored by either increasing the taper coupling or the backscatter coupling.

9.3 Phase-locking of counter-propagating solitons

Measurement

In addition to locking at identical repetition rates (degenerate locking), the soliton pulse streams are also observed to lock when their repetition rates are different. Fig. 9.4(a) illustrates the principle of this locking mechanism. Therein, hypothetical soliton spectra for CW and CCW directions are presented. A zoom-in of the higher frequency portion of the spectra is shown in which the respective soliton spectral lines are superimposed next to shaded areas representing the cavity resonances. The mode index $\mu = 0$, which is by convention the optical pump, is also indicated. As required for DKS generation, this pump frequency and the other soliton comb teeth are red-detuned in frequency relative to their respective cavity resonances. At $\mu = 0$, the two pump lines are separated by the pump frequency difference, $\Delta\nu$. Under conditions where these pump frequencies are well separated so that degenerate rate locking does not occur (see Figure 9.2(d)), the soliton having the more strongly red-detuned pump will feature a slightly lower repetition rate on account of the self-Raman-effect discussed previously. Accordingly, the CW and CCW comb teeth will shift in frequency so as to become more closely spaced as μ decreases. For a certain negative value of μ the CW and CCW comb teeth will achieve closest spectral separation. In the illustration, this occurs at comb tooth $\mu = r$ where CW and CCW comb teeth have frequency separation $\delta = \Delta\nu + r\Delta f$. Backscattering within the resonator will couple power between these nearly resonant lines. This power coupling is shown later to induce locking of the solitons such that $\delta = 0$. Accordingly, the following relationship holds,

$$\Delta f = -\Delta\nu/r. \quad (9.12)$$

This result shows that pulse rates have a relative stability completely determined by the radio frequency signal used to set the pump frequency offset, $\Delta\nu$. As a result, the beat signal between the CCW and CW solitons exhibits very high stability when the system is locked in this way. The above relation also shows that the locked CP solitons play the role of a frequency divider of the pump frequency difference into the pulse-rate difference frequency, Δf . The phase noise of the rate difference is therefore r^2 lower than the phase noise of the relative pump signal,

$$S_{\Delta f} = \frac{1}{r^2} S_{\Delta\nu}, \quad (9.13)$$

where $S_{\Delta f}$ and $S_{\Delta\nu}$ are the phase noise spectral density functions of the inter-soliton fundamental beat signal and the pump difference signal.

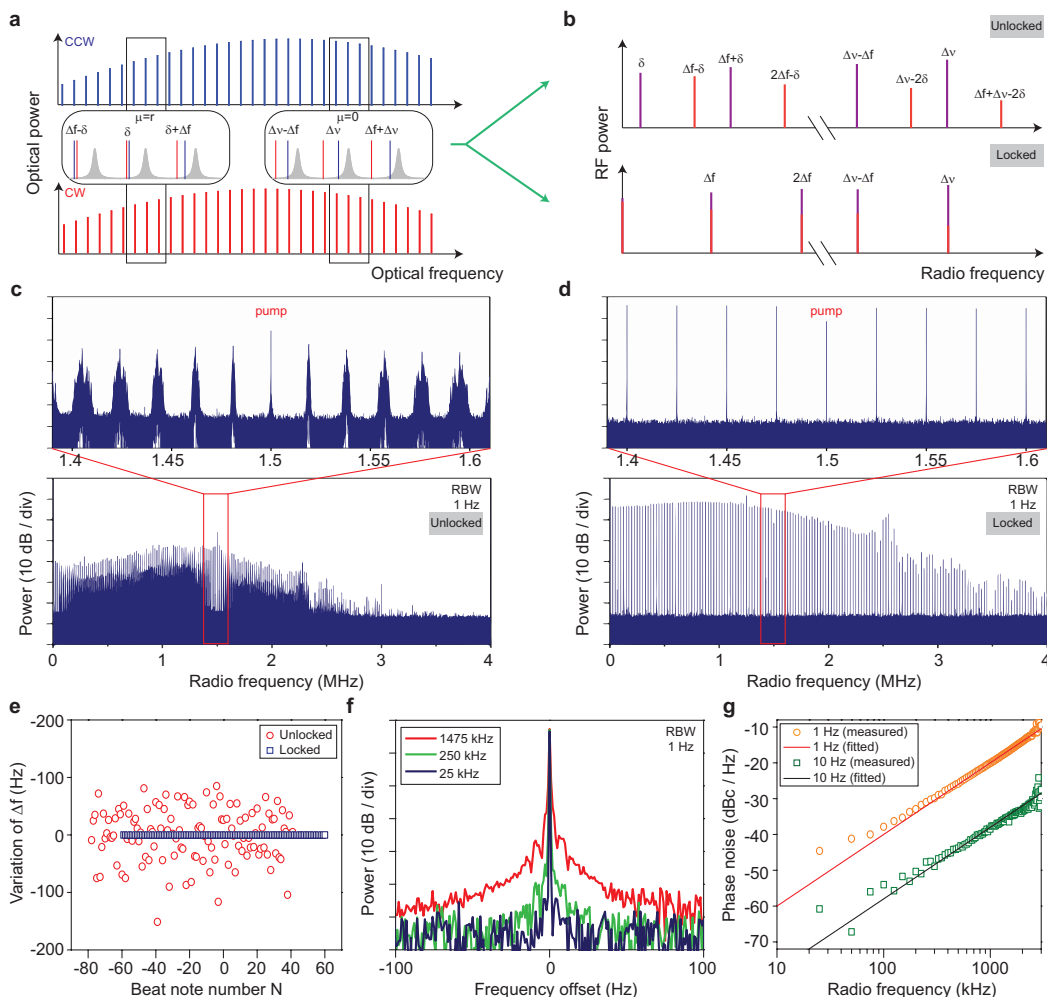


Figure 9.4: Counter-propagating soliton phase locking at different repetition rates. (a) Schematic view of the counter-propagating soliton comb teeth. $\Delta\nu$ and Δf denote the pump frequency and repetition rate differences, respectively, and μ is mode number relative to the pump mode ($\mu = 0$). (b) Illustration of inter-soliton radio-frequency (RF) beatnotes produced under locked and unlocked conditions. (c) Measured RF beatnotes of unlocked CP solitons ($\Delta\nu = 1.5$ MHz). (d) Measured RF beatnotes of locked CP solitons ($\Delta\nu = 1.5$ MHz, $\Delta f = 25$ kHz). (e) Measured beat-note frequency spacing for locked and unlocked conditions plotted versus beatnote number. (f) High-resolution, zoom-in spectrum of RF beatnotes in (c). The corresponding beat note frequency is provided in the legend (25kHz is the fundamental beat note frequency). (g) Phase noise of the beatnotes at 1 Hz and 10 Hz offset frequencies in the phase noise spectrum plotted versus beatnote frequency. The fitting lines have an f^2 dependence.

Figure 9.4(b) illustrates the effect of the locking condition on the electrical spectrum produced by photodetection of combined CCW and CW soliton streams. Under

unlocked conditions, the electrical spectrum will feature two distinct spectra with spacing Δf . However, under locked conditions the difference in the frequency of the comb teeth at $\mu = 0$ (i.e., optical pumps) is an integer multiple of the difference in the repetition rates. As result, the two electrical spectra merge to form a single spectrum.

Figure 9.4(c) shows a typical measured RF spectrum in the unlocked state. It is obtained by Fourier transforming the photodetected interferogram recorded over 1s. Here, the beat between the CCW and CW comb teeth corresponding to the pumps is indicated and is very stable. However, all other spectral lines are noisier. This noise results from fluctuations of the absolute pump frequencies which in turn induce fluctuations in the CW and CCW soliton repetition rates [84]. The resulting frequency noise is multiplied with each comb tooth index relative to the pump comb tooth. As an aside, the high stability of the pump line in Figure 9.4(c) confirms the relative optical coherence of the solitons as a result of pumping from a common laser source.

In contrast to the unlocked case, the RF spectrum in the locked state (Figure 9.4(d)) is a set of narrow, spectral lines with a 50 dB signal-to-noise ratio (SNR) at the 1 Hz resolution bandwidth (RBW). In this measurement, $\Delta\nu$ is set to be 1.5 MHz which is 60 times $\Delta f = 25$ kHz. To illustrate the stability improvement that results from locking Figure 9.4(e) plots the average frequency spacing between neighboring RF comb teeth in Figure 9.4(c) and Figure 9.4(d) versus beat note number (relative to the pump). Locking results in a collapse to a sub-Hz stability. To test the frequency division model noted above three inter-soliton beatnotes are shown in Figure 9.4(f). The fundamental beatnote (difference in repetition rates) has the narrowest linewidth while beatnotes at increasing multiples of 25 kHz are wider. A more quantitative illustration of frequency division on noise is provided in Figure 9.4(g) where the phase noise of intersoliton beats is plotted versus the beatnote frequency at phase noise spectra offsets of 1 Hz and 10 Hz. The quadratic scaling predicted in Eq. (9.13) is apparent in the plots (solid lines). It is noted that the inferred linewidth for the lowest order beatnote is 40 μ Hz (assuming that it is limited by white frequency noise).

It is important to note that stability improvement in both the interferogram and its Fourier transform (i.e., Figure 9.4(d)) are directly transferrable to improved sensitivity of dual comb spectroscopy and dual comb LIDAR systems. For example, the spectrum shown in Figure 9.4(d) would carry the absorption spectra information in

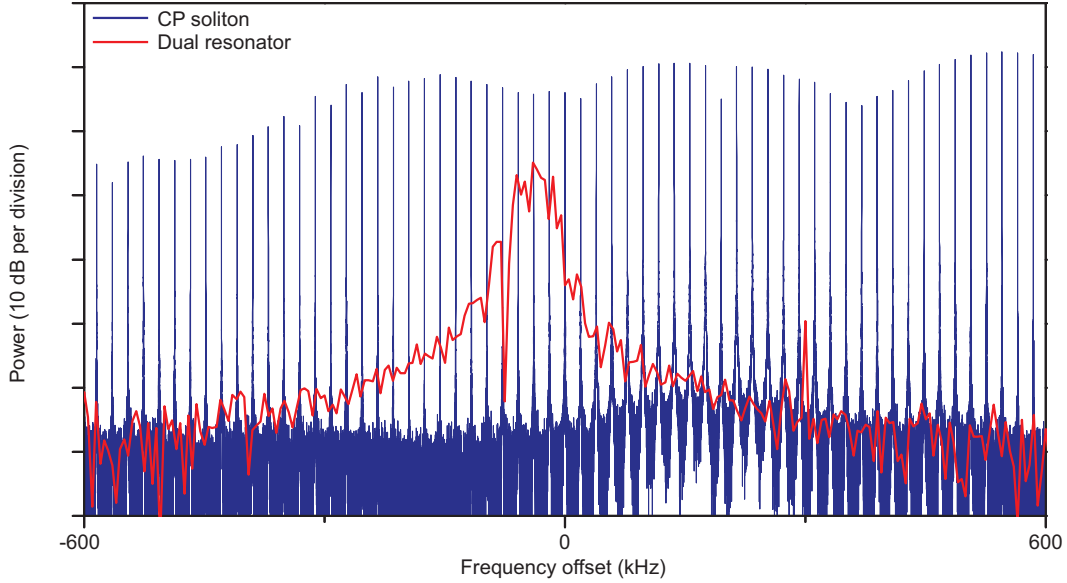


Figure 9.5: Zoom-in of RF spectra showing dual soliton beatnotes. The blue trace denotes the CP solitons with integration time 50 ms. The red trace represents the results from solitons generated in two distinct microresonators with integration time 200 μ s.

a dual comb spectroscopy measurement. Typically, distinct locked frequency combs would be used to generate this spectrum. In the present case, the two combs are provided by a single resonator and locking occurs through the counter-propagating soliton interaction. The resulting improvement in interferogram stability relative to prior microcomb dual-comb spectroscopy results [105] is provided in Figure 9.5. The soliton locking is possible over a set of repetition rates subject to the constraint imposed by coupling of respective r^{th} comb teeth as detailed here.

Theory

Below the locking of CP solitons at different repetition rates is modeled. We start with the Lugiato-Lefever equation augmented by the Raman term [87, 88, 127]. The presence of scattering centers can induce coupling between the CP solitons as follows:

$$\begin{aligned} \frac{\partial A(\phi, t)}{\partial t} = & -\left(\frac{\kappa}{2} + i\delta\omega_A\right)A + i\frac{D_2}{2}\frac{\partial^2 A}{\partial \phi^2} + F_A + ig|A|^2A \\ & + ig\tau_R D_1 A \frac{\partial |A|^2}{\partial \phi} + i \int_0^{2\pi} \Gamma(\theta)B(\phi - 2\theta, t)e^{-i\Delta\omega t}d\theta. \end{aligned} \quad (9.14)$$

$$\begin{aligned} \frac{\partial B(\phi, t)}{\partial t} = & -\left(\frac{\kappa}{2} + i\delta\omega_B\right)B + i\frac{D_2}{2}\frac{\partial^2 B}{\partial\phi^2} + F_B + ig|B|^2B \\ & + ig\tau_R D_1 B \frac{\partial|B|^2}{\partial\phi} + i\int_0^{2\pi} \Gamma^*(\theta)A(\phi + 2\theta, t)e^{i\Delta\omega t}d\theta \end{aligned} \quad (9.15)$$

Here A and B denote the slowly varying field envelopes of the CW and CCW solitons, respectively. ϕ is the angular coordinate in the rotational frame [66]. g is the normalized Kerr nonlinear coefficient [66, 88], F_A (F_B) denotes the normalized continuous-wave pump term for field A (B) and $\Gamma(\theta)$ represents the backscattering coefficient in the lab frame θ .

Considering the spectral misalignment of CP soliton comb teeth presented in Figure 9.4(a), it is assumed that only the r -th comb teeth will induce inter-soliton coupling. Accordingly, the equation of motion for the soliton field amplitude A , Eq. (9.14), is reduced to the following:

$$\begin{aligned} \frac{\partial A(\phi, t)}{\partial t} = & -\left(\frac{\kappa}{2} + i\delta\omega_A\right)A + i\frac{D_2}{2}\frac{\partial^2 A}{\partial\phi^2} + F + ig|A|^2A \\ & + ig\tau_R D_1 A \frac{\partial|A|^2}{\partial\phi} + iGb_r e^{ir\phi}, \end{aligned} \quad (9.16)$$

where the expansion $B(\phi, t)e^{i\Delta\omega t} = \sum_{\mu} b_{\mu}e^{i\mu\phi}$ is used to extract the r -th comb tooth from soliton field B . A similar equation of motion to Eq. (9.16) holds for the amplitude B (with corresponding expansion $A(\phi, t) = \sum_{\mu} a_{\mu}e^{i\mu\phi}$). The coupling coefficient $G = \int \Gamma(\theta) \exp(-2ir\theta)d\theta$.

The soliton field amplitude in the presence of the soliton self-frequency shift can be expressed as [88, 133]

$$A = B_s \text{sech}[(\phi - \phi_{Ac})/D_1\tau_s]e^{i\mu_A(\phi - \phi_{Ac}) + i\psi_A}, \quad (9.17)$$

where B_s and τ_s are the pulse amplitude and duration, respectively. μ_A is the mode number of the soliton spectral maximum ($\mu = 0$ is the mode number of the pump mode). This mode number is related to the soliton self-frequency shift by $\Omega_R = \mu_A D_1$. ψ_A is a constant phase determined by the pump [66, 88]. ϕ_{Ac} is the peak position of the CW soliton, which is coupled to μ_A by [88]

$$\frac{\partial\phi_{Ac}}{\partial t} = \mu_A D_2. \quad (9.18)$$

The soliton energy E_A and the spectral maximum mode number μ_A are given by

$$E_A = \sum_{\mu} |a_{\mu}|^2 = \frac{1}{2\pi} \int_{-\pi}^{+\pi} |A|^2 d\phi = B_s^2 \tau_s D_1 / \pi \quad (9.19)$$

$$\mu_A = \frac{\sum_{\mu} \mu |a_{\mu}|^2}{E_A} = \frac{-i}{4\pi E_A} \int_{-\pi}^{+\pi} (A^* \frac{\partial A}{\partial \phi} - A \frac{\partial A^*}{\partial \phi}) d\phi. \quad (9.20)$$

Taking the time derivative of Eq. (9.20) and substituting $\partial A/\partial t$ using Eq. (9.16), the equation of motion for μ_A is obtained as

$$\begin{aligned} \frac{\partial \mu_A}{\partial t} = & -\kappa \mu_A - \frac{g\tau_R D_1}{2\pi E_A} \int_{-\pi}^{+\pi} (\frac{\partial |A|^2}{\partial \phi})^2 d\phi \\ & - \frac{1}{2\pi E_A} \int_{-\pi}^{+\pi} (G^* b_r^* e^{-ir\phi} \frac{\partial A}{\partial \phi} - irGA^* b_r e^{ir\phi}) d\phi. \end{aligned} \quad (9.21)$$

The second term on the right-hand-side corresponds to the steady-state Raman-induced center shift [87, 88] and is denoted by κR_A . The third term is the soliton spectral shift caused by coupling to the opposing CP soliton through its comb tooth b_r . By using $A = \sum_{\mu} a_{\mu} e^{i\mu\phi}$, Eq. (9.21) yields

$$\begin{aligned} \frac{\partial \mu_A}{\partial t} = & -\kappa \mu_A + \kappa R_A - \frac{ir}{E_A} (a_r b_r^* G^* - \text{c.c.}) \\ = & -\kappa \mu_A + \kappa R_A + \frac{2r}{E_A} |a_r b_r G| \sin \Theta, \end{aligned} \quad (9.22)$$

where $\Theta = (\psi_{rA} - \psi_{rB} - \psi_G)$ with the phases, ψ_{rA} and ψ_{rB} , of the comb teeth a_r and b_r given by the following expression,

$$\psi_{rA} = \psi_A - r\phi_{Ac}. \quad (9.23)$$

$$\psi_{rB} = \psi_B - r\phi_{Bc} + \Delta\omega t. \quad (9.24)$$

Also, Ψ_G is the phase of the backscatter coefficient G . The time dependence of ψ_{rA} can be derived from Eq. (9.18) as

$$\frac{\partial \psi_{rA}}{\partial t} = -r \frac{\partial \phi_{Ac}}{\partial t} = -r\mu_A D_2. \quad (9.25)$$

Similarly, the derivative of the phase of b_r is given by

$$\frac{\partial \psi_{rB}}{\partial t} = -r\mu_B D_2 + \Delta\omega. \quad (9.26)$$

Therefore the time derivative of the phase term $\Theta = (\psi_{rA} - \psi_{rB} - \psi_G)$ is given by

$$\frac{\partial \Theta}{\partial t} = \Delta\omega + rD_2(\mu_B - \mu_A) = 2\pi(\Delta\nu + r\Delta f) = 2\pi\delta. \quad (9.27)$$

Similar to Eq. (9.22), a parallel equation exists for the soliton B and is given by

$$\frac{\partial \mu_B}{\partial t} = -\kappa \mu_B + \kappa R_B - \frac{2r}{E_B} |a_r b_r G| \sin \Theta. \quad (9.28)$$

Taking a time derivative of Eq. (9.27) and using Eq. (9.22) and Eq. (9.28) gives the following equation of motion for the relative phase Θ ,

$$\frac{\partial^2 \Theta}{\partial t^2} + \kappa \frac{\partial \Theta}{\partial t} = -2r^2 D_2 \left(\frac{1}{E_A} + \frac{1}{E_B} \right) |a_r b_r G| \sin \Theta + 2\pi \kappa \delta', \quad (9.29)$$

where $2\pi\delta' = \Delta\omega + rD_2(R_B - R_A)$ is the frequency difference between the r th comb teeth induced by the shifted pumps and Raman SSFS when the CP solitons have no interaction. The above equation is similar to the Alder equation of injection locking [223], only with an additional second order time-derivative term. Setting the time derivatives of Θ equal to zero gives the locking bandwidth, ω_L , of δ' as

$$\omega_L = 4\pi |\delta'_{\max}| = \frac{4r^2 D_2}{\kappa} \left(\frac{1}{E_A} + \frac{1}{E_B} \right) |a_r b_r G|. \quad (9.30)$$

Moreover, Eq. (9.27) gives $\delta = 0$ so that the pump frequency difference $\Delta\nu$ is divided by Eq. (9.12).

In the measurement, the loss rate is $\kappa/2\pi = 1.5$ MHz. $D_2/2\pi = 16$ kHz and $r = -60$. For a soliton with $\tau_s = 150$ fs, the mode number of the Raman SSFS is $\mu_R \sim -20$ and the ratio $|a_r|^2/E_A = D_1 \tau_s \text{sech}^2[\pi(r - \mu_R)D_1 \tau_s/2]/8 \sim 7 \times 10^{-4}$. As the CP solitons have similar powers, the locking bandwidth is estimated as $\omega_L \sim |G|/4$. In this case a backscattering rate of 4 kHz can provide a 1 kHz locking bandwidth.

9.4 Conclusion

In summary, counter-propagating solitons have been demonstrated in a high-Q optical microresonator. Both the relative repetition rates and the relative spectral location for the clockwise and counter-clockwise directions are independently tuned by tuning of the corresponding optical pumping frequencies. Two distinctly different locking phenomena have also been observed. In the first, the repetition rates lock to the same value. The pumping frequencies are different when this locking occurs so that the two soliton comb spectra are offset slightly in the optical frequency, but have identical comb tooth spacing. The interferogram of the two pulse trains has no baseband time dependence when this locking occurs. In the second form of locking, the pumps are typically tuned apart to larger difference frequencies and the solitons are observed to lock at different repetition rates with a difference that divides into the pump-frequency difference. The origin of this locking is associated with optical locking of two comb teeth, one from each soliton. Since the two pumps are derived from the same laser, this additional comb tooth locking effectively results in the two comb spectra being locked at two different positions in their spectra.

The resulting high level of mutual soliton coherence is observable in the baseband inter-soliton beat spectra which features very narrow spectral lines spaced by the difference in the locked soliton repetition rates. In effect, this second form of locking creates two frequency combs in the same device with distinct repetition rates and optical frequencies, but that are optically locked. It is potentially useful in dual comb spectroscopy and dual comb LIDAR applications [111] where it would obviate the need for two separate frequency combs and the associated inter-comb locking hardware. In the next chapter, its application as a Vernier spectrometer will be discussed [109]. Finally, it is noted that while single clockwise and counter-clockwise solitons have been generated, it is also possible to create states containing multiple solitons.

VERNIER SPECTROMETER USING COUNTERPROPAGATING SOLITON MICROCOMBS

¹Frequency-agile lasers are ubiquitous in sensing, spectroscopy and optical communications [224–226] and measurement of their optical frequency for tuning and control is traditionally performed by grating and interferometer-based spectrometers, but more recently these measurements can make use of optical frequency combs[43]. Frequency combs provide a remarkably stable measurement grid against which optical signal frequencies can be determined subject to the ambiguity introduced by the equally spaced comb teeth. The ambiguity is resolved for continuously frequency swept signals by counting comb teeth [154] relative to a known comb tooth, and this method has enabled measurement of remarkably high chirp rates [227]. However, many signal sources will experience intentional or unintentional frequency jumps. Here, the ambiguity can be resolved using a second frequency comb that has a different comb tooth spacing so as to provide a frequency Vernier scale for comparison with the first comb [36, 228, 229]. This Vernier concept is also used in dual comb spectroscopy[105, 211], but in measuring active signals the method can be enhanced to more directly (and hence quickly) identify signal frequencies through a signal correlation technique [36]. Moreover, continuous as opposed to discretely sampled frequencies are measured in the active approach. The power of the Vernier-based method relies upon mapping of optical comb frequencies into a radio-frequency grid of frequencies, the precision of which is set by the relative line-by-line frequency stability of the two frequency combs. This stability can be guaranteed by self-referencing each comb using a common high-stability radio-frequency source or through optical locking of each comb to reference lasers whose relative stability is ensured by mutual locking to a common optical cavity.

In this chapter, we show that a single microresonator provides rapid and broad-band measurement of optical frequencies with a relative frequency precision comparable to conventional dual frequency comb systems. Dual-locked counter-propagating (CP) solitons having slightly different repetition rates are used to implement a Vernier spectrometer. Laser tuning rates as high as 10 THz/s, broadly step-tuned

¹Work presented in this chapter has been published in “Vernier spectrometer using counterpropagating soliton microcombs”, *Science* 363, 965-968 (2019).

lasers, multi-line laser spectra and also molecular absorption lines are characterized using the device. Besides providing a considerable technical simplification through the dual-locked solitons and enhanced capability for measurement of arbitrarily tuned sources, our results reveal possibilities for chip-scale spectrometers that exceed the performance of table-top grating and interferometer-based devices.

10.1 Concept of Vernier spectrometer and measurement of static lasers

We demonstrate a broad-band, high-resolution Vernier microresonator soliton spectrometer (MSS) using a single miniature comb device that generates two mutually phase-locked combs. The principle of operation relies upon an optical phase locking effect observed in the generation of counter-propagating solitons within high- Q whispering gallery resonators [99]. Soliton generation in microresonators is being studied for miniaturization to the chip-scale of complete comb systems and these soliton microcombs have now been demonstrated in a wide range of microresonator systems [70]. It has been shown that counter-propagating solitons can have distinct, controllable repetition rates and that their underlying comb spectra can be readily phase locked at two spectral points [99]. This mutual double-locking creates line-by-line relative frequency stability for the underlying microcomb spectra that is more characteristic of fully self-referenced dual comb systems. The resulting Vernier of comb frequencies in the optical domain maps to an exceptionally stable radio frequency grid for implementation of the spectrometer.

Phase-locked CP solitons

The spectral relationship of the doubled-locked cw and ccw solitons reveals the inherent optical frequency Vernier (Figure 10.1(A)). A single laser source is modulated (Figure 10.1(B)) to produce the two mutually-coherent pump lines at order $\mu = N$ with frequency separation $\Delta\nu$ (MHz range). The distinct pump frequencies cause the soliton repetition rates to differ by Δf_r as a result of the Raman self-frequency-shift [87, 88, 90, 99, 166]. As detailed elsewhere, the cw and ccw combs will experience frequency locking (induced by optical backscattering) at order $\mu = 0$ for certain pumping frequencies [99]. This locking requires that $\Delta\nu = N\Delta f_r$. Also, because the two pump frequencies are derived from radio-frequency modulation of a single laser source, they have a high relative frequency stability ($\Delta\nu$ is very stable) and are effectively locked at order $\mu = N$. This double locking sets up a stable Vernier in the respective soliton comb frequencies. The counter-propagating solitons are generated in a high- Q silica microresonator with 3 mm diameter (22

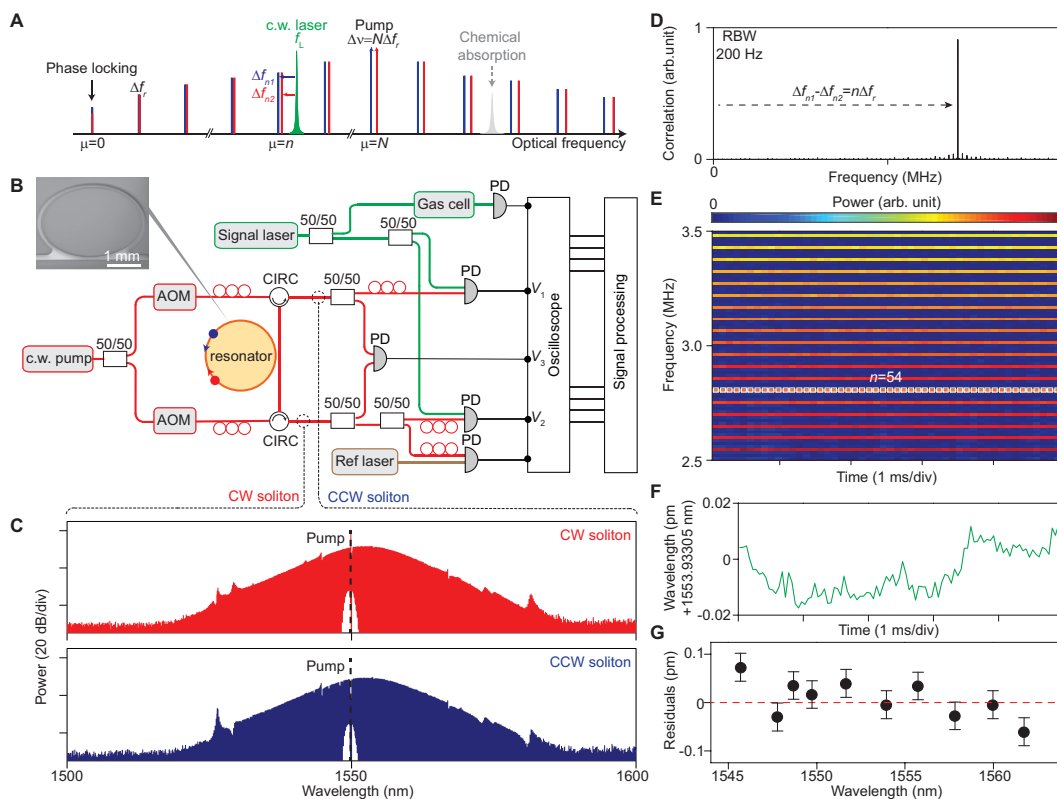


Figure 10.1: Spectrometer concept, experimental setup and static measurement. (A) Counter propagating soliton frequency combs (red and blue) feature repetition rates that differ by Δf_r , phase-locking at the comb tooth with index $\mu = 0$ and effective locking at $\mu = N$ thereby setting up the Vernier spectrometer. Tunable laser and chemical absorption lines (grey) can be measured with high precision. (B) Experimental setup. AOM: acousto-optic modulator; CIRC: circulator; PD: photodetector. Small red circles are polarization controllers. Inset: scanning electron microscope image of a silica resonator. (C) Optical spectra of counter-propagating solitons. Pumps are filtered and denoted by dashed lines. (D) Typical measured spectrum of $V_1 V_2$ used to determine order n . For this spectrum: $\Delta f_{n1} - \Delta f_{n2} = 2.8052$ MHz and $\Delta f_r = 52$ kHz giving $n = 54$. (E) The spectrograph of the dual soliton interferogram (pseudo color). Line spacing gives $\Delta f_r = 52$ kHz. White squares correspond to the index $n = 54$ in panel C. (F) Measured wavelength of an external cavity diode laser operated in steady state. (G) Residual deviations between ECDL laser frequency measurement as given by the MSS and a wavemeter. Error bars give the systematic uncertainty as limited by the reference laser in panel B.

GHz soliton repetition rate) [55]. Details on the soliton generation process can be found elsewhere [67, 99, 156]. Typical optical spectra of cw and ccw solitons span the telecommunication C-band (Figure 10.1(C)).

Operation principle

The spectrometer operates as follows. A test laser frequency f_L is measured using either of the following expressions: $f_L = n f_{r,2} + \Delta f_{n,2} + f_0$ where n is the comb order nearest to the laser frequency, $f_{r,2}$ are the comb repetition rates, $\Delta f_{n,2}$ are the heterodyne beat frequencies of the test laser with the two frequency comb teeth at order $\mu = n$, and f_0 is the frequency at $\mu = 0$. $f_{r,2}$ and $\Delta f_{n,2}$ are measured by co-detection of the combs and the test laser to produce the electrical signals $V_{1,2}$ in Fig. 1B. Fast Fourier transform (FFT) of $V_1 V_2$ gives the spectral line at $n \Delta f_r$ (Fig. 1D) using the correlation method [36] and in turn the order n . The correlation method can be understood as a calculation of the frequency difference $\Delta f_{n2} - \Delta f_{n1} = n \Delta f_r$ by formation of $V_1 V_2$ followed by fast Fourier transform (FFT). The FFT spectrum of $V_1 V_2$ gives the spectral line at $n \Delta f_r$ (Fig. 1D). To determine n requires $\Delta f_r = f_{r2} - f_{r1}$ which is measured by heterodyne of the solitons to produce electrical signal V_3 . Figure 1E is a narrow frequency span of the FFT of V_3 and shows how the optical frequency Vernier is mapped into a stable radio-frequency grid with line spacing Δf_r . The order corresponding to the FFT of the $V_1 V_2$ signal (Fig. 1D spectrum) is also indicated. These steps are performed automatically to provide a real time measurement of f_L relative to f_0 . f_0 is determined by applying this procedure to the reference laser frequency f_{ref} (stabilized using an internal molecular reference). All of these data inputs are automatically processed in real time to measure f_L .

Measurement of a static laser

As a preliminary test, the frequency of an external-cavity-diode-laser is measured and compared against a wavemeter. Figures 10.1(D) and (E) ($n = 54$) are from this measurement. The real-time measured wavelength of the laser (Figure 10.1(F)) fluctuates within ± 0.02 pm over a 5 ms time interval. The measurement was repeated from 1545 to 1560 nm with residual deviations less than 0.1 pm versus the wavemeter measurement (Figure 10.1(G)). These deviations are believed to be limited by the wavemeter resolution (± 0.1 pm). The systematic uncertainty of absolute wavelength in the current setup is set by the reference laser to around ± 4 MHz (± 0.03 pm).

10.2 Measurement of dynamic lasers and high-resolution spectroscopy

The large, microwave-rate free-spectral range of the MSS enables tracking of lasers undergoing fast-chirping or discontinuous broadband tuning. Although correlation is performed with a time interval $T_W = 1/\Delta f_r$, the instantaneous frequency of

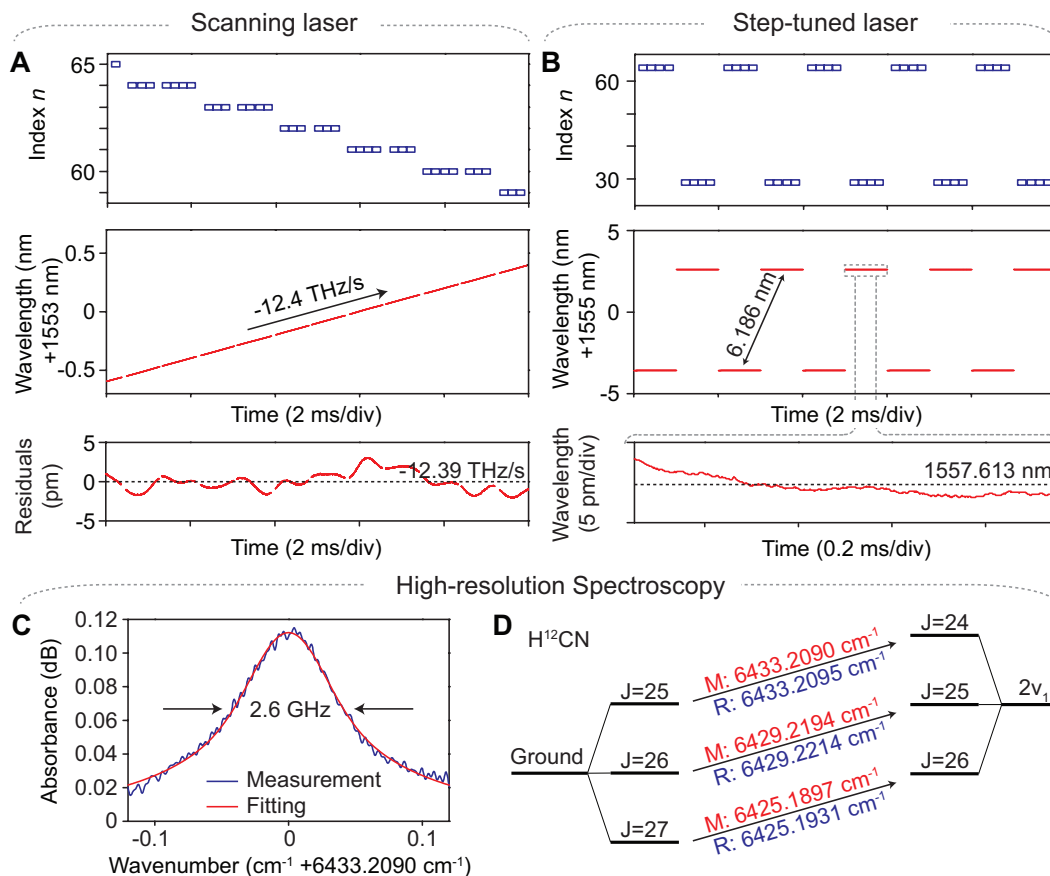


Figure 10.2: Laser tuning and spectroscopy measurements. (A) Measurement of a rapidly tuning laser showing index n (upper), instantaneous frequency (middle), and higher resolution plot of wavelength relative to average linear rate (lower), all plotted versus time. (B) Measurement of a broadband step-tuned laser as for laser in panel A. Lower panel is a zoom-in to illustrate resolution of the measurement. (C) Spectroscopy of $\text{H}^{12}\text{C}^{14}\text{N}$ gas. A vibronic level of $\text{H}^{12}\text{C}^{14}\text{N}$ gas at 5 Torr is resolved using the laser in panel A. (D) Energy level diagram showing transitions between ground state and $2\nu_1$ levels. The measured (reference) transition wavenumbers are noted in red (blue).

the laser relative to the combs can be acquired at a much faster rate set by the desired time-bandwidth-limited resolution. To avoid aliasing of the correlation measurement (i.e., to determine n uniquely), the amount of frequency-chirping should not exceed the repetition rate f_r within the measurement window T_W , which imposes a maximum resolvable chirping-rate of $f_r \times \Delta f_r$. This theoretical limit is 1 PHz/s for the MSS and represents a boost of 100 \times compared with previous Vernier spectrometers [36].

Measurement of rapid continuous-tuning of an external cavity diode laser is shown

in Figure 10.2(A). The correlation measurement evolves as the laser is tuned over multiple FSRs of the comb and thereby determines the index n as a function of time (Figure 10.2(A) upper panel). Measurement of the linear frequency chirp (-12.4 THz/s) as well as the frequency versus time at high resolution (by subtracting the average linear frequency ramp) are shown in the Figure 10.2(A) middle and lower panels, respectively. The discontinuities in the measurement are caused by electrical frequency dividers used to reduce the detected signal frequency for processing by a low-bandwidth oscilloscope. The dividers can be eliminated by using a faster oscilloscope. In Figure 10.2(B) measurement of broadband step tuning (mode hopping) of an integrated-ring-resonator tunable III-V/Silicon laser diode [230] is presented. Fast step tuning between 1551.427 nm and 1557.613 nm every 1 ms with the corresponding index n stepping between $n = 64$ and $n = 29$ is observed. The lower panel in Figure 10.2(B) gives a higher resolution zoom-in of one of the step regions. The data points in these measurements are acquired over $1\ \mu\text{s}$ so the resolution is approximately 1 MHz.

This combination of speed and precision is also useful for spectroscopic measurements of gas-phase chemicals using tunable, single-frequency lasers. To demonstrate, an absorption line of $\text{H}^{12}\text{C}^{14}\text{N}$ at 5 Torr is obtained by a scanning laser calibrated using the MSS (Figure 10.2(C)). The linewidth is around 2.6 GHz and the absorbance is as weak as 0.12 dB. Separate measurements on vibronic transitions between the ground state and $2\nu_1$ states were performed. The corresponding transition wavenumbers obtained by pseudo-Voigt fitting are in excellent agreement with the HITRAN database (Figure 10.2(D)) [231].

10.3 Measurement of multi-line spectra

To illustrate a measurement of more complex multi-line spectra, a fiber mode-locked laser (FMLL) is characterized (Figure 10.3(A)). The FMLL full spectrum (Figure 10.3(B)) was first bandpass filtered to prevent detector saturation. Also, the frequency extraction procedure is modified to enable unique identification of many frequencies. The reconstructed FMLL spectrum measured using the MSS is plotted in Figure 10.3(C). In an additional study of the FMLL, the MSS is used to measure 6 closely-spaced-in-frequency groups of lines located at various spectral locations spanning 2500 free-spectral-range's of the mode locked laser (Figure 10.3(D)). A linear fitting defined as $f_m = f_o + mf_{\text{rep}}$ is plotted for comparison by using the photodetector-measured FMLL repetition rate $f_{\text{rep}} = 249.7$ MHz, where m and f_o represent the relative mode index and fitted offset frequency at $m = 0$,

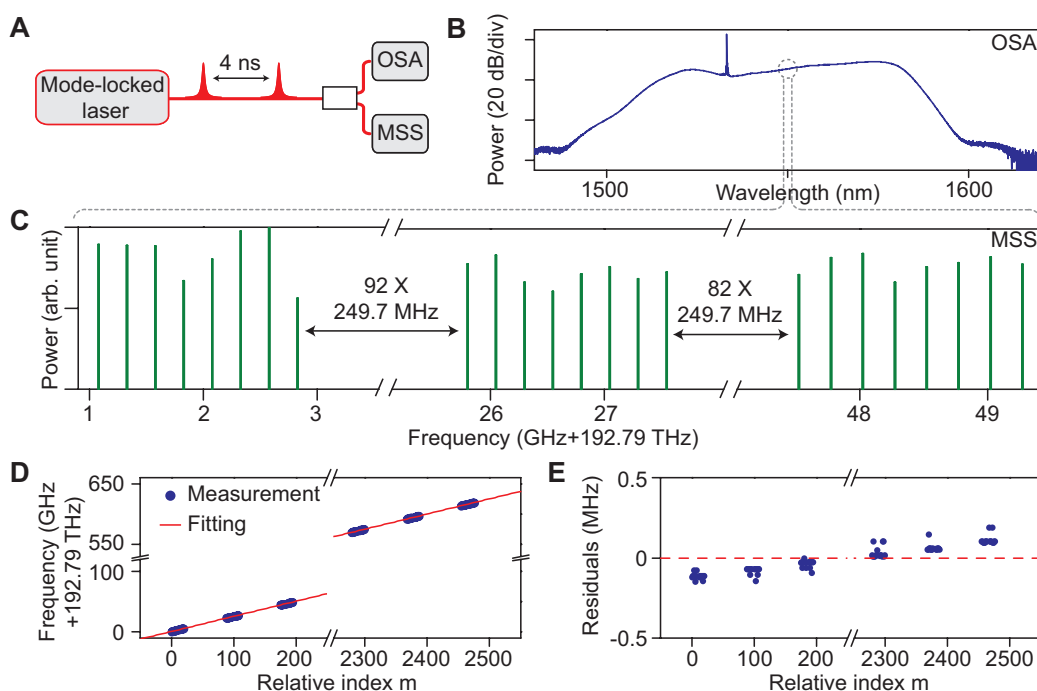


Figure 10.3: Measurement of a fiber mode-locked laser. (A) Pulse trains generated from a fiber mode-locked laser (FMLL) are sent into an optical spectral analyzer (OSA) and the MSS. (B) Optical spectrum of the FMLL measured by the OSA. (C) Optical spectrum of the FMLL measured using the MSS over a 60-GHz frequency range (indicated by dashed line). (D) Measured (blue) and fitted (red) FMLL mode frequencies versus index. The slope of the fitted line is set to 249.7 MHz, the measured FMLL repetition rate. (E) Residual MSS deviation between measurement and fitted value.

respectively. The residual deviation between the measurement and linear fitting is shown in Figure 10.3(E) and gives good agreement. The slight tilt observed in Figure 10.3(E) is believed to result from drifting of soliton repetition rates which were not monitored real-time. Also, variance of residuals within each group comes from the 300 kHz linewidth of each FMLL line. Drifting of the reference laser and FMLL carrier-envelope offset also contribute to the observed residuals across different measurements.

10.4 Signal processing

In this section, the algorithms used to extract the absolute frequencies of lasers are presented.

Single frequency laser

Through heterodyne of the test laser with the nearest comb teeth, the phase ψ of the test laser is related to the electrical signals $V_{1,2}$ by

$$V_{1,2} \propto \cos(\psi - 2\pi\nu_{n1,2}t), \quad (10.1)$$

where $\nu_{n1,2}$ represent the frequencies of nearest comb teeth and have order n . We also have $\nu_{n2} - \nu_{n1} = n\Delta f_r$ as a result of the CP soliton locking. A Hilbert transform is used to extract the time-dependent phase $\psi - 2\pi\nu_{n1,2}t$ from $V_{1,2}$ which thereby gives the heterodyne frequencies via

$$\Delta f_{n1,2} = \dot{\psi}/2\pi - \nu_{n1,2}. \quad (10.2)$$

Each data point of $\Delta f_{n1,2}$ is obtained by linear fitting of the phase over a specified time interval that sets the frequency resolution. Similarly, the heterodyne frequency between the reference laser and the soliton comb can be retrieved to determine the frequency f_0 (see discussion in main text).

The Fourier transform of the product $V_1 V_2$ is given by

$$\begin{aligned} \widetilde{V_1 V_2}(f) &\propto \int_0^{T_W} \frac{e^{i(\psi-2\pi\nu_{n1}t)} + e^{-i(\psi-2\pi\nu_{n1}t)}}{2} \frac{e^{i(\psi-2\pi\nu_{n2}t)} + e^{-i(\psi-2\pi\nu_{n2}t)}}{2} e^{-2\pi i f t} dt \\ &\propto \delta(|f| - n\Delta f_r), \end{aligned} \quad (10.3)$$

where sum frequency terms in the integral are assumed to be filtered out and are therefore discarded. To accurately extract the above spectral signal the acquisition time window T_W should be an integer multiple of $1/\Delta f_r$, which is also related to the pump frequency offset $\Delta\nu$ by $T_W = N_W N / \Delta\nu$ where N is the pump order and N_W is an integer. Moreover, the number of sampled points, which equals the product of oscilloscope sampling rate f_{samp} and T_W , should also be an integer (i.e., $f_{\text{samp}} N_W N / \Delta\nu$ is an integer). Here, f_{samp} is usually set to 2.5 or 5 GHz/s and it is found that simple adjustment of $\Delta\nu$ is sufficient to satisfy this condition. As a result it is not necessary to synchronize the oscilloscope to external sources. It is noted that this method is simpler than the asynchronous detection used in previous work [36].

On account of the limited bandwidth of the oscilloscope used in work, it was necessary to apply electrical frequency division to the detected signals for processing by the oscilloscope. When frequency dividers are used (division ratio $r = 8$), the

divided electrical signals (indicated by superscript d) yield

$$V_{1,2}^d \propto \cos((\psi - 2\pi\nu_{n1,2}t)/r). \quad (10.4)$$

As a result, the divided frequencies also satisfy $\Delta f_{n1,2}^d = \Delta f_{n1,2}/r$ and the correlation between the divided signals scales proportionally by

$$\Delta f_{n1}^d - \Delta f_{n2}^d = n\Delta f_r/r. \quad (10.5)$$

Therefore the required resolution bandwidth to resolve the ambiguity n from the measured correlation is $\Delta f_r/r$ which increases the minimal acquisition time to $T_W^d = rT_W$.

Multi-line spectra

The algorithm used here to extract a large number of frequencies simultaneously using the MSS is different from the previous single-frequency measurements. Rather than multiplying the signals V_1 and V_2 followed by Fast Fourier Transform (FFT) in order to determine the microcomb order, we directly FFT the signals V_1 and V_2 followed by filtering and then frequency correlation. This avoids the generation of ambiguities. To explain the approach, first consider an implementation similar to that reported in the main text. There, a fiber mode locked laser (FMLL) comb with free-spectral-range (FSR) of about 250 MHz was optically filtered to create a narrower frequency range of FMLL laser lines extending over only a few microcomb teeth. The signals V_1 and V_2 upon FFT therefore produce a large set of frequencies representing the individual beats of each FMLL laser line (index m) with microcomb modes (index n). Figure 10.4(A) gives a narrow frequency span of a typical FFT generated this way for both the V_1 and V_2 signals. A zoom-in of one pair of V_1 and V_2 signals is provided in Figure 10.4(B) and a remarkably precise frequency separation between the beats (in view of the spectral breadth of each beat) can be determined by correlating the upper (blue) and lower (red) spectrum (see Figure 10.4(C)). This precision results from the underlying high relative frequency stability of the cw and ccw microcomb frequencies. As described in the main text this frequency separation is a multiple of Δf_r and plot of the correlation versus the frequency separation (in units of Δf_r) is provided in Figure 10.4(C) where the peak of the correlation gives the index $n = 63$ for this pair of beat frequencies. Proceeding this way for each pair of peaks in Figure 10.4(A) allows determination of n from which the frequency of the corresponding FMLL line can be determined. It is interesting to note that in Figure 10.4(A), there are two sets of peaks that give $n=63$, 64 and 65. These

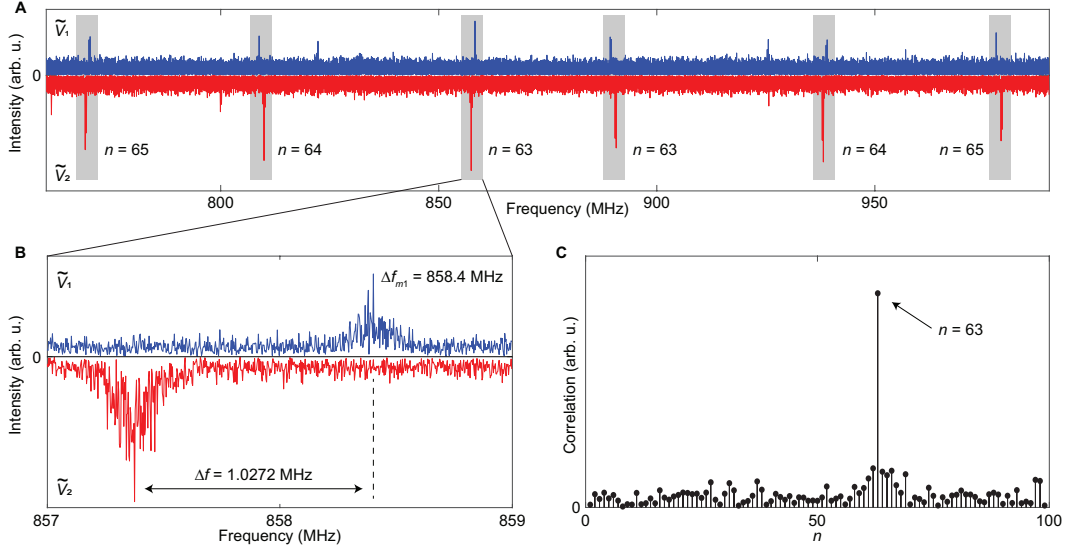


Figure 10.4: Multi-frequency measurements. (A) A section of $\tilde{V}_{1,2}$. Pairs of beatnotes coming from the same laser are highlighted and the derived n value is marked next to each pair of beatnotes. (B) Zoom-in on the highlighted region near 858 MHz in (A). Two beatnotes are separated by 1.0272 MHz. (C) Cross-correlation of \tilde{V}_1 and \tilde{V}_2 is calculated for each n and the maximum can be found at $n = 63$.

correspond to FMLL lines that are higher and lower in frequency relative to the microcomb modes with indices $n=63$, 64, and 65. The relative alignment of the blue and red peaks which switches sign for these sets of beat frequencies allows determination of which FMLL line is lower and higher in frequency relative to the microcomb teeth.

To provide more rigor to this explanation, the electrical signals consist of multiple beat components given by,

$$V_{1,2} = \sum_m V_{m1,2}, \quad V_{m1,2} \propto \cos(\psi_m - 2\pi\nu_{\mu(m)1,2}t), \quad (10.6)$$

where ψ_m and $\nu_{\mu(m)1,2}$ represent the phase of the m -th FMLL mode and the frequencies of the microcomb order nearest to this FMLL mode, respectively, and where $\mu(m)$ denotes the comb order nearest the m -th FMLL mode. As described in the main text the frequencies $\nu_{\mu(m)1,2}$ are related to the repetition rate difference by $\nu_{\mu(m)2} - \nu_{\mu(m)1} = \mu(m)\Delta f_r$. The FFT of $V_{1,2}$ is denoted by $\tilde{V}_{1,2}$ and the correlation given in Figure 10.4(C) (and used to determine the comb order n of each spectral

component) is given by

$$\begin{aligned}
& \int_{\Delta f_{m1}-\kappa/2}^{\Delta f_{m1}+\kappa/2} \tilde{V}_1(f) \tilde{V}_2^*(f+n\Delta f_r) df \\
& \approx \int_{-\infty}^{\infty} df \int V_{m1}(t) e^{2\pi i f t} dt \int V_{m2}(t') e^{-2\pi i (f+n\Delta f_r) t'} dt' \\
& = \int V_{m1}(t) V_{m2}(t) e^{-2\pi i n \Delta f_r t} dt \tag{10.7} \\
& \propto \int \frac{e^{i(\psi_m - 2\pi \nu_{\mu 1} t)} + e^{-i(\psi_m - 2\pi \nu_{\mu 1} t)}}{2} \frac{e^{i(\psi_m - 2\pi \nu_{\mu 2} t)} + e^{-i(\psi_m - 2\pi \nu_{\mu 2} t)}}{2} e^{-2\pi i n \Delta f_r t} dt \\
& \propto \delta(\mu(m) - n),
\end{aligned}$$

where Δf_{m1} denotes the peak frequency of the beatnote, κ is a predetermined range of integration to cover the linewidth of the beatnote (here $\kappa = 2$ MHz), and where sum frequency terms in the integral have been discarded. Therefore for each spectral component m , its associated microcomb order number $\mu(m)$ can be determined by varying n in the above correlation until it reaches maximum (see Figure 10.4(C)). The n value with the maximum correlation will be assigned to the peak as the tooth number $\mu(m)$ and then the absolute frequency can be recovered.

The limit of this process to accommodate more FMLL frequencies is much higher than that given by the filter bandwidth studied in this work. It is instead set by the spectral density of FMLL-microcomb beat lines that can be reasonably resolved within the microcomb FSR spectral span.

10.5 Conclusion

Our soliton spectrometer uses dual-locked counter-propagating soliton microcombs to provide high resolution frequency measurement of rapid continuously and step tuned lasers as well as complex multi-line spectra. In combination with a tunable laser, the spectrometer also enables precise measurement of absorption spectra including random spectral access (as opposed to only continuous spectral scanning). Further optimization of this system could include generation of solitons from distinct mode families thereby allowing tens-of-MHz repetition rate offset to be possible [100]. If such solitons can be dual-locked, the increased acquisition speed would enable measurement of chirping-rates much higher than PHz/s. Operation beyond the telecommunications band would also clearly be useful and could use internal [68] or on-chip spectral broadeners [232], and methods for generation of soliton microcombs into the visible band are possible [116]. Besides the performance enhancement realized with the soliton microcombs, the use of dual-locked counter-

propagating solitons provides a considerable technical simplification by eliminating the need for a second mutually phase locked comb. Finally, chip integrable versions of the current device employing silicon nitride waveguides are possible [73]. These and other recently demonstrated compact and low-power soliton systems [85, 86] point towards the possibility of compact microresonator soliton spectrometers.

IMAGING SOLITON DYNAMICS IN MICRORESONATORS

¹Temporal solitons are indispensable in optical fiber systems [119] and exhibit remarkable nonlinear phenomena [233]. The potential application of solitons to buffers and memories [69, 157] as well as interest in soliton physics has stimulated approaches for experimental visualization of multi-soliton trajectories. Along these lines, the display of solitons trajectories in a co-moving frame [234] allows an observer to move with the solitons and is being used to monitor soliton control and interactions of all types in fiber systems [195, 234–240]. However, this useful data visualization method relies upon soliton pulse measurements that are either limited in bandwidth (pulse resolution) or record length. It is therefore challenging to temporally resolve solitons over the periods often required to observe their complete evolution. For example, the time-lens method [241] can provide the required femtosecond-resolution, but has a limited record length set by the pump pulse. Also, while the relative position of closely-spaced soliton complexes [239] can be inferred over time from their composite DFT spectra [242], Fourier inversion requires the constituent solitons to have similar waveforms which restricts the generality of the technique. Efforts that combine these two methods were also reported very recently [243, 244].

These limitations are placed in sharp focus by recent demonstrations of soliton generation in microresonators [66–68, 72, 76, 77, 245]. This new type of dissipative soliton [125] was long considered a theoretical possibility [157] and was first observed in optical fiber resonators [69]. Their microresonator embodiment poses severe challenges for imaging of dynamical phenomena by conventional methods, because multi-soliton states feature inherently closely spaced solitons. Preliminary real-time measurements using time lens [246] and direct detection [96] were explored, but were limited in either recording length or pulse resolution. Nonetheless, the compactness of these systems has practical importance for miniaturization of frequency comb technology [43] through chip-based microcombs [51, 52]. Indeed, spectroscopy systems [105, 107], coherent communication [114], ranging [110, 111], and frequency synthesis [104] demonstrations using the new miniature

¹Work presented in this chapter has been published in “Imaging soliton dynamics in optical microcavities”, *Nat. Commun.* 9(1):3565 (2018).

platform have already been reported. Moreover, the unique physics of the new soliton microresonator system has led to observation of many unforeseen physical phenomena involving compound soliton states, such as Stokes solitons [89], soliton number switching [247], and soliton crystals [98].

In this chapter, we report imaging of a wide range of soliton phenomena in microresonators. Soliton formation, collisions [238], breathing [94, 235, 248, 249], Raman shifting [87, 250] as well as soliton decay are observed. Significantly, femtosecond-time-scale resolution over arbitrary time spans (distances) is demonstrated (and required) in these measurements. Also, real-time spectrograms are produced along-side high-resolution soliton trajectories. These features are derived by adapting coherent linear optical sampling [251] and electric-field cross correlation [252] to the problem of microresonator soliton imaging. Beyond the necessity to employ a new method for imaging soliton motion in microresonators, the high repetition rate of microresonator solitons (10s of GHz and higher) is advantageous in sampling-based recording of motion.

11.1 Coherent sampling of soliton motion

Concept of coherent sampling

To image the soliton trajectories, a separate optical probe pulse stream is generated at a pulse rate that is close to the rate of the solitons to be imaged in the microresonator. The small difference in these rates causes a pulse-to-pulse temporal shift of the probe pulses relative to the microresonator signal pulses as illustrated in Figure 11.1(a). By heterodyne detection of the combined streams, the probe pulses coherently sample the microresonator signal producing a temporal interferogram [38, 211] shown in Figure 11.1(a). Ultimately, the time shift per pulse accumulates so that the sampling repeats in the interferogram at the ‘frame rate’ which is described below, and is close in value to the difference of sampling and signal rates. Probe pulses have a sub-picosecond temporal resolution that enables precise monitoring of the temporal location of the soliton pulses. Moreover, the coherent mixing of probe and soliton pulses allows extraction of each soliton’s spectral evolution by fast Fourier transform of the interferogram. In principle, the probe pulses can be generated by a second microresonator soliton source operating in steady state. However, in the present measurement, an electro-optical (EO) comb is used [252–254]. The EO comb pulse rate is conveniently adjusted electronically to match the rates of various phenomena being probed within the microresonator. The experimental layout of the EO comb will be shown later in this chapter.

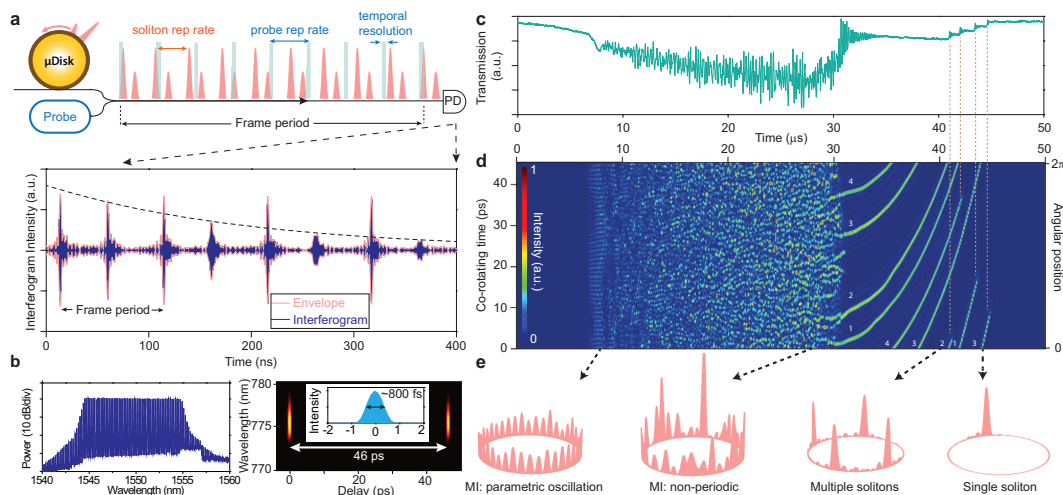


Figure 11.1: Coherent sampling of dissipative Kerr soliton dynamics. (a) Conceptual schematic showing microresonator signal (red) combined with the probe sampling pulse train (blue) using a bidirectional coupler. The probe pulse train repetition rate is offset slightly from the microresonator signal. It temporally samples the signal upon photo detection to produce an interferogram signal shown in the lower panel. The measured interferogram shows several frame periods during which two solitons appear with one of the solitons experiencing decay. (b) Left panel is the optical spectrum and right panel is the FROG trace of the probe EO comb (pulse repetition period is shown as 46 ps). An intensity autocorrelation in the inset shows a full-width-half-maximum pulse width of 800 fs. (c) Microresonator pump power transmission when the pump laser frequency scans from higher to lower frequency. Multiple ‘steps’ indicate the formation of solitons. (d) Imaging of soliton formation corresponding to the scan in panel (c). The x-axis is time and the y-axis is time in a frame that rotates with the solitons (full scale is one round-trip time). The right vertical axis is scaled in radians around the microresonator. Four soliton trajectories are labeled and fold-back into the cavity coordinate system. The color bar gives their signal intensity. (e) Soliton intensity patterns measured at four moments in time are projected onto the microresonator coordinate frame. The patterns correspond to initial parametric oscillation in the modulation instability (MI) regime, non-periodic behavior (MI regime), four soliton and single soliton states.

Soliton and EO frequency combs

The soliton signal is produced by a 3 mm diameter silica wedge resonator with FSR of 22 GHz and intrinsic quality factor above 200 million [55, 67]. The device generates femtosecond soliton pulses when pumped at frequencies slightly lower than a cavity resonant frequency [67]. To sample the 22 GHz soliton signal the EO comb was formed by modulation of a tunable continuous wave (CW) laser. The EO comb features ~ 1.3 THz optical bandwidth (within 1 dB power variation) and

an 800 fs FWHM pulse width measured by frequency-resolved optical gating and autocorrelation as shown in Figure 11.1(b). Further details on the experimental setup are provided in the Discussion section. In all presented measurements, the pump laser of the resonator scans linearly from higher to lower frequency to initiate parametric oscillation [61] in the microresonator followed by chaotic dynamics. Ultimately, ‘step-like’ features are observable in the resonator transmitted power (Figure 11.1(c)) indicating the formation of soliton states [66]. The typical pump power and laser scan speed are ~ 70 mW and ~ -1 MHz/ μ s, respectively.

As described above, heterodyne-detection of the soliton signal and the EO-comb pulse produces the electrical interferogram. The period of the signals in the interferogram is adjusted by tuning the EO-comb repetition rate. In the initial measurements, it is set to ~ 10 MHz lower than the rate of the microresonator signal so that the nominal period in the interferogram is ~ 100 ns. To display the interferogram signal a co-rotating frame is applied. First, a frame period T is chosen that is close to the period of signals of interest in the interferogram. Integer steps (i.e., mT) are plotted along the x-axis while the interferogram is plotted along the y-axis, but offset in time by the x-axis time step (i.e., $t - mT$). To make connection to the physical time scale of the solitons, the y-axis time scale is also compressed by the same bandwidth compression factor ($T \times \text{FSR}$) that accompanies the sampling process. The y-axis scale is accordingly set to span one microresonator round-trip time. A typical measurement plotted in this manner is given in Figure 11.1(d). Because this way of plotting the data creates a co-rotating reference frame, a hypothetical soliton pulse with an interferogram period equal to the frame rate T would appear as a horizontal line in Figure 11.1(d). On the other hand, slower (higher) rate solitons would appear as lines tilted upward (downward) in the plot. In creating the imaging plot, a Hilbert transformation is applied to the interferogram followed by taking the square of its amplitude to produce a pulse envelope intensity profile. The vertical co-rotating time axis can be readily mapped into an image of the soliton angular position within the circular microresonator as shown in Figure 11.1(d).

Imaging of soliton motion

Imaging of soliton formation and multi-soliton trajectories is observable in Figure 11.1(d). For comparison with the transmitted power, the time-axis scale is identical in Figure 11.1(c) and Figure 11.1(d). As the pump laser frequency initially scans towards the microresonator resonant frequency its coupled power increases. At ~ 8 μ s the resonator enters the modulation instability regime [66, 69, 157]. Ini-

tially, a periodic temporal pattern is observable in Figure 11.1(d) corresponding to parametric oscillation [61]. Soon after, the cavity enters a regime of non-periodic oscillation. At $\sim 31 \mu\text{s}$, this regime suddenly transitions into four soliton pulses. The soliton positions evolve with scan time and disappear one-by-one. All solitons have upward curved trajectories, showing that the soliton repetition rate decreases as the scan progresses. This soliton rate shift is caused by the combination of the Raman self-frequency shift effect and anomalous dispersion in the silica resonator [87, 88] and a similar effect on soliton trajectory is observed in optical fiber resonators [250]. Finally, the cavity states at four moments in time are plotted within the circular microresonator in Figure 11.1(e). These correspond to parametric oscillation, non-periodic modulational instability, four soliton, and single soliton states.

11.2 Observation of transient soliton dynamics

A variety of non-repetitive multi and single soliton phenomena were measured in both temporal and spectral domains. To enable more rapid imaging the repetition rate of EO comb was adjusted to produce an interferogram at a rate of approximately 50 MHz. The frame period, T , was then reduced accordingly to approximately 20 nsec.

Soliton collisions

Fig. 11.2 presents observations of two solitons interacting. Soliton annihilation is observed in Figure 11.2(a), wherein two solitons move towards each other, collide, create an intense peak upon collision and then disappear. A new phenomena, a ‘wave splash’, is observed immediately following the collision. While this phenomenon has never before been discussed or observed, it is worthwhile to note that it appears in recently reported simulations [240]. In Figure 11.2(b), two solitons collide but quickly recover and then collide again, after which point one soliton is annihilated. Fig. 11.2(c) shows a third example in which solitons merge and a single soliton emerges. In a fourth case shown in Figure 11.2(d), soliton ‘hopping’ accompanies annihilation of a soliton. Interestingly, all soliton collisions are observed at the beginning of soliton formation (in the soliton breathing regime). After this regime, the soliton relative motion quickly stabilizes preventing collisions. This stabilization process is investigated in a later section. Also, as noted earlier, the observation of these complex motions requires measurement of events in close temporal proximity over long time spans. Finally, numerical simulations of soliton collisions are shown as inset panels in Figure 11.2. The collisional features observed in experiments,

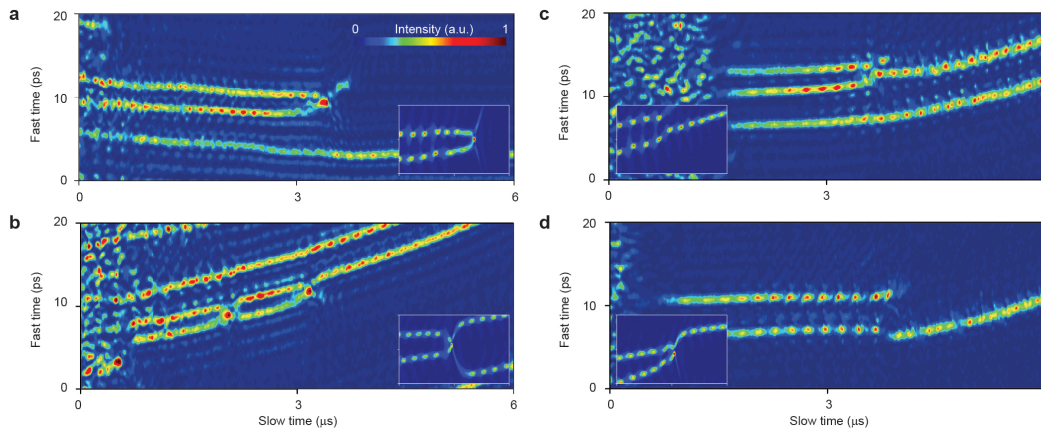


Figure 11.2: Measurements of non-repetitive soliton events. (a) Two solitons collide and annihilate. A wave splash appears in the collision. (b) Two solitons survive a collision, but collide again and one soliton is annihilated. (c) Two solitons collide and merge into a single soliton. (d) A soliton hops in location when another soliton is annihilated. The measurement frame rate is 50 MHz in all panels. Inset panels show similar collision events from numerical simulation, including the appearance of the wave splash (inset in panel (a)).

including the wave splash in Figure 11.2(a), are reproduced in the simulations.

Soliton breathing

Figure 11.3 shows measurement of a breathing soliton [248] in both the temporal and frequency domains. The intensity of an individual breather soliton is imaged in Figure 11.3(a). Spectral breathing was explored in fiber-ring resonators using the DFT method [235]. In this work, the spectral breathing is observed by applying a Fourier transform to the interferogram signal [211]. Figure 11.3(b) shows the resulting spectrogram plotted over the same time interval as Figure 11.3(a), wherein the spectrum is widest when the breather soliton has its maximum peak power. This spectrum also reveals the changing breather period with frequency scan, which has previously been observed by measurement of soliton power [94, 96]. A zoom-in of the soliton temporal breathing is shown in Figure 11.3(c). The combined high frame rate and sub-ps temporal resolution enable the corresponding amplitude and pulse width of the breather to be extracted and these are plotted in Figure 11.3(d). As an observation unrelated to the breathing action, the soliton spectral envelope in Figure 11.3(b) is continuously red shifted in frequency by the Raman self-frequency shift [67, 87] as its average power increases (increasing time in the plot).

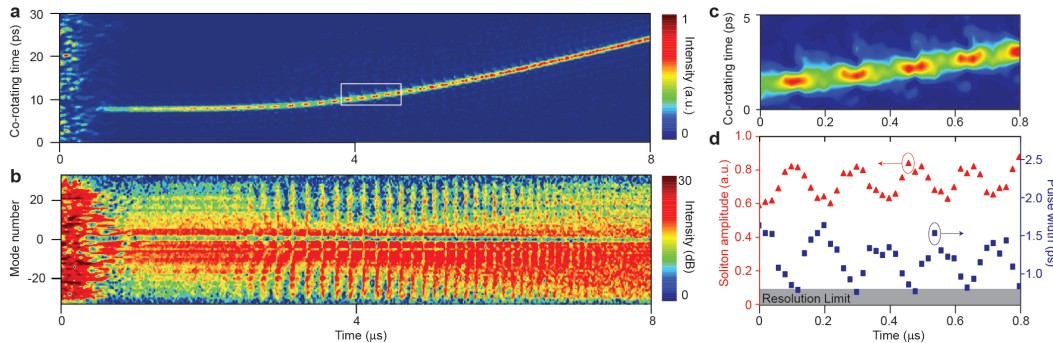


Figure 11.3: Temporal and spectral measurements of breather solitons. (a) Motion of a single soliton state showing peak power breathing along its trajectory. Panel (c) presents the zoom-in view of the white rectangular region. (b) Spectral dynamics corresponding to panel (a). The y-axis is the relative longitudinal mode number corresponding to specific spectral lines of the soliton. Mode zero is the pumped microresonator mode. The soliton spectral width breaths as the soliton peak power modulates. The spectrum is widest when peak power is maximum. (c) Zoom-in view of the white rectangular region in panel (a). (d) Soliton amplitude and pulse width breathing corresponding to panel (c). The frame rate is 50 MHz for all panels.

11.3 Tracking relative soliton motion and soliton decay

Monitoring relative soliton position in real time is important for study of soliton optical memories [69, 157], their interaction and control [195, 234] as well as in soliton crystals [98]. Previously, microresonator soliton relative positions have been measured by auto-correlation [156], frequency-resolved optical gating [66] and synchronized cross-correlation [98]. However, with an update rate limited by a mechanical delay line, these methods are only useful for measurement of steady-state phenomena. In this work, relative soliton positions can be measured in real time from the interferogram thereby enabling study of their relative motion dynamics. To plot soliton relative position, one soliton is selected to be the reference (i.e., zero point of the angular position) and the angular position relative to the reference soliton is defined from $-\pi$ to π . Two representative measurements are shown in Figures 11.4(a)-(b) wherein the laser frequency is scanned from high to low frequency. Even though the reference-soliton round-trip rate is changing as the laser frequency is scanned (see, for example, Figure 11.1(d)), the solitons experience extended stable relative motion relative to one another. In Figure 11.4(a), the solitons stabilize relative to each other within a few μs after formation and in Figure 11.4(b), the relative positions are stable from 9 to 22 μs and then destabilize. It is believed that the stabilization of solitons is related to the presence of a dispersive wave caused

by an avoided mode crossing [84, 247]. Note that ultimately, all of the solitons in both panels are annihilated when the laser tunes beyond the existence detuning range [66].

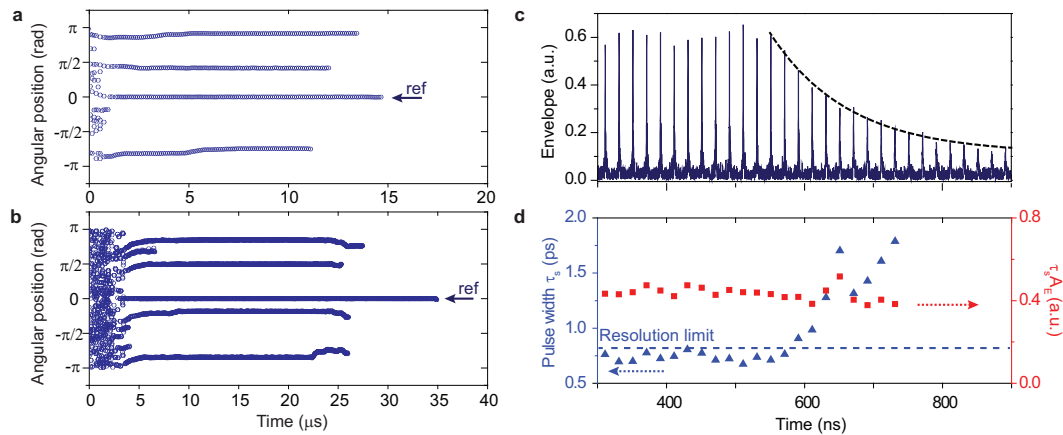


Figure 11.4: Measurement of relative soliton positions and soliton decay. (a) Plot of the relative positions of four solitons while the pumping laser frequency is scanned (high to low). The reference soliton, used to establish zero angular position, is indicated and all solitons have stable relative positions after only several μs of motion. (b) The relative positions of five solitons is measured versus time as the pump laser frequency is scanned. The soliton relative positions stabilize and then destabilize at $22 \mu\text{s}$. The frame rates for panels (a) and (b) are 10 and 50 MHz, respectively. (c) Interferogram envelope showing a single soliton experiencing decay. An exponential fitting is given as the dashed black line. (d) The measured pulse width (blue) is plotted versus time and its resolution limit (dashed blue line) is set by the EO comb pulse width. The product of soliton amplitude and pulse width is plotted in red.

Soliton decay is also analyzed using the sampling method. The measurement results are shown in Figures 11.4(c)-(d). In the experiment, the pump laser frequency is continuously tuned towards lower frequencies. After soliton formation, at some point the cavity-laser frequency detuning exceeds the soliton existence range and the soliton decays [66, 67]. Figure 11.4(c) shows the interferogram signal just before and during the decay. Pulse widths (τ_s) are extracted during the decay process and are plotted in Figure 11.4(d). Also plotted in Figure 11.4(d) is the product of pulse width and soliton peak amplitude (A_E). Curiously, the soliton pulse width and peak amplitude preserve the same soliton product relationship as prior to decay. This is an indication that the decaying soliton pulse in the microresonator is constantly adapting itself to maintain the soliton waveform. A similar behavior is known to occur for conventional solitons in optical fiber [128]. To the authors knowledge, this

is the first time this behavior has been observed in real time. In the Methods section the amplitude decay of the soliton in the interferogram, trace is analyzed to extract a decay time and the cavity Q factor.

11.4 Numerical simulation

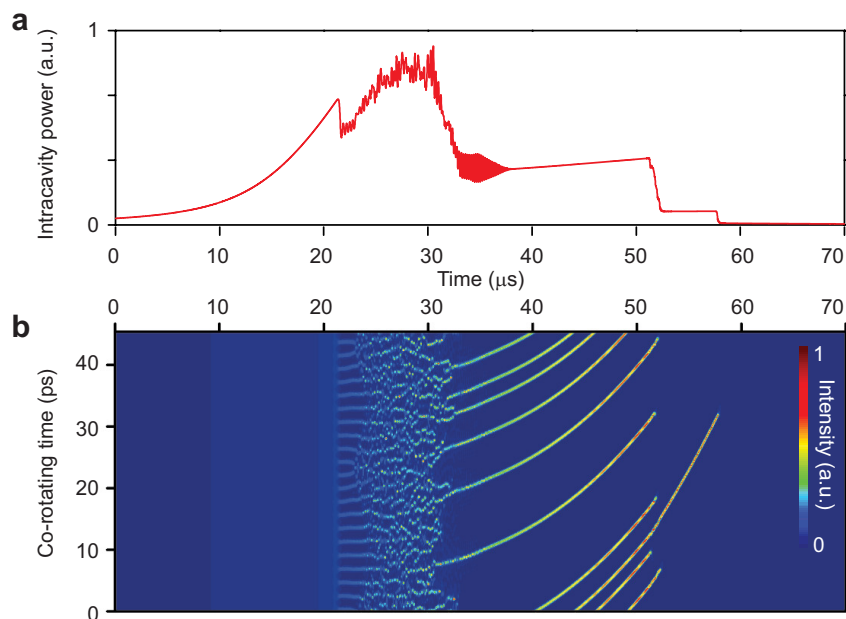


Figure 11.5: Simulation of microresonator soliton formation. (a) Simulated intracavity power plotted versus time as the pumping laser is tuned across a cavity resonance from higher to lower frequencies. The step features correspond to the formation of solitons. (b) Simulation results corresponding to panel (a) and showing the formation of multiple solitons. In the simulation, the Raman effect and avoided mode crossing are included.

The soliton dynamics are governed by the Lugiato-Lefever (LL) equation [127] augmented by Raman [87, 88] and avoided mode crossing [153] effects. The LL equation can be simulated numerically using the split-step method [128]. Simulated intracavity power versus temporal profiles for soliton formation are presented Figure 11.4(a) and, for comparison with the imaging data in Figure 11.1(d), the corresponding simulated multi-soliton trajectories are plotted in Figure 11.4(b). In the simulation, the laser frequency is linearly scanned from higher to lower frequency. Moreover, the Raman effect and one avoided mode crossing are included in the simulation. Concerning the vertical axis scale, it is noted that because the periodicity of the soliton interferogram signals varies by less than 1 % during the scan, the vertical co-rotating time axis can be readily mapped into the soliton angular position axis

within the circular microresonator as shown in Figures 11.1(d) and (e). The features of soliton formation and evolution observed in Figure 11.1(d) compare well with the numerical simulation.

11.5 Experimental details

Figure 11.6 divides the experimental setup into three sections. In the microresonator section, a tunable, continuous-wave (cw) laser is used to pump the microresonator for production of solitons. An erbium-doped fiber amplifier (EDFA) amplifies its power to 500 mW and an acousto-optic modulator (AOM) is used for rapid control of power to the microresonator. A tunable bandpass filter (BPF) is used to block the spontaneous emission noise from the EDFA. The pump is coupled into the microresonator through a tapered-fiber [130, 139]. The emitted power from the microresonator (along with transmitted pump power) is split by a 90/10 fiber coupler. 10 percent of the power is sent to a fiber-Bragg grating (FBG) filter to separate the pump power and the microcomb power. The drop port output is the pump power transmission, while the through-port output is the comb power. Both the pump transmission and the microcomb power are detected with photodetectors (125 MHz bandwidth). The other 90 percent of the power is combined with the electro-optic (EO) modulation comb sampling pulse using a second fiber coupler.

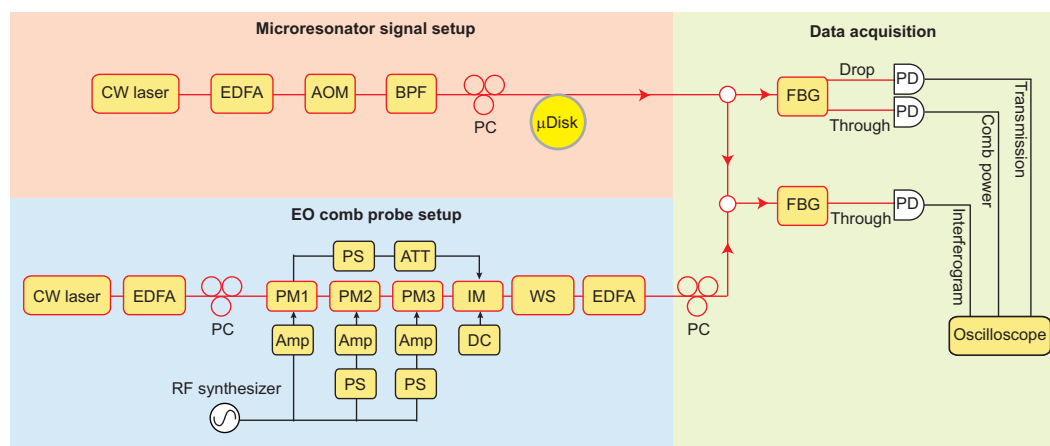


Figure 11.6: Experimental setup. Schematic showing the three functional sections in the experiment. CW laser: continuous-wave laser; EDFA: erbium-doped-fiber-amplifier; AOM: acousto-optic modulator; BPF: bandpass filter; PC: polarization controller; PM: phase modulator; IM: intensity modulator; PS: phase shifter; ATT: attenuator; Amp: RF amplifier; DC: DC voltage source; WS: optical waveshaper; FBG: fiber-Bragg-gating; PD: photodetector.

In the EO comb setup, a pump laser is amplified by an EDFA to 200 mW and

then phase modulated by three tandem lithium niobate modulators. The EO comb and microresonator setup can share the same pump laser when the acousto-optic modulator can provide a frequency offset higher than half of the electrical bandwidth of the interferogram signal (to avoid frequency folding). This is the case in Figure 11.1. However, they can also use separate pump lasers, which is demonstrated in Figure 11.2 and Figure 11.3. The modulators are driven by amplified electrical signals (frequency close to 22 GHz) that are synchronized by electrical phase shifters. The output power of the electrical amplifiers is 33 dBm. The phase modulated pump is then coupled to an intensity modulator to select only portions of the waveform with a uniform chirp. The intensity modulator is driven by the recycled microwave signal from the external termination port of the first phase modulator. The modulation intensity and phase are controlled by an electrical attenuator and phase shifter. A programmable line-by-line waveshaper is used to flatten the EO comb optical spectrum and to nullify the linear chirping so as to form a transform-limited sinc-shaped temporal pulse. The average power from the waveshaper output is around 100 μ W. The EO pulses are amplified by an EDFA before combining with the microresonator signal.

In the interferogram measurement, the microresonator signal and the EO pulses are combined in a 90/10 coupler and are then detected by a fast photodetector with 50 GHz bandwidth. An FBG filter is used to block the pump laser of the microresonator to avoid saturation in the photodetector. All photodetected signals are recorded using a 4 GHz bandwidth, 20 GSa/s sampling rate oscilloscope. The center frequencies for the interferogram are around 0.7 GHz and 2.1 GHz for 10 MHz and 50 MHz frame rate, respectively. The compression factors for the interferograms are 2200 and 440 for the 10 MHz and 50 MHz frame rate measurements, respectively.

11.6 Conclusion

Imaging of nonlinear dynamical phenomena including complex soliton interactions with high temporal/spatial resolution over arbitrary time/length spans has been demonstrated. The temporal resolution in the current experiment is limited to 800 fs; however, resolution at the 10s of fs level is possible by spectrally broadening the EO comb [50] used for coherent sampling. It is also possible to replace the EO-comb with a microcomb that is closely matched to the FSR of a microresonator to be sampled. Such matching has been recently used to implement dual soliton microcomb spectroscopy measurements [105, 107]. In this case, even higher sampling rates would be possible that would enable GHz-scale frame rates. The coherent

sampling method can serve as a general real-time state visualization tool to monitor the dynamics of microresonator systems. It would provide an ideal way to monitor the formation and evolution of soliton complexes such as Stokes solitons [89], soliton number switching [247], and soliton crystals [98]. It can also be used to monitor the state of chip-based optical memories based on microresonator solitons.

*Chapter 12***SUMMARY**

The success of soliton microcombs over past years is a milestone of integrated photonics. It does not only provide a miniaturized platform for precise measurement, but also open up a pyramid of novel physical phenomena. In this thesis we have shown a series of nonlinear process related to soliton microcombs, including their formation, impact of Raman nonlinearity and mode interactions, and dynamics of counter-propagating solitons. We have also demonstrated applications such as dual-comb spectroscopy and vernier spectrometer based on soliton microcombs. The future of microcombs is undoubtedly promising. Using more advanced microfabrication techniques, microresonators with higher Q factors are anticipated, which would significantly reduce the power budget so as to bring fully-integrated microcomb sources to life.

BIBLIOGRAPHY

- [1] Haswell, J. E. *Horology* (Chapman & Hall, 1928).
- [2] Hall, E. L., Heaton, V. E. & Lapham, E. G. The national primary standard of radio frequency. *J. Res. Natl. Bur. Stand.* **14**, 85–98 (1935).
- [3] Sullivan, D. Time and frequency measurement at nist: The first 100 years. In *Proc. IEEE Intl. Freq. Cont. Symp.*, 4–17 (IEEE, 2001).
- [4] Lyons, H. The atomic clock. *Instruments* **22**, 133–135 (1949).
- [5] Rabi, I., Millman, S., Kusch, P. & Zacharias, J. The molecular beam resonance method for measuring nuclear magnetic moments. *Phys. Rev.* **55**, 526–535 (1939).
- [6] Ramsey, N. F. A molecular beam resonance method with separated oscillating fields. *Phys. Rev.* **78**, 695–699 (1950).
- [7] Essen, L. & Parry, J. V. An atomic standard of frequency and time interval: a caesium resonator. *Nature* **176**, 280–282 (1955).
- [8] Phillips, W. D. Nobel lecture: Laser cooling and trapping of neutral atoms. *Rev. Mod. Phys.* **70**, 721–741 (1998).
- [9] Chu, S. Nobel lecture: The manipulation of neutral particles. *Rev. Mod. Phys.* **70**, 685–706 (1998).
- [10] Cohen-Tannoudji, C. N. Nobel lecture: Manipulating atoms with photons. *Rev. Mod. Phys.* **70**, 707–719 (1998).
- [11] Wynands, R. & Weyers, S. Atomic fountain clocks. *Metrologia* **42**, S64 (2005).
- [12] Jaksch, D., Bruder, C., Cirac, J. I., Gardiner, C. W. & Zoller, P. Cold bosonic atoms in optical lattices. *Phys. Rev. Lett.* **81**, 3108–3111 (1998).
- [13] Jennings, D. *et al.* Direct frequency measurement of the λ 2-stabilized he–ne 473-thz (633-nm) laser. *Opt. Lett.* **8**, 136–138 (1983).
- [14] Hall, J. L. Nobel lecture: Defining and measuring optical frequencies. *Rev. Mod. Phys.* **78**, 1279 (2006).
- [15] Hänsch, T. W. Nobel lecture: Passion for precision. *Rev. Mod. Phys.* **78**, 1297 (2006).
- [16] Hargrove, L., Fork, R. L. & Pollack, M. Locking of he–ne laser modes induced by synchronous intracavity modulation. *Appl. Phys. Lett.* **5**, 4–5 (1964).

- [17] Mocker, H. W. & Collins, R. Mode competition and self-locking effects in aq-switched ruby laser. *Appl. Phys. Lett.* **7**, 270–273 (1965).
- [18] DeMaria, A., Stetser, D. & Heynau, H. Self mode-locking of lasers with saturable absorbers. *Appl. Phys. Lett.* **8**, 174–176 (1966).
- [19] Ippen, E., Shank, C. & Dienes, A. Passive mode locking of the cw dye laser. *Appl. Phys. Lett.* **21**, 348–350 (1972).
- [20] Dudley, J. M., Genty, G. & Coen, S. Supercontinuum generation in photonic crystal fiber. *Rev. Mod. Phys.* **78**, 1135 (2006).
- [21] Ranka, J. K., Windeler, R. S. & Stentz, A. J. Visible continuum generation in air–silica microstructure optical fibers with anomalous dispersion at 800 nm. *Opt. Lett.* **25**, 25–27 (2000).
- [22] Diddams, S. A. *et al.* Direct link between microwave and optical frequencies with a 300 thz femtosecond laser comb. *Phys. Rev. Lett.* **84**, 5102 (2000).
- [23] Diddams, S. *et al.* An optical clock based on a single trapped $^{199}\text{Hg}^+$ ion. *Science* **293**, 825–828 (2001).
- [24] Udem, T., Holzwarth, R. & Hänsch, T. W. Optical frequency metrology. *Nature* **416**, 233–237 (2002).
- [25] Diddams, S., Bergquist, J., Jefferts, S. & Oates, C. Standards of time and frequency at the outset of the 21st century. *Science* **306**, 1318–1324 (2004).
- [26] Takamoto, M., Hong, F.-L., Higashi, R. & Katori, H. An optical lattice clock. *Nature* **435**, 321–324 (2005).
- [27] Ludlow, A. D. *et al.* Sr lattice clock at 1×10^{-16} fractional uncertainty by remote optical evaluation with a ca clock. *Science* **319**, 1805–1808 (2008).
- [28] Ludlow, A. D., Boyd, M. M., Ye, J., Peik, E. & Schmidt, P. O. Optical atomic clocks. *Rev. Mod. Phys.* **87**, 637 (2015).
- [29] Marti, G. E. *et al.* Imaging optical frequencies with 100 μ hz precision and 1.1 μ m resolution. *Phys. Rev. Lett.* **120**, 103201 (2018).
- [30] Holzwarth, R. *et al.* Optical frequency synthesizer for precision spectroscopy. *Phys. Rev. Lett.* **85**, 2264 (2000).
- [31] Jones, D. J. *et al.* Carrier-envelope phase control of femtosecond mode-locked lasers and direct optical frequency synthesis. *Science* **288**, 635–639 (2000).
- [32] Jones, R. J. & Diels, J.-C. Stabilization of femtosecond lasers for optical frequency metrology and direct optical to radio frequency synthesis. *Phys. Rev. Lett.* **86**, 3288 (2001).

- [33] Ma, L.-S. *et al.* Optical frequency synthesis and comparison with uncertainty at the 10⁻¹⁹ level. *Science* **303**, 1843–1845 (2004).
- [34] Diddams, S. A., Hollberg, L. & Mbele, V. Molecular fingerprinting with the resolved modes of a femtosecond laser frequency comb. *Nature* **445**, 627–630 (2007).
- [35] Coddington, I., Swann, W. C. & Newbury, N. R. Coherent multiheterodyne spectroscopy using stabilized optical frequency combs. *Phys. Rev. Lett.* **100**, 013902 (2008).
- [36] Giorgetta, F., Coddington, I., Baumann, E., Swann, W. & Newbury, N. Fast high-resolution spectroscopy of dynamic continuous-wave laser sources. *Nat. Photon.* **4**, 853–857 (2010).
- [37] Cingöz, A. *et al.* Direct frequency comb spectroscopy in the extreme ultraviolet. *Nature* **482**, 68–71 (2012).
- [38] Coddington, I., Swann, W., Nenadovic, L. & Newbury, N. Rapid and precise absolute distance measurements at long range. *Nat. Photon.* **3**, 351–356 (2009).
- [39] Li, C.-H. *et al.* A laser frequency comb that enables radial velocity measurements with a precision of 1 cm s⁻¹. *Nature* **452**, 610–612 (2008).
- [40] Steinmetz, T. *et al.* Laser frequency combs for astronomical observations. *Science* **321**, 1335–1337 (2008).
- [41] Wilken, T. *et al.* A spectrograph for exoplanet observations calibrated at the centimetre-per-second level. *Nature* **485**, 611–614 (2012).
- [42] Krausz, F. & Ivanov, M. Attosecond physics. *Rev. Mod. Phys.* **81**, 163 (2009).
- [43] Diddams, S. A. The evolving optical frequency comb. *J. Opt. Soc. Am. B* **27**, B51–B62 (2010).
- [44] Yariv, A. Internal modulation in multimode laser oscillators. *J. Appl. Phys.* **36**, 388–391 (1965).
- [45] Haus, H. A. *et al.* Mode-locking of lasers. *IEEE J. Sel. Top. Quantum Electron.* **6**, 1173–1185 (2000).
- [46] Spence, D. E., Kean, P. N. & Sibbett, W. 60-fsec pulse generation from a self-mode-locked Ti:sapphire laser. *Opt. Lett.* **16**, 42–44 (1991).
- [47] Tamura, K., Ippen, E., Haus, H. & Nelson, L. 77-fs pulse generation from a stretched-pulse mode-locked all-fiber ring laser. *Opt. Lett.* **18**, 1080–1082 (1993).

- [48] Kobayashi, T., Sueta, T., Cho, Y. & Matsuo, Y. High-repetition-rate optical pulse generator using a fabry-perot electro-optic modulator. *Appl. Phys. Lett.* **21**, 341–343 (1972).
- [49] Kourogi, M., Nakagawa, K. & Ohtsu, M. Wide-span optical frequency comb generator for accurate optical frequency difference measurement. *IEEE J. Quantum Electron.* **29**, 2693–2701 (1993).
- [50] Carlson, D. R. *et al.* Ultrafast electro-optic light with subcycle control. *Science* **361**, 1358–1363 (2018).
- [51] Del’Haye, P. *et al.* Optical frequency comb generation from a monolithic microresonator. *Nature* **450**, 1214–1217 (2007).
- [52] Kippenberg, T. J., Holzwarth, R. & Diddams, S. Microresonator-based optical frequency combs. *Science* **332**, 555–559 (2011).
- [53] Vahala, K. J. Optical microcavities. *Nature* **424**, 839–846 (2003).
- [54] Grudin, I. S., Ilchenko, V. S. & Maleki, L. Ultrahigh optical Q factors of crystalline resonators in the linear regime. *Phys. Rev. A* **74**, 063806 (2006).
- [55] Lee, H. *et al.* Chemically etched ultrahigh-Q wedge-resonator on a silicon chip. *Nat. Photon.* **6**, 369–373 (2012).
- [56] Ilchenko, V. & Gorodetskii, M. Thermal nonlinear effects in optical whispering gallery microresonators. *Laser Phys.* **2**, 1004–1009 (1992).
- [57] Carmon, T., Yang, L. & Vahala, K. Dynamical thermal behavior and thermal self-stability of microcavities. *Opt. Express* **12**, 4742–4750 (2004).
- [58] Spillane, S., Kippenberg, T. & Vahala, K. Ultralow-threshold raman laser using a spherical dielectric microcavity. *Nature* **415**, 621–623 (2002).
- [59] Carmon, T. & Vahala, K. J. Visible continuous emission from a silica microphotonic device by third-harmonic generation. *Nat. Phys.* **3**, 430–435 (2007).
- [60] Kippenberg, T. J. & Vahala, K. J. Cavity optomechanics: back-action at the mesoscale. *science* **321**, 1172–1176 (2008).
- [61] Kippenberg, T. J., Spillane, S. M. & Vahala, K. J. Kerr-nonlinearity optical parametric oscillation in an ultrahigh-Q toroid microcavity. *Phys. Rev. Lett.* **93**, 083904 (2004).
- [62] Herr, T. *et al.* Universal formation dynamics and noise of Kerr-frequency combs in microresonators. *Nat. Photon.* **6**, 480–487 (2012).
- [63] Li, J., Lee, H., Chen, T. & Vahala, K. J. Low-pump-power, low-phase-noise, and microwave to millimeter-wave repetition rate operation in microcombs. *Phys. Rev. Lett.* **109**, 233901 (2012).

- [64] Saha, K. *et al.* Modelocking and femtosecond pulse generation in chip-based frequency combs. *Opt. Express* **21**, 1335–1343 (2013).
- [65] Del’Haye, P. *et al.* Phase steps and resonator detuning measurements in microresonator frequency combs. *Nat. Commun.* **6**, 5668 (2015).
- [66] Herr, T. *et al.* Temporal solitons in optical microresonators. *Nat. Photon.* **8**, 145–152 (2014).
- [67] Yi, X., Yang, Q.-F., Yang, K. Y., Suh, M.-G. & Vahala, K. Soliton frequency comb at microwave rates in a high- Q silica microresonator. *Optica* **2**, 1078–1085 (2015).
- [68] Brasch, V. *et al.* Photonic chip-based optical frequency comb using soliton Cherenkov radiation. *Science* **351**, 357–360 (2016).
- [69] Leo, F. *et al.* Temporal cavity solitons in one-dimensional Kerr media as bits in an all-optical buffer. *Nat. Photon.* **4**, 471–476 (2010).
- [70] Kippenberg, T. J., Gaeta, A. L., Lipson, M. & Gorodetsky, M. L. Dissipative Kerr solitons in optical microresonators. *Science* **361** (2018).
- [71] Liang, W. *et al.* High spectral purity Kerr frequency comb radio frequency photonic oscillator. *Nat. Commun.* **6**, 7957 (2015).
- [72] Obrzud, E., Lecomte, S. & Herr, T. Temporal solitons in microresonators driven by optical pulses. *Nat. Photon.* **11**, 600 (2017).
- [73] Yang, K. Y. *et al.* Bridging ultrahigh- Q devices and photonic circuits. *Nat. Photon.* **12**, 297–302 (2018).
- [74] Lu, Z. *et al.* Deterministic generation and switching of dissipative kerr soliton in a thermally controlled micro-resonator. *arXiv preprint arXiv:1810.04983* (2018).
- [75] Zhang, S. *et al.* Sub-milliwatt-level microresonator solitons with extended access range using an auxiliary laser. *Optica* **6**, 206–212 (2019).
- [76] Wang, P.-H. *et al.* Intracavity characterization of micro-comb generation in the single-soliton regime. *Opt. Express* **24**, 10890–10897 (2016).
- [77] Joshi, C. *et al.* Thermally controlled comb generation and soliton modelocking in microresonators. *Opt. Lett.* **41**, 2565–2568 (2016).
- [78] Bao, H. *et al.* Laser cavity-soliton microcombs. *Nat. Photon.* (2019).
- [79] Yu, M., Okawachi, Y., Griffith, A. G., Lipson, M. & Gaeta, A. L. Mode-locked mid-infrared frequency combs in a silicon microresonator. *Optica* **3**, 854–860 (2016).

- [80] He*, Y. *et al.* A self-starting bi-chromatic LiNbO₃ soliton microcomb. *arXiv preprint arXiv:1812.09610* (2018).
- [81] Gong, Z. *et al.* High-fidelity cavity soliton generation in crystalline aln micro-ring resonators. *Opt. Lett.* **43**, 4366–4369 (2018).
- [82] Li, Q. *et al.* Stably accessing octave-spanning microresonator frequency combs in the soliton regime. *Optica* **4**, 193–203 (2017).
- [83] Pfeiffer, M. H. *et al.* Octave-spanning dissipative Kerr soliton frequency combs in si₃n₄ microresonators. *Optica* **4**, 684–691 (2017).
- [84] Yi, X. *et al.* Single-mode dispersive waves and soliton microcomb dynamics. *Nat. Commun.* **8**, 14869 (2017).
- [85] Liu, J. *et al.* Ultralow-power chip-based soliton microcombs for photonic integration. *Optica* **5**, 1347–1353 (2018).
- [86] Stern, B., Ji, X., Okawachi, Y., Gaeta, A. L. & Lipson, M. Battery-operated integrated frequency comb generator. *Nature* **562**, 401–405 (2018).
- [87] Karpov, M. *et al.* Raman self-frequency shift of dissipative Kerr solitons in an optical microresonator. *Phys. Rev. Lett.* **116**, 103902 (2016).
- [88] Yi, X., Yang, Q.-F., Yang, K. Y. & Vahala, K. Theory and measurement of the soliton self-frequency shift and efficiency in optical microcavities. *Opt. Lett.* **41**, 3419–3422 (2016).
- [89] Yang, Q.-F., Yi, X., Yang, K. Y. & Vahala, K. Stokes solitons in optical microcavities. *Nat. Phys.* **13**, 53–57 (2017).
- [90] Yang, Q.-F., Yi, X., Yang, K. Y. & Vahala, K. Spatial-mode-interaction-induced dispersive-waves and their active tuning in microresonators. *Optica* **3**, 1132–1135 (2016).
- [91] Bao, C. *et al.* Spatial mode-interaction induced single soliton generation in microresonators. *Optica* **4**, 1011–1015 (2017).
- [92] Lucas, E., Guo, H., Jost, J. D., Karpov, M. & Kippenberg, T. J. Detuning-dependent properties and dispersion-induced instabilities of temporal dissipative kerr solitons in optical microresonators. *Phys. Rev. A* **95**, 043822 (2017).
- [93] Guo, H. *et al.* Intermode breather solitons in optical microresonators. *Phys. Rev. X* **7**, 041055 (2017).
- [94] Bao, C. *et al.* Observation of fermi-pasta-ulam recurrence induced by breather solitons in an optical microresonator. *Phys. Rev. Lett.* **117**, 163901 (2016).

- [95] Yu, M. *et al.* Breather soliton dynamics in microresonators. *Nat. Commun.* **8**, 14569 (2017).
- [96] Lucas, E., Karpov, M., Guo, H., Gorodetsky, M. & Kippenberg, T. Breathing dissipative solitons in optical microresonators. *Nat. Commun.* **8**, 736 (2017).
- [97] Weng, W. *et al.* Heteronuclear soliton molecules in optical microresonators. *arXiv preprint arXiv:1901.04026* (2019).
- [98] Cole, D. C., Lamb, E. S., Del’Haye, P., Diddams, S. A. & Papp, S. B. Soliton crystals in Kerr resonators. *Nat. Photon.* **11**, 671 (2017).
- [99] Yang, Q.-F., Yi, X., Yang, K. Y. & Vahala, K. Counter-propagating solitons in microresonators. *Nat. Photon.* **11**, 560–564 (2017).
- [100] Lucas, E. *et al.* Spatial multiplexing of soliton microcombs. *Nat. Photon.* **12**, 699–705 (2018).
- [101] Jang, J. K. *et al.* Synchronization of coupled optical microresonators. *Nat. Photon.* **12**, 688–693 (2018).
- [102] Xue, X. *et al.* Normal-dispersion microcombs enabled by controllable mode interactions. *Laser Photonics Rev.* **9**, L23–L28 (2015).
- [103] Newman, Z. *et al.* Photonic integration of an optical atomic clock. *arXiv preprint arXiv:1811.00616* (2018).
- [104] Spencer, D. T. *et al.* An optical-frequency synthesizer using integrated photonics. *Nature* **557**, 81–85 (2018).
- [105] Suh, M.-G., Yang, Q.-F., Yang, K. Y., Yi, X. & Vahala, K. J. Microresonator soliton dual-comb spectroscopy. *Science* **354**, 600–603 (2016).
- [106] Pavlov, N. *et al.* Soliton dual frequency combs in crystalline microresonators. *Opt. Lett.* **42**, 514–517 (2017).
- [107] Dutt, A. *et al.* On-chip dual-comb source for spectroscopy. *Science advances* **4**, e1701858 (2018).
- [108] Yu, M. *et al.* Silicon-chip-based mid-infrared dual-comb spectroscopy. *Nat. Commun.* **9**, 1869 (2018).
- [109] Yang, Q.-F. *et al.* Vernier spectrometer using counterpropagating soliton microcombs. *Science* **363**, 965–968 (2019).
- [110] Trocha, P. *et al.* Ultrafast optical ranging using microresonator soliton frequency combs. *Science* **359**, 887–891 (2018).
- [111] Suh, M.-G. & Vahala, K. J. Soliton microcomb range measurement. *Science* **359**, 884–887 (2018).

- [112] Obrzud, E. *et al.* A microphotonic astrocomb. *Nat. Photon.* **13**, 31 (2019).
- [113] Suh, M.-G. *et al.* Searching for exoplanets using a microresonator astrocomb. *Nat. Photon.* **13**, 25 (2019).
- [114] Marin-Palomo, P. *et al.* Microresonator-based solitons for massively parallel coherent optical communications. *Nature* **546**, 274–279 (2017).
- [115] Mazur, M. *et al.* Enabling high spectral efficiency coherent superchannel transmission with soliton microcombs. *arXiv preprint arXiv:1812.11046* (2018).
- [116] Lee, S. H. *et al.* Towards visible soliton microcomb generation. *Nat. Commun.* **8**, 1295 (2017).
- [117] Yi, X., Yang, Q.-F., Yang, K. Y. & Vahala, K. Imaging soliton dynamics in optical microcavities. *Nat. Commun.* **9** (2018).
- [118] Mollenauer, L. F., Stolen, R. H. & Gordon, J. P. Experimental observation of picosecond pulse narrowing and solitons in optical fibers. *Phys. Rev. Lett.* **45**, 1095 (1980).
- [119] Kivshar, Y. S. & Agrawal, G. *Optical solitons: from fibers to photonic crystals* (Academic press, 2003).
- [120] Strecker, K. E., Partridge, G. B., Truscott, A. G. & Hulet, R. G. Formation and propagation of matter-wave soliton trains. *Nature* **417**, 150–153 (2002).
- [121] Khaykovich, L. *et al.* Formation of a matter-wave bright soliton. *Science* **296**, 1290–1293 (2002).
- [122] Hasegawa, A. & Kodama, Y. *Solitons in optical communications*. 7 (Oxford University Press, USA, 1995).
- [123] Picholle, E., Montes, C., Leycuras, C., Legrand, O. & Botineau, J. Observation of dissipative superluminous solitons in a brillouin fiber ring laser. *Phys. Rev. Lett.* **66**, 1454 (1991).
- [124] Vanin, E. *et al.* Dissipative optical solitons. *Phys. Rev. A* **49**, 2806 (1994).
- [125] Akhmediev, N. & Ankiewicz, A. *Dissipative solitons: from optics to biology and medicine*, vol. 751 (Springer Science & Business Media, 2008).
- [126] Coen, S., Randle, H. G., Sylvestre, T. & Erkintalo, M. Modeling of octave-spanning Kerr frequency combs using a generalized mean-field lugiato-lefever model. *Opt. Lett.* **38**, 37–39 (2013).
- [127] Lugiato, L. A. & Lefever, R. Spatial dissipative structures in passive optical systems. *Phys. Rev. Lett.* **58**, 2209 (1987).

- [128] Agrawal, G. P. *Nonlinear fiber optics* (Academic press, 2007).
- [129] Shabat, A. & Zakharov, V. Exact theory of two-dimensional self-focusing and one-dimensional self-modulation of waves in nonlinear media. *Sov. Phys. JETP* **34**, 62 (1972).
- [130] Spillane, S., Kippenberg, T., Painter, O. & Vahala, K. Ideality in a fiber-taper-coupled microresonator system for application to cavity quantum electrodynamics. *Phys. Rev. Lett.* **91**, 043902 (2003).
- [131] Chembo, Y. K. & Menyuk, C. R. Spatiotemporal lugiato-lefever formalism for Kerr-comb generation in whispering-gallery-mode resonators. *Phys. Rev. A* **87**, 053852 (2013).
- [132] Matsko, A. B. *et al.* Mode-locked Kerr frequency combs. *Opt. Lett.* **36**, 2845–2847 (2011).
- [133] Matsko, A. B. & Maleki, L. On timing jitter of mode locked Kerr frequency combs. *Opt. Express* **21**, 28862–28876 (2013).
- [134] Grelu, P. *Nonlinear Optical Cavity Dynamics: From Microresonators to Fiber Lasers* (John Wiley & Sons, 2015).
- [135] Guo, H. *et al.* Universal dynamics and deterministic switching of dissipative Kerr solitons in optical microresonators. *Nat. Phys.* **13**, 94–102 (2017).
- [136] Armani, D., Kippenberg, T., Spillane, S. & Vahala, K. Ultra-high-Q toroid microcavity on a chip. *Nature* **421**, 925–928 (2003).
- [137] Suh, M.-G. & Vahala, K. Gigahertz-repetition-rate soliton microcombs. *Optica* **5**, 65–66 (2018).
- [138] Yang, K. Y. *et al.* Broadband dispersion-engineered microresonator on a chip. *Nat. Photon.* **10**, 316 (2016).
- [139] Cai, M., Painter, O. & Vahala, K. J. Observation of critical coupling in a fiber taper to a silica-microsphere whispering-gallery mode system. *Phys. Rev. Lett.* **85**, 74 (2000).
- [140] Li, J., Lee, H., Yang, K. Y. & Vahala, K. J. Sideband spectroscopy and dispersion measurement in microcavities. *Opt. Express* **20**, 26337–26344 (2012).
- [141] Savchenkov, A. *et al.* Kerr combs with selectable central frequency. *Nat. Photon.* **5**, 293–296 (2011).
- [142] Riemensberger, J. *et al.* Dispersion engineering of thick high-Q silicon nitride ring-resonators via atomic layer deposition. *Opt. Express* **20**, 27661–27669 (2012).

- [143] Okawachi, Y. *et al.* Bandwidth shaping of microresonator-based frequency combs via dispersion engineering. *Opt. Lett.* **39**, 3535–3538 (2014).
- [144] Liu, Y. *et al.* Investigation of mode coupling in normal-dispersion silicon nitride microresonators for Kerr frequency comb generation. *Optica* **1**, 137–144 (2014).
- [145] Ramelow, S. *et al.* Strong polarization mode coupling in microresonators. *Opt. Lett.* **39**, 5134–5137 (2014).
- [146] Grudinin, I. S. & Yu, N. Dispersion engineering of crystalline resonators via microstructuring. *Optica* **2**, 221–224 (2015).
- [147] Soltani, M., Matsko, A. & Maleki, L. Enabling arbitrary wavelength frequency combs on chip. *Laser Photonics Rev.* **10**, 158–162 (2016).
- [148] Yang, Y. *et al.* Four-wave mixing parametric oscillation and frequency comb generation at visible wavelengths in a silica microbubble resonator. *Opt. Lett.* **41**, 5266–5269 (2016).
- [149] Oh, D. Y. *et al.* Coherent ultra-violet to near-infrared generation in silica ridge waveguides. *Nat. Commun.* **8**, 13922 (2017).
- [150] Moss, D. J., Morandotti, R., Gaeta, A. L. & Lipson, M. New CMOS-compatible platforms based on silicon nitride and Hydex for nonlinear optics. *Nat. Photon.* **7**, 597–607 (2013).
- [151] Hausmann, B., Bulu, I., Venkataraman, V., Deotare, P. & Lončar, M. Diamond nonlinear photonics. *Nat. Photon.* **8**, 369–374 (2014).
- [152] Xiong, C. *et al.* Aluminum nitride as a new material for chip-scale optomechanics and nonlinear optics. *New J. Phys.* **14**, 095014 (2012).
- [153] Herr, T. *et al.* Mode spectrum and temporal soliton formation in optical microresonators. *Phys. Rev. Lett.* **113**, 123901 (2014).
- [154] Del’Haye, P., Arcizet, O., Gorodetsky, M. L., Holzwarth, R. & Kippenberg, T. J. Frequency comb assisted diode laser spectroscopy for measurement of microcavity dispersion. *Nat. Photon.* **3**, 529 (2009).
- [155] Liu, J. *et al.* Frequency-comb-assisted broadband precision spectroscopy with cascaded diode lasers. *Opt. Lett.* **41**, 3134–3137 (2016).
- [156] Yi, X., Yang, Q.-F., Youl, K. & Vahala, K. Active capture and stabilization of temporal solitons in microresonators. *Opt. Lett.* **41**, 2037–2040 (2016).
- [157] Wabnitz, S. Suppression of interactions in a phase-locked soliton optical memory. *Opt. Lett.* **18**, 601–603 (1993).

- [158] Bao, C. *et al.* Nonlinear conversion efficiency in Kerr frequency comb generation. *Opt. Lett.* **39**, 6126–6129 (2014).
- [159] Atieh, A., Myslinski, P., Chrostowski, J. & Galko, P. Measuring the raman time constant (t_r) for soliton pulses in standard single-mode fiber. *J. Lightwave Technol.* **17**, 216–221 (1999).
- [160] Mitschke, F. M. & Mollenauer, L. F. Discovery of the soliton self-frequency shift. *Opt. Lett.* **11**, 659–661 (1986).
- [161] Gordon, J. P. Theory of the soliton self-frequency shift. *Opt. Lett.* **11**, 662–664 (1986).
- [162] Li, J., Lee, H., Chen, T. & Vahala, K. J. Characterization of a high coherence, brillouin microcavity laser on silicon. *Opt. Express* **20**, 20170–20180 (2012).
- [163] Loh, W. *et al.* Dual-microcavity narrow-linewidth brillouin laser. *Optica* **2**, 225–232 (2015).
- [164] Lee, H. *et al.* Spiral resonators for on-chip laser frequency stabilization. *Nat. Commun.* **4**, 2468 (2013).
- [165] Gambetta, A., Ramponi, R. & Marangoni, M. Mid-infrared optical combs from a compact amplified er-doped fiber oscillator. *Opt. Lett.* **33**, 2671–2673 (2008).
- [166] Milián, C., Gorbach, A. V., Taki, M., Yulin, A. V. & Skryabin, D. V. Solitons and frequency combs in silica microring resonators: Interplay of the raman and higher-order dispersion effects. *Phys. Rev. A* **92**, 033851 (2015).
- [167] Blow, K. J. & Wood, D. Theoretical description of transient stimulated raman scattering in optical fibers. *IEEE J. Quantum Electron.* **25**, 2665–2673 (1989).
- [168] Lin, Q. & Agrawal, G. P. Raman response function for silica fibers. *Opt. Lett.* **31**, 3086–3088 (2006).
- [169] Hasegawa, A. Soliton-based optical communications: An overview. *IEEE J. Sel. Top. Quantum Electron.* **6**, 1161–1172 (2000).
- [170] Herr, T., Gorodetsky, M. L. & Kippenberg, T. J. Dissipative Kerr solitons in optical microresonators. *arXiv preprint arXiv:1508.04989* (2015).
- [171] Skryabin, D., Luan, F., Knight, J. & Russell, P. S. J. Soliton self-frequency shift cancellation in photonic crystal fibers. *Science* **301**, 1705–1708 (2003).
- [172] Hasegawa, A. & Tappert, F. Transmission of stationary nonlinear optical pulses in dispersive dielectric fibers. i. anomalous dispersion. *Appl. Phys. Lett.* **23**, 142–144 (1973).

- [173] Haus, H. A. & Wong, W. S. Solitons in optical communications. *Rev. Mod. Phys.* **68**, 423 (1996).
- [174] Cundiff, S. Soliton dynamics in mode-locked lasers. In *Dissipative Solitons*, 183–206 (Springer, 2005).
- [175] Islam, M. N. Raman amplifiers for telecommunications. *IEEE J. Sel. Topics Quantum Electron.* **8**, 548–559 (2002).
- [176] Headley, C. & Agrawal, G. P. Unified description of ultrafast stimulated raman scattering in optical fibers. *J. Opt. Soc. Am. B* **13**, 2170–2177 (1996).
- [177] Bao, C., Chang, W., Yang, C., Akhmediev, N. & Cundiff, S. T. Observation of coexisting dissipative solitons in a mode-locked fiber laser. *Phys. Rev. Lett.* **115**, 253903 (2015).
- [178] Soto-Crespo, J. M. & Akhmediev, N. Composite solitons and two-pulse generation in passively mode-locked lasers modeled by the complex quintic swift-hohenberg equation. *Phys. Rev. E* **66**, 066610 (2002).
- [179] Menyuk, C. R. Stability of solitons in birefringent optical fibers. i: Equal propagation amplitudes. *Opt. Lett.* **12**, 614–616 (1987).
- [180] Islam, M., Poole, C. & Gordon, J. Soliton trapping in birefringent optical fibers. *Opt. Lett.* **14**, 1011–1013 (1989).
- [181] Cundiff, S. *et al.* Observation of polarization-locked vector solitons in an optical fiber. *Phys. Rev. Lett.* **82**, 3988 (1999).
- [182] Collings, B. C. *et al.* Polarization-locked temporal vector solitons in a fiber laser: experiment. *J. Opt. Soc. Am. B* **17**, 354–365 (2000).
- [183] Hasegawa, A. Self-confinement of multimode optical pulse in a glass fiber. *Opt. Lett.* **5**, 416–417 (1980).
- [184] Crosignani, B. & Di Porto, P. Soliton propagation in multimode optical fibers. *Opt. Lett.* **6**, 329–330 (1981).
- [185] Renninger, W. H. & Wise, F. W. Optical solitons in graded-index multimode fibres. *Nat. Commun.* **4**, 1719 (2013).
- [186] Wai, P., Menyuk, C. R., Lee, Y. & Chen, H. Nonlinear pulse propagation in the neighborhood of the zero-dispersion wavelength of monomode optical fibers. *Opt. Lett.* **11**, 464–466 (1986).
- [187] Akhmediev, N. & Karlsson, M. Cherenkov radiation emitted by solitons in optical fibers. *Phys. Rev. A* **51**, 2602 (1995).
- [188] Cherenkov, P. A. Visible emission of clean liquids by action of γ radiation. *Doklady Akademii Nauk SSSR* **2**, 451 (1934).

- [189] Brasch, V., Lucas, E., Jost, J. D., Geiselmann, M. & Kippenberg, T. J. Self-referenced photonic chip soliton Kerr frequency comb. *Light Sci Appl.* **6**, e16202 (2017).
- [190] Cheng, J. *et al.* Intermodal čerenkov radiation in a higher-order-mode fiber. *Opt. Lett.* **37**, 4410–4412 (2012).
- [191] Manili, G. *et al.* Gigantic dispersive wave emission from dual concentric core microstructured fiber. *Opt. Lett.* **37**, 4101–4103 (2012).
- [192] Modotto, D. *et al.* Efficiency of dispersive wave generation in dual concentric core microstructured fiber. *J. Opt. Soc. Am. B* **32**, 1676–1685 (2015).
- [193] Haus, H. A. & Huang, W. P. Coupled-mode theory. *Proc. IEEE* **79**, 1505–1518 (1991).
- [194] Wiersig, J. Formation of long-lived, scarlike modes near avoided resonance crossings in optical microcavities. *Phys. Rev. Lett.* **97**, 253901 (2006).
- [195] Jang, J. K., Erkintalo, M., Coen, S. & Murdoch, S. G. Temporal tweezing of light through the trapping and manipulation of temporal cavity solitons. *Nat. Commun.* **6** (2015).
- [196] Del’Haye, P., Arcizet, O., Schliesser, A., Holzwarth, R. & Kippenberg, T. J. Full stabilization of a microresonator-based optical frequency comb. *Phys. Rev. Lett.* **101**, 053903 (2008).
- [197] Papp, S. B. *et al.* Microresonator frequency comb optical clock. *Optica* **1**, 10–14 (2014).
- [198] Huang, S.-W. *et al.* Smooth and flat phase-locked Kerr frequency comb generation by higher order mode suppression. *Scientific reports* **6**, 26255 (2016).
- [199] Santhanam, J. & Agrawal, G. P. Raman-induced spectral shifts in optical fibers: general theory based on the moment method. *Opt. Commun.* **222**, 413–420 (2003).
- [200] Fortier, T. M. *et al.* Generation of ultrastable microwaves via optical frequency division. *Nat. Photon.* **5**, 425–429 (2011).
- [201] Schiller, S. Spectrometry with frequency combs. *Opt. Lett.* **27**, 766–768 (2002).
- [202] Keilmann, F., Gohle, C. & Holzwarth, R. Time-domain mid-infrared frequency-comb spectrometer. *Opt. Lett.* **29**, 1542–1544 (2004).
- [203] Coddington, I., Swann, W. & Newbury, N. Coherent dual-comb spectroscopy at high signal-to-noise ratio. *Phys. Rev. A* **82**, 043817 (2010).

- [204] Giaccari, P., Deschênes, J.-D., Saucier, P., Genest, J. & Tremblay, P. Active fourier-transform spectroscopy combining the direct rf beating of two fiber-based mode-locked lasers with a novel referencing method. *Opt. Express* **16**, 4347–4365 (2008).
- [205] Bernhardt, B. *et al.* Cavity-enhanced dual-comb spectroscopy. *Nat. Photon.* **4**, 55–57 (2010).
- [206] Ideguchi, T., Poisson, A., Guelachvili, G., Picqué, N. & Hänsch, T. W. Adaptive real-time dual-comb spectroscopy. *Nat. Commun.* **5** (2014).
- [207] Okubo, S. *et al.* Ultra-broadband dual-comb spectroscopy across 1.0–1.9 μm . *Appl. Phys. Express* **8**, 082402 (2015).
- [208] Minoshima, K. & Matsumoto, H. High-accuracy measurement of 240-m distance in an optical tunnel by use of a compact femtosecond laser. *Appl. Opt.* **39**, 5512–5517 (2000).
- [209] Ye, J. Absolute measurement of a long, arbitrary distance to less than an optical fringe. *Opt. Lett.* **29**, 1153–1155 (2004).
- [210] Swann, W. C. & Newbury, N. R. Frequency-resolved coherent lidar using a femtosecond fiber laser. *Opt. Lett.* **31**, 826–828 (2006).
- [211] Coddington, I., Newbury, N. & Swann, W. Dual-comb spectroscopy. *Optica* **3**, 414–426 (2016).
- [212] Savchenkov, A. A. *et al.* Tunable optical frequency comb with a crystalline whispering gallery mode resonator. *Phys. Rev. Lett.* **101**, 093902 (2008).
- [213] Grudinin, I. S., Yu, N. & Maleki, L. Generation of optical frequency combs with a CaF_2 resonator. *Opt. Lett.* **34**, 878–880 (2009).
- [214] Papp, S. B. & Diddams, S. A. Spectral and temporal characterization of a fused-quartz-microresonator optical frequency comb. *Phys. Rev. A* **84**, 053833 (2011).
- [215] Okawachi, Y. *et al.* Octave-spanning frequency comb generation in a silicon nitride chip. *Opt. Lett.* **36**, 3398–3400 (2011).
- [216] Savchenkov, A. A. *et al.* Low threshold optical oscillations in a whispering gallery mode c a f 2 resonator. *Phys. Rev. Lett.* **93**, 243905 (2004).
- [217] Hugi, A., Villares, G., Blaser, S., Liu, H. & Faist, J. Mid-infrared frequency comb based on a quantum cascade laser. *Nature* **492**, 229–233 (2012).
- [218] Villares, G., Hugi, A., Blaser, S. & Faist, J. Dual-comb spectroscopy based on quantum-cascade-laser frequency combs. *Nat. Commun.* **5** (2014).

- [219] Rösch, M. *et al.* On-chip, self-detected terahertz dual-comb source. *Appl. Phys. Lett.* **108**, 171104 (2016).
- [220] Fleisher, A. J. *et al.* Mid-infrared time-resolved frequency comb spectroscopy of transient free radicals. *J. Phys. Chem. Lett.* **5**, 2241–2246 (2014).
- [221] Reber, M. A., Chen, Y. & Allison, T. K. Cavity-enhanced ultrafast spectroscopy: ultrafast meets ultrasensitive. *Optica* **3**, 311–317 (2016).
- [222] Jost, J. *et al.* Counting the cycles of light using a self-referenced optical microresonator. *Optica* **2**, 706–711 (2015).
- [223] Adler, R. A study of locking phenomena in oscillators. *Proc. IEEE* **34**, 351–357 (1946).
- [224] Willner, A., Yu, C. & Pan, Z. *Optical Fiber Telecommunications VB (Fifth Edition): Chapter 7* (Academic Press, 2008).
- [225] Allen, M. G. Diode laser absorption sensors for gas-dynamic and combustion flows. *Meas. Sci. Technol.* **9**, 545–562 (1998).
- [226] Choma, M. A., Sarunic, M. V., Yang, C. & Izatt, J. A. Sensitivity advantage of swept source and fourier domain optical coherence tomography. *Opt. Express* **11**, 2183–2189 (2003).
- [227] Coddington, I., Giorgetta, F. R., Baumann, E., Swann, W. C. & Newbury, N. R. Characterizing fast arbitrary cw waveforms with 1500 thz/s instantaneous chirps. *IEEE J. Sel. Top. Quantum Electron.* **18**, 228–238 (2012).
- [228] Ma, L.-S., Zucco, M., Picard, S., Robertsson, L. & Windeler, R. S. A new method to determine the absolute mode number of a mode-locked femtosecond-laser comb used for absolute optical frequency measurements. *IEEE J. Sel. Top. Quantum Electron.* **9**, 1066–1071 (2003).
- [229] Peng, J.-L., Liu, T.-A. & Shu, R.-H. Optical frequency counter based on two mode-locked fiber laser combs. *Appl. Phys. B* **92**, 513–518 (2008).
- [230] Tran, M. A., Huang, D., Komljenovic, T., Peters, J. & Bowers, J. E. A 2.5 khz linewidth widely tunable laser with booster soa integrated on silicon. *Proceedings of the 2018 IEEE International Semiconductor Laser Conference, Santa Fe 1–2* (2018).
- [231] Gordon, I. E. *et al.* The HITRAN2016 molecular spectroscopic database. *Journal of Quantitative Spectroscopy and Radiative Transfer* **203**, 3–69 (2017).
- [232] Lamb, E. S. *et al.* Optical-frequency measurements with a Kerr microcomb and photonic-chip supercontinuum. *Phys. Rev. Appl.* **9**, 024030 (2018).

- [233] Dudley, J. M., Dias, F., Erkintalo, M. & Genty, G. Instabilities, breathers and rogue waves in optics. *Nat. Photon.* **8**, 755–764 (2014).
- [234] Jang, J. K., Erkintalo, M., Murdoch, S. G. & Coen, S. Ultraweak long-range interactions of solitons observed over astronomical distances. *Nat. Photon.* **7**, 657–663 (2013).
- [235] Luo, K., Jang, J. K., Erkintalo, M., Murdoch, S. G. & Coen, S. Real-time spectral evolution of breathing temporal cavity solitons. In *European Quantum Electronics Conference*, EF_P_18 (Optical Society of America, 2015).
- [236] Luo, K., Jang, J. K., Coen, S., Murdoch, S. G. & Erkintalo, M. Spontaneous creation and annihilation of temporal cavity solitons in a coherently driven passive fiber resonator. *Opt. Lett.* **40**, 3735–3738 (2015).
- [237] Anderson, M., Leo, F., Coen, S., Erkintalo, M. & Murdoch, S. G. Observations of spatiotemporal instabilities of temporal cavity solitons. *Optica* **3**, 1071–1074 (2016).
- [238] Jang, J. K. *et al.* Controlled merging and annihilation of localised dissipative structures in an ac-driven damped nonlinear schrödinger system. *New J. Phys.* **18**, 033034 (2016).
- [239] Herink, G., Kurtz, F., Jalali, B., Solli, D. & Ropers, C. Real-time spectral interferometry probes the internal dynamics of femtosecond soliton molecules. *Science* **356**, 50–54 (2017).
- [240] Anderson, M. *et al.* Coexistence of multiple nonlinear states in a tristable passive Kerr resonator. *Phys. Rev. X* **7**, 031031 (2017).
- [241] Foster, M. A. *et al.* Silicon-chip-based ultrafast optical oscilloscope. *Nature* **456**, 81–84 (2008).
- [242] Goda, K. & Jalali, B. Dispersive fourier transformation for fast continuous single-shot measurements. *Nat. Photon.* **7**, 102–112 (2013).
- [243] Ryzkowski, P. *et al.* Real-time full-field characterization of transient dissipative soliton dynamics in a mode-locked laser. *Nat. Photon.* **12**, 221 (2018).
- [244] Tikan, A., Bielawski, S., Szwaj, C., Randoux, S. & Suret, P. Single-shot measurement of phase and amplitude by using a heterodyne time-lens system and ultrafast digital time-holography. *Nat. Photon.* **12**, 228 (2018).
- [245] Lobanov, V. E. *et al.* Harmonization of chaos into a soliton in Kerr frequency combs. *Opt. Express* **24**, 27382–27394 (2016).
- [246] Okawachi, Y. *et al.* Asynchronous single-shot characterization of high-repetition-rate ultrafast waveforms using a time-lens-based temporal magnifier. *Opt. Lett.* **37**, 4892–4894 (2012).

- [247] Wang, Y. *et al.* Universal mechanism for the binding of temporal cavity solitons. *Optica* **4**, 855–863 (2017).
- [248] Akhmediev, N. & Korneev, V. Modulation instability and periodic solutions of the nonlinear schrödinger equation. *Theor. Math. Phys.* **69**, 1089–1093 (1986).
- [249] Leo, F., Gelens, L., Emplit, P., Haelterman, M. & Coen, S. Dynamics of one-dimensional Kerr cavity solitons. *Opt. Express* **21**, 9180–9191 (2013).
- [250] Wang, Y., Anderson, M., Coen, S., Murdoch, S. G. & Erkintalo, M. Stimulated raman scattering imposes fundamental limits to the duration and bandwidth of temporal cavity solitons. *Phys. Rev. Lett.* **120**, 053902 (2018).
- [251] Coddington, I., Swann, W. C. & Newbury, N. R. Coherent linear optical sampling at 15 bits of resolution. *Opt. Lett.* **34**, 2153–2155 (2009).
- [252] Ferdous, F., Leaird, D. E., Huang, C.-B. & Weiner, A. Dual-comb electric-field cross-correlation technique for optical arbitrary waveform characterization. *Opt. Lett.* **34**, 3875–3877 (2009).
- [253] Murata, H., Morimoto, A., Kobayashi, T. & Yamamoto, S. Optical pulse generation by electrooptic-modulation method and its application to integrated ultrashort pulse generators. *IEEE J. Sel. Top. Quantum Electron.* **6**, 1325–1331 (2000).
- [254] Durán, V., Tainta, S. *et al.* Ultrafast electrooptic dual-comb interferometry. *Opt. Express* **23**, 30557–30569 (2015).